

Alma Mater Studiorum - Università di Bologna

DOTTORATO DI RICERCA IN
NANOSCIENZE PER LA MEDICINA E PER L'AMBIENTE

Ciclo 35

Settore Concorsuale: 03/A2 - MODELLI E METODOLOGIE PER LE SCIENZE CHIMICHE

Settore Scientifico Disciplinare: CHIM/02 - CHIMICA FISICA

STUDY OF MATERIALS AND INTERPHASES FOR ELECTROCHEMICAL
ENERGY STORAGE FROM RENEWABLE SOURCES

Presentata da: Giampaolo Lacarbonara

Coordinatore Dottorato

Dario Braga

Supervisore

Catia Arbizzani

Esame finale anno 2023

Table of Contents

SUMMARY.....	1
1. INTRODUCTION.....	4
1.1. Energy needs	4
1.2. Energy storage systems	5
2. ELECTROCHEMICAL ENERGY STORAGE SYSTEMS	8
2.1. Cell Components	8
2.2. Principles of Operation of a Cell	9
2.3. Crucial battery metrics.....	14
3. DIFFERENT SYSTEMS FOR DIFFERENT TASKS	16
4. LITHIUM-ION BATTERIES (LIB)	19
4.1. Positive electrode materials	22
4.3 Electrolyte	24
4.4. Separator.....	28
4.5. Negative electrodes	28
4.5.1. The problem of volume expansion and gas evolution	33
4.5.2. Metal oxides as alternative negative electrodes for LiBs	48
4.5.3. Carbon from CO ₂ -capture.....	49
4.5.4. MnO _x - graphitic carbon composite from CO ₂ for sustainable Li-ion battery anodes	53
4.6. Application and specifications	69
5. LITHIUM METAL BATTERIES	72
5.1. Solid Electrolyte Interphase	72
5.2. Lithium metal batteries and the dendritic growth.....	77
5.3. Strategy to inhibit dendrites formation	78
5.4. Processes studied with operando techniques	80
5.5. Operando Raman spectroscopy of lithium metal symmetric cell.....	82
5.6. Application and specifications	99
6. REDOX FLOW BATTERIES (RFB).....	102
6.1. Standard configuration	104
6.1.1. Vanadium-based systems.....	104
6.1.2. Organic redox flow batteries.....	106
6.2. Hybrid configurations	107

6.2.1. Zinc-based systems.....	107
6.2.2. All-iron RFBs	109
7. ALL-COPPER RFBs	110
7.1. Principle of operation	111
7.2. Formation of chlorocomplexes	113
7.4. Cell components.....	142
7.4.1. Negative electrode.....	142
7.4.2. Positive electrode.....	143
7.4.2.1. Short thermal treatment of carbon felts for CuRFBs.....	144
7.4.3. Membranes.....	166
7.4.4. Scanning electrochemical microscopy method for Cu^{2+} permeability investigation on membranes for Redox Flow Battery.....	167
7.5. SoC sensors	179
7.6 Applications and specifications	186
8. CONCLUSIONS	188
9. APPENDIX	193
9.1. List of publications.....	193
9.2. Participation at conferences.....	195
ACKNOWLEDGMENTS	197
REFERENCES.....	199

Summary

The concept of electrification is accompanied by higher demand for energy storage systems. Ideally, new technologies must have an ever-higher energy density, lower costs, more extended durability, and the use of more sustainable materials.

Nowadays, mostly lithium-ion batteries are used for different purposes. Batteries should be refined depending on their application for a future in which the sustainable energy demand increases. On the one hand, it is fundamental to improve their safety, prevent failures and damages, increase energy density, and reduce production costs. On the other hand, new battery materials and architecture are required to satisfy the growing demand. A clear understanding of materials and processes during operation must be established to move these technologies closer to realization.

This thesis explores different electrochemical storage systems and new methodologies to investigate complex and dynamic processes to make the future battery even more reliable. Chapter 1 introduces the energy transition's importance and the energy storage system's role. Among them, electrochemical energy storage systems are generally described in Chapter 2 with a focus on batteries. The electrochemical processes that make the battery operate are present with the description of the most used metrics. Chapter 3 introduces an essential concept for the employment of batteries: different systems are needed to perform different tasks. In Chapter 4, the most employed electrochemically stored system is presented. Lithium-ion batteries are described in all their cell components. The activities performed on this technology are summarized in sections 4.5.1 and 4.5.4. In lithium-ion systems, this thesis looks mainly into negative electrodes. Both the development of new sustainable materials and new in situ characterization of the electrode processes were explored.

Chapter 5 focuses on the lithium metal anode presented as a beyond lithium-ion technology. The criticism of the lithium metal utilization is presented, and the experimental work is reported in section 5.5. In lithium-metal systems, this thesis looks mainly into the stabilization of the electrode-electrolyte interphase by using additives. As a sustainable alternative for stationary applications, Redox Flow Batteries (RFBs) are presented in Chapter 6. As a versatile and modular battery architecture, the state of

the art of different battery chemistries is reported. Among them, all-copper RFBs (CuRFB) are the object of Chapter 7. I investigate all the cell components and redox species reactivity on this technology. The results are presented in sections 7.2, 7.4.2.1, 7.4.4, and 7.5. The optimization of these diverse systems is crucial for the future battery panorama.

In Li-ion systems, in-situ electrochemical dilatometry has been used to predict structural changes and the related process of a model electrode. On the material side, a MnO_x -graphitic carbon composite obtained by electrolysis of CO_2 via molten Li_2CO_3 is characterized and used to prepare a negative electrode for LiBs with an environmentally sustainable aqueous process. The activities carried out on the in situ electrodilatometric system were conducted in collaboration with Marposs S.p.a., while studies on MnO_x -graphitic carbon composite was linked to a collaboration with the National Institute of Physics and Biophysics of Tallinn. The latter work set the groundwork for the EIT Raw Materials European Project CO_2 Carbon (2022-2023).

One strategy to achieve a high energy density storage system is employing lithium metal anodes. In this framework, controlling the lithium electrolyte interphase is fundamental to limit the uncontrolled dendritic deposition responsible for safety issues. Ammonium hexafluorophosphate is demonstrated to be a suitable additive modifying the interphase. Galvanostatic deposition/stripping cycles, electrochemical impedance spectroscopy, in situ optical microscopy, and operando confocal Raman spectroscopy have been used to study lithium metal-electrolyte interphase in the presence of the additive. A preparatory assessment of the conditions required to carry out an in situ TEM experiment of lithium deposition/stripping has been set out with the idea of evaluating the effect of the additives on the process in the framework of the ENEA project.

RFBs are an ideal choice for large stationary applications because they generally use low-cost and earth-abundant raw materials. In the H2020 European project, CuBER, an all-copper aqueous RFB (CuRFB), has been studied in all its aspects. The stabilization of cupric cation in the aqueous electrolyte is solved by complexation with chloride anions. Hence, optimizing the electrolyte composition is essential to achieve a stable system. Spectro-electrochemical test in diluted solution has been used to get

information on the electrochemical behaviour of electrolytes with a different chloro-complexes distribution. In concentrated solutions, electrolyte composition was optimized by varying copper-to-chloride ratios, the concentration, and the counter-ion of the chloride complexing agent.

On the electrode side, Carbon Felts (CF) are interesting materials with low cost and adequate electrical conductivity. Optimizing thermal treatment was carried out to improve the kinetics of the reaction. Thermal treatment of 6 hours at 400 °C was proved to be a favourable compromise between the electrochemical performance of the electrode and the carbon footprint associated with the manufacturing processes. In RFC configuration, although there are margins of optimization, an efficiency of 92% (30 mA cm⁻²) and the ability to sustain currents up to 50 mA cm⁻² were achieved.

One of the main obstacles in RFB commercialization is deputed to the crossover of the redox species through the membrane. A new method for permeability studies was designed using scanning electrochemical microscopy (SECM). The Cu(II) permeability of several commercial and modified membranes was tested, obtaining direct visualization of copper (II) concentration in space. As expected, the Cu(II) permeability with commercial membranes follows the trend: porous membranes > cation exchange membranes > anion exchange membranes. The best performing SPEEK-modified membranes demonstrated that this method can assist membrane research. Also, the contact-angle measurements were performed to evaluate membranes wettability. This information contribute to understanding permeation in different time scales. The copper cations crossover produces electrolyte unbalancing or self-discharge. For this purpose, monitoring the state of charge (SoC) during the RFB operation is fundamental. Two different spectrophotometric approaches were designed for SoC monitoring systems for negative and positive half-cells.

The publication used in this thesis are indicated in the text with the roman notation and reported at the beginning of the Reference section.

In summary, my PhD's experimental work led to the production of eleven scientific papers (five published, one accepted, one in revision and four in preparation), one book chapter and participation in ten conferences (eight oral and four poster contributions).

1. Introduction

This chapter introduces the importance of energy transition and presents the different energy storage systems.

1.1. *Energy needs*

Before technological developments with the first industrial revolution of the mid-1700s, human energy needs were limited to the sun, burned wood, straw, and dung. The concept of mobility was tied to horses and sailing ships. Also, processing and manufacturing, and all the work that we could not perform with our labour, were devolved into simple machines that used the energy of animals.

The first changes in human energy consumption arose with ramping up of the evolution of steam engines in the 17th and 18th centuries and the breakthrough of Thomas Newcomen and James Watt in the mid-1700s that gave rise to the modern steam engine. At that time, coal replaced wind, water, and animals' food as energy sources. In less than one year, coal was used for heating, powering steam engines motor and generating electricity (1880).

Just few years later, oil was recognized as a fuel capable of lighting better than whale oil and processed into gasoline, able to fire internal combustion engines. At that time, the first steps toward sustainability and environmental preservation were taken with hydroelectric plants and the development of the first electric car in 1896 by Henry Ford. Moreover, when gas powered cars adopted electric starting, their superior range quickly brought them to the top of the market.

With the low-cost automobile and the spread of electricity, our society's energy proliferated, doubling every ten years. After World War II, the employment of unsustainable energy sources rose out of control until the Great Energy Crash in 1973 with the Arab oil-producing nations stopped. [1]

This event highlighted for the first time the world's continued dependency on fossil fuels. This topic seems more relevant than ever given the energy crisis we are experiencing in 2022. In addition, the unchecked exploitation of fossil fuels is falling in dramatic increase in greenhouses gas emission and climatic changes relative issues. In 2018, primary energy consumption in Europe was 635 million tonnes of oil equivalent (Mtoe) spread over a range of different energy sources, with renewable

energy sources contributing more than one third (34.2%) of the EU's total production (Figure 1.1). This energy fraction has increased significantly in the last decades in combination with the increased energy demand [2].

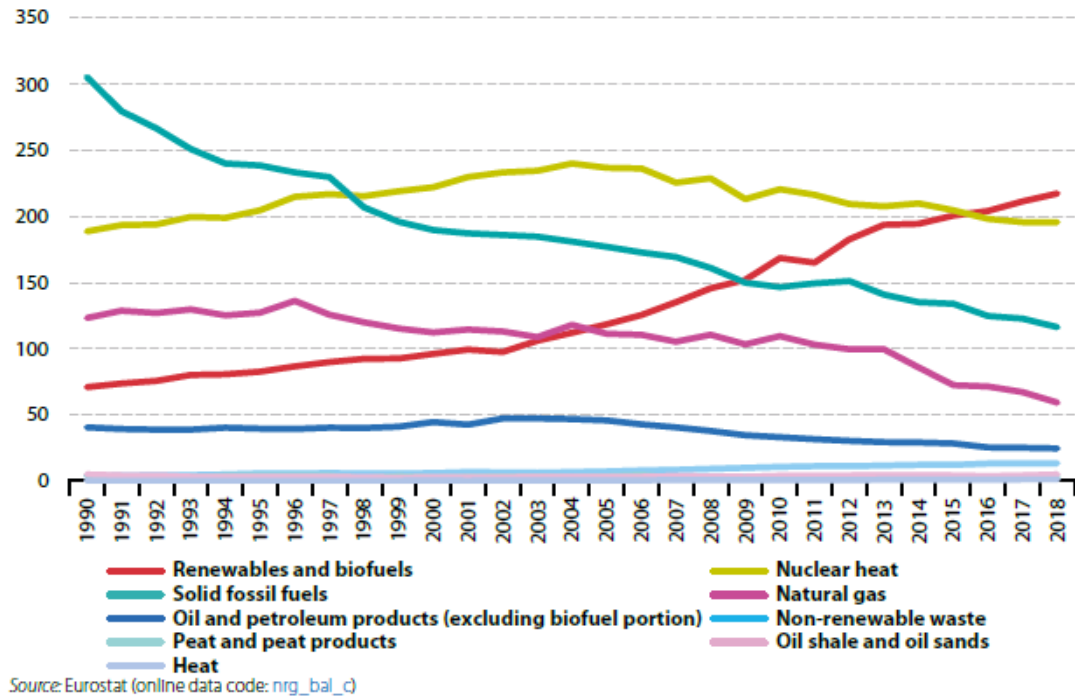


Figure 1.1. Primary energy production EU-27, 1990-2018 (million tonnes of oil equivalent).

1.2. Energy storage systems

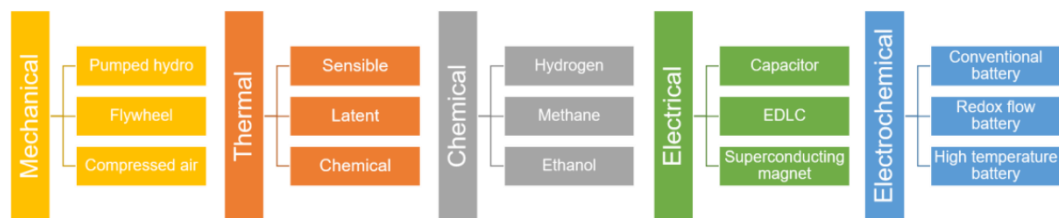
Renewable energy sources (especially wind and solar) are intermittent, stochastic and characterized by their time variability. Therefore, the desire to boost their permeation in the energetic mix must be faced with the integration of generation units that can compensate for the gap between energy generated and demand [3]. Energy storage can be incorporated into the grid to act as a buffer. Added to the energy grid, these systems can compensate for the power difference between renewable energy generation and demand [4].

In this perspective, storage can play this role in different time scales [5]:

- Energy storage can be used continuously to completely decouple the timing of generation and consumption (Bulk energy storage or energy management storage media)

- Storage systems can be used for peak shaving acting for seconds to minutes to assure continuity of service when switching from one energy source to another (Distributed generation or bridging power).
- Energy storage systems, applied for seconds or less, can assure continuity of quality power (Power quality or end-use reliability).

In this wide context, energy storage systems can act and store energy by taking advantage of different mechanisms. In Scheme 1.1 the most significant energy storage systems are summarized. As expected, not all the energy storage systems are suitable for all the applications. In fact, diverse energy storage physics and chemistries have advantages and limitations.



Scheme 1.1. Classification of energy storage system depending on the kind of energy stored: mechanical, thermal, chemical, electrical and electrochemical.

- Mechanical energy storage systems (e.g flywheel) can readily deliver the energy whenever required for mechanical works and are easily adaptable. On the other hand, they need much maintenance by formed staff and with high costs [6].
- Chemical energy storage (e. g. coal, gasoline, diesel fuel, natural gas, liquefied petroleum gas (LPG), propane, butane, ethanol, biodiesel and hydrogen) stores the energy in the chemical bonds and, releases it by reaction converting the chemical species to a less energetic one. If this source seems easy to consume, store and transport from a certain perspective, it is often harmful to the environment and non-renewable. Thermal energy storage systems (e. g. Concentrated Solar Tower Power Plant, molten salts) [7,8] has the potential for higher efficiency and lower costs. But the selection of a latent heat storage material is not trivial. The most significant standard materials have a restricted

utilization of latent heat storage in terms of the number of cycles with no change in the properties.

- Electric energy storage systems (capacitors and supercapacitor, and magnetic/current energy storage system) [9] represent the best energy storage technologies in terms of power densities (supercapacitor) with limits for energy densities which make supercapacitors uneconomical in stationary applications. In addition, they often suffer high level of self-discharge, and, in the case of magnetic based systems cooling to below $-200\text{ }^{\circ}\text{C}$ is needed.
- Electrochemical energy storage systems (EESS) (e. g. batteries) are characterized by high level of efficiency, fast response time, low self-discharge. Their applications and limitations are highly dependent on the chemistry on which they are based and will be discussed extensively in the following sections.

2. Electrochemical energy storage systems

As reported at the end of chapter 1, energy storage systems were classified depending on the kind of energy stored. In this chapter, EESSs are described and presented, focusing on the cell components, the principle of operation and the commonly used metrics used to define the system performance.

2.1. Cell Components

The history of stationary EESS dates to the 1920s, when power plants were often shut down overnight, with lead-acid accumulators (invented in the mid-19th century) delivering the residual loads on DC grids [10].

Beyond that, regardless of chemistry, all the batteries share certain features. They are composed by single or multi-electrochemical cells, which can be connected in series/parallel to achieve the desired voltage or/and capacity. As shown in Figure 2.1, each cell consists of two electrodes, positive and negative electrode, divided by a separator and immersed in electrolyte solution.

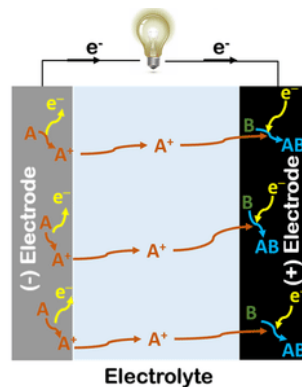


Figure 2.1. Electrochemical cell scheme.

Electrodes should withstand certain properties:

- Low reduction potential for the material operating as a negative electrode and high reduction potential for the one operating as a positive electrode. Therefore, high Fermi energy for the negative electrode (but lower than the lowest unoccupied molecular orbital (LUMO) of the electrolyte) and low Fermi energy for the positive electrode (but higher than the highest occupied

molecular orbital (HOMO) of the electrolyte), so that the materials are compatible with the stability window of the electrolyte.

- Reversible faradaic reactions, accompanied by small volume changes, in case in which the electrode is electrochemically active. Minimal structural changes to avoid loss of electrical contact and, hence, to ensure long cycle lives.
- Electrode material as light as possible to ensure a high specific capacity of the material (cells with high potentials and high specific capacity are characterized by high specific energies).
- Sufficiently high electronic and ionic conductivity (for metal-ions battery) and low charge transfer resistance to ensure fast electrode kinetics and thus high battery power.
- Environmental compatibility (non-toxic materials) and low cost.

The separator is placed between the electrodes to prevent short-circuiting and simultaneously allow ion transport. Usually, a microporous layer of polymer membrane (made by electrospinning) or non-woven fabric is used as a separator. It must be chemically and electrochemically stable towards the electrolyte and electrode materials.

Structurally, the separator must have sufficient porosity to absorb the liquid electrolyte and have high ionic conductivity. The presence of the separator adds electrical resistance to the system.

Thus, the separator itself does not participate in the reactions occurring within the cell, but its structure and properties largely affect the performance of the cell [11-13].

2.2. *Principles of Operation of a Cell*

A cell can be schematically represented as two electrodes divided by an electrically insulating membrane and an electrolytic medium (Figure 2.2). Thus, when a spontaneous redox reaction takes place, current flows in the external circuit. This is how a battery works during the discharge process, transforming chemical energy (of the reactants) into electrical energy.

To recharge the cell, it is necessary to restore the reactants, so it is necessary to let the reaction happen in the opposite direction. This will only be possible by spending external electrical energy. During the charge of a cell, there is the conversion of electric

energy into chemical energy; for this reason, these cells are storage systems because they reversibly convert the energy.

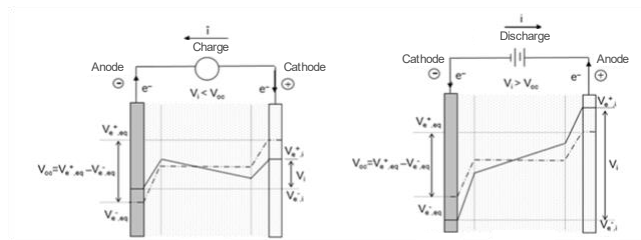
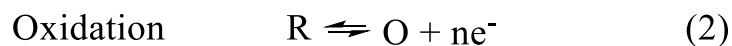


Figure 2.2. Variation of the electrode potentials of an operating electrochemical cell.

During the spontaneous discharging process, at the negative electrode oxidation occurs, while at the positive electrode reduction takes place with electrons flowing in the external circuit from the negative electrode to the positive one (by convention the current direction is the opposite). Instead, during the charging process, the current flows in the opposite direction. At the negative electrode, the reduction happens and at the positive one the oxidation occurs.



Three multiple steps are involved at a minimum:

- a. Mass transport of the electroactive species in the electrolyte (from the bulk of the solution to the electrode).
- b. Charge transfer reaction at the electrode surface.
- c. In case of electrode material that insert cations, diffusion of the metal cations in the electrode bulk.

a. In order to react at the electrode interphase, the electroactive species must be transported to the electrode from the solution. The main mass transport mechanisms are convection, migration and diffusion. Each of these mechanisms is controlled by its equation. Usually to solve mass transport equations, conditions and constraints to neglect the first two components are adopted. The diffusion is well-described by Fick laws (3) where the Fick first law explains the flux of a specie O proportionality to the concentration gradient $\partial C_o/\partial x$ for a linear (one-dimensional) diffusion.

$$-J(x, t) = D_O \frac{\partial C_O(x, t)}{\partial x} \quad (3)$$

Fick's second law (4) pertains to the change in concentration of O with time:

$$\frac{\partial C_O(x, t)}{\partial t} = D_O \frac{\partial^2 C_O(x, t)}{\partial x^2} \quad (4)$$

For a planar electrode and semi-infinite diffusion, the diffusion limited current is described as described in (5)

$$i_d(t) = \frac{nFAD_O^{1/2}C_O^*}{\pi^{1/2}t^{1/2}} \quad (5)$$

which is known as the Cottrell equation (5) where A is the electrode area, F is the Faraday constant, and n the number of electrons involved.

b. At the electrode surface, the electron transfer reaction from the electrode to the electroactive species occurs (in case of a reduction). For one-step electron processes, the electrode kinetics is described by the Butler-Volmer expression (6). With its empirical nature, this fundamental equation, describes the dependency of the current i in function of the potentials (E).

$$i = nFAk^0 \left[C_O(0, t)e^{-\frac{\alpha F}{RT}(E-E^{0'})} - C_R(0, t)e^{\frac{(1-\alpha)F}{RT}(E-E^{0'})} \right] \quad (6)$$

Where F is the Faraday constant, R is the gas constant, T is the temperature, α , the transfer coefficient, can range from zero to unity, depending on the shape of the intersection region between the free energy curve of the reactants and the products. k_0 is a measure of the kinetic facility of a redox couple, it is called standard rate constant that contains information about the process activation energies ΔG . While $E-E^{0'}$ is called charge-transfer overpotential η_{ct} [14,15].

c. The ion diffusion coefficients regulate the metal-ion insertion (e. g. Li^+ , Na^+ or K^+) in the solid. This phenomenon also depends on eventually present phase changes of the host material upon insertion/deinsertion of the guest.

These mechanisms and equations represent the basis-set for the cell (and battery) operation. In fact, the slowest step will govern the speed of the electrode process and thus the value of the current and the electric power (P) defined as expressed in equation (7).

$$P = i \times V \quad (7)$$

Where V is the cell (or battery) voltage.

The cell voltage is defined by the electrode potentials based on the spontaneous redox reactions at the electrode surfaces. These redox reactions have their standard redox potential measured versus the standard hydrogen electrode (SHE). The cell standard voltage is given by the difference between the electrode standard potentials related to the Gibbs free energy of the redox reactions as shown in equations (8) and (9).

$$E_{Cell}^0 = E_{positive}^0 - E_{negative}^0 \quad (8)$$

$$\Delta G^0 = -nFE^0 \quad (9)$$

However, the value of potential reported are in standard condition. To provide a linkage between electrode potential $E^{0'}$ and the concentrations of the participants to the reactions, Nernst equation (10) predicts the potential for practical reversible systems under equilibrium at a constant temperature.

$$E_{eq} = E^{0'} + \frac{RT}{nF} \ln \frac{C_O}{C_R} \quad (10)$$

At the equilibrium, the electrode is in a state of dynamic equilibrium: the rate at which the oxidized form O at the interphase accepts electrons from the metal is equal to the rate at which the reduced form R gives them up, so the cathodic component of the current, i_c (which is the measure of the rate at which O is reduced to R), is equal in absolute value to the anodic component, i_a , (which is the measure of the rate at which R is oxidized to O), so $i_{tot} = i_c + i_a = 0$, and the value of $i_c = -i_a$ is called the exchange current, i_0 .

This condition is often not established in batteries because of a spontaneous redox reaction. In fact, the voltage of a cell when $i_{tot} \rightarrow 0$ is called open circuit voltage (V_{oc} or OCV), and it is measured using high resistance ($>10 \text{ M}\Omega$) electronic voltmeters to meet the $i_{tot} \rightarrow 0$ condition. [16].

When $i \neq 0$, for example, while discharging a battery, there are some changes to the interfaces compared to the equilibrium situation. A deviation from E_{eq} of the electrode potential is observed. These deviations are called polarization and cause the so-called overpotentials, η .

During discharge, the real potential must be calculated considering all the overpotentials (11).

$$E_{\text{real}} = V_{oc} - \sum |\eta| - iR \quad (11)$$

where iR is the ohmic drop in the solution, while η arise from different factors. Charge-transfer overpotential or activation overpotential is related to the charge transfer at the electrode/solution interphase described in the Butler-Former equation. The diffusion overvoltage or concentration polarization, η_{conc} , is related to the depletion or accumulation of electroactive material at the electrode surface.

Figure 2.3 shows a typical potential vs current profile and the contribution of the overpotentials.

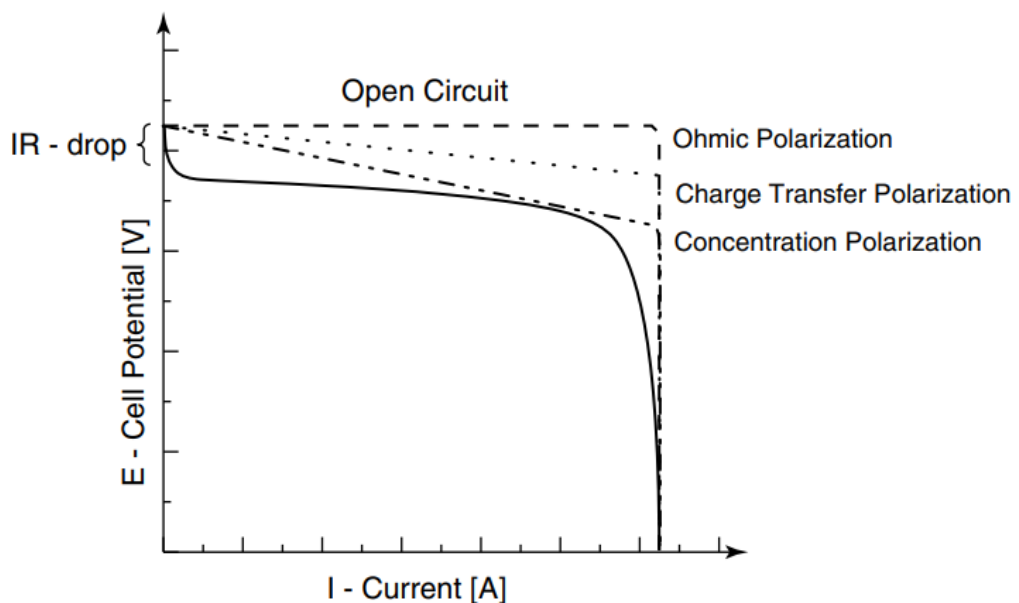


Figure 2.3. Contribution of the overpotential on a potential- current curve.

All these factors establish the specification of a cell (in these case for the unit constituting a battery).

2.3. *Crucial battery metrics*

For battery purposes, the charge the system can deliver is fundamental. In order to determine the maximum charge that a cell can deliver, it is important to clarify that for each active material exists a theoretical specific capacity that depends on the molecular weight and the number of the electrons transferred during electrochemical reaction. It can be calculated for each electrode material as $Q = nF/MW$ where MW is the active material molecular weight. This can be calculated by measuring the current and integrating it with respect to time. The experimentally observed capacity is commonly reported as a specific capacity in mAh g^{-1} normalizing by the mass of the electrode material (or of the cell).

In a well-functioning cell, the anode and cathode should have the same capacity in absolute terms $C_A m_A = C_C m_C$, where C_C and m_C are the theoretical specific capacity and the active material mass of the cathode, and $C_A m_A$ are referred to the anode. Hence, the capacity of the cell $C_{\text{cell}} = C_C m_C / (m_C + m_A)$. In the presence of a limiting electrode, the maximum theoretical capacity can be estimated from the capacity of the limiting electrode. The maximum theoretical specific capacity is given by the capacity of the limiting electrode divided by the weight of the active materials of both electrodes. A more plausible estimate is obtained by dividing by the total weight of the composite electrodes. However, the current collectors, separator, electrolyte and container must also be considered. The specific values given by the manufacturer consider the weight of all the components.

In battery science, a commonly used charge-discharge visualization is the voltage profile with respect to time. Figure 2.4 reports an example of the voltage profile curve. Usually, battery or cell discharge capacity is provided with a value for the current applied, named C-rate. This defines the rate of time in which the cell takes to charge or discharge. The ratio between the discharge and the charge processes. is the coulombic efficiency ($\text{CE}\%$), and it is calculated as follows:

$$CE(\%) = \frac{Q_{discharge}}{Q_{charge}} \times 100 \quad (12)$$

CE% is also referred to as a single electrode in half-cell configuration experiments in the following sections. In this case, coupling the electrode material under study (Working electrode – WE) with an electrode (Counter electrode - CE) that does not limit the WE, makes possible to determine the efficiency of the single process [17,18].

The ratio between the average voltage calculates the values of voltage efficiency during discharge mode (V_{dis}) and average voltage during charge mode (V_{ch}):

$$VE(\%) = \frac{V_{dis}}{V_{ch}} * 100\% \quad (13)$$

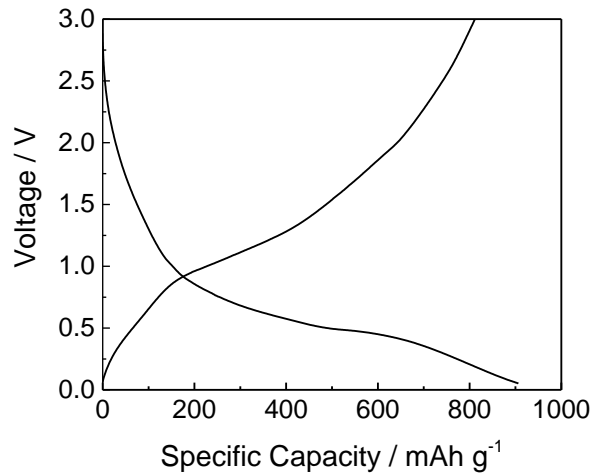


Figure 2.4. Voltage profile vs specific capacity during a charge-discharge cycle.

In addition, a commonly used quantity to compare the battery specification are the energy density/Wh L⁻¹ (or specific energy/Wh kg⁻¹) and the power density/W kg⁻¹. The first is obtained as $\int V I dt$, while the latter as energy/t.

3. Different systems for different tasks

Chapter 3 introduces the importance of choosing appropriate energy storage systems for a specific application. This is useful for integrating energy storage systems in the energy transition plan.

The growing energy demand and the proliferation of distributed renewable power sources have been causing the intensification of the adoption of EESS. Nowadays, mostly lithium-ion batteries are adopted for different purposes. For a future in which the sustainable energy demand increases, batteries should be refined depending on what a battery is used for. Indeed, material composition and morphology must vary to achieve the desired technical features. For example, some battery applications require lightweight (e.g., portable electronics and biomedical devices), others high power or very fast charging (e.g., power tools and electric vehicles – EVs).

Indeed, the technical requirement for batteries mainly depends on the application and, specifically, on the amount of energy that needs to be stored, the charge and discharge duration and the cycle life.

Looking at the usual duration, electrochemical energy storage systems like capacitors and supercapacitors (SCs) are compatible with short operation periods. In fact, they can be used for harvesting energy with high pulse power for short periods [21]. For this reason, they can find applications in electronic devices like mobile phones, wearable devices, health monitors, sensors, LED displays, bar code scanners, and GPS chips [22].

Lithium-ion batteries and its analogous represent the best choice when the time scale increases and hours of duration are needed. They commonly provide high energy density for longer times. In addition, LiBs are best suited for specific applications depending on the type of electrode materials.

From an economic point of view, electrochemical storage systems such as lithium-ion batteries are not suitable for storing large quantities of energy and power– such as the capacity needed for offsetting seasonal fluctuations of power generated by wind

turbines or photovoltaic systems – for long periods. At this time scale, redox flow batteries (RFBs) represent an ideal choice due to the modular design. Therefore, it can be assumed that implementing RFBs will be cost-effective when large amounts of energy have to be stored over long periods [23].

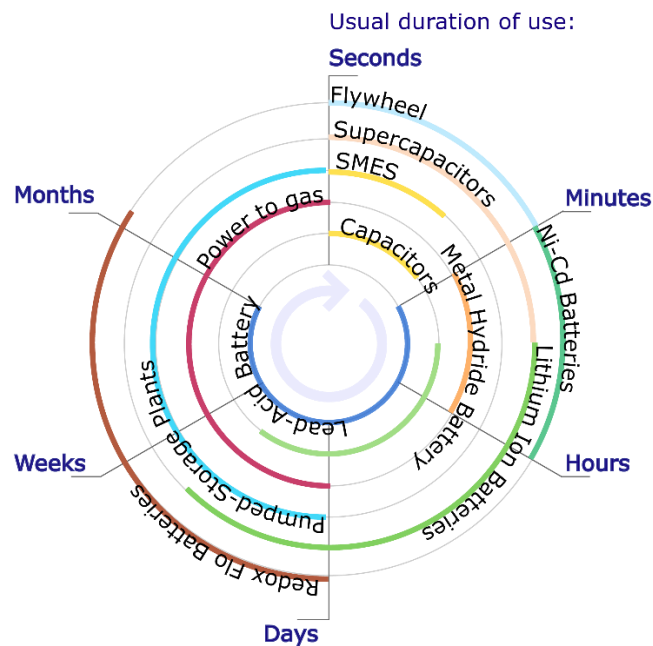


Figure 3.1. Energy storage systems and typical duration of use.

In addition to the consideration of the duration of operation, as mentioned, also power and energy density are important to define the applicability of an EESS. A Ragone plot is used to compare different energy storage systems in terms of energy and power density (Figure 3.2). For example, the systems that best fit the first task ought to be characterized by high energy density and placed in the plot's right part. On the contrary, systems able to deliver high power are placed in the top left part of the plot.

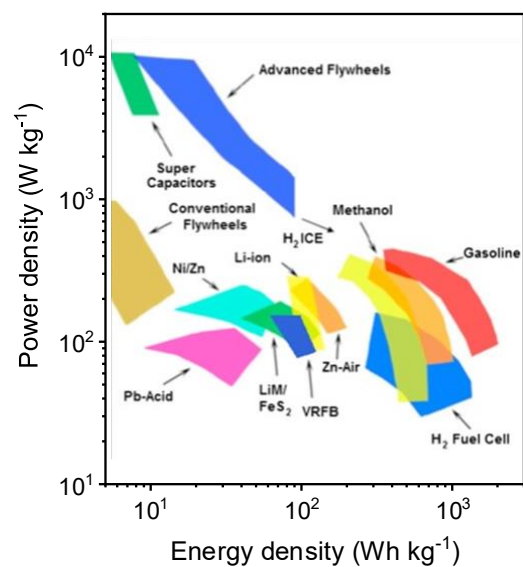


Figure 3.2. Ragone plot of various energy storage devices (modified from [25]).

In this thesis, the attention will be mainly focused on lithium-based technologies and redox flow batteries, covering most of the time and energy requirements needed for the electrification of our society. These arguments will be called back in sections 4.6, 5.6 and 7.6.

4. Lithium-ion Batteries (LiB)

Chapter 4 aims to introduce the concept behind lithium-ion batteries and their criticism. All properties and processes involving the cell components were analysed. Among the cell components and methodologies, the experimental activity presented mainly focuses on negative electrode materials [I] and new in situ methods for investigating electrode processes [II].

Lithium-ion batteries have been one of the most used EESSs since 1991. However, there has been a long way to go for their development. The starting point can be found in Italy in the 1800s, when the competition between Luigi Galvani (University of Bologna) and Alessandro Volta, a professor at the University of Pavia, led the latter to travel to Napoleon's court in France to reveal his 'electric battery'. Volta's work had an enormous impact on the progress of electrochemical science, catalysing the rapid evolution of battery history with the cumulative discovery of many important electrochemical systems. In less than two centuries, we progressed from the zinc-manganese oxide cell (1866 - Georges-Lionel Leclanche) to the first secondary lead-acid cell (1859 - Gaston Plante) and nickel-cadmium cell (1901 - Waldmar Jungner). Although with some important variations from the original design, it is remarkable to note that these systems are still in use today with different applications. Just think of lead-acid and the ignition of car engines or the Leclanche cells that gave birth to alkaline batteries.

As recounted in Section 1.1, there has been an increasing demand for energy, and the search for new storage systems has continued over time.

Thus, it was that in the 1980s a battery came along that combined lithium metal with iodine. The use of the most electropositive metal on the periodic table as well as the lightest alkali metal led to the development of a cell with a practical energy density of around 250 Wh/kg [26].

This technology has found its impetus in the application of pacemakers, where the energy density is reflected in a reduction in battery weight and a longer battery life, reducing the number of patient surgeries.

Mater artium necessitas or "Necessity is the mother of invention", the demand for devices capable of combining good power operation with a small volume and low price has driven research in the field of storage systems.

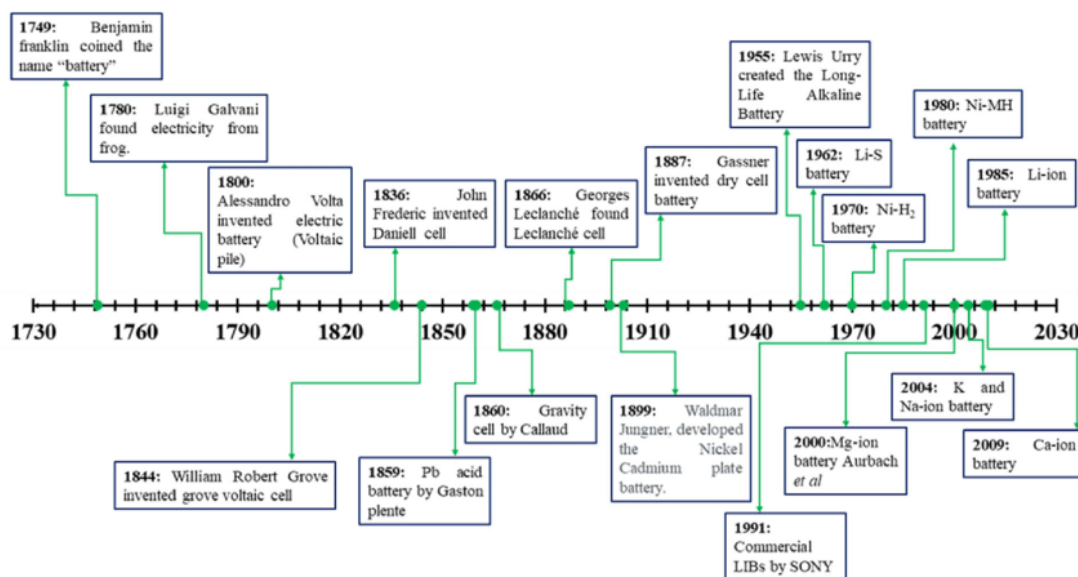


Figure 4.1. Timeline of battery development from 1730 to 2020 ([27] article distributed under the terms and conditions of the Creative Commons Attribution (CC BY) license).

At this point, it was necessary to switch from primary cells to secondary cells that could be recharged.

The breakthrough came in 70' with the contribution of Besenhard and one of the three 2018's Nobel laureates S. Whittingham with the development of so-called 'insertion' or 'intercalation' electrodes [28,29]. These are typically based on compounds that can host and release lithium ions reversibly inside and outside their open structure. However, the cell thus obtained proved to be unstable and dangerous. Most of the problems were associated with the presence of lithium metal. Its very high reactivity with the electrolyte and irregularities on the surface can lead to non-uniform deposition of lithium during charging, forming dendrites that eventually grow, short-circuiting the cell.

In order to guarantee cycle life and safety, two approaches were possible: (1) a careful choice of electrolytic system to ensure optimised and homogenous lithium deposition, or (2) replacing the lithium metal with a less aggressive anodic material.

The first approach is the one leading to the lithium metal cells described in section 5.3, while the second is the one leading to lithium-ion batteries.

Lithium-ion batteries (Figure 4.2) are mainly composed of four components: anode, cathode, electrolyte and separator. These constitute the elemental battery unit, the electrochemical cell. During the cell operation, the oxidation and reduction reaction on the cathode and anode are accompanied by shuttling back and forth of Li-ions and electrons through the cell and external circuit, respectively. Every component result fundamental for the device's functioning, and many research efforts have been made to balance the costs, the safety, the energy and power densities and the stability of the components.

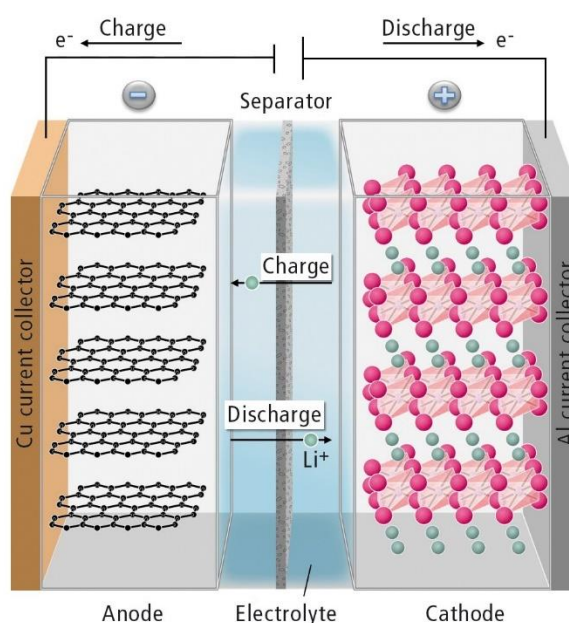


Figure 4.2. Schematic diagram of lithium-ion battery (LiB) [30].

In these cells, two intercalation electrodes are combined. During charging, the negative intercalation electrode acts as the 'lithium sink' and the positive one as the 'lithium source', and the total electrochemical process of the cell involves the transfer of x equivalents of lithium ions between the two intercalation electrodes. The process is then reversed on discharge and repeated cyclically. These systems have also been called lithium rocking-chair batteries [31].

This architecture succeeded in being commercialised by Sony in 1991 [32]. The winning feature of the Sony battery lay in selecting of suitable electrode materials, with graphite as the anode and lithium cobalt oxide (Goodenough in 1980 [33]) as the

cathode. In this system, the cathode provides the lithium ions to ensure the electrochemical process and accepts them back reversibly to ensure process reversibility.

4.1. Positive electrode materials

In lithium-ion batteries, the electroactive species are not in solution, confined on electrodes. This means that the electrode materials determine the capacity and voltage of the cell.

The positive electrode is the main contributor in the LiB cost, and its properties and stability are strongly linked with the LiB performance and suitability. The mostly used cathodic materials differ for the crystal structures and the lithium diffusion channels and are showed in Figure 4.3:

1. Layered oxides LiMO_2 (M= Mn, Co and Ni)
2. Spinel (LiMn_2O_4)
3. Olivines (LiFePO_4)

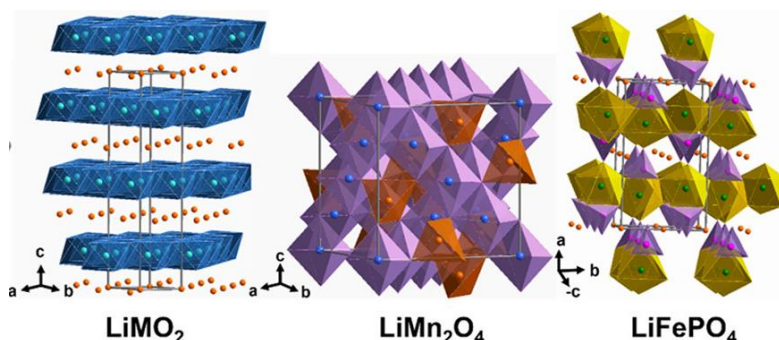


Figure 4.3. Crystal structures of layered LiMO_2 (M = Mn, Co, and Ni), spinel LiMn_2O_4 , and olivine LiFePO_4 .

Layered materials were the first cathodic material adopted in LiBs by Goodenough and Mizushima [34,35]. In that case, LiCoO_2 guarantees a practical capacity of around 140 mAh g^{-1} and a potential of the plateau of $3.9 \text{ V vs Li}^+/\text{Li}$. Generally, layered structured material shows the highest practical capacity (currently up to 180 mAh g^{-1}) among the three classes but suffers from structural and/or chemical instabilities during cycling depending on the chemical composition and state of charge. As an example, LiMnO_2 (LMO) is highly attractive due to its low cost, abundance, and decent electrochemical properties. LMO shows a large specific capacity of 147 mAh g^{-1} [37]

with a cell voltage reaching the 4.3 V. However, upon intercalation, the active material has a structural transition to LMn_2O_4 with a spinel structure. In addition, Mn^{3+} is unstable to the disproportionation at elevated temperatures and slows down its implementation in a commercial cell. Alternatively, in LCO, Co^{3+} offers excellent structural stability, but it suffers from poor chemical stability on extracting >50% lithium from LiCoO_2 (>50% charge).

In addition, cost and toxicity must be considered. While Mn is the cheapest and less toxic, it is also less performing with respect to the expensive and toxic cobalt. Indeed, Co is also considered a critical raw material, and many research efforts are focused on reducing or replacing Co inside the lithium-ion battery cell. In order to reduce the Co active material content, mixed metal-oxide active materials have been developed with the general formula $\text{LiNi}_{1-x-y}\text{Mn}_x\text{Co}_y\text{O}_2$ called NMC [37].

Considering the advantages and disadvantages of the three, the industry largely uses compositions such as $\text{LiNi}_{1/3}\text{Mn}_{1/3}\text{Co}_{1/3}\text{O}_2$ (NMC-333). Nevertheless, to further decrease the cobalt content, composition like NMC-811 has also been studied. In the last years, NMC attracted great interest thanks to its good reversible capacity (160-200 mAh g^{-1}) and high-capacity retention even at elevated temperatures and high current rates [38].

The effort to replace the cobalt from the active material, combined with the challenge of increasing the cell voltage find part of the achievement in the $\text{LiNi}_x\text{Mn}_{2-x}\text{O}_4$ ($0 < x < 0.5$) (LNMO).

LNMO can be considered the most interesting spinel structured active material because the highly reversible oxidations of $\text{Mn}^{3+}/\text{Mn}^{4+}$ (only in the disordered form) and Ni^{2+} up to Ni^{4+} occurring between 4.70-4.75 V vs Li^+/Li with a decent theoretical specific capacity of 147 mAh g^{-1} [40]. The high energy density that this material can provide, coupled with the lowest price enabled this material to be included among the candidates for next generation cell chemistries [41]. However, a disproportionation reaction of Mn^{3+} may occur, leading to the active material dissolution into the electrolyte and, consequentially, capacity fade and relevant safety problems. In addition, the electrolyte degradation due to the high potential leads to a generally low $\text{CE}_\%$ [42].

Olivine positive electrodes as LFP represent one of the most commercialized cathodes with diverse battery applications. All this success is due to this material's multiple

attributes, including low-cost, earth abundance, low toxicity, and safety. Indeed, iron is even more abundant than manganese in the Earth's crust [43]. LFP guarantees a good thermal stability, long cycle life and low impact in terms of cost and environment. Looking deeper into the performances, LFP has a decent theoretical specific capacity of 170 mAh g⁻¹ with an operating voltage of 3.4 V vs Li⁺/Li. The latter is responsible for the high stability and long cycle life. In fact, the lower voltage discourages electrolyte degradation reactions typical of high-voltage systems (e.g LMNO).

The main drawbacks of LFP concern the poor ionic conductivity, the intrinsic low electronic conductivity < 10⁻⁹ S cm⁻¹ [36] and the low volumetric energy density. In addition, the theoretical density of lithium iron phosphate is 3.6 g/cm³, much lower than that of lithium cobalt oxide (5.1 g/cm³). In Table 4.1 are summarized the main positive electrode materials for LiBs.

Crystal structure	Compound	Theoretical/experimental specific capacity mAhg ⁻¹	Theoretical/typical capacity mAhcm ⁻³	Volumetric	Voltage V
Layered	LiTiS ₂	225/210	697		1.9
	LiCoO ₂	274/148	1363/550		3.8
	LiNiO ₂	275/150	1280		3.8
	LiMnO ₂	285/140	1148		3.3
	LiNi _{0.33} Mn _{0.33} Co _{0.33} O ₂	280/160	1333/600		3.7
	Li ₂ MnO ₃	458/180	1708		3.8
Spinel	LiMn ₂ O ₄	148/120	596		4.1
	LiCo ₂ O ₄	142/84	704		4.0
Olivine	LiFePO ₄	170/165	589		3.4
	LiMnPO ₄	171/168	567		3.8
	LiCoPO ₄	167/125	510		4.2

Table 4.1. Crystal structure, theoretical/experimental/ gravimetric and volumetric capacities and, average potentials of representative intercalation cathode compounds [44].

4.3 Electrolyte

In lithium-ion batteries with liquid electrolytes, the electrolyte is mainly composed of lithium salts of poorly coordinating anion dissolved in organic aprotic solvents. The most important requirements for suitable electrolytes are high conductivity, thermal stability, wide electrochemical stability window, and chemical inertness toward the other components of the cell. In addition to these characteristics, low toxicity and acceptable cost are desired.

In metal-ion and metal batteries, the electrolyte should withstand the strong reducing and oxidizing potentials at the negative as well as the positive electrode.

For this reason, choosing an appropriate electrolyte plays a role in the electrode performance. The electrolyte influences the processes and modification at the solid/liquid interphase. The control over the structure interface is fundamental to optimize and tailoring the properties of an electrochemical system. The interface nature affects the double layer properties, the electrode wettability, the kinetics of the charge transfer, the activation overpotentials, the chemical/electrochemical reaction of species with the electrode surface.

Usually, organic solvents are linear or cyclic aliphatic as ethylene carbonate (EC) and propylene carbonate (PC), and linear carbonates including dimethyl carbonate (DMC), diethyl carbonate (DEC), and ethyl methyl carbonate (EMC). As summarized in Table 4.2, cyclic carbonates are characterized by a high dielectric constant, important for lithium salt dissociation but with higher viscosity. The latter can be guaranteed by linear carbonate that shows ion mobility. For this reason, commercial electrolytes are often a mixture of different solvents to benefit from the combination of these properties.

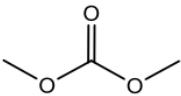
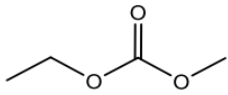
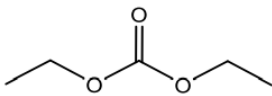
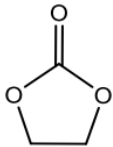
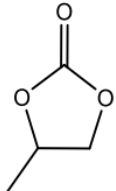
Solvent	Structure	M.W. g mol ⁻¹	Dielectric constant	Viscosity cP	Density g cm ⁻³
DMC		90	3.12	0.63	1.063
EMC		104	2.93	0.65	1.007
DEC		118	2.82	0.77	0.969
EC		88	90.0	1.9	1.327
PC		102	64.9	2.53	1.201

Table 4.2. Properties of the most used organic carbonates solvents.

Other solvents used in batteries are aliphatic ethers, such as dimethoxyethane (DME), tetraethylene glycol dimethyl ether (TEGDME) and dioxolane (DOL). However, these solvents are mainly used for next-generation batteries based on lithium metal.

As in every type of electrochemical cell, the salt needs to be electrochemically and thermally stable in a wide range, completely soluble and dissociated, chemically inert towards the other components of the cell, and they must have low environmental impact and toxicity. As discussed in the next section, the chemical inertia is only sometimes complete (especially vs the negative electrodes) and often needs to be controlled.

In Li-ion batteries, the most common salt used is lithium hexafluorophosphate (LiPF_6) due to its good ionic conductivity, wide electrochemical stability window, and the ability to form a protective aluminium (oxy-)fluoride layer on the cathode aluminium current collector. However, LiPF_6 suffers high moisture sensitivity. In the presence of water, it spontaneously reacts by substitution eliminating hydrofluoric acid (HF) [45]. Imide-based lithium salts, like lithium bis(fluorosulfonyl)imide (LiFSI), lithium bis(trifluoromethanesulfonyl)imide (LiTFSI) exhibit good ionic conductivity, electrochemical and thermal stability, and safer hydrolysis, which leads to a negligible release of HF. They are particularly adapting in relatively low voltage batteries while they may show problems at high potential due to their inability to passivate the aluminium current collector.

Lithium tetrafluoroborate (LiBF_4) is a highly studied salt in LiB. Its success is primarily due to the chemical inertia to moisture and its capability to passivate the aluminium current collector. The main drawback is represented by the strict ionic couple between lithium ion and the anion and, consequently, the poor ionic conductivity in carbonate-based solvents. Recently, lithium bis(oxalate)borate (LiBOB) was studied, it is characterized by relatively low toxicity, electrochemical stability, and limited reactivity in the presence of moisture. However, the bulkiness of the bis(oxalate)borate anion the bulky anion limits the conductivity added to its instability with LCO-cathodes [46].

Lithium hexafluoroarsenate (LiAsF_6) and perchlorate (LiClO_4) have been widely used for their excellent electrochemical stability and ionic conductivity. However, they are slowly being abandoned: the former can form highly toxic AsF_3 , and the latter is explosive.

Finally, ionic liquids (ILs) are highly studied systems but will not be an object of study in the present thesis. It is important to highlight that ILs are salts with a low melting point, indeed, at room temperature, they are present in the molten state. To achieve this peculiarity, ILs are composed of a bulky, asymmetric organic cation (e.g., pyrrolidinium, piperidinium and imidazolium derivatives) and a bulky inorganic/organic anion. The ionic couple must be weak. This guarantees a non-flammable, thermally and chemically stable electrolyte with negligible vapour pressure. Their employment, despite high ionic conductivity and a wide electrochemical stability window, is primarily limited by their high costs [47].

4.4. Separator

As described above, the electrolyte is a key component that allows the movement of ions by balancing the flow of electrons occurring in the external circuit. The separator is placed between the electrodes to prevent short-circuiting and at the same time permit the transport of ions.

The separator is a critical component in batteries with liquid electrolytes. Separators are usually membranes, which may be porous (organic), composite (one part organic and one part inorganic) or woven-nonwoven (fibers).

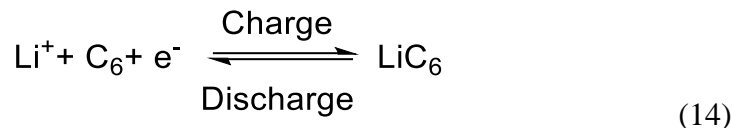
The essential function of a separator is to prevent physical contact between anode and cathode while allowing ion exchange. The separator itself does not therefore participate in the reactions occurring within the cell, but its structure and properties largely influence the performance of the cell [48]. It is important to define:

- a. Chemical stability: the separator must be chemically stable once in contact with the electrolyte and electrodes, especially when subjected to highly reductive and oxidative environments when the cell is fully charged [49,50].
- b. Thickness: a uniform thickness of the separator promotes homogeneous ion distribution. It must achieve a compromise between energy density and mechanical strength.
- c. Porosity: A separator must have a uniform distribution of pores on the surface, in which case cell resistance (increases with decreasing pore size) and safety in the event of shut down (pores too large) must be balanced.
- d. Mechanical resistance: the separator must withstand all cell assembly operations unaffected.
- e. Wettability: The separator must absorb enough electrolyte and retain it in the pores during cell operations. If wettability is high, the cell's ionic strength decreases, increasing the cell's performance. On the other hand, a non-uniform ion distribution occurs if it is low. Wettability is crucial for both the cell's capacity and its lifetime.

4.5. Negative electrodes

On the anode side, graphite is the most widely used electrode material today. It provides a high theoretical capacity (372mAh g^{-1}) and a low potential (-2.92 V vs. NHE) for the Li intercalation reaction. In addition, graphite shows good dimensional

stability. Due to the carbon host's electrochemical reduction (charge), lithium ions diffuse from the electrolyte penetrating the carbon and forming a lithium/carbon compound (Scheme 14).



Typically, the intercalation in graphite follows the so-called stage formation. The insertion of lithium ions proceeds progressively occupying different layers in the graphite structure occurring only at prismatic surfaces. [51]

This is mainly due to the repulsive interaction between lithium ions as well as the rising energy required to expand the gap between graphene layers. The stage formation can be observed electrochemically in the voltage profile of a polycrystalline graphitic electrode (as shown in Figure 4.4).

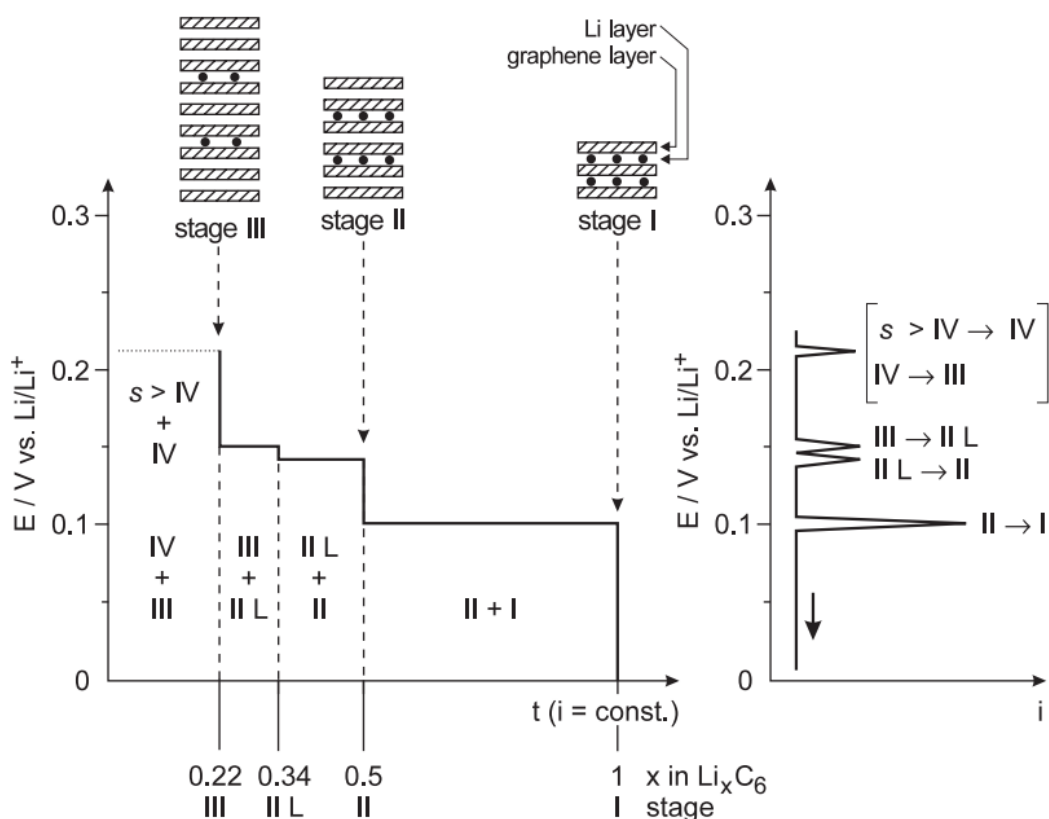


Figure 4.4. Stage formation during electrochemical intercalation of lithium into graphite. Left: schematic galvanostatic curve. Right: schematic voltammetric curve. Reproduced from reference [52] with permission from Wiley-VCH GmbH.

In addition, the electrolyte has an important role in determining the interphase's reactivity (Figure 4.5). In a full cell, the negative and the positive electrode have their intrinsic electrochemical potentials, μ_a and μ_c . These two potentials vary upon cycling as a consequence of the voltage variation of the cell. However, the cell voltage is limited by the electrochemical stability window. This one is defined as the energy difference between the highest occupied molecular orbital (HOMO) and the lowest unoccupied molecular orbital (LUMO). If the potential of the negative electrode is higher than the electrolyte's LUMO, a spontaneous reaction of the electrolyte at the electrode interphase occurs. The product of this reaction constitutes the so-called Solid Electrolyte Interphase (SEI). Identically, the so-called CEI (cathode electrolyte interphase) is formed if the positive electrode potential is lower than the electrolyte's HOMO and spontaneous reactions between the positive electrode and the electrolyte occur. The SEI and CEI layers block further reactions of the electrolyte.

The positive electrode operates at low energies/high potentials, whereas the negative one operates at high energies/low potentials. Stable interfaces are the key to the realization of next-generation low-voltage negative electrodes and high-voltage positive electrodes [53]. Indeed, a good SEI should allow Li^+ transport and blocks electrons to prevent further electrolyte decomposition and ensure the good coulombic efficiency of the electrochemical reactions under study. Generally, the SEI layer is formed during the first cycles when the bare electrode reacts with the electrolyte components generating various species. In Figure 4.5b are reported the calculated reduction potential of typical electrolytic components towards metallic lithium.

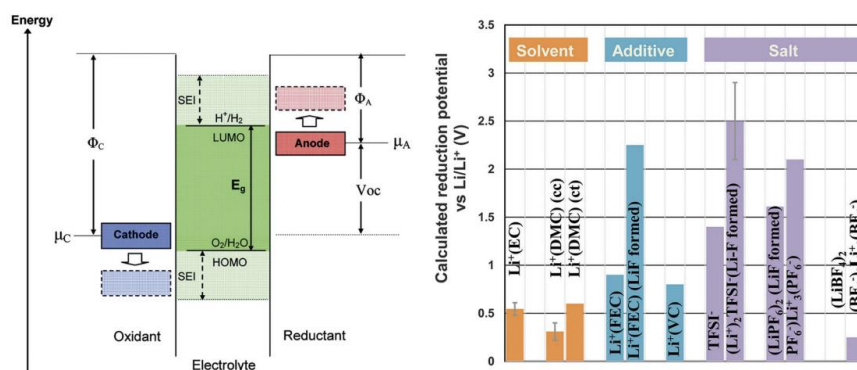


Figure 4.5. (a) Negative and positive potentials for the electrolyte stability, and the energy levels of HOMO and LUMO; (b) calculated reduction potential of typical electrolytic components towards metallic lithium [54].

As can be seen, most of the electrolytic components spontaneously react forming the SEI. As SEI formation cannot be avoided, many research efforts focused on the SEI composition's control and tailoring to ensure the formation of a stable interphase.. In order to make it possible, the selection of appropriate electrolyte results fundamental. Typically, in LiBs the electrolyte is composed of a mixture of organic carbonates with fluorinated lithium salts. LiPF_6 is the most used salt in LiBs due to its high solubility and ionic conductivity [54]. It can cooperate with cyclic carbonate to form a stable F-rich interlayer. The main drawback results in the instability of the hexafluorophosphate to the hydrolysis leading to the formation of HF. The former can dissolve the cathodic active material damaging the electrodes and consequently lowering the electrode's safety, stability, and capacity.

For example, in dimethyl carbonate/ ethylene carbonate (DMC/ EC) based electrolytes, there are the advantages of the DMC that exhibits a low viscosity and of the EC that shows excellent filming capabilities that ensure the formation of a stable solid electrolyte interphase (SEI). On the contrary, the cointercalation of propylene carbonate (PC) with lithium ions dramatically exfoliates graphite. Without additives with filming capabilities graphite exfoliation occurs a less the 0.8/0.9 V vs Li^+/Li without wrecking the bulk structure but bringing progressive changes in surface structure and affecting the cycle life of the electrode (and of the whole cell).

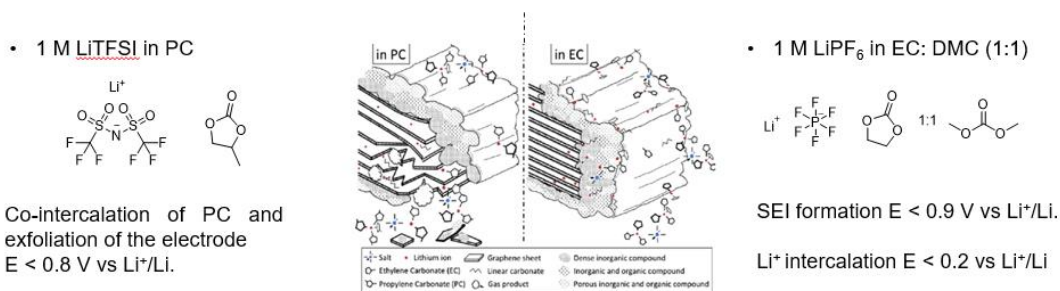


Figure 4.6. SEI formation in two different electrolytic systems.

The main drawback of graphite electrodes is a relatively low charge rate which limits the battery power density [55].

To overcome this drawback, many other negative electrodes has been investigated to replace traditional graphite as negative electrode for LiBs, including nanostructured carbon [56, 57] (e.g., graphene, carbon nanofibers, carbon nanotubes, etc), silicon-based materials [58], lithium titanate oxide (LTO) [59], and transition metal oxides [60].

Material	Lithiation potential V	Delithiation potential V	Theoretical specific capacity mAhg ⁻¹	Volume changes %
Graphite	0.07-0.19	0.1-0.23	372	10
LTO	1.55	1.58	168	>1
Si	0.05-0.21	0.31-0.47	4200	440
Ge	0.2-0.5	0.5-0.62	1600	240
Sn	0.4-0.69	0.58-0.78	994	255

Table 4.3. Characteristic potentials, theoretical specific capacity and volume changes of anodic materials for LiBs.

On top of that, nanostructured carbon allotropes show high specific capacity (500-1500 mAh g⁻¹) but most of carbon precursors are expensive and need a complex treatment process [61]. In addition, as with graphite electrode, all the carbonaceous electrolyte suffers from strong reactivity that should be controlled. The proximity of the carbonaceous materials reduction process to the lithium plating potential opens the possibility of lithium plating when a high current is applied, increasing the risk of short-circuit of the cell due to lithium dendrites formation.

Silicon-based anodes can guarantee high theoretical specific capacities of about 4200 mAh g⁻¹ because they can alloy 4.4 Li for each Si atom. Si has a low alloying potential that guarantees a high energy density. The main drawback of this material is represented by the huge volumetric expansion (up to 400%) that limits the electrode stability over cycling [62].

Lithium titanate Li₄Ti₅O₁₂ (LTO) represents an interesting material for the dimensional stability. It is well-known as a zero-strain material with a very stable spinel-framework structure and for the negligible reactivity toward the most used electrolytic solution. However, the low theoretical specific capacity (168 mAh g⁻¹) coupled with the high average discharge voltage (1.56 V) make it unfit for high energy density applications. On the other hand, the high-rate capability makes LTO suitable for high-power applications.

4.5.1. The problem of volume expansion and gas evolution

The case of silicon-based materials shows how much important is the dimensional stability of an electrode for a having a good capacity retention.

Indeed, faradic processes involve reversible insertion of ions in the lattice of the electrodes. The insertion of ions often implies changes in volume and in some cases, huge expansion of the electrodes. The magnitude of this phenomenon depends on the available hosting position and on the dimensions of the guests. While lithium insertion in LiFePO_4 results in an expansion of 6.8 %, sodium insertion in NaFePO_4 leads to a thickness increase of 12.8 % [63].

Uncontrolled expansions can lead to failures and damages to the materials, such as exfoliation in layered materials [64] or irreversible shrinking in insertion materials [65].

Hence, the study of volumetric stability of the electrodes under cycling is fundamental to detect materials damage, to better analyze consequent materials failure, to precisely predict the lifetime and long-term stability of the cell and to improve battery safety [66].

In situ electrochemical dilatometry can be used to record macroscopic expansion and contraction of materials during reactions in combination with electrochemical techniques.

This technique is especially useful to evaluate those systems in which volume changes lead to mechanical degradation or the formation of unstable solid electrolyte interphase (SEI) that can severely affect safety [67-70]. In situ dilatometry allows mechanistic studies in systems characterized by several intermediate species as in composite sulphur/carbon electrodes adopted in lithium-sulfur batteries [71,72].

In previous works [72–77], in situ dilatometry allowed the monitoring and predicted the behavior of systems.

For this purpose, I focused on developing new methodologies to get different information on the cells. In collaboration with Marposs S.p.a. a novel electrochemical dilatometer was designed and tested. The presented tests set the groundwork for new optimization and designs for the above-mentioned system which can detect the volume variation during an electrochemical experiment with the additional feature of applying controlled pressure on the cell. This new system enables the control of the force in a

broad range of values and the detection of the volumetric changes of electrode materials in different conditions. Hence, the studies were carried out on well-known electrode models with diverse electrolytic mixtures during cyclic voltammetry cycles. This novel apparatus could be used to evaluate the phenomena occurring during insertions processes such as SEI formation, gas evolution, solvent evaporation, and exfoliation under different applied forces.

Results presented in this section are reported in Paper I (see List of Publication).

- Materials and methods

A dilatometer (Marposs S.p.A., Bentivoglio, Italy), equipped for cell testing, was used to measure the volume changes during charge/discharge cycles in electrochemical cells. The dilatometer is composed of a solid steel structure, a measuring system for the sample volume variations, a manual adjusting system for tuning of acting force on the sample and a removable sealed sample holder, is equipped with electronics for sensors reading and acquisition, as shown in Figure 4.7. Contactless measuring system detects the volume changes minimizing the influence of the gauge on the measure itself and that of the expansion of the sample during the tests. The inductive magnetic gauge used has a measuring range of 500 μm , a resolution of 0.01 μm with a maximum non-linearity error of 0.1 μm . Two temperature sensors continuously detect the internal temperature of the cell and the external temperature. Through a ring nut, it's possible to adjust the force acting on the sample under test in a range from about 10 N to 100 N: this peculiarity is very useful in the study of batteries where this parameter is crucial. The sample holder can be easily removed and reassembled on the instrument when dry-box setup operations are needed. The dilatometric equipment is able to record the total deformation of the cell.

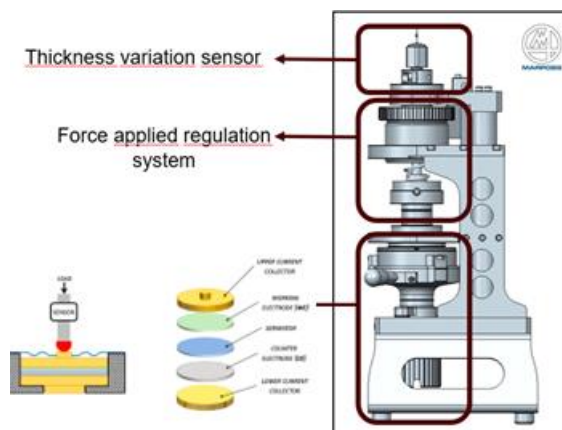
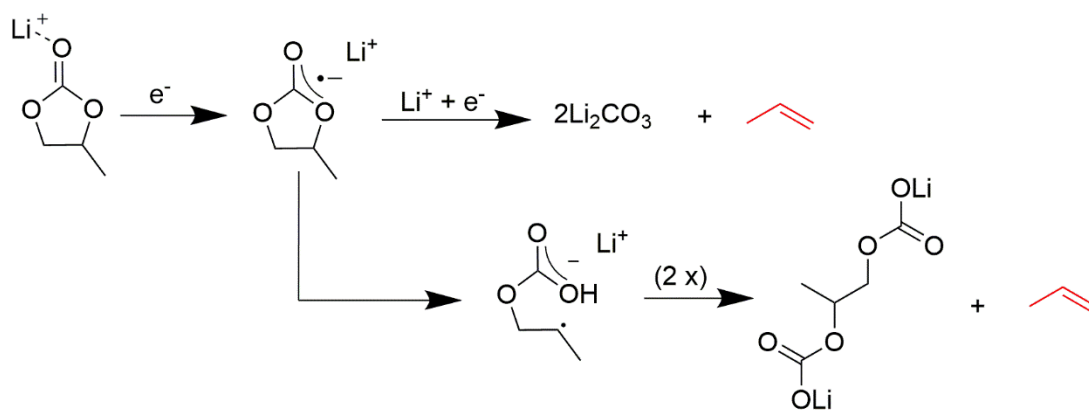


Figure 4.7. Marposs electrochemical dilatometer.

Instrument validation

In order to distinguish the different contributions of the cell components, a capacitive positive electrode has been chosen. Thanks to capacitive charge/discharge processes, the positive electrode that doesn't change too much its dimension. In addition, we started the test after 2 hours, when all the materials had reached a stable thickness.

As working and investigated electrode, graphite electrodes has been tested in two different electrolytes. EC-based electrolytes are well-known for their good compatibility with graphite. EC shows excellent filming capabilities that ensure the formation of a good and stable SEI and DMC decreases the viscosity of the solvent mixture. EC-DMC containing LiPF_6 salt is a standard electrolyte (LP30) due to the broad electrochemical stability and high ionic conductivity as well as to the good protection of the most common aluminium current collector [78,79]. On the contrary, the cointercalation of PC with lithium ions in graphite leads to a dramatic exfoliation of the electrode [80] according to scheme 4.1. In the absence of additives with filming capabilities, graphite exfoliation occurs at less than 0.9 V vs Li^+/Li without wrecking the bulk structure completely but bringing progressive changes in surface structure. [81]. This degradation makes this electrolyte unsuitable for most graphite-based LiBs. In the following paragraphs, the dilatometric results of Li^+ intercalation in graphite will be described in EC:DMC-based electrolytes and compared with those in PC-based ones under an applied force.



Scheme 4.1. Possible reductive degradation pathways of EC with gas phase co-products (red labelled).

Deformation of the cell components under 10N

Information about the strain response to controlled applied stresses associated to an electrochemical system gave the possibility to get information about the importance of the deformation of materials on the thickness variation observed during electrochemical experiments according to Figure 4.8x.

The thickness of the different cell components was monitored in the electrochemical chamber of the dilatometer under a force applied of 10 N (157 kPa for 9 mm disc and 127 kPa for 10 mm disk) by adding LP30 electrolytic solution or PC-1M LiTFSI (150 μ L for the full cell and 75 μ L for the cell components).

Under the applied pressure, all the materials respond with a deformation that leads to a fast decrease of thickness in the first 2 hours (Figure 4.9).

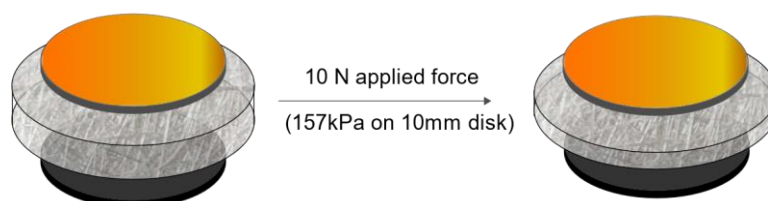


Figure 4.8. Effect of the applied force on the cell components.

Absolute and percentual thickness variation of the cell components in LP30 are reported in Figure 4.9a and 4.9b. The separator and the CE showed the smallest thickness decrease around 13.0 μ m (-9.2 %) and 2.6 μ m (-0.7 %) after 14 hours, respectively. This behaviour was expected for CE. The selection of a CE based on

activated carbon, indeed, was done because of its capacitive properties. It accumulates charge without ion insertion in the electrode bulk active mass, limiting the electrode deformation.

On the other hand, the graphite electrode showed higher deformation that stabilizes after 14 hours (-123 % with respect to the dry electrode). Such a high thickness variation could be justified by the increased thickness of the wet electrode taken as starting reference value. The electrode wetting and related thickness change deserve further investigation. In LP30, indeed, both DMC evaporation and graphite deformation act on swelled materials.

The cell deformation (52 μm , -9.2%) was smaller than the sum of the variation of the individual components. It is reasonable that the stress induced by the applied force was distributed on the various components and causes the deformation mostly on the weakest material.

In PC-based electrolyte (Figure 4.9c and 4.9d), the less deformable materials (after 14 hours) were again the separator and the CE with 3.7 μm (2.9 %) and 7.3 μm (1.8 %), and the graphite electrode showed the highest deformation, around 11.8 μm (25 %). The thickness variation observed in LP30 electrolyte compared with that of the same components in PC suggests that the recorded compression could depend both on the deformation of the materials and on the presence of DMC that evaporates, evidenced by salt traces in the cell holder. Indeed, in the PC-based electrolyte, the magnitude of the deformation of all materials is three up to five times lower. With the PC-based electrolyte, it is possible to assume that the response observed is entirely due to the compression of the examined materials.

The highest deformation in graphite results also predictable if correlated to the softness of the materials itself due to the weak π - π stacking interactions between the graphitic layers. By combining graphite with the stable activated carbon CE, it is likely that the former mostly originates thickness variations in the full cell.

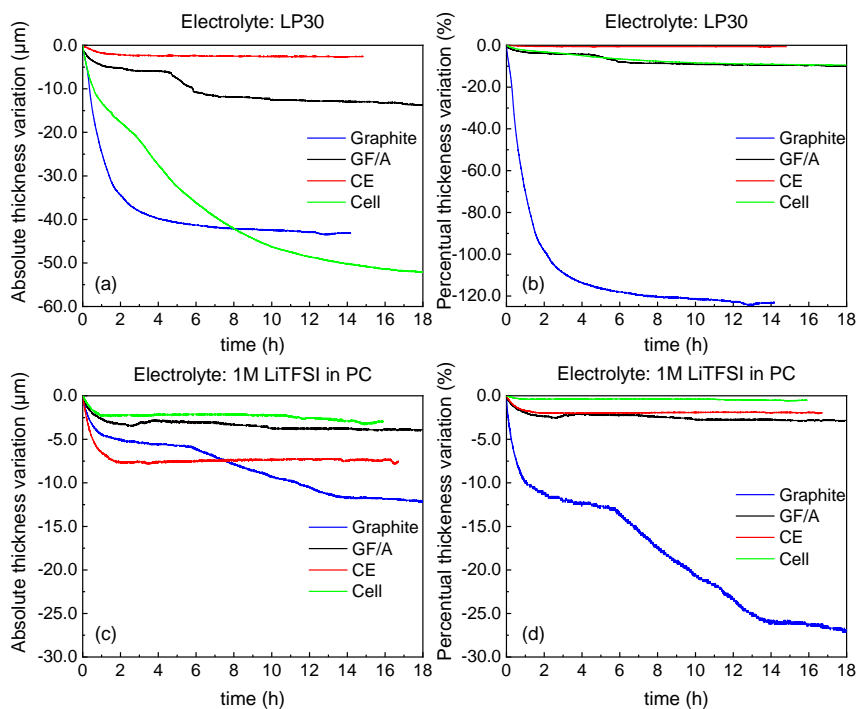


Figure 4.9. Absolute (a, c) and percentual (b, d) deformation of cell components and of the whole cell under 10 N force with different electrolytes, LP30 (a,b) and PC-1 M LiTFSI (c,d).

EC: DMC-based electrolyte

The voltage window of the electrodilatometric tests has been set after having monitored the electrode potentials vs Li in a Bola cell during cyclic voltammetry (CV) carried out in 2-electrode mode for simulating the experiments in the dilatometer cell holder. Indeed, it is mandatory to evaluate the potential range of the processes in a T-shaped cell operating in two-electrode mode with the monitoring of the electrode potentials vs. a reference Li electrode, and to verify the reproducibility of the experiments in the dilatometer cell. After assembly, the potentials were measured versus an internal lithium metal reference electrode. In LP30 electrolyte, the open-circuit potential (OCP) was -40 mV that corresponds to 3.40 V vs Li⁺/Li for the anode and 3.44 V vs Li⁺/Li for the cathode. Considering that the two electrodes have similar potential, cyclic voltammeteries (CV) have been performed at 2 mV s⁻¹ from the OCP to increasingly negative potential (Figure 4.10). The voltammograms show the typical profile associated with the redox process of the graphite during insertion/deinsertion of lithium ions in the layers of graphite. In the first cycle is evident the reduction

process of EC to produce the SEI. The potentials of each electrode vs. lithium metal RE were reported in Table 4.4. At - 4 V the potentials of the anode and the cathode were 50 mV vs Li⁺/Li and 4.05 V vs Li⁺/Li, respectively. Hence, - 4 V was chosen as the limit for the CV experiments. The electrode potential values recorded during CVs in PC-1M LiTFSI are very similar.

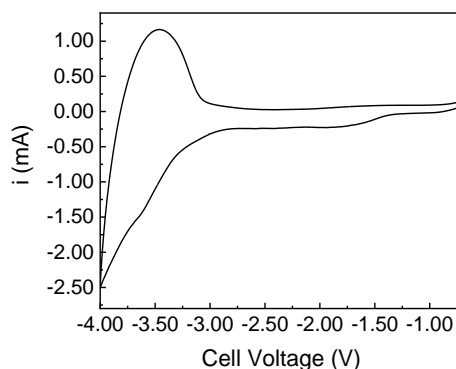


Figure 4.10. Preliminary CV experiments in LP30 (2 mV s^{-1}) in a T-shaped cell. The CV were carried out in two electrode mode, but the graphite WE and activated carbon CE potentials were monitored and measured vs lithium RE. The potential values are reported in Table 4.4.

Cell Voltage (V)	E_G (V) vs Li ⁺ /Li	E_{AC} (V) vs Li ⁺ /Li
-0.04	3.40	3.44
-1.00	2.05	3.05
-2.00	1.18	3.18
-2.50	0.84	3.34
-3.00	0.59	3.59
-3.50	0.38	3.87
-3.80	0.15	3.95
-4.00	0.05	4.05

Table 4.4. Graphite (G) and activated carbon (AC) electrode potentials measured vs lithium RE in the T-shaped cell.

After getting an insight about the pressure effect on the samples as previously described, and having established the potential window, the dilatometric tests were

carried during CVs at 2 mV s^{-1} and under an applied force of 10 N. The assembled cell showed an OCV of -74 mV .

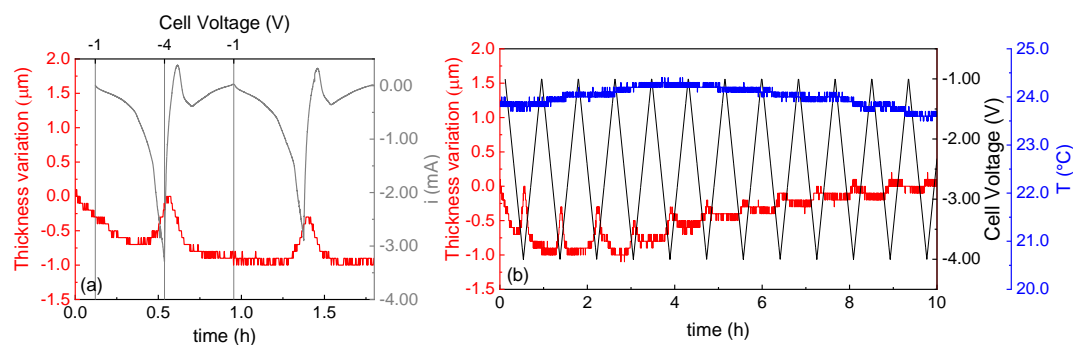


Figure 4.11. . (a) Thickness variation (red) and current (grey) during the first two CVs of the graphite//CE in dilatometer cell (2 mV s^{-1}); (b) thickness variation (red), voltage (black) and temperature (blue) during 10 continuous CVs of the graphite//CE in dilatometer cell (2 mVs^{-1}). WE: graphite, CE-RE: activated carbon, separator Whatmann: GF/A, 150 μL LP30.

In Figure 4.11a are reported the thickness variation (red) and the current (gray) during the first two CVs with the cell voltage on the top axis. The grey vertical lines indicate the cut-off voltages of the CV. The dilatometric profile is characterized by small expansion/shrinking peaks (less than $1 \mu\text{m}$) originated from the reduction/oxidation of the graphite electrode and the corresponding insertion/deinsertion of lithium ions within the graphitic layers. The expansions begin close to a cell voltage of -3 V that corresponds to $\approx 0.6 \text{ V vs Li}^+/\text{Li}$.

Additionally, a significant expansion that raises the baseline was observed over the initial ten CV cycles (Figure 4.11b). The expansion was ascribed to the gas evolution due to the decomposition of EC during the SEI formation as discussed in detail in the variable forces section. The thickness increase due to the gassing phenomena partially covers the thickness variations during insertion/deninsertion processes. It is partially compensated by the thickness decreasing phenomena due to the compression of the cell components under 10 N force as reported in Figure 4.10.

PC-based electrolyte

The potential window of the electrode materials in 1 M LiTFSI in PC has been set by monitoring the electrode potentials vs Li reference electrode in the same configuration

reported in the previous section. The electrode potential values were very similar to those reported for LP30 in Table 4.5.

The experiments in PC-1 M LiTFSI were performed in two different potential ranges with the lower graphite potential limited to 0.9 V vs Li⁺/Li to restrain the exfoliation of the graphite or set to ≈ 50 mV vs Li⁺/Li for reaching the exfoliation condition.

Figure 4.12a demonstrates the thickness variation (red) and the current (grey) during the first two CVs with the cell voltage on the top axis. The grey vertical lines indicate the cut-off voltages of the CV. The dilatometric profile shows bigger expansion/shrinking peaks than those in LP30. The expansion/shrinking peaks aligned with the insertion/deinsertion of lithium-ion in the layered material are reversible in accordance with the imposed cell voltage that prevents the complete exfoliation of the material. The progressive decrease of the baseline observed in Figure 4.12b retraces the temperature variation (reported in blue) during the experiments that were carried out at room temperature.

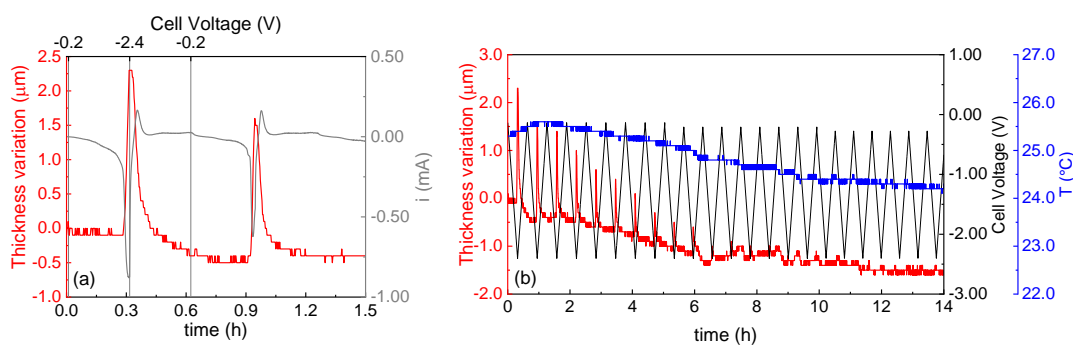
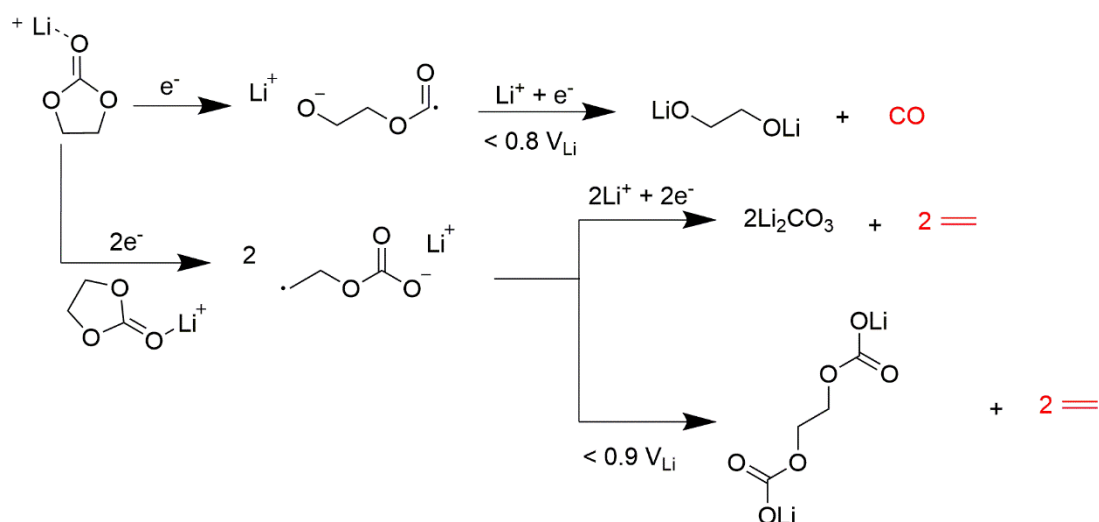


Figure 4.12. (a) Thickness variation (red) and current (grey) during the first two CVs of the graphite//CE in dilatometer cell (2 mV s^{-1}); (b) thickness variation (red), voltage (black) and temperature (blue) during 10 continuous CVs of the graphite//CE in dilatometer cell (2 mVs^{-1}). WE: graphite, CE-RE: activated carbon, separator Whatmann: GF/A, $150 \mu\text{L}$ PC- 1 M LiTFSI

Variable forces experiment

SEI formation mechanisms often involve the release of gas-phase products such as CO_2 , H_2 , CO , and $\text{C}_n < 3$ hydrocarbons [82]. As reported in Scheme 4.2, in EC/DMC mixtures the reduction of EC and DMC to form lithium alkylcarbonate compounds produces hydrocarbons as co-products. Liu and co-workers [83] determined by in situ differential electrochemical mass spectroscopy (DEMS) measurements that the main

gases originated during SEI formation on graphite electrodes in the first cycle are ethylene and CO₂ [84-86]. Bernard et al.'s investigation on graphite electrode with on-line DEMS reveals that the first negative scan leads to a breakdown of the 0.3% of the total amount of EC in 1 M EC: diethyl carbonate (DEC) 3: 7 wt%). In the reported condition, that corresponds to 0.293 μmol of EC [87] that decomposes to give 0.15 μmol of propylene.



Scheme 4.2. Possible reductive degradation pathways of PC with gas phase co-products (red labelled).

In order to make considerations about gassing in common alkyl-carbonate electrolytes, controlled hydrogen evolution experiments were carried out at different applied forces in order to assess the gassing detection ability of the dilatometer.

In a chronoamperometric experiment, 1 V was applied between two platinum electrodes and H₂ evolution occurs. The micromolar amount of hydrogen evolved was detected as a slight raising (0.6 μm) of the thickness variation curve that stops when the chronoamperometry ends. From the integral of the current curve over time, the amount of 5 μmol of H₂ was estimated to be produced during the test. Given that the temperature was constant, the thickness variation observed was ascribable to the gas formed. By increasing the force up to 20 N, the entity of the observed expansion decreases from 0.6 μm to 0.3 μm, even if the amount of H₂ produced was higher ($\approx 25 \mu\text{mol}$), as shown in Figure 4.13a and 4.13b.

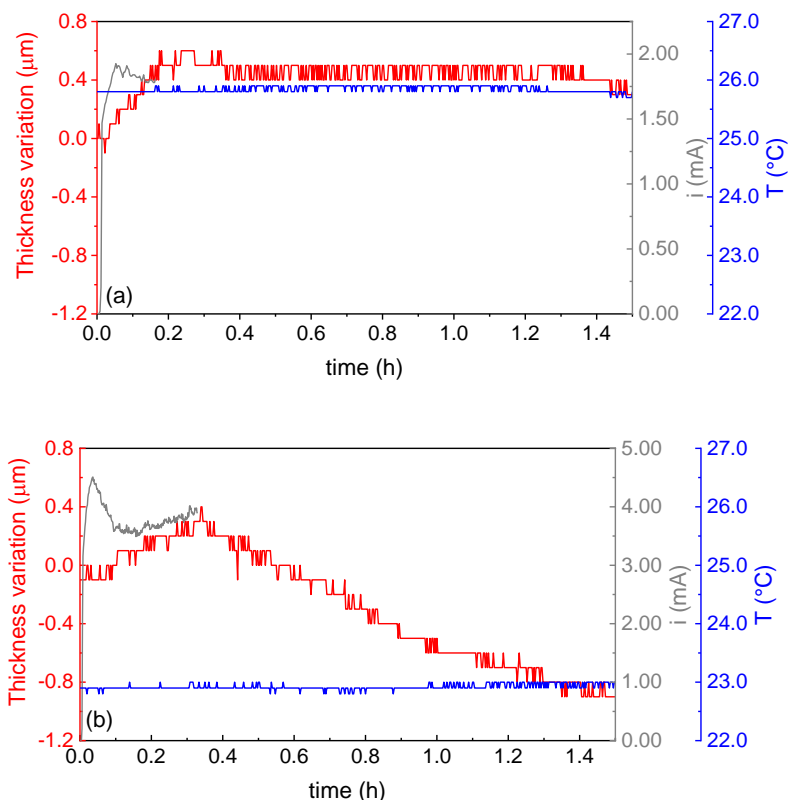


Figure 4.13. Thickness variation during hydrogen evolution (red) under an applied potential of 1 V in 1 M NaCl aqueous solution, current (grey) and temperature (blue). WE: Platinum 10 mm diameter, Separator Whatman GF/A, CE-RE: Platinum 8 mm diameter, 350 μ L 1 M NaCl in H₂O. (a) 10 N and (b) 20 N applied force.

In these experiments, the pressure resulting from the hydrogen evolution is not enough to contrast the applied force. However, the behaviour at 20 N leads us to suggest a mechanism in which the gas formed can be trapped by the porous separator that amplifies the thickness response. The application of a higher force decreases the porosity of the separator and less H₂ can be trapped inside the pores, thus justifying the lower thickness variation with 20 N applied. After voltage removal, when 10 N are applied, the pressure is not sufficient to force out the gas from the porosity of the separator and, indeed the thickness remains constant. On the other hand, the 20 N applied force leads to gas release from the separator, which results in continuous thickness decrease as reported in Figure 4.14.

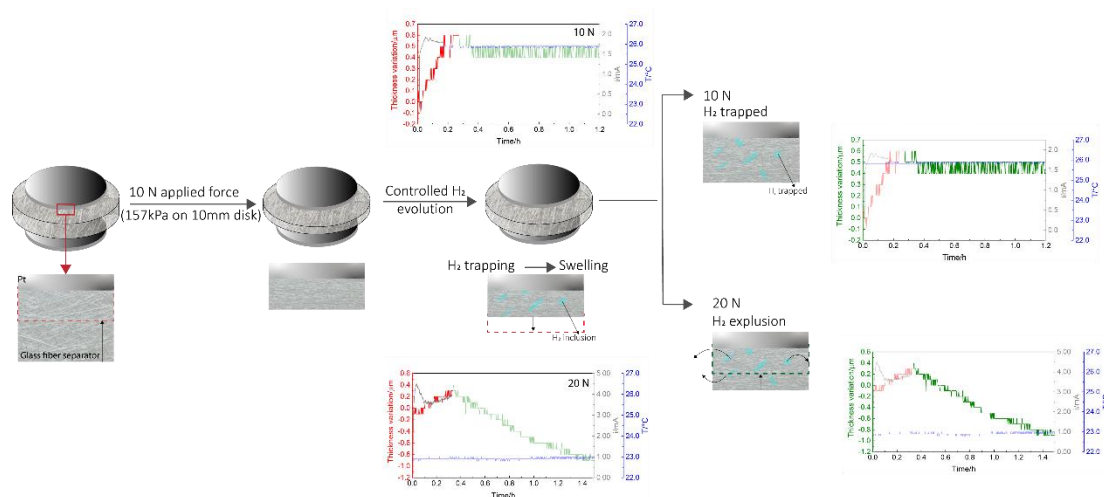


Figure 4.14. Schematic representation of the mechanism proposed for the hydrogen evolution experiment.

Graphite was then tested in PC-1 M LiTFSI in exfoliation condition with 10 N and 20 N applied. The dilatometer cell underwent a linear sweep voltammetry experiment from -0.1 V (open circuit potential) to -4 V. The cell was discharged later and after a few hours underwent three CV cycles. The thickness variation was continuously monitored during the whole experiment as shown in Figure 4.15a. At the cell voltage of -2.5 V (≈ 0.9 V vs Li^+/Li) co-intercalation of $\text{Li}^+(\text{PC})_n$ occurs. The dilatometric curve records a large expansion in electrode thickness (10-12 μm) that represents a 35% change in thickness upon intercalation. This variation is consistent with the co-intercalation of $\text{Li}^+(\text{PC})_n$ and corresponding exfoliation of the graphite. The related linear sweep voltammetry (Figure 4.15c) appears noisy due to gas evolution originating from the reductive degradation of PC in propylene [89,90]. Consequently, in addition to the intercalation of solvated lithium ions in the material, the formation of propylene gas causes crack and exfoliation of the graphite layers. The resultant dilatometric curve (Figure 4.15c) is given by the combination of the exfoliation and the gas evolution.

The force adjustment system and the control of the applied pressure allow to get insight into the contribution of the gas formation during the expansion as shown before for H_2 evolution, and Figure 4.15b,e,f displays the thickness variation of the cell operating in exfoliation condition with 20 N applied force. The expansion decrease was observed, as expected. The first cycle expansion corresponds to 13 μm and 8 μm for 10 N and 20 N experiments, respectively. The pore volume filled by the evolved gas

is smaller when external high force is applied and, in turn, the recorded expansion as schematized in Figure 4.16.

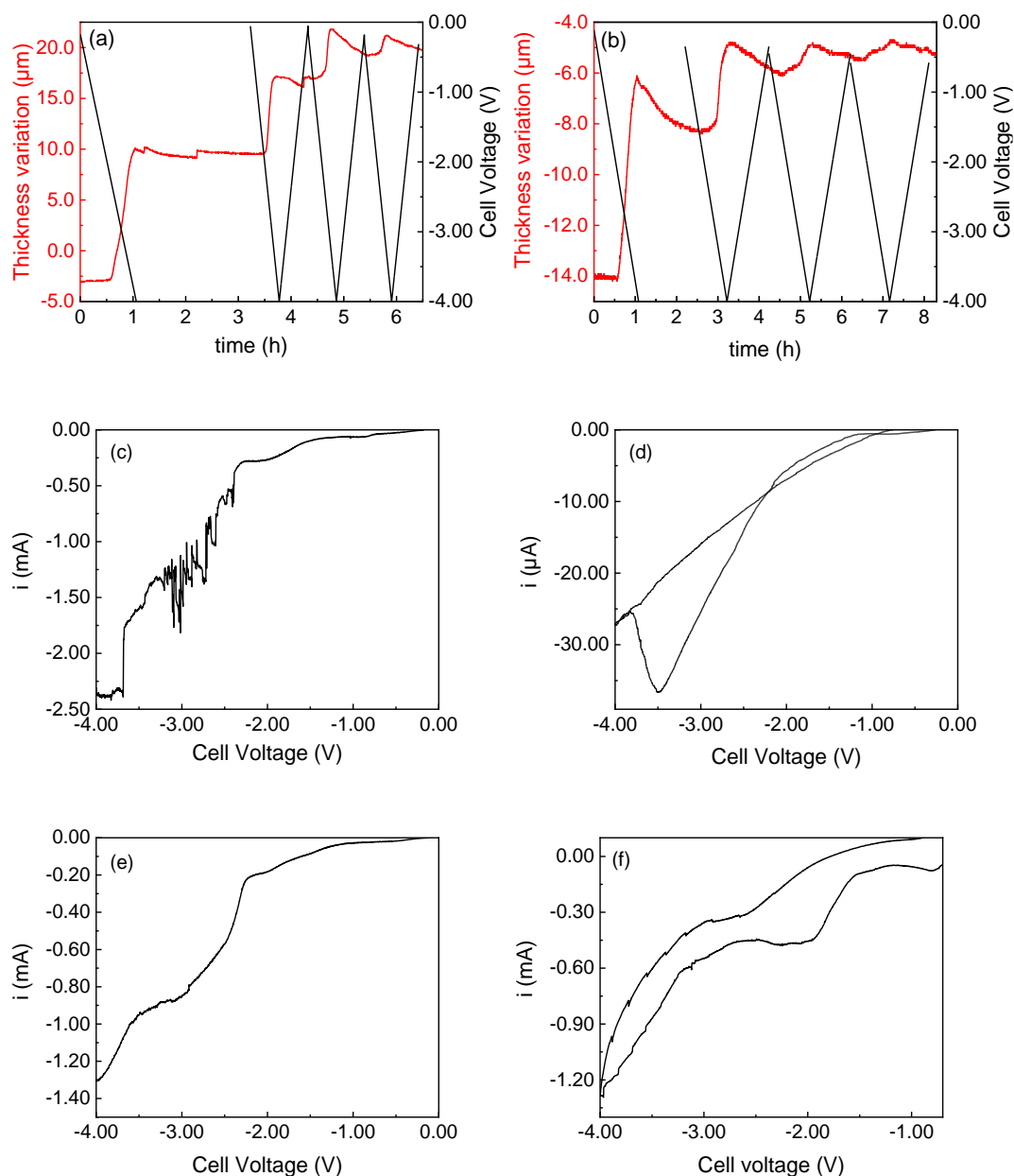


Figure 4.15. Electrochemical tests under 10 N applied force; (a) Thickness variation (red) and cell voltage (black) during electrochemical experiments under 10 N. (c) linear sweep voltammetry from OCP to -4 V, 1 mV s^{-1} ; (d) 1st CV from OCV to -4 V, 1 mV s^{-1} . Electrochemical tests under 20 N applied force; Thickness variation (red) and cell voltage (black) during electrochemical experiments under 10 N (b) linear sweep voltammetry from OCP to -4 V, 1 mV s^{-1} ; (f) 1st CV from OCV to -4 V, 1 mV s^{-1} . WE: graphite, CE-R: activated carbon, separator Whatman: GF/A, $150 \mu\text{L}$ PC- 1 M LiTFSI.

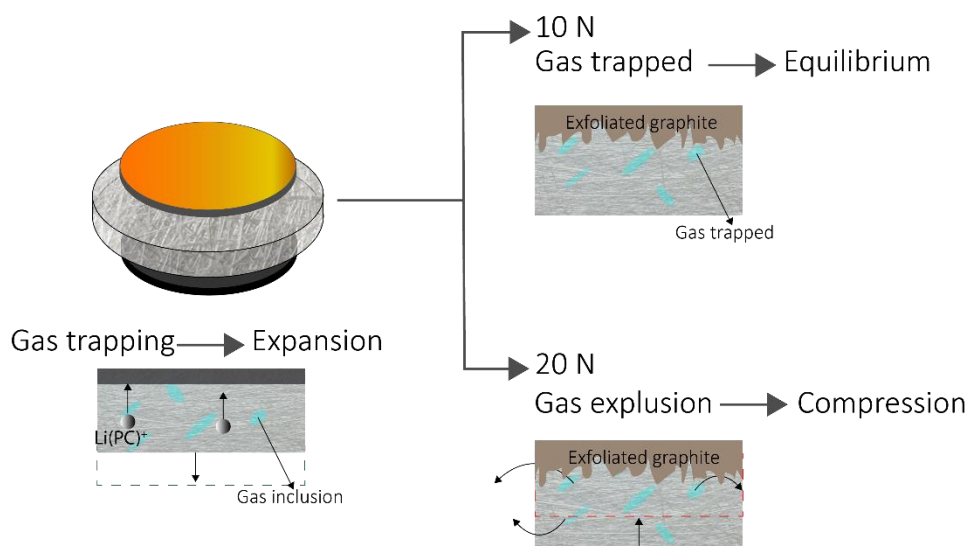


Figure 4.16. Schematic illustration of the mechanism proposed for the experiments at variable forces.

Chemical-physical characterization

SEM measurements were carried out on the graphite electrodes to get information about the consequences of the cycling (ten CVs) and of the applied force. Figure 4.17 depicts the SEM images of the pristine graphite electrode (Figure 4.17a) and of the graphite electrodes after cycling in the two electrolytic mixtures (Figure 4.17b and 4.17c). While from SEM images it is difficult to realize the difference between the pristine graphite electrode and the one cycled in EC: DMC (Figure 4.17b), the exfoliation of the electrode cycled in PC is evident on the bottom-right corner of the image (Figure 4.17c) in which expanded graphitic layers are visible.

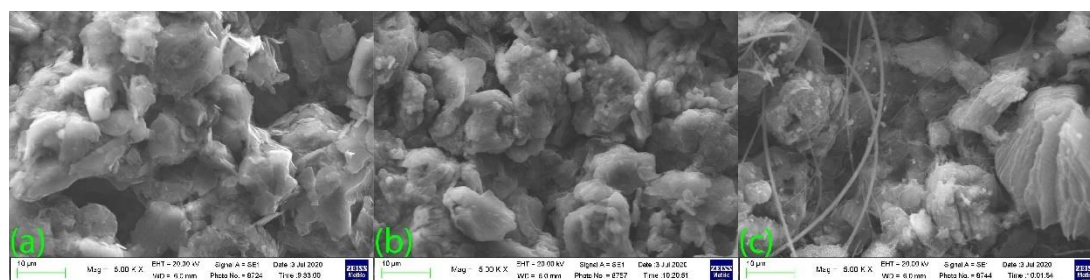


Figure 4.17. SEM images of (a) pristine graphite electrode, (b) graphite electrode cycled in LP30 and (c) graphite electrode cycled in exfoliation condition in PC-1 M LiTFSI.

Raman spectroscopy was used as a very effective way to investigate the bonding structure of graphite before cycling and the modification due to the cycling in the two

electrolytes. The Raman spectra of the graphite after cycling with 10 N force applied by the dilatometer were recorded and compared to the spectrum of the pristine electrode material (Figure 4.18). Samples rest 20 hours inside the electrochemical chamber of the dilatometer under a force applied of 10 N in two electrolytes to reach complete dimensional stability.

The characteristic graphite D, G, and 2D bands are present at 1350, 1580, and 2450 cm^{-1} , respectively. Additionally, the Raman spectrum of the pristine graphite spectrum shows a peak at 1564 cm^{-1} related to the D' band [91].

The graphite tested in LP30 evidenced the SEI formation only after cycling attributed to the peaks present in the low-frequency region of the spectrum in Figure 4.18a. The spectrum of the graphite before cycling in PC in Figure 4.18b also displays an additional peak that could be ascribed to an uncompleted removal of PC from the electrode. After cycling in PC in exfoliation condition, the D band in the Raman spectrum of graphite decreases, and the spectrum appears similar to that of the high ordered graphite [92]. The co-intercalation of PC molecules gradually damages the electrode and causes cracks and exfoliation of graphitic particles and, amorphous and small-sized carbon particles are the first to be detached from the electrode. The graphene sheets obtained were not detectable in the spectrum because of the washing step done on the material before recording the spectrum. Hence, only less damaged graphite particles remain attached to the current collector.

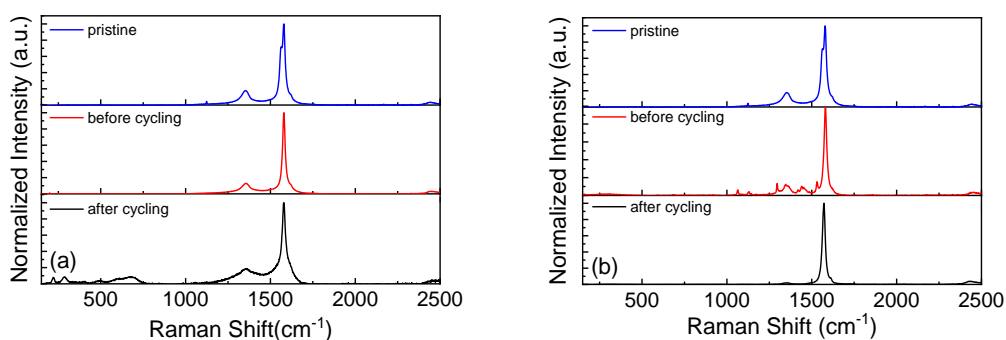


Figure 4.18. Raman spectrum of graphite electrode before and after cycling (a) in LP30 and (b) in PC - 1 M LiTFSI.

In conclusion, to predict the lifetime and the long-term stability of the cell new methods and techniques are needed. As an example, the thickness variation of the

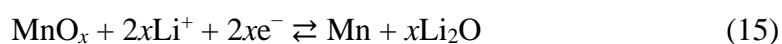
graphite electrode in EC: DMC-based electrolyte revealed simultaneous processes (insertion/deinsertion, solvent evaporation, SEI formation and gas evolution). In a different electrolytic system, such as PC-based electrolyte, the phenomena are different. In this case, the variation of an external force is extremely useful in distinguishing the solvent evaporation, which could be responsible of the capacity fading, or gassing process.

However, the applied force should not be so high to cause material deformation during measurements, or if high force is needed, the test should start after a resting time that assures the system components have reached their stable dimension. It has been demonstrated that this equipment can provide significant practical information on the behaviour of the cell, considering all its components. The deep understanding of the individual electrode behaviour is necessary.

4.5.2. Metal oxides as alternative negative electrodes for LiBs

Transition metal oxides have attracted major attention as negative electrode materials for the first time by Poizot et al. [93]. For instance, manganese oxides result interesting because of the multiple valence states of manganese ions and numerous possible crystalline structures and a high specific capacity (up to 1230 mAh g⁻¹ vs commercial graphite (372 mAh g⁻¹)) [94]. In addition, manganese oxide may exhibit one of the lowest potentials for the conversion reaction than other metal oxides. The resulting potential higher energy density and the high abundance of manganese on the earth's crust make it promising for the negative electrode in LiBs [95].

Specifically for these materials, the faradic process consists of the conversion of manganese cations to metallic manganese with the co-formation of lithium oxide, as shown in (15).



In this system, the oxidation state of the manganese and the crystalline form concur to determine the specific capacity and potential at which the conversion process between MnO_x and metallic Mn takes place with the formation of Li₂O as summarized in Table 4.5.

Mn-oxide	Potential V vs Li ⁺ /Li	Theoretical specific capacity mAhg ⁻¹
MnO	0.2	756
Mn ₃ O ₄	0.37	937
Mn ₂ O ₃	0.3	1019
MnO ₂	0.4	1223
CoMn ₂ O ₄	0.3	921
ZnMn ₂ O ₄	0.3	1008

Table 4.5. Experimental values of process potential and theoretical specific capacities Mn-based oxides active materials [96].

However, for this material, the conversion mechanism of the faradic process is the main obstacle that keeps it from practical application, which is described in Section 4.5.4.

The conversion of manganese oxide leads to a structural reorganization of the active material and to the formation of Li₂O. The latter can passivate the electrode responsible for manganese materials' capacity fade.

To solve this drawback several strategies have been adopted, combining the formation of porous nanostructures as 3D hollow or hierarchical porous nanostructures [97], hollow nanotubes [98], 1D nanorods/nanowires [99] and 2D nanoflakes [100].

The present strategies ensure high capacity and better stability but represent drawbacks for the integration in industrial production.

Another pursued strategy consists of introducing a considerable amount of carbon into the Mn oxide-based active material to form composites [101]. This approach aims to solve the volume strain problem due to the structural changes by a cushion effect acted by the carbonaceous phase. Meanwhile, the carbonaceous phase can also improve the electrical conductivity of the composite.

4.5.3. Carbon from CO₂-capture

As described in Section 4.6, graphite is the most used negative electrode material in LiBs. This material can be natural or synthetic [102]. The European Union now consider the formera critical raw material. The latter is commonly produced by

pyrolysis of petroleum derivatives. To achieve an acceptable degree of graphitization (high electric conductivity), the material needs to be thermally treated at elevated temperatures (2500 °C) for several days in some cases [103-107]. That influences material very high price with respect to natural analogous (20 US\$ kg⁻¹ vs 8-11 US\$ kg⁻¹, respectively [107]).

In addition, these steps increase the environmental footprint of synthetic graphite and make the greenhouse gas (GHG) emissions comparable to those of natural graphite [106].

To this purpose, many efforts have been carried out to identify a sustainable synthetic strategy that paves the way to the independency from natural graphite resources and expensive and non-environmentally friendly synthetic graphite.

A carbon dioxide sequestration and/or transformation technology is a valuable approach to decrease CO₂ emission into the atmosphere [108]. Splitting this molecule into C and O₂, a dangerous greenhouse gas can be transformed into a valuable resource. One proposed method for splitting CO₂ is the molten salt CO₂ capture and electrochemical transformation (MSCC-ET) method [109,110]. Various carbon products, such as carbon nanofibers (CNFs), carbon nanotubes (CNTs), graphite and graphene, have been successfully prepared in molten salts via electrolytic reduction processes [111]. Alternatively, carbonaceous materials can be obtained from the electroreduction of dissolved CO₂ in carbonates [112].

The MSCC-ET process is based on concurrent chemical and electrochemical processes, in which the overall aim is to capture CO₂ from the surrounding atmosphere and split it into solid carbon and molecular oxygen in a molten salt environment. The basic concept of splitting an alkali carbonate-containing salt into elemental carbon and its regeneration from gaseous CO₂ has been known for over a century [113]. To understand the concept, it is useful to imagine first, for example, a pure lithium carbonate salt at a sufficiently high temperature that it is melted (>730 °C). This liquid will contain lithium cations (Li⁺) and carbonate anions (CO₃²⁻) but also oxide (O²⁻) resulting from the dissociation of carbonate anions (A schematic representation of the MSCC-ET reactor is given in Figure 4.19).

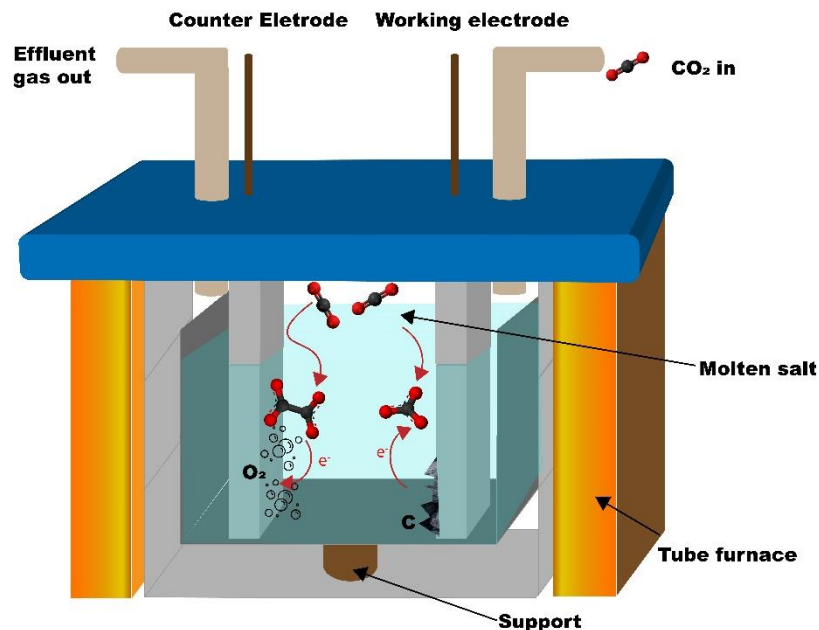


Figure 4.19. Schematic of the MSCC-ET reactor (Paper II).

The selfdissociation equilibrium can be expressed as in equation (16) [114]:



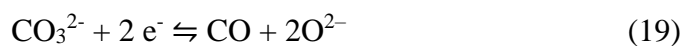
and is determined by the ionic activities and the partial pressure of CO_2 (the vapor pressure of lithium oxide is sufficiently low to ignore it at atmospheric pressure [115]). Thus, the molten lithium carbonate always contains some amount of dissolved lithium oxide, which is in equilibrium with CO_2 in the surrounding atmosphere. This equilibrium forms the basis of capturing CO_2 into the electrolyte in the MSCC-ET process. In addition, it has been shown that CO_2 can also be chemically dissolved in the carbonate to form dicarbonate anions ($\text{C}_2\text{O}_5^{2-}$) [114]:



The electrolytic splitting process relies on an electrochemical reduction reaction of the carbonate anion [116-118]:



At sufficiently low temperatures, this is the only cathode reaction, but at higher temperatures (for pure lithium carbonate, $>900^\circ\text{C}$ [119,120], CO will also be formed:



while on the anode, oxygen evolution takes place:



The overall reaction can be written as:



with the free energy change of this reaction determining the electrode potential. The excess O^{2-} anion will react with CO_2 from the surrounding atmosphere to regenerate the carbonate anion and thus, CO_2 can be captured from the gaseous atmosphere surrounding the MSCC-ET reactor and transformed into solid carbon.

The Mn-carbon composite material used in this thesis has been synthesized by the National Institute of Physics and Biophysics (NICPB) in Tallin from CO_2 using the molten salt CO_2 capture and electrochemical transformation (MSCC-ET) method with a previously used method. In the synthesis were used a nickel-chromium anode and a Zn-steel cathode. The cathode, on which carbonaceous material deposition takes place, has part of the Ni dissolved in the carbonate salt acting as a nucleation point for carbon nanofibers and other graphitic carbon structures (reactor scheme in Figure 4.19).

Important parameters to evaluate are represented by the average electrical efficiency that is given by the charge required to deposit the carbonaceous material divided by the charge supplied ($\approx 85\%$), the CO_2 conversion efficiency that can be evaluated by the ratio between the mass of the obtained carbon and the theoretical mass of carbon that should have been obtained with the used amount of electricity ($\approx 100\%$).

Considering that under 900°C in Li_2CO_3 , only solid carbon can be formed from CO_2 , the used amount of CO_2 used during the synthesis can be obtained from the molar masses. Indeed, each atom of carbonaceous material formed correspond to one CO_2 molecule.

4.5.4. MnO_x- graphitic carbon composite from CO₂ for sustainable Li-ion battery anodes

It has recently been shown that carbon material derived from CO₂ can be doped in situ while being deposited using additives in the electrolyte mixture or by modified electrodes. This has allowed for the design of nanostructured carbon materials decorated with metals as well as the synthesis of carbon/metal oxide composites [103,121]. For example, the zinc used in the cathode of galvanized steel used in the synthesis is an excellent catalyst for graphitization. On the contrary, steel can be unstable in the molten electrolyte, being the metals contained in steel, even in traces, leached into the electrolyte and incorporated inside the synthesis product [122-124].

As described above, manganese is a promising material as a negative electrode for LiBs and one strategy for its use involves the use of metal-carbon composites.

In addition, Mn can be used as a catalyst for the graphitization of carbon materials at high temperatures (>1400 °C) and can also graphitize precursors containing carbon such as lignin at 900 °C [125-127].

As a result, the MSCC-ET method has been used to directly synthesise carbon-manganese oxide composites in which the carbonaceous material accretes directly onto manganese oxide crystals.

The obtained material has been characterized by scanning electron microscopy (SEM), high annular dark field (HADF), scanning transmission electron microscopy (STEM) images, selected area electron diffractograms (SAED), X-Ray diffraction pattern (XRD) and X-ray photoelectron spectroscopy (XPS) spectra. The results presented in this section comes from ref. [III].

Carbon material characterization

A carbon portion (2 g) was ground in a mortar and then in a planetary mill (Pulverisette 6, Fritsch) with a 14 cm³ WC jar and 10 WC balls (5 mm diam.) for 15 min at 600 rpm and for 45 min at 450 rpm with the addition of a small amount of water (ca. 2 mL) to improve the grinding (C). Scanning electron microscopy images and electron diffraction spectroscopy analysis are reported in Figure 4.20a and Table 4.6). Another portion of carbon (2 g) was ground for 2 hours at 400 rpm in a 70 cm³ agate jar with 13 agate balls (10 mm diam.) and 4 balls (20 mm diam.). The powder was then sieved

with 50 and 20 μm sieves. About 60% of C was collected under the 20 μm sieve (C-20) and 30% under the 50 μm sieve (C-50). The latter portion of material with particle/agglomerate size between 20 μm and 50 μm , was mainly used for physicochemical characterization.

Slurries were prepared by using polyvinylidene difluoride (PVDF, Kynar HSV 900, Arkema) as binder soluble in N-methylpyrrolidone (NMP, Sigma-Aldrich). Slurries and solid composites were prepared with sodium alginate (SA, Sigma Aldrich), Teflon suspension (PTFE, Du Pont aqueous dispersion, TeflonTM 60 wt.%, density 1.5 g cm^{-3}), Na carboxymethyl cellulose (CMC, Sigma Aldrich, ultra-low viscosity) and styrene-butadiene rubber (SBR, Zeon BM 400b) as binder soluble in water. SuperC65 and SuperC65 (Imerys) were used as conducting agents. The formulations were C:PVDF (80:10) for the slurry in NMP, C:SA (87:3), C:CMC:SBR (85:7:3), C:CMC:PTFE (85:7:3) for the slurry in water:isopropanol (80:20) and C:PTFE (90:5) for the free standing electrode. The remaining percentage is carbon additive, as indicated in Table 4.12. The free-standing electrodes were calendared in order to obtain two different loadings (see Table 4.12). The slurries were prepared by ball milling carbons in a WC jar with the addition of the binder dissolved in a low amount of water for 90 min at 450 rpm. The slurries were deposited on a Cu foil with a Mini Coating Machine (Hohsen Corporation) at 0.3 cm s^{-1} and dried at RT overnight. Hence, the electrodes were cut (9 mm diameter) and pressed at 2 tons for 2 min. While the adhesion of the slurry with PVDF is good, that of the slurry with SA is poor.

Physico-chemical characterization of carbons

The scanning electron microscopy (SEM) images of the carbonaceous material is in Figure 4.20c and the EDS analysis of the selected area is shown in Figure 4.20d, with the data reported in Table 4.6 and 4.7. The SEM images in Figure 4.20a and 4.20b show the great heterogeneity of C despite grinding. Big particles and aggregates are present together with smaller particles, which affects the contact with the current collector. Bright spots in the images indicates the presence of metals. EDS analysis (Table 4.6) confirmed the presence of W (from the jar of the first sample grinding) and of other metals, specifically of Mn (up to 12% atomic, 33% weight), and a great amount of oxygen (44% atomic, 34% weight). To avoid the presence of W in the electrode preparation, the second sample of the pristine carbonaceous material was

ground in an agata jar. The sample ground in agata jar does not show any contaminant coming from the milling.

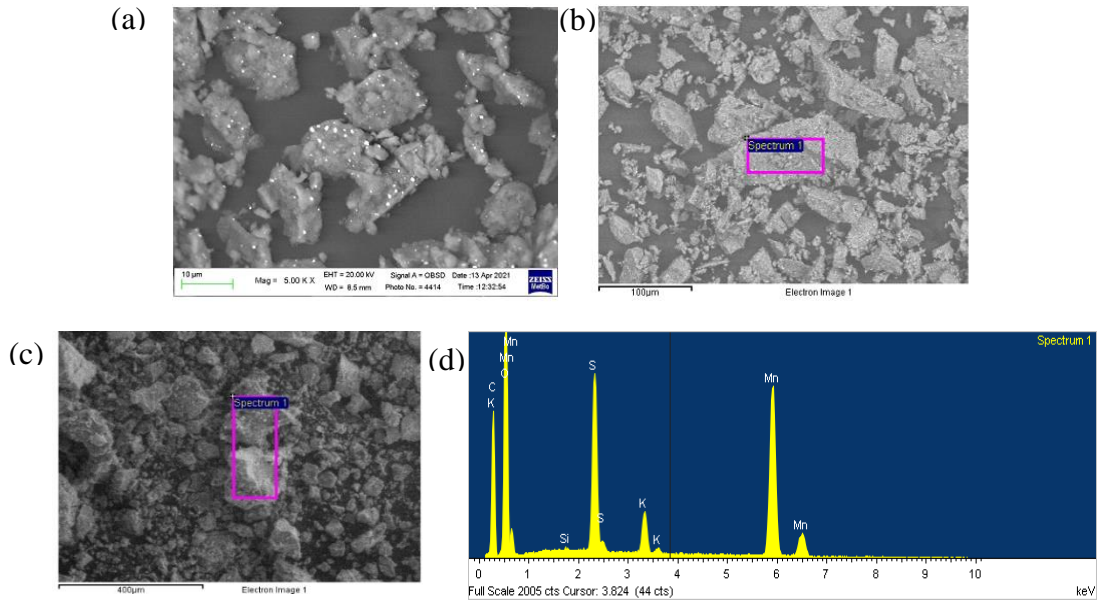


Figure 4.20. SEM images of (a, b) pristine carbon ground in W mortar, (c) pristine carbon ground in agata mortar (d) EDS analysis of the carbon ground in mortar.

Element	App Conc.	Intensity Corrn.	Weight%	Weight% Sigma	Atomic%
C K	60.97	0.5238	21.98	1.01	38.19
O K	149.85	0.8409	33.64	0.70	43.89
S K	25.14	0.9194	5.16	0.16	3.36
K K	16.87	1.0810	2.95	0.12	1.57
Mn K	147.37	0.8522	32.65	0.59	12.40
Co K	2.89	0.8048	0.68	0.15	0.24
W M	10.95	0.7031	2.94	0.29	0.33

Table 4.6. Elemental analysis of C ground in WC jar

Element	App	Intensity	Weight%	Weight%	Atomic%
	Conc.	Corrn.		Sigma	
C K	196.56	0.5795	33.78	0.59	47.86
O K	282.36	0.7028	40.01	0.48	42.56
Si K	0.73	0.8522	0.09	0.03	0.05
S K	53.01	0.9518	5.55	0.10	2.94
K K	17.78	1.0621	1.67	0.05	0.73
Mn K	154.40	0.8126	18.92	0.25	5.86

Table 4.7. Elemental analysis of C ground in agate mortar

The synthesized material contains Mn and O, other than carbon arising from the galvanized steel cathode used in the MSCC-ET process. Since the MnO_2 is present even after purification in 5 mol L^{-1} HCl, it is likely that the MnO_2 is protected by a graphitic carbon layer impenetrable by liquid solutions. After milling and sieving with $20 \mu\text{m}$ sieve (C-20) and $50 \mu\text{m}$ sieve (C-50), the presence of MnO_x is evidenced by high annular dark field (HADF) scanning transmission electron microscopy (STEM) images, selected area electron diffractograms (SAED), X-Ray diffraction pattern (XRD) and X-ray photoelectron spectroscopy (XPS) spectra, demonstrating the embedding of MnO_x inside the carbon matrix.

STEM images revealed that MnO_2 is embedded in the carbonaceous matrix (Figure 4.21a) indeed. Selected area diffraction (SAED) pattern (Figure 4.22b) reveals the polycrystallinity of MnO_2 with nanocrystals diameter from 10 to 50 nm. The satisfied diffraction condition of the sample's crystal structure observed in the SAED all corresponds with the $\text{Mn}_{7.98}\text{O}_{16}$.

In the present work, after milling the sample, the MnO_2 is exposed and can contribute to the performance of the cell [128]. Carbon/transition metal oxide composites can have increased power performance and cycling behavior due to pseudocapacitive processes, meaning that the MnO_2 leached from the electrode has a positive effect in this case. However, in the case of undesired phases, further purification of the carbon via treatment in concentrated acids and other oxidizers such prior to HCl washing to expose the metal/metal oxide particles is possible, however, such harsh treatments also modify the structure of the carbon material itself [129].

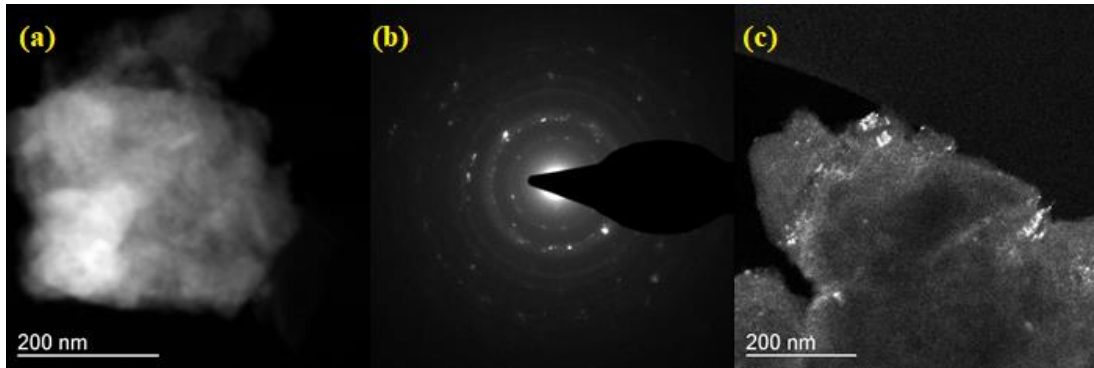


Figure 4.22. HADF-STEM images of C50 carbon. (b) SAED pattern acquired over an area of 200 nm. (c) HADF-STEM image of C-50 sample selecting the reflection at ($d=0.31\text{nm}$) in the SAED pattern.

The XRD pattern of the pristine synthesized carbon and of C-50 are shown in Figure 4a. In the diffractograms the typical carbon reflections at 26° and 55° are present in addition to several reflections associate to a $\text{Mn}_{7.84}\text{O}_{16}$ pattern and other metal impurities in the 40° - 45° range. By contrast, the latter are less intense in the pattern of the pristine synthesized carbon before grinding, except that below 20° . This confirms the exposure of MnO_x by milling. X-ray diffraction patterns of manganese oxides materials consist of small signals on a diffuse background due to structural defects. As showed by Julien et al. [128], the particle size and the chemistry of defects lead to the structural differences in the materials. In the material reported, the presence of potassium (Figure 4.23a) could influence the reflection positioning and intensity.

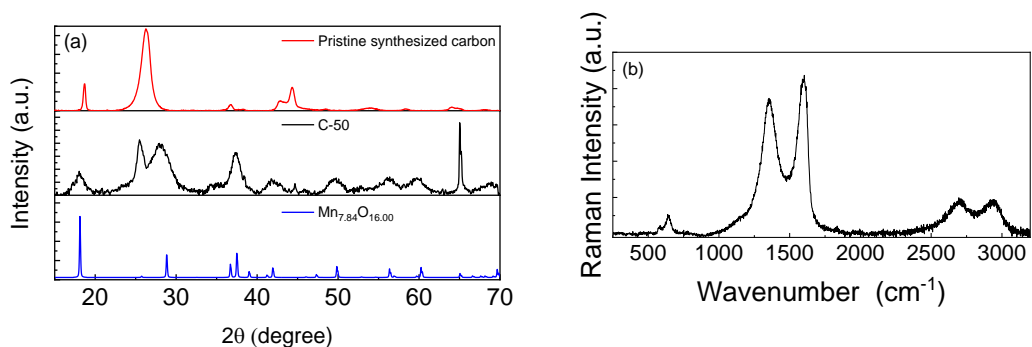


Figure 4.23. (a) X-ray diffraction pattern of pristine synthesized carbon (red), C-50 (black) and diffractogram of $\text{Mn}_{7.84}\text{O}_{16}$ (reference code 96-151-4117). (b) Raman spectrum of the carbon ground in agate mortar.

Raman spectra in Figure 4.23b also confirmed that the synthesized carbonaceous material is graphitic. The characteristic graphite D, G, and 2D bands are present at ca. 1350, 1580, and 2700 cm^{-1} , respectively. Additionally, the Raman spectrum showed reflections that could be attributed to Mn^{2+} at ca. 700 cm^{-1} . The general peculiarity of the vibrational features MnO_2 is their low Raman activity. Generally, the spectrum is characterized by three bands at 500–510, 575–585 and 625–650 cm^{-1} . The two high-wavenumber bands have a higher Raman intensity, while low-frequency bands are not visible in the spectrum reported. The two high-frequency bands at 640 and 580 cm^{-1} indicate the presence of MnO_2 as romachenite [129].

The full survey XPS spectrum (Figure 4.24a) of C-50 carbon shows the characteristic peaks of C1s, K2p, O1s, and Mn2p at 284 eV, 292.5 eV, 532 eV, and 641.9 eV, respectively. Atomic percentage quantification is reported in Table 4.8, weighted composition is obtained by correcting the bands area for the atomic mass. The carbonaceous material shows great presence of carbon and manganese with the oxygen that is involved in manganese oxide phase and oxygen-functional groups in carbon phase. Indeed, the carbon phase contains a 15% of oxygen functionalities in the structure (Table 4.9).

The XPS high resolution of C1s (Figure 4.24b) exhibits contributions of C=C carbon at 284.1 eV, C-H at 284.9 eV, C-O-R at 286.0 eV, and C=O at 288.2 eV [130, 131]. These signals overlay with the less intense K2p signals. Also, S2p shows the typical $2p_{3/2}/2p_{1/2}$ doublet separation of 1.18 eV with peaks constrained to a 2/1 area ratio ($2p_{3/2} / 2p_{1/2}$) (Figure 4.24e) [132].

The O1s region (Figure 4.24c) presents at least three contributions indicating the Mn-O bonds with a prevalence of Mn-O-H terminals (75% from the integrated deconvolution reported in Table 4.10). This agrees with the presence of a nanocrystalline material with extended boundaries. The Mn2p region (Figure 4.24d) shows the two signals related to the spin-orbit coupling ($\text{Mn}2p_{3/2}$ and $\text{Mn}2p_{1/2}$). The manganese bands result from the contribution of MnO_2 phase at 641.3 eV [133, 134] and Mn_2O_3 at 642.6 eV [133, 134] in a 4:6 ratio (Table 4.11).

	Binding energy (eV)	Abundance (%)	Weighed abundance (%)
C	1s 284.4	25.9	15.7
K	2p 292.5	1.9	3.2
O	1s 531.5	51.7	35.7
S	2p 168.4	3.2	4.4
Mn	2p _{3/2} 642.2	17.3	41.0

Table 4.8. Atomic content of C-50 from integrals of C1s, K2p, O1s, S2p, and Mn2p signals.

C1s	Binding energy (eV)	Abundance (%)
C=C	284.4	45.6
C-H	285.3	34.6
C-O-R	286.4	10.6
COOH	288.0	4.3
π - π	288.9	5

Table 4.9. Integrals of deconvoluted high-resolution XPS spectra of C1s region.

O1s	Binding energy (eV)	Abundance (%)
MnOMn	529.6	8.9
MnOH	531.6	75.2
OH	533.1	15.8

Table 4.10. Integrals of deconvoluted high-resolution XPS spectra of O1s region.

Mn2p _{3/2}	Binding energy (eV)	Abundance (%)	Abundance vs. total (%)	O bonded to Mn (%)
Mn ₂ O ₃	641.2	57.5	9.8	14.7
MnO ₂	642.6	42.5	7.4	14.8

Table 4.11. Integrals of deconvoluted high-resolution XPS spectra of Mn2p_{3/2} region.

The carbon and manganese oxides weight content were estimated from XPS deconvolution (Table 4.11). Material composition is expected to be homogenous in consequence of the grinding protocol. The atomic percentage of Mn and their

composition obtained from the Mn2p high-resolution XPS spectrum deconvolution were used to split the atomic oxygen percentage in the fraction bonded to the Mn and the part involved in the oxygen-functional groups the carbonaceous phase. The atomic fraction of oxygen involved in the Mn-oxide phase (At_{O-Mn}) corresponds to the sum of the oxygen involved in the Mn_2O_3 phase ($At_{Mn_2O_3}$) and the oxygen in the MnO_2 phase (At_{MnO_2}). The weight percentages were obtained by dividing the atomic percentage for the atomic weight (21).

$$At_{O-Mn} (\%) = At_{Mn_2O_3} + At_{MnO_2} = 29.5 \text{ (20.4 \% wt.)} \quad (21)$$

The percentual weight of the manganese phase ($m_{Mn-oxides}$) was obtained summing the corresponding weight percentage from XPS deconvolution of Mn ($m\%_{Mn}$) and oxygen ($m\%_O$)

$$M_{Mn-oxides} (\%) = m\%_{Mn} + m\%_O = 61.4\% \quad (22)$$

From the C1s high-resolution XPS deconvolution, the atomic percentage of oxygen contained in oxygen functional groups of the carbonaceous phase was 22.2 % (15.3% wt.). The sum of the oxygen-carbon bounded ($m\%_{O-C}$), and carbon abundance ($m\%_C$) was taken as amount of the graphitic carbon phase (m_{carbon}).

$$m_{carbon} (\%): m\%_{O-C} + m\%_C = 31.1\% \quad (23)$$

The remaining 7.5% is attributed to sulphur and potassium traces in the synthesized active material.

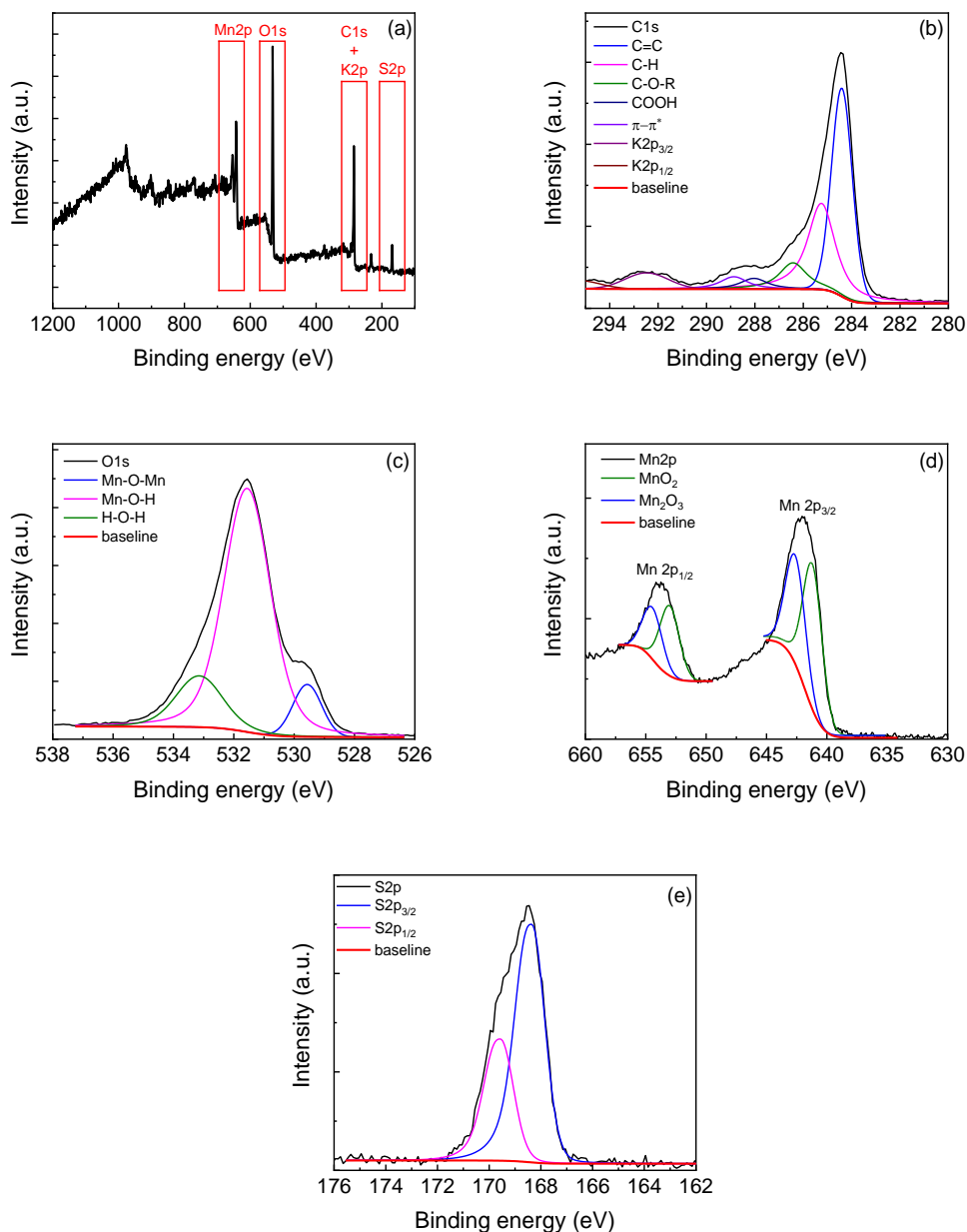


Figure 4.24. (a) XPS survey spectra of C-50, high-resolution XPS spectra of (b) C1s region, (c) O1s region, (d) Mn2p region and, (e) S2p region of the carbon material ground in agata jar.

Figure 4.25a shows the TGA analysis in thermal as well as thermo-oxidative conditions. These curves are totally different from pure graphitic materials and evidence the presence of metal oxides. The two curves display almost the same behavior up to 200°C. The sample is stable in Ar up to 500°C, as expected. Hence, above 600°C the mass continues to decrease but at low rate, with a total mass decrease of 45%. This would mean that 55% of C-50 is constituted by inorganic material

(presumably oxides), in agreement with SAED and XPS analysis. Hence, the residual quantity, 55% of the total mass, agrees with the MnO_x observed by XPS analysis. The TGA curve in O_2 displays a mass decrease occurring by steps, starting around 250°C, 400°C and 750°C, with a final residue of 45%. This curve is very similar to that of MnO_2 [135], where the mass decreases up to 400°C is explained by the removal of adsorbent, the transformation of MnO_x to the other crystalline oxide phases up to the conversion of MnO_2 to Mn_2O_3 above 700°C with oxygen release. Figure 4.25b shows the XRD patterns of the residues from the two TGA analyses in Ar and O_2 . The patterns display the presence of MnO in the residue after the TGA in an inert atmosphere, and the presence of oxides of Mn(III) and Mn(IV) formed throughout the TGA in oxygen.

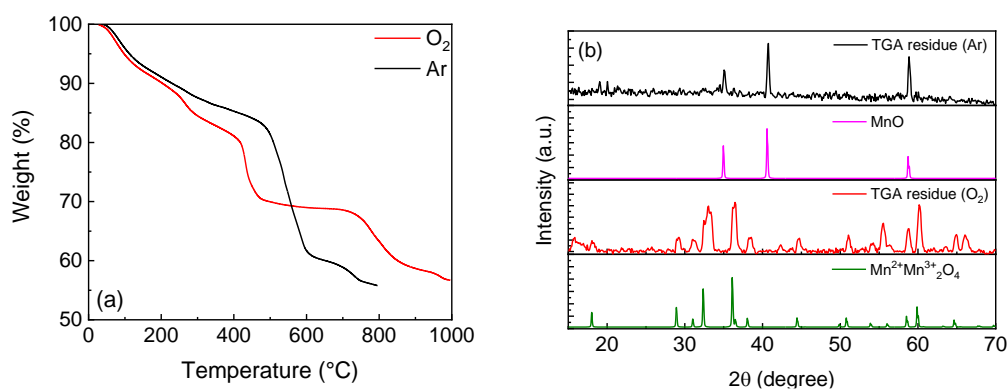


Figure 4.25. a) TGA curves of C-50 in Ar and in O_2 at $10^\circ\text{C min}^{-1}$. b) XRD patterns of the residues from the TGA of Figure 6a, MnO (reference code 01-075-0626) and Mn_3O_4 (reference code 01-089-4837).

We can estimate that in the reported samples the content of C is less than 50%, by considering that the decrease below 200°C could be also due the adsorbed water and to the oxygen-containing functional groups (15% from XPS analysis) and the remaining ash is mainly constituted of metal oxides.

Electrochemical characterization of carbons

The high inorganic material content could affect adhesion on Cu current collectors. Indeed, we did not observe any improvement in passing from the coarse C to the more homogeneous C-20 with SA binder, even by changing the conductive carbon Super C65 with the Super C45, more suitable for aqueous processes. The formation of agglomerate is evident in all the formulation with SA binder and could be justified by

the presence of manganese cations that could have a mild and unsteady complexing effect on SA[134]. With the carbon C and C-20 different formulations have been prepared and reported in Table 4.12.

SEM images of the electrodes with formulation #1 and #4 are in Figure 4.26. The heterogeneity of the material particles used in electrodes with formulations #1-#3 causes inhomogeneous electrode surfaces that could affect the solid electrolyte interface layer (SEI) formation and cycling. The self-standing electrodes (Figure 4.26a,b) seem more compact than those from the slurries #2-#3 (Figure 4.26c-f). Electrode obtained from C-20 (Figure 4.26g,h) shows increase homogeneous composite with numerous cracks. It's also worth noting that, if the fractures are present only on the electrode surface could positively affect the electrochemical performance, allowing a better wetting of the electrode.

Free-standing electrodes (#1) were too resistive, even the thinnest ones. The electrodes with formulations #2, #3 and #4 gave the voltametric response of the first two cycles is shown in Figure 4.27.

#	Carbon %	Binder %	Additive %	Solvent mix	Formulation type	Current collector	Adhesion	mg cm ⁻² active
1	C 90	PTFE 5	Super C65 5	ethanol	solid	none	n.a.	19.8±0.7 3.13±0.06
2	C 80	PVDF 10	Super C65 10	NMP	slurry	Cu	good	3.6±1.2*
3	C 87	SA 3	Super C65 10	water:isopropanol 80:20	slurry	Cu	poor	2.7±0.5
4	C-20 87	SA 3	Super C45 10	water: isopropanol 80:20	slurry	Cu	poor	2.9±1.2*

Table 4.12. Self-standing and slurries formulation prepared to test the carbonaceous material (indicated as Carbon and abbreviated as C) from MSCCT-ET process.

*The high absolute error is due to the detachment of small portions of the deposit from the current collector. The weight of each electrode was considered for the specific capacity evaluation, not the mean values.

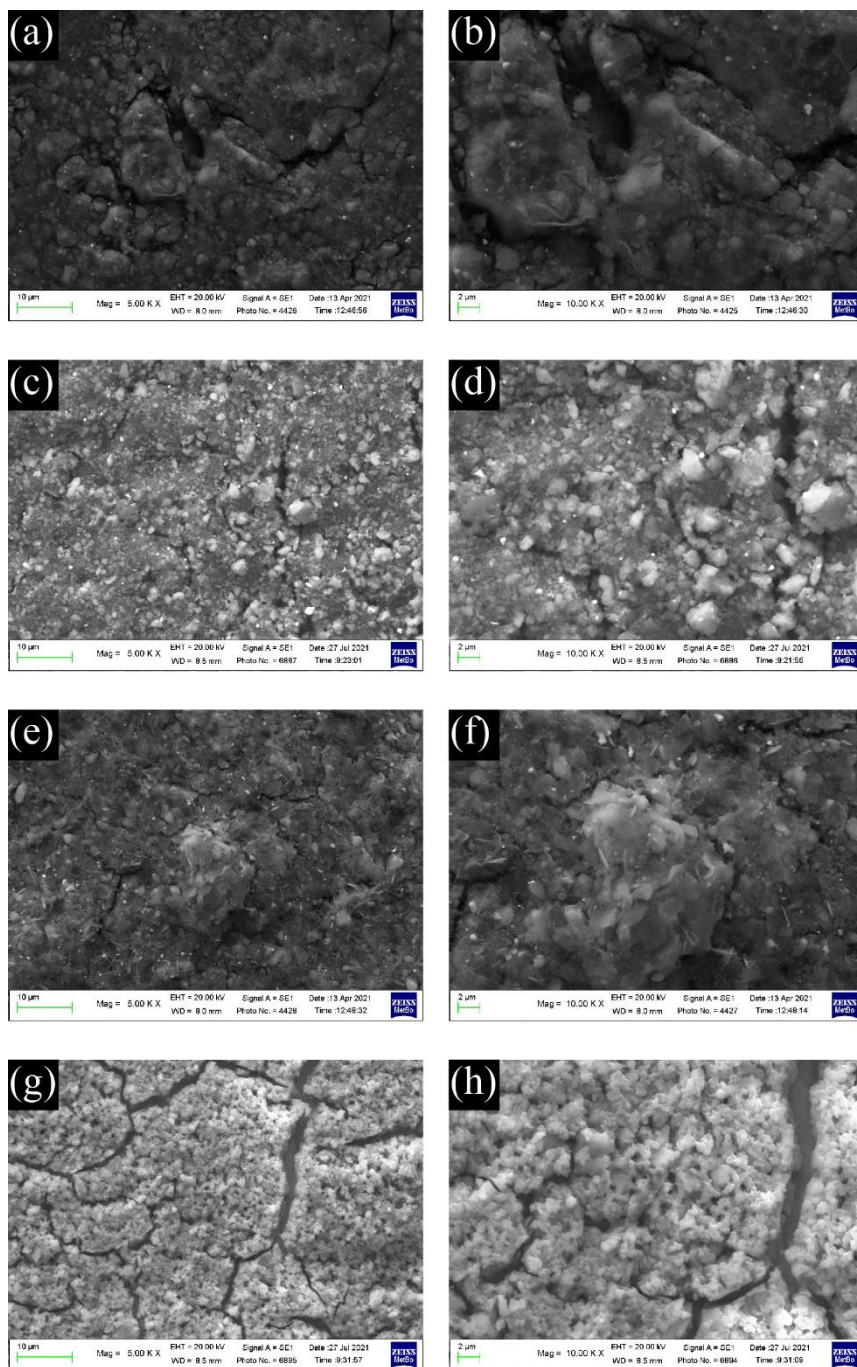


Figure 4.26. SEM images of electrodes from formulations #1 (a,b), #2 (c,d), #3 (e,f), and #4 (g,h).

As expected, the shape of the CVs is different from that of pure graphite [137]. During the first cycle, in addition to the reduction peak of EC at ca. 0.75 V [138], other reduction processes are present and disappear in the second cycle. The reduction peak is near 0.25 V for both samples, and the oxidation peak is at ca. 1.0 V. These processes are ascribed to the reduction of Mn^{4+} to $Mn(0)$ and to the oxidation of metallic Mn to

Mn²⁺. The further oxidation of Mn²⁺ occurs at potentials higher than 2 V [139]. In the 2nd CV, the reduction broad peak shifts at ca. 0.5 V and remains constant also for the following cycles, indicating the conversion of the Mn₂O₃ and MnO₂ phase (observed in XPS) to MnO. The reduction of Mn⁴⁺ and Mn³⁺ to Mn²⁺ occurs during the first reduction process with the formation of Li₂O [128, 140]. In addition, MnO₂ can be lithiated and converted to LiMnO₂. In this case, part of the irreversible capacity loss of the first cycle can be attributed to lithium consumption. Also, the conversion reaction of Mn²⁺/Mn⁰ lead to the formation of Li₂O. Li₂O could passivate the electrode, given its not conductive nature, and be responsible for manganese materials' capacity fade [140]. Moreover, the electrode operating potential window was limited to 2V to keep the Mn²⁺ oxidation state. Indeed, besides the redox processes occurring between 0 and 2.0 V, the specific capacity of MnO is 756 mAh g⁻¹ [140].

The electrode with PVDF binder (#2) displays a lower coulombic efficiency than the electrodes with SA binder (#3 and #4). The higher concentration and more uniform distribution of the carboxylic groups along the SA chains facilitate Li⁺ movement and hence, the insertion/deinsertion processes, and can improve the quality of the SEI. For this and other advantageous properties, like the need of lower percentages of binder in the electrode formulation, it was first proposed as a binder for Si-based anode materials [141] and for high voltage cathodes like LiNi_{0.5}Mn_{1.5}O₄ [142, 143].

The capacity performance of the formulation #3 with SA was tested in LP30 and in LP30- 2% VC. The rate capability was also compared to that of #2. The current calculated in the rate capability experiments are based on the mass of the active material (carbon and MnO_x).

Figures 4.28a and 4.28b report the rate capability and stability tests of formulations #3 (see also Figure 4.29a). GCD cycles demonstrated that the formulation with PVDF is worse than that with SA, as expected from the low coulombic efficiency evinced from CVs of Figure 4.27, although the electrode adhesion to current collector is better. The electrode #3 tested in LP30 - 2% VC shows smaller specific capacity at different current regimes. The coulombic efficiency gives scattered values (Figure 4.28b), indicating that the formed SEI is quite unstable without significantly affecting capacity retention. The addition of VC seems not to improve either the capacity performance or cycle stability. However, the difficulties of obtaining electrodes with a good adhesion may have a role in this evaluation and work in progress to evaluate other

current collectors. The stability of #3 electrodes were evaluated after the rate capability test, considering the percentage variation of the electrode theoretical capacity (t. c.) that was obtained from the active material composition from XPS studies as follows.

The active material's percentual composition ($m_{\text{Mn-oxides}}$ and m_{carbon}) was used to calculate the respective contribution to the electrode capacity. As an example, for 1g of active material, 0.31 g are graphitic carbon (theoretical capacity: 372 mAh g^{-1}), and 0.61 g are present as manganese oxides. (756 mAhg^{-1}). Hence, the two separate contributions (c_{carbon} and $c_{\text{Mn-oxides}}$) to the theoretical capacity of 1g of active material corresponds to:

$$c_{\text{carbon}} = m_{\text{carbon}} (\text{g}) \times 372 \text{ mAh g}^{-1} = 115.3 \text{ mAh} \quad (24)$$

$$c_{\text{Mn-oxides}} = m_{\text{Mn-oxides}} (\text{g}) \times 756 \text{ mAh g}^{-1} = 461.2 \text{ mAh} \quad (25)$$

Hence, the active material theoretical capacity c_{active} is:

$$c_{\text{active}} = c_{\text{carbon}} + c_{\text{Mn-oxides}} = 576.5 \text{ mAh} \quad (26)$$

The percentual contribution of the two phases can be found as:

$$c\%_{\text{carbon}} = \frac{c_{\text{carbon}}}{c_{\text{active}}} \times 100 = 20 \% \quad (27)$$

$$c\%_{\text{Mn-oxides}} = \frac{c_{\text{Mn-oxides}}}{c_{\text{active}}} \times 100 = 80 \% \quad (28)$$

A 31% graphitic carbon (t. c. 372 mAhg^{-1}) contributes to the 20% electrode capacity, while 61% of manganese oxides phase (considered t. c. 756 mAhg^{-1}) determines the remaining 80%. Upon cycling (Figure 4.28b), the electrode capacity approach asymptotically the theoretical capacity of the graphitic phase. Thus, during cycling, the formation of Li_2O lead to an unstable Mn/Mn^{2+} conversion reaction without affecting the insertion/deinsertion process of graphitic carbon. Also, graphitic carbon seems to exhibit a high capacity approaching the theoretical capacity even if part of the Mn-phase is still electrochemically active.

As the best case for graphite, it has been considered that the capacity loss over cycling is mainly due to the MnO_2 (high loss of the first cycles). It is not possible to assert that graphite remains unaltered over cycling or its specific capacity near the theoretical

one. If the graphite has a lower specific capacity, the results indicates that a higher amount of MnO_2 is still working after 200 cycles.

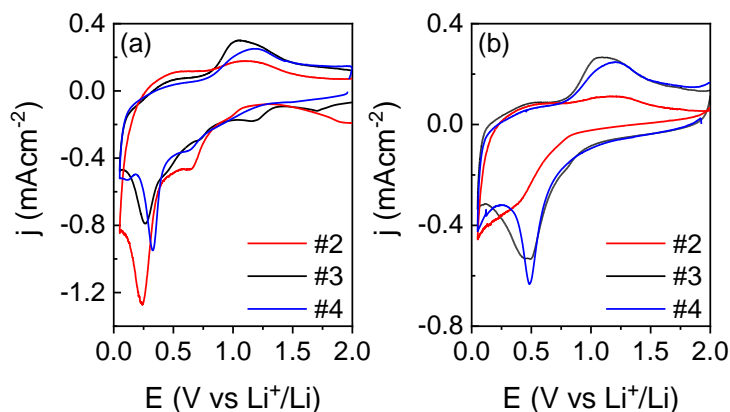


Figure 4.27. 1st CV (a) and 2nd (b) CV at $50 \mu\text{V s}^{-1}$ in LP30, WE: carbon electrodes, CE-RE: lithium, separator Whatman: GF/A.

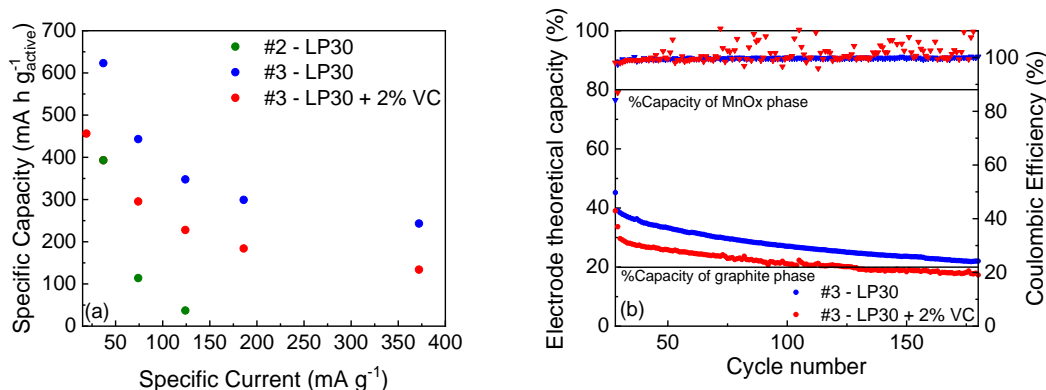


Figure 4.28. Specific capacity and coulombic efficiency of #3 in LP30 (blue) and LP30 + 2% VC (red) and of #2 in LP30 (green). (a) rate capability test at different specific currents, and (b) stability test at 371 and 186 mA g^{-1} in LP30 and LP30 + 2% VC, respectively.

In Figure 4.29a and 4.29b are reported the rate capability performance of #3 with and without the vinylene carbonate (VC) additive to 1M LiPF_6 EC:DMC 1:1 electrolyte. The C-rates reported have been calculated on the theoretical capacity of graphite (372 mAh g^{-1}). A significant difference in the initial capacity in the two conditions was observed. The #3 in LP30 shows the first cycle with a specific capacity during the insertion and the SEI formation of 662 mAh g^{-1} and 582 mAh g^{-1} during the deinsertion with a quite high coulombic efficiency (88%). On the other hand, rate capability tests

in LP30 + 2% VC (Figure 4.29b) showed a first cycle with a specific capacity of 1062 mAh g⁻¹ during the insertion and the SEI formation, and of 384 mAh g⁻¹ during the deinsertion with a low coulombic efficiency (36%). Until the 5th-6th cycle, the electrode capacity critically drops around 400 mAh g⁻¹. Then the specific capacity slowly decreases; evidence of this, the second series of C/5 cycles results more stable than the first C/5 cycles with a specific capacity comparable to the last cycle of the previous C/5 series. The high irreversible capacity of the first cycles is attributed to both the SEI formation and the partial deactivation of the material due to the formation of lithium oxide (as shown in Equation (15)). SEI formation follows the mechanism already described in Scheme 4.2.

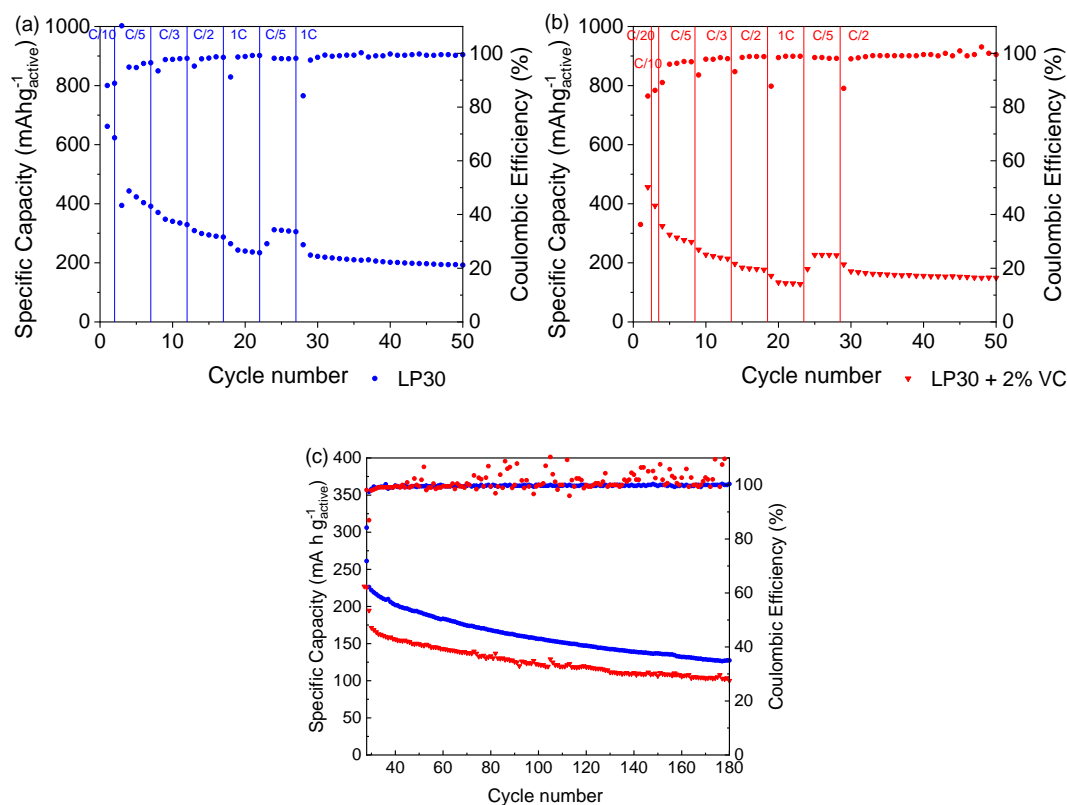


Figure 4.29. Rate capability of #3 in (a) LP30 and (b) LP30 + 2% VC. (c) Specific capacity and coulombic efficiency stability of C-W in LP30 and LP30 +2% VC.

Limiting the specific current to 100 mA g⁻¹, the GDC cycles demonstrated that the manganese oxides' cycling stability improves with a mild cycling protocol and that the inorganic phase is electrochemically active (Figure 4.30). The specific capacity is higher if compared to the results reported in Figure 4.28a at a similar current. This is because the electrode has not performed the initial cycles at very low current rates as

in the rate capability test of Figure 4.28a, where the material stability could have been affected by unwanted and/or irreversible processes, as the low coulombic efficiencies of these cycles testify (Figure 4.29).

The discharge voltage plateau is around 0.5 V, and a not well-defined charge voltage plateau appears around 1.0 V, corresponding to the formation and decomposition of Li_2O and metal nanocrystals with a coulombic efficiency of around 92%. Hence, the repeated volume expansion and contraction of the active particle during cycling affects cycling stability. However, these results indicate that the graphite phase displays a high specific capacity and that the inorganic phase is electrochemically active, even if the stability must be optimized.

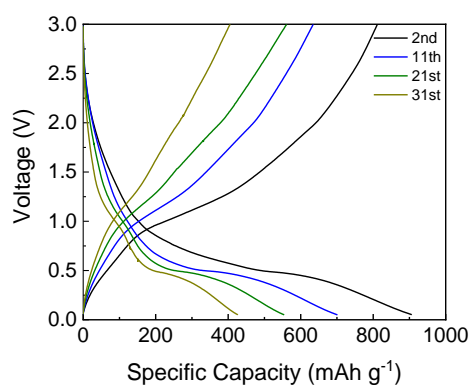


Figure 4.30. GDC profiles of #3 in LP30 at 100 mA g^{-1} .

This indicates that the graphitic carbon obtained from MSCC-ET is electrochemically active and the control on the MnO_x content needs to be investigated deeper to exploit the properties of both active materials. Stabilization of MnO_x , reduction of material with H_2 treatment and creation of oxygen vacancies on MnO_2 particles or reducing the amount of MnO_2 with additional acid treatment could be suitable options.

4.6. Application and specifications

As it is well known, lithium-ion batteries represent one of the most used technologies for consumer electronics. They can reach efficiencies over 95% [40] without giving up to the energy density ($90\text{--}190 \text{ Whkg}^{-1}$) [41], and lifetime (up to 10000 cycles) [24], [25]. However, these systems' electrochemical performances and properties strongly depend on the electrodes' chemical composition.

Li-ion battery chemistries can be compared along six dimensions as specific power (mass power density [W kg^{-1}]), specific energy (mass energy density [Wh kg^{-1}]), performance, lifetime, cost and safety [148].

Every chemistry has its properties and can be adopted for a specific target application. For example, the LFP-based systems are characterized by a long lifetime and safety despite a reduced energy density, while the NMC chemistry has a reduced cycle life offering a high energy density. Moreover, this specification can be combined with the different requirements of the system in which batteries have to be used.

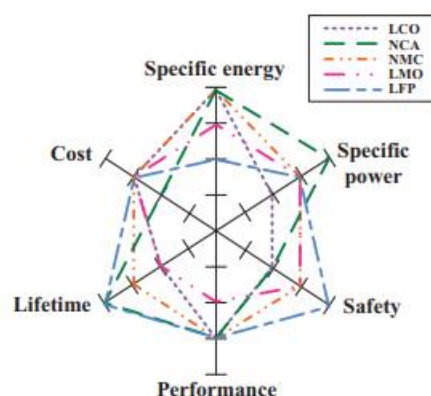


Figure 4.31. Comparison of different electrode active materials for LiBs, modified from [148].

Material	Specific Capacity mAh g^{-1}	Voltage V	Energy density Wh kg^{-1}	Cycle life	Properties
LCO	140	3.7	110-190	500-1000	High safety risk, good lifetime
LMO	146	3.8	100-120	1000	Cheap, safe
NCA	180	3.6	100	2000-3000	High energy, high density, expensive
NMC	145	3.6	100-170	2000-3000	High voltage, good capacity, high safety risk, good lifetime
LFP	170	3.3	90-115	>3000	Long lifetime, cheap, high stability
LTO	170	2.2	60-75	>5000	Negligible expansion, low-cost, stable thermally and electrochemically

Table 4.13. Specification and properties of different electrode materials for LiBs. Energy density obtained with graphite negative electrode.

Table 4.13 indicates the suitability of different Li-ion battery chemistries for stationary, automotive and back-up applications. As an example, for grid frequency regulation, the battery must contribute to frequency regulation in the grid by discharging or stabilizing frequency fluctuations. This means that high power is needed while the energy density can be decent. On the other hand, for application in back-up systems such as UPS, the self-discharge rate should be as low as possible, considering that the batteries are infrequently used.

As can be seen, none of the present Li-ion battery chemistries can be used in all the services (Table 4.14). Consequently, choosing the appropriate Li-ion battery chemistry based on the targeted applications is fundamental.

Application		LiBs chemistries						
		LCO	LMO	LNO	NCA	NMC	LFP	LTO
Stationary	Grid frequency regulation			Yes		Yes	Yes	Yes
	Forecast accuracy improvement				Yes	Yes	Yes	
	Power gradient reduction	Yes	Yes	Yes	Yes	Yes	Yes	Yes
Automotive	EV	Yes	Yes		Yes	Yes	Yes	
	HEV	Yes	Yes		Yes	Yes	Yes	Yes
	PHEV		Yes		Yes	Yes	Yes	
Back-up	UPS			Yes	Yes	Yes		

Table 4.14. LiBs chemistry applicability in stationary, automotive and back-up applications [10].

5. Lithium metal batteries

As discussed in Chapter 4, one of the possible strategies is employing lithium metal anodes to overcome the actual limits of LiB. This Chapter investigates the suitability of lithium metal as the anode in lithium batteries. The reactivity of the lithium metal and the importance of the morphology of the electrodeposited lithium will be introduced and explored in the following sections. The experimental work presented in section 5.5. is focused on the stabilization and characterization of the lithium-electrolyte interphase that will be presented as fundamental for the suitability of this technology [III].

Lithium metal is the lightest metal in the periodic table. This guarantees the high specific capacity of 3860 mAh g^{-1} and the most negative redox potential (-3.04 V vs standard hydrogen electrode) [149]. With lithium metal negative electrodes, the electrochemical process involves the metal deposition/stripping on the electrode surface. Depending on the positive electrode, the energy density of lithium metal batteries with Li metal anode can reach 5210 Wh kg^{-1} (for Li-air batteries) and 2600 Wh kg^{-1} (for Li-sulphur batteries). However, the uncontrolled deposition of lithium leads to safety issues caused by the formation of Li dendrites. In addition, as for graphite electrodes, the negative potential leads to electrolyte decomposition forming the SEI. An unstable solid electrolyte interface (SEI) lowers the $\text{CE}_{\%}$ hindering this electrodes's practical application.

5.1. Solid Electrolyte Interphase

In section 4.3 was described the importance of the electrolyte in the formation of the electrode-electrolyte interphase. The composition of the SEI (and CEI) strongly depends on the electrolyte composition from which it is originated. Typically, salts enrich the SEI with insoluble inorganic compounds like LiF, LiCl and Li_2O . Meanwhile, solvent reductions/oxidation produce soluble and insoluble components like semicarbonates, oligomers, and Li_2CO_3 .

Ideally, the SEI (and CEI) should exhibit the following properties:

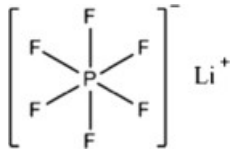
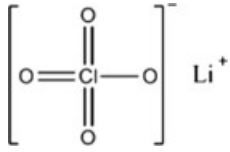
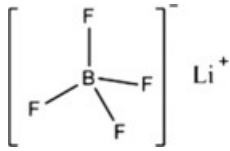
- High electrical resistance to prevent further reaction of the electrolyte.
- High cation selectivity and permeability to allow the lithium-ion transport.

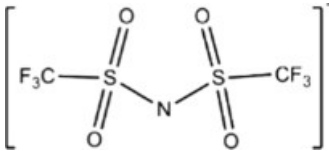
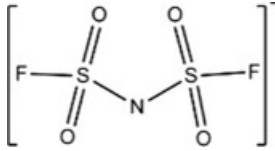
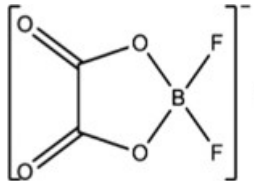
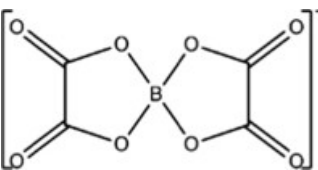
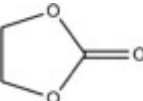
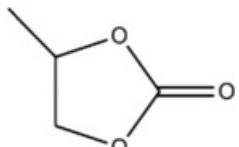
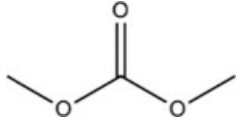
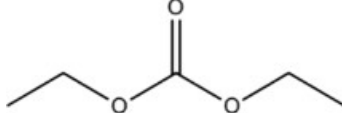
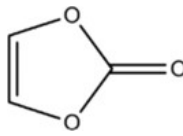
- Thickness close to a few nanometres to not increase the cell resistance.
- High strength, the SEI (and CEI) must withstand to expansion and contraction of the sub-surfaces during cycling.
- Insolubility in the electrolyte.
- Stability over a wide range of operating temperatures and potentials.

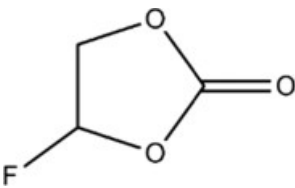
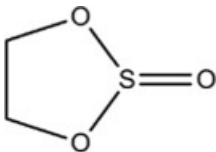
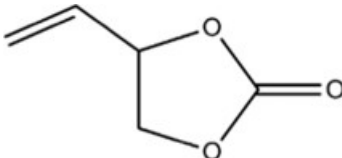
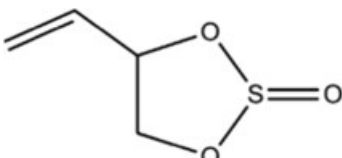
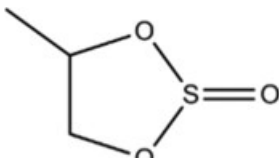
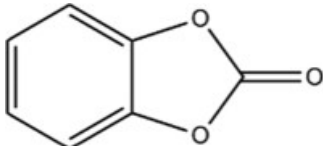
If SEI does not yet show enough stability, it grows uncontrollably over repeated cycling. This event negatively affects the cell life by consuming the electrolyte and increasing the cell resistance [150]. For this reason, it is essential to consciously select and choose the electrolyte components. Accordingly, the SEI formation and composition can be controlled by understanding electrolyte reduction mechanisms and looking at the different reduction potentials of the component used.

Given that the topic of the chapter is lithium metal batteries, in the following only the SEI will be discussed in detail.

The most used salts, solvents and additives have been investigated by computational methods in order to achieve a common goal of tailoring and designing the SEI. Table 5.1 summarizes the most commonly used components and their reduction voltages.

Name	Structure	Reduction Voltage (V)
Salts LiPF ₆		2.1 (complex reduction) (Cal) 1.61 (dimer reduction with LiF formed) (Cal)
LiClO ₄		LiClO ₄ > LiTFSI > LiBF ₄ > LiPF ₆
LiBF ₄		0.2–0.3 (complex reduction) (Cal); 0.0 (dimer reduction) (Cal)

Lithium bis(trifluoromethanesulfonyl)imide, LiTFSI		1.4 (direct reduction) (Cal); 2.1–2.9 (LiF formed) (Cal)
Lithium di(fluorosulfonyl)imide, LiFSI		1.6–2.3 (Exp)
Lithium difluoro(oxalate)borate, LiDFOB		LiBOB > LiDFOB > FEC > PC 1.57 (Cal) 2.12 (Dimer) (Cal)
Lithium bis(oxalate)borate, LiBOB		1.5 ~ 1.8 (Exp)
High dielectric solvents	Ethylene carbonate, EC 	0.8-1.36 (Exp)
	Propylene carbonate, PC 	1.0–1.6 (Exp)
Low dielectric solvents	Dimethyl carbonate, DMC 	1.32 (Exp)
	Diethyl carbonate, DEC 	1.32 (Exp)
Other components	Vinylene carbonate, VC 	1.40 (Exp) first-electron reduction: EC > PC > VC > DMC > E

		MC > DEC (Cal) second-electron reduction: VC > EC > PC (Cal)
Fluoroethylene carbonate, FEC		0.7 (Exp) >PC 0.9 (without F transfer) (Cal) 2.25 (with F transfer by forming LiF) (Cal)
Ethylene sulfite, ES		1.8 ~ 2.0 (Exp) 1.9 (Cal)
Vinyl ethylene carbonate, VEC		2.2 (Exp)
Vinyl ethylene sulfite, VES		ES > VES > VEC > VC > PC (Exp & Cal)
Butylene sulfite, BS		BS > PC > EC (Exp & Cal)
1,3-benzodioxol-2-one, BO		> PC
Sulfuric esters, SE		2.13 (Exp) SE > EC > EMC (Cal)

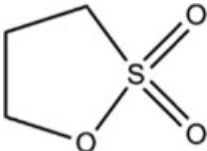
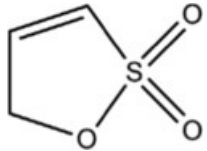
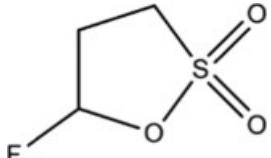
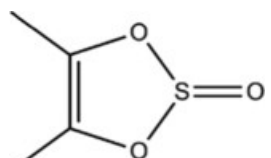
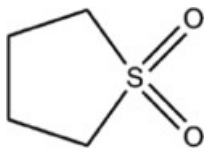
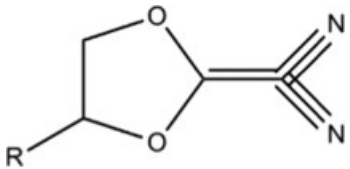
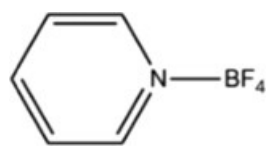
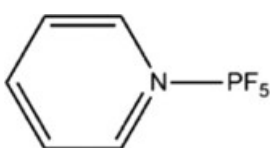
1,3-propane sultone, PS		0.46 0.71 (Exp) > PC	(Cal)
Prop-1-ene-1,3- sultone, PES		0.9 V (Cal)	
3-fluoro-1,3- propane sultone, FPS		1.02 FPS > VC > PS > EC (Cal)	(Exp)
4,5-Dimethyl- [1,3]dioxol-2-one, DMDO		1.35 (Exp)	
Sulfolane, SL		> EC > EMC	
Dicyanoketene ethylene, DCKEA and Dicyanoketene propylene acetals, DCKPA	 (R=H, CH ₃)	~ 1.46 (Exp)	
Pyridine boron trifluoride, PBF		1.2-1.3 1.27-1.3 (Cal)	(Exp)
Pyridine phosphorus pentafluoride, PPF		1.4 1.41 (Cal)	(Exp)

Table 5.1. Summary of the reduction voltages of electrolyte species [52, 151].

As it is clear from the reduction voltage in Table 5.1, lithium metal reacts spontaneously with most of the electrolytic components. Typical organic solvents for lithium metal batteries are alkyl carbonates and ethers.

5.2. *Lithium metal batteries and the dendritic growth*

Without control, the SEI formation inevitably produces morphological and compositional inhomogeneity. Thus, lithium-ion diffusion and deposition follow preferential pathways. Repeated cycling exaggerates this phenomenon causing lithium deposition in the form of filaments and dendrites. Once formed, dendrites become preferential sites for further lithium deposition due to inhomogeneities of the electric field.

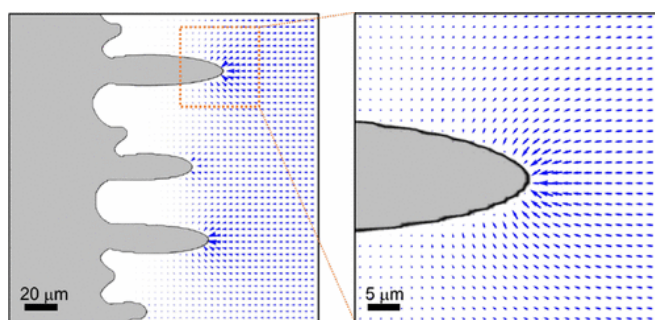


Figure 5.1. Inhomogeneity of the electric fields in presence of metal asperities [152].

When the current density is above a critical value, called critical current density, it can only be sustained until metal ions are close to the surface. Above the critical current density, the cations depletion leads to the formation of local space charge generating non-planar metal deposition [153]. The presence of inhomogeneous the SEI layer enhances this phenomenon. The microstructural morphology of the electrode surface can alter the electric fields. Indeed, asperities of the electrode possess a higher electric field and attract more ions influencing their migration [154]. For lithium metal deposition, this phenomenon arises at current densities higher than $\sim 0.1 \text{ mA cm}^{-2}$ favouring a non-uniform deposit morphology.

On the other hand, high deposition rates ($\sim 1 \text{ mA cm}^{-2}$) favour the growth of dendritic morphologies. This phenomenon also strongly depends on the temporal extension of the deposition. Thus, the appearance of dendrites nucleation spots also depends on the

charge density (mAh cm^{-2}). Increasing this last parameter, keeping constant the current density, can lead to the system becoming diffusion-limited, inducing large cation depletion [156]. Once they have been formed, lithium stripping is favoured at sites with lower impedance than the freshly deposited metal during the stripping processes. This mechanism is further assisted by lithium electrode volume expansion upon cycling, causing the cracks into the SEI layer from which lithium dendrites are freely to grow.

In this scenario, dendrites can be eroded, generating electrically isolated lithium called “dead lithium” [157]. Sequent cycling leads to several problems for the cell:

- Excessive dead lithium, resulting in reduced ion transport and capacity fading.
- Progressive fracturing of the SEI layer and its re-formation consuming electrolyte.
- Growing dendrites until they pierce the separator and eventually reach the cathode, shorting the cell.

The dynamics of lithium metal dendrites formation are schematized in Figure 5.2.

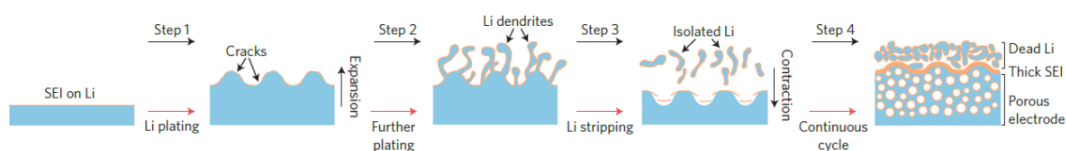


Figure 5.2. Schematic representation of the dynamics of the dendrite growth evolution on lithium metal anodes [156].

Thus, a homogeneous SEI layer on the lithium metal surface is one of the solutions to stabilize these typical problems of lithium metal batteries [156].

5.3. Strategy to inhibit dendrites formation

To counter dendrite problems, there are mainly three approaches:

- Physical barrier: the formed dendrites are confined, preventing the short-circuit with a physical barrier. The use of separators with high elastic modulus is

functional to deviate the lithium dendrite, resulting in the dendrite being unable to perforate the separator, causing a short-circuit.

- “Active” barrier: the dendrite growth direction is controlled with a porous separator having a 3D structure that can control the lithium flux producing a uniform electric field or with additional layers that can be functionalized to provide controlled nucleation sites. As an example of the latter, separators can be decorated with functionalized nanocarbon (FNC) containing Li ions. In these layers, during cycling, the Li dendrites grow toward each other simultaneously [158]. The functionalization with TiO_2 , SiO_2 and Si are also “active” in consuming dendrites via lithiation reaction [159].
- Tailored or artificial SEI layer: additives or co-solvents in the commonly used electrolytes can modify the SEI composition or the growth of an artificial tuneable inorganic protective layer.

The last one is the approach followed in this thesis. In these years, the electrolyte composition has been varied to enrich the SEI layer of both inorganic compounds, namely LiF, Li_2CO_3 , Li_xNO_y or Li_3N , and organic species. Generally, fluorine-containing additives have exceptional reactivity, resulting in a stable SEI due to their bipolar nature [160].

Fluoropyridines (FP) are additives for carbonate and ether-based electrolytes. In these molecules, the C-F bonds break, releasing fluoride and enriching the SEI layer of LiF [161,162]. Hence, FP can regulate the initial Li nucleation process and induce a protective layer leading to dendrite-free, uniform Li deposition.

The presence of lithium fluoro(oxalato)borates additives can modify the electrode’s surface layer composition. These additives produce a LiF-free surface film on the Li-rich cathode, while on the anode, they produce a LiF-rich surface film. The uniform presence of LiF in the SEI composition can decrease the diffusion barrier of Li^+ , limiting the formation of dendrites [163].

In addition, hexafluoroisopropyl trifluoromethanesulfonate (HFPTf), heptafluorobutyric anhydride (HFA) and, bisfluoroacetamide (BFA) [164,165] can be used to form a uniform LiF-rich SEI. Also, in these cases, the presence of LiF increases the lithophilicity of the surface. The homogenous lithium deposition is mainly reached thanks to the rapid and uniform Li^+ diffusion.

Alternatively, phosphorus pentasulfide (P_2S_5) forms a lightweight and conductive coating on the Li metal anode, suppressing the shuttling of polysulfides and Li dendrite growth during cell activity [166].

The additive's molecular structure must also be tailored to reach the desired properties. As an example, in phenyl sulfones (PS), the aromatic ring of the compound helps in maintaining the stability of SEI and the sulphur moiety ensures high ionic conductivity [167]. On the other hand, the structure of Vinyl Ethylene Carbonate (VEC) can solvate Li^+ ions able to permeate through the SEI. The permeability can be controlled using donor number of solvents. In this system, the reduction potential of VEC can be reduced by introducing a cyano-substituent [168].

Artificial SEIs must be highly electronic insulators, highly lithium-ion conductors, chemically and mechanically stable, and sufficiently thick without dead zones [169,170].

For this purpose, nitrogen-based artificial SEIs, including lithium phosphorous oxynitride (LiPON) [171] and Li_3N [172] are promising candidates that fulfil the requirements. Also, nitrogen-defective graphite-like carbon nitrides have been studied as coatings to attain homogeneous deposition of lithium metal and block the formation of lithium dendrites [173].

As an example, Li_3N possesses high ionic conductivity ($\sim 10^{-3} S cm^{-1}$), low electronic conductivity (less than $10^{-12} S cm^{-1}$) [174], and thermodynamic stability versus lithium metal [175,176]. It can be obtained through direct exposure of the Li surface to N_2 gas [175].

5.4. *Processes studied with operando techniques*

Due to the complex reaction chemistry and their instability in the atmosphere, the characterization of metal anodes is quite challenging. So far, conventional electrochemical measurements, such as cyclic voltammetry (CV), galvanostatic charge-discharge (CD) cycles at different currents, and electrochemical impedance spectroscopy (EIS), are helpful methods for estimating the electrochemical properties of negative metal electrodes. These measurements are indispensable to evaluating capacity, voltage, rate capability, coulombic efficiency, impedance, and lifetime. These techniques do not provide sufficient information regarding the mechanisms.

These techniques can be coupled with easy-to-access ex situ characterization techniques, such as X-ray diffraction (XRD), scanning electron microscopy (SEM), transmission electron microscopy (TEM), X-ray photoelectron spectroscopy (XPS), Raman spectroscopy, FT-IR spectroscopy. However, these techniques require cell disassembly after cycling and the inspection of the cell components. This operation and the sequent investigation must be performed in a controlled atmosphere to not modify the metal surface composition. Nevertheless, even with this caution, any action may impact the battery's performance or influence the results.

To overcome the limit of ex situ characterization, it is possible to investigate the materials without disassembling the cell but stopping its operation. The in situ approach does not disturb the cell components, but unstable intermediate products are hard to detect. In addition, physical or chemical processes are not observed during their happening but are hypothesized, looking at their consequences.

Operando measurements represent the answer to the limits of in situ measurements. In operando measurements, the status of the materials can be monitored while the cell is being cycled. These correlative studies continuously probe a region in space, gaining real-time insight into physical or chemical processes. In addition, as with the in situ investigation, the analytical measurements are undisturbed, but unlike them, the electrochemical measurements proceed.

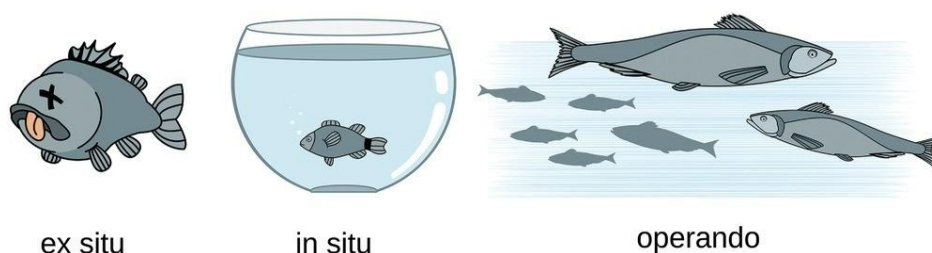


Figure 5.3. Representation of the differences between ex situ, in situ and operando observation.

Considering the complexity of the solid–dissolution–redeposition reaction mechanism, operando characterization techniques are ideal for exploring the real-time electrochemical reactions during cycling [177, 179]. Techniques commonly used operando are Raman spectroscopy, UV-vis spectroscopy, X-ray absorption spectroscopy, electron paramagnetic resonance spectroscopy, X-ray tomographic microscopy, SEM and TEM.

When designing operando experiments, the choice of analytical techniques must consider spatial and temporal resolutions. Some experiments require an entire field of view others requires techniques to probe reactions or species that are specific to certain regions in the cell. In electrochemical systems, the temporal domain is determined by the rate of the electrochemical process. Fast charge/discharge cycles require fast measurements in order to have very little change to the cells taking place during each measurement.

In this chapter, confocal Raman spectroscopy is used to get information from a confined area, which helps to probe reactions at the lithium metal electrode interface.

These concepts will be resumed in Section 7.5 in which investigation of species concentration in an electrolyte as a function of state of charge will be considered.

5.5. Operando Raman spectroscopy of lithium metal symmetric cell

As reported in Section 5.2, the central issue for Li-metal anode is represented by the tendency to be deposited in a dendritic and mossy form [180,181]. For this purpose, several studies have focused on understanding dendrites' dynamics and the strategies aiming to suppress their formation. In particular, fundamental studies employed microscopies and optical techniques [182]. As an example, SEM studies have shown the correlation between the nuclei density and the overpotential [183]. Typically, in situ TEM and SEM [184] experiments are limited to not very volatile electrolytes with low viscosity. Nevertheless, they allow reaching nanoscale imaging [184] with detailed local characterizations of the interphase. However, it is important to consider the potential influence of the electron beam on the electrochemical reactions. Alternatively, operando ^7Li NMR spectroscopy was reported as a promising technique to monitor and recognize different lithium- containing compounds in SEI. [185]. Synchrotron X-ray tomography microscopy has been used to observe the early stage of dendritic lithium formation [186]. Confocal Raman spectroscopy represents a promising technique for performing operando measurements on batteries. Especially thanks to its non-destructive nature, data acquisition is possible over numerous cycles with a high acquisition speed (< 60 s). The spatial resolution depends on the laser spot size. The latter can be regulated and reduced up to $f = 2.4 \mu\text{m}$,

As reported in Section 5.2, Li metal stabilization is essential for practical application. However, complicated and high-cost strategies for Li metal protection are not recommended. Ideally, low-cost, one-step in situ methods to improve the SEI are desirable. Furthermore, controls over the film thickness by simply changing few parameters should be favourable.

In this section, operando confocal Raman spectroscopy has been used to study lithium metal –electrolyte interphase in a carbonate-based electrolyte in the presence of an additive, NH_4PF_6 . Ammonium cation has been used aiming to perform an in situ modification of the SEI layer (results from ref. [III]).

The electrochemical behaviour of Li symmetric cells in the selected electrolyte has been explored through galvanostatic charge/discharge cycles and EIS, to evaluate the effect of additives on the electrochemical performance.

- Materials and methods

The materials used for the preparation of electrodes and electrolytes have been the following: lithium metal ribbon (Sigma Aldrich, 0.75 mm thick, 99,9%), ethylene carbonate (EC, Sigma Aldrich, >99%), dimethyl carbonate (DMC, Sigma Aldrich, >99), lithium bis(trifluoromethanesulfonyl)imide (LiTFSI, Sigma Aldrich, 99,5%), ammonium hexafluorophosphate (NH_4PF_6 , Fluorochem Co., >99%).

The electrolyte solutions to study the effect of the NH_4PF_6 as an additive for the formation of stable SEI have been prepared starting from the electrolyte, 1 M LiTFSI in EC:DMC 1:1 wt/wt, without any additive. The concentrations of the ammonium salt additives are 50, 100 and 250 mM, which are about 1, 2, and 2.5% wt/wt, respectively. The pure electrolyte 1 M LiTFSI EC:DMC, has been chosen because of its low viscosity (2.88 mPa s^{-1}) with respect to commonly used 1M LiPF_6 EC:DMC (4.15 mPa s^{-1}) [187].

Electrochemical Swagelok cells with two electrodes have been assembled in a glovebox (Mbraun Labmaster SP) in inert argon atmosphere ($\text{O}_2 < 0.1 \text{ ppm}$ and $\text{H}_2\text{O} < 0.1 \text{ ppm}$) using stainless steel cells (Swagelok, Swagelok Company) with glass microfiber separators (Whatman, GF/A), which were pre-dried and deaerated in an oven (B-585 Kugelrohr, BÜCHI) at $120 \text{ }^\circ\text{C}$ under vacuum for 12 h.

The electrochemical tests have been performed with a BioLogic VSP potentiostat/galvanostat. Potentiostatic electrochemical impedance spectroscopy

(PEIS) experiments have been acquired in frequency range 100 kHz – 100 mHz, with a perturbation of amplitude 10 mV around OCV, recording 20 points per decade. The PEIS have been fit using equivalent circuits composed of resistors (R) and constant phase elements (Q). Instead of an ideal capacitor, the Q is used to account for nonideal capacitive behaviours originating from the rough and imperfect surface. The impedance of the constant phase element is $Z_{CPE} = 1/[Q(i\omega)^a]$ with Q expressed in $F \cdot s^{-(1-a)}$ (or $\Omega^{-1} s^a$) and angular velocity $\omega = 2\pi\nu$. From the fitting results, the capacitance can be obtained as $C = (Q R^{1-a})^{1/a}$ [188]. Each process has its characteristic time constant $\tau = RC$ and, it appears in the impedance spectrum at a relative frequency of $\nu = 1/(2\pi\tau)$.

Operando measurements were performed using a different two-electrode cell (EL-cell), shown in Figure 5.3. Lithium foil was cut into a 9 mm disk for the counter electrode placed at the bottom of the cell. A 10 mm lithium ring with a 2 mm hole in the center was used as a working electrode, and a 20 mm Cu ring with a 3 mm hole current collector was used. The assembled cells were connected to a galvanostat/potentiostat Biologic SP-300.

Raman measurements were made using a LabRAM Confocal Raman Spectrometer with a Peltier cooled CCD, a x50 objective, 300 and 600 grooves/mm grating, and red incident laser 1054 nm (power 50 mW 10% filtered). Before analysis, the spectra were baseline corrected. The laser spot was focused in two positions: between the Whatman separator and the working lithium metal and 50 μm away from the lithium interphase. Stripping deposition measurements were made using a Li/Li symmetric cell with the pure electrolyte or the electrolyte containing the additive by filling the internal volume of the cell with a syringe. Deposition/stripping cycles were carried out applied a current density of 0.5 mA cm^{-2} or 1 mA cm^{-2} with a charge of 0.5 or 1 mAh cm^{-2} , respectively.

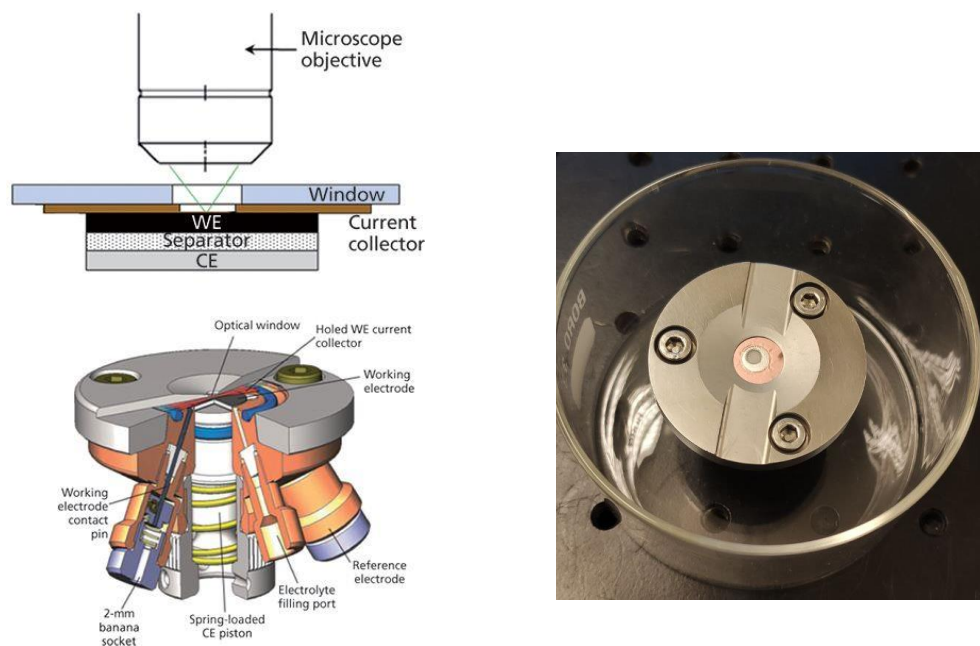
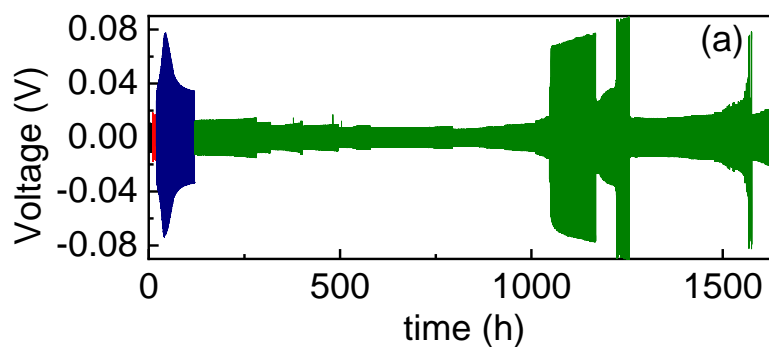


Figure 5.3. (a) Commercial operando Raman cell set-up, CE: 10 mm lithium disk on stainless steel current collector, separator: glass fiber, WE: lithium ring on copper ring current collector. (b) Top view of an assembled Raman cell, view on copper current collector, lithium ring and separator.

- Results and discussions

As a protic salt, the action exerted by NH_4PF_6 relies on direct reaction with lithium with substantial variation in the chemical composition of the interphase.

Deposition/stripping cycles and PEIS experiments have investigated the electrolyte's behaviour. The polarization obtained is reported in Figure 5.4. The presence of ammonium salt induces a comparable but more stable overvoltage for the electrolyte without the additive.



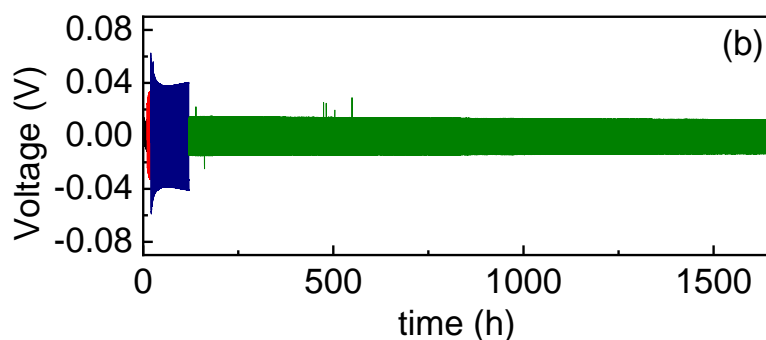


Figure 5.4. Li//Li symmetric cell voltage profile in (a) 1M LiTFSI EC: DMC and (b) 1M LiTFSI in EC:DMC + 50 mM NH_4PF_6 in EC: DMC. ■ 0.125 mA cm^{-2} , ■ 0.250 mA cm^{-2} , ■ 0.500 mA cm^{-2} , ■ 0.125 mA cm^{-2} .

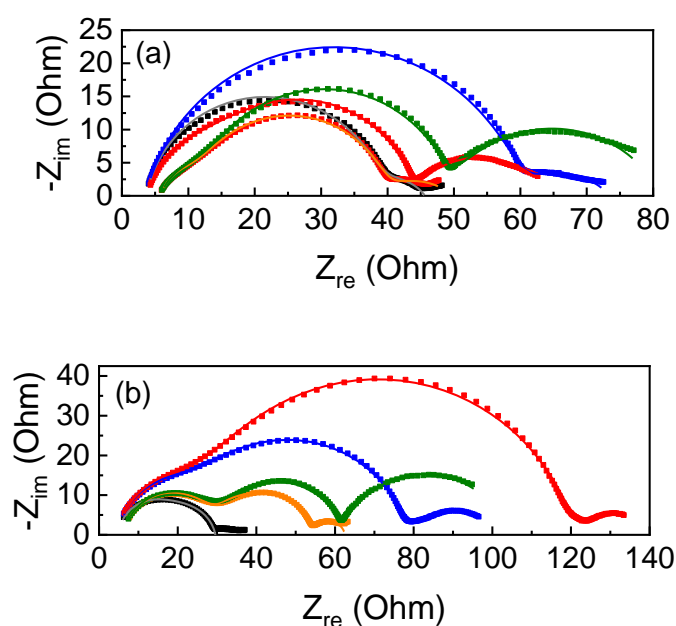


Figure 5.5. Li//Li symmetric cell EIS in (a) 1M LiTFSI EC: DMC and (b) 1M LiTFSI in EC:DMC + 50 mM NH_4PF_6 in EC: DMC after a different number of cycles: ■ 0 cycle, ■ 10 cycles, ■ 20 cycles, ■ 120 cycles, ■ 130 cycles.

The PEIS's fitting results are reported in Table 5.2 and Table 5.3. The PEIS (Figure 5.5) were fitted with an $R_1(R_2/Q_2)(R_3/Q_3)(R_4/Q_4)$ equivalent circuit (EqC). R_1 corresponds to the ohmic resistance of the electrolyte, R_2 and Q_2 are related to the bulk SEI impedance, while R_3/Q_3 can be ascribed to the grain boundaries inside the SEI and between lithium and SEI layer. R_4/Q_4 are related to the charge transfer process between the liquid electrolyte and lithium electrode across the SEI [188]. In the absence of the

additive, the processes related to the SEI are not well visible, and contributions given by the bulk and grain boundaries of the SEI are indistinct.

EqC	0 cycle	10 th cycle	20 th cycle	120 th cycle	130 th cycle
R ₁ / Ω	3.66 ± 0.08	3.53 ± 0.07	4.28 ± 0.07	5.94 ± 0.07	5.91 ± 0.07
R ₂ / Ω	35 ± 1	56 ± 1	8 ± 2	5.2 ± 0.4	6.9 ± 0.5
Q ₂ / F · s ^{a-1}	(2.8 ± 0.3) · 10 ⁻⁶	(4.0 ± 0.3) · 10 ⁻⁶	(1.3 ± 0.4) · 10 ⁻⁶	(7 ± 2) · 10 ⁻⁶	(1.3 ± 0.4) · 10 ⁻⁵
a ₂	0.89 ± 0.01	0.854 ± 0.007	1.00 ± 0.04	0.90 ± 0.3	0.84 ± 0.03
C ₂ / F	(9 ± 2) · 10 ⁻⁷	(1.0 ± 0.1) · 10 ⁻⁶	(1.3 ± 0.7) · 10 ⁻⁶	(2 ± 1) · 10 ⁻⁶	(2 ± 1) · 10 ⁻⁶
v ₂ / s ⁻¹	(5 ± 1) · 10 ³	(2.9 ± 0.3) · 10 ³	(1.6 ± 0.9) · 10 ⁴	(1.4 ± 0.7) · 10 ⁴	(1.1 ± 0.5) · 10 ⁴
R ₃ / Ω			32 ± 2	27.8 ± 0.9	35.9 ± 0.7
Q ₃ / F · s ^{a-1}			(6.7 ± 0.8) · 10 ⁻⁶	(2.4 ± 0.2) · 10 ⁻⁵	(2.0 ± 0.1) · 10 ⁻⁵
a ₃			0.90 ± 0.02	0.88 ± 0.02	0.90 ± 0.01
C ₃ / F			(2.5 ± 0.7) · 10 ⁻⁶	(8 ± 2) · 10 ⁻⁶	(9 ± 1) · 10 ⁻⁶
v ₃ / s ⁻¹			(2.0 ± 0.6) · 10 ³	700 ± 20	490 ± 60
R ₄ / Ω	7 ± 2	14 ± 2	21 ± 1	10 ± 2	33 ± 1
Q ₄ / F · s ^{a-1}	(3 ± 2) · 10 ⁻³	(1.3 ± 0.3) · 10 ⁻²	(1.4 ± 0.1) · 10 ⁻²	(3.5 ± 0.4) · 10 ⁻²	(1.06 ± 0.04) · 10 ⁻²
a ₄	0.6 ± 0.2	0.53 ± 0.09	0.63 ± 0.03	0.47 ± 0.07	0.70 ± 0.02
C ₄ / F	(4 ± 7) · 10 ⁻⁴	(3 ± 2) · 10 ⁻³	(7 ± 1) · 10 ⁻³	(1.1 ± 0.5) · 10 ⁻²	(6.7 ± 0.5) · 10 ⁻³
v ₄ / s ⁻¹	60 ± 200	4 ± 3	1.1 ± 0.2	1.3 ± 0.6	0.72 ± 0.05

Table 5.2. Results from the fitting of the EIS reported in 1M LiTFSI EC:DMC.

EqC	0 cycle	10 th cycle	20 th cycle	120 th cycle	130 th cycle
R ₁ / Ω	5.0 ± 0.1	5.04 ± 0.06	4.97 ± 0.08	6.3 ± 0.1	6.3 ± 0.1
R ₂ / Ω	12 ± 4	16.8 ± 0.7	18.6 ± 0.6	21.8 ± 0.4	22.9 ± 0.5
Q ₂ / F · s ^{a-1}	(5 ± 2) · 10 ⁻⁷	(5.6 ± 0.6) · 10 ⁻⁷	(6.9 ± 0.8) · 10 ⁻⁷	(1.0 ± 0.1) · 10 ⁻⁶	(1.1 ± 0.1) · 10 ⁻⁶
a ₂	1.00 ± 0.05	0.98 ± 0.01	0.96 ± 0.01	0.916 ± 0.009	0.91 ± 0.01
C ₂ / F	(5 ± 4) · 10 ⁻⁷	(4.4 ± 0.7) · 10 ⁻⁷	(4.2 ± 0.7) · 10 ⁻⁷	(3.7 ± 0.6) · 10 ⁻⁷	(3.7 ± 0.7) · 10 ⁻⁷
v ₂ / s ⁻¹	(3 ± 2) · 10 ⁴	(2.1 ± 0.4) · 10 ⁴	(2.0 ± 0.4) · 10 ⁴	(2.0 ± 0.3) · 10 ⁴	(1.9 ± 0.4) · 10 ⁴
R ₃ / Ω		56 ± 0.9	97 ± 1	26.8 ± 0.6	32.5 ± 0.6
Q ₃ / F · s ^{a-1}		(6.6 ± 0.3) · 10 ⁻⁶	(7.2 ± 0.3) · 10 ⁻⁶	(6.6 ± 0.6) · 10 ⁻⁵	(5.0 ± 0.5) · 10 ⁻⁵
a ₃		0.860 ± 0.008	0.851 ± 0.006	0.81 ± 0.01	0.84 ± 0.01
C ₃ / F		(1.8 ± 0.2) · 10 ⁻⁶	(2.0 ± 0.2) · 10 ⁻⁶	(1.5 ± 0.3) · 10 ⁻⁵	(1.6 ± 0.3) · 10 ⁻⁵
v ₃ / s ⁻¹		(1.6 ± 0.3) · 10 ³	820 ± 70	390 ± 70	320 ± 50
R ₄ / Ω	13 ± 4	25 ± 1	23 ± 4	8 ± 1	42 ± 2
Q ₄ / F · s ^{a-1}	(8 ± 2) · 10 ⁻⁶	(2.2 ± 0.1) · 10 ⁻²	(3.9 ± 0.4) · 10 ⁻²	(2.2 ± 0.4) · 10 ⁻²	(1.40 ± 0.04) · 10 ⁻²
a ₄	0.88 ± 0.06	0.57 ± 0.03	0.55 ± 0.07	0.89 ± 0.08	0.80 ± 0.02
C ₄ / F	(2 ± 2) · 10 ⁻⁶	(1.5 ± 0.2) · 10 ⁻²	(3.5 ± 0.8) · 10 ⁻²	(1.7 ± 0.4) · 10 ⁻²	(1.22 ± 0.05) · 10 ⁻²
v ₄ / s ⁻¹	(5 ± 4) · 10 ³	0.44 ± 0.05	0.20 ± 0.06	1.2 ± 0.3	0.31 ± 0.02

Table 5.3. Results from the fitting of the EIS reported in 1M LiTFSI EC:DMC + 50 mM NH₄PF₆.

Without the additive (Figure 5.5a and Table 5.2), the SEI resistance related to the grain boundaries is characterized by an almost constant value. At the same time, the contribution of the SEI_{bulk} to the total impedance becomes visible after 20 cycles and distinguishable, with the presence of a well-developed semicircle, only after 120 cycles, corresponding to the higher current density applied during the experiment. Both the resistances related to the SEI_{bulk} and SEI_{gb} show a decrease after the 120th cycle with the contemporary increase of the capacitance associated with the grain boundaries. The growth in capacitance of about one order of magnitude causes a shift in the characteristic frequency of the process so that the two semicircles appear distinct. The electrode is subjected to developing a porous morphology by cycling at high current density, which explains the observed changes in capacitance and resistance. The charge transfer resistance follows the same trend, experiencing the effect of the 100 cycles at 0.5 mA cm^{-2} .

At t_0 , the cell with the additive (Figure 5.5b and Table 5.3) exhibits lower impedance. The contribution of the SEI_{bulk} and SEI_{gb} are distinguishable almost from the first spectrum. The time evolution of the associated parameters is characterized by the resistance associated with SEI_{gb} , which keeps growing until the 20th cycle. In contrast, the resistance related to SEI_{bulk} shows a monotonic increase until the last spectrum is recorded. Both these interphases are more resistive than the ones observed in the bare electrolyte. The addition of the ammonium does not dramatically alter the charge transfer resistance, with the exclusion of the resistance at 130 cycles which is substantially higher.

The PEIS data clearly shows that adding ammonium drastically leads to different well-developed interphase from the earliest cycling stage. It is important to understand the composition of the formed interlayer. Insight about the species that participate in the interlayer can be obtained by operando Raman spectroscopy. The laser can be focused close to the lithium-electrolyte interphase in a confocal Raman spectrometer. From previous experiments, the presence of the additive improves the deposition/stripping cycling stability due to the formation of an interlayer.

Electrolyte Raman Spectrum

First, the Raman spectra of the electrolytic solutions must be studied to find the region of interest for the operando measurements. The Raman spectra recorded in the

operando Raman cell of the electrolytic solutions are shown in Figure 4a, and all the signals were assigned. The presence of NH_4PF_6 is not visible at this low additive concentration. The only signal present is the one at 732 cm^{-1} associated with the PF_6^- anion. For the analysis, two bands were identified with information from all the electrolyte components (Figure 5.6).

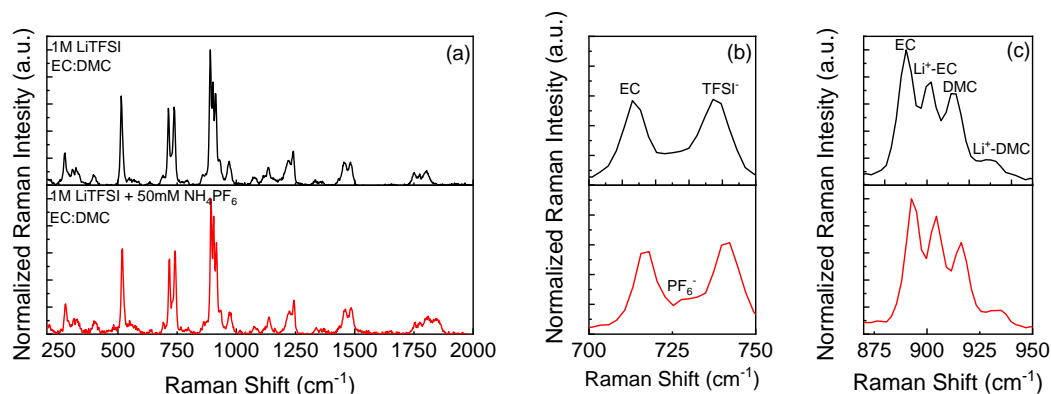


Figure 5.6. (a) Raman spectra of the electrolytes, (b) $700\text{-}750\text{ cm}^{-1}$ bands, (c) $880\text{-}940\text{ cm}^{-1}$ bands.

The operando Raman spectra were integrated and divided into areas of interest. Table 5.4 reports the integrated bands with the corresponding electrolyte components [190,191].

Electrolyte component	Wavenumber (cm^{-1})
EC	705-725
PF_6^-	725-734
LiTFSI	734-750
EC	880-900
$\text{Li}^+\text{-EC}$	900-910
DMC	910-920
$\text{Li}^+\text{-DMC}$	925-945

Table 5.4. List of the selected band in the Raman spectrum

Operando Raman experiment

The assembled cells were cycled at 0.5 mAcm^{-2} with a charge capacity of 0.5 mAh cm^{-2} . In situ optical microscopy images were captured before and after the cycling (Figure 5.7).

During the experiments, different areas of the samples were probed with the laser to find a spot that was close enough to probe the variation in the electrolyte composition and far enough not to focus the laser on the lithium electrode directly. These distance changes between the samples and an acceptable compromise were found by focusing the laser 50 μm far from the interphase. The images before and after cycling show the dendritic formation after ten deposition/stripping cycles with a current density of 0.5 mA cm^{-2} and a charge capacity of 0.5 mAh cm^{-2} .

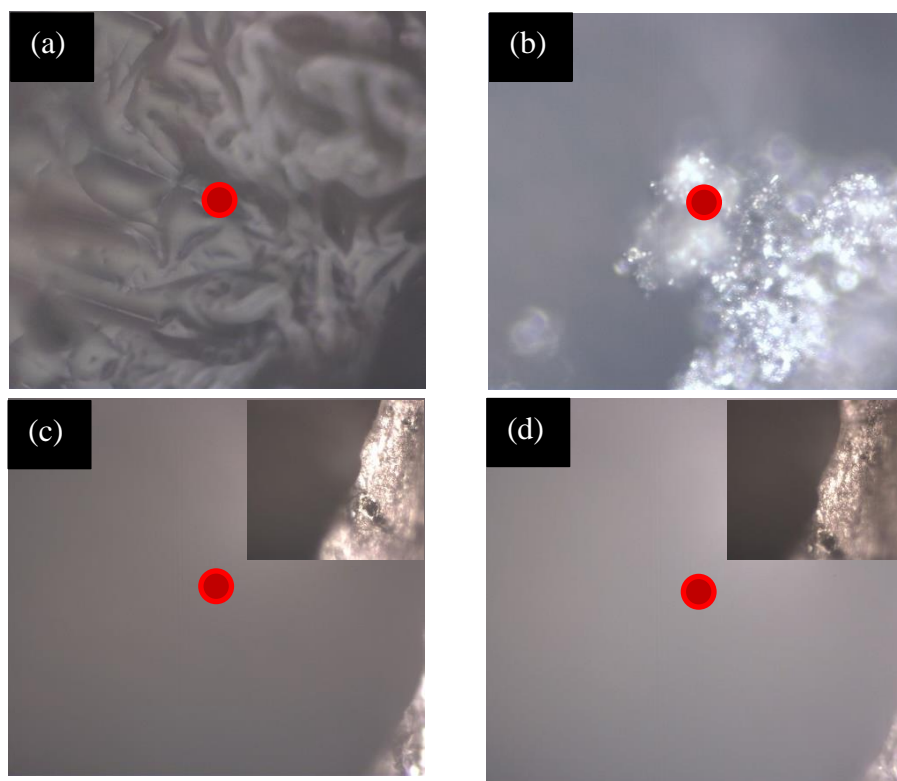


Figure 5.7. In situ optical microscopy images (50x) (a,c) before and (b,d) after cycling at 0.5 mA cm^{-2} in 1M LiTFSI EC:DMC and (c,d) 1M LiTFSI EC:DMC + 50 mM NH_4PF_6 . The red spot indicates the position in which the laser has been focused.

As shown by the in situ microscopy images, in the absence of NH_4PF_6 (Figure 5.7a,b), the lithium growth enters the area hit by the laser showing an unstripped polycrystal structure. This suggests that the density of the freshly deposited metal is lower than the bulk electrode. In the presence of NH_4PF_6 , the lithium dimension are unvaried (Figure 5.7c,d), without any dendrites in the micrometre scale. This suggests a higher efficiency of the lithium deposition/stripping process or a denser morphology of the deposited lithium.

In addition, the two electrolytic systems' voltage profiles (Figure 5.8) differ in shape and overpotentials. The voltage is higher and more stable in the absence of the additive, typical of a Li//Li symmetric cell. Meanwhile, when the additive is present, the voltage profile, initially lower, increases progressively, reaching 0.04 V. After five cycles (10 h), the voltage profile stabilizes around 20mV, suggesting a formation of interphase that increases the cell resistance leading to an increase in the voltage.

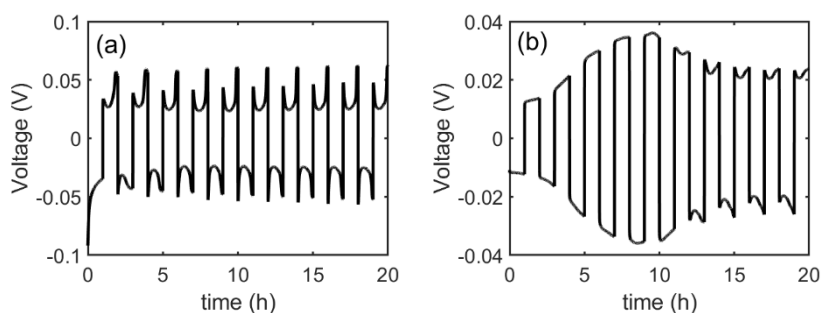


Figure 5.8. Deposition-stripping cycles of symmetric Li//Li cells in (a) 1M LiTFSI EC:DMC and (b) 1M LiTFSI EC:DMC + 50 mM NH_4PF_6 at current density of 0.5 mA cm^{-2} and a charge capacity of 0.5 mAh cm^{-2} .

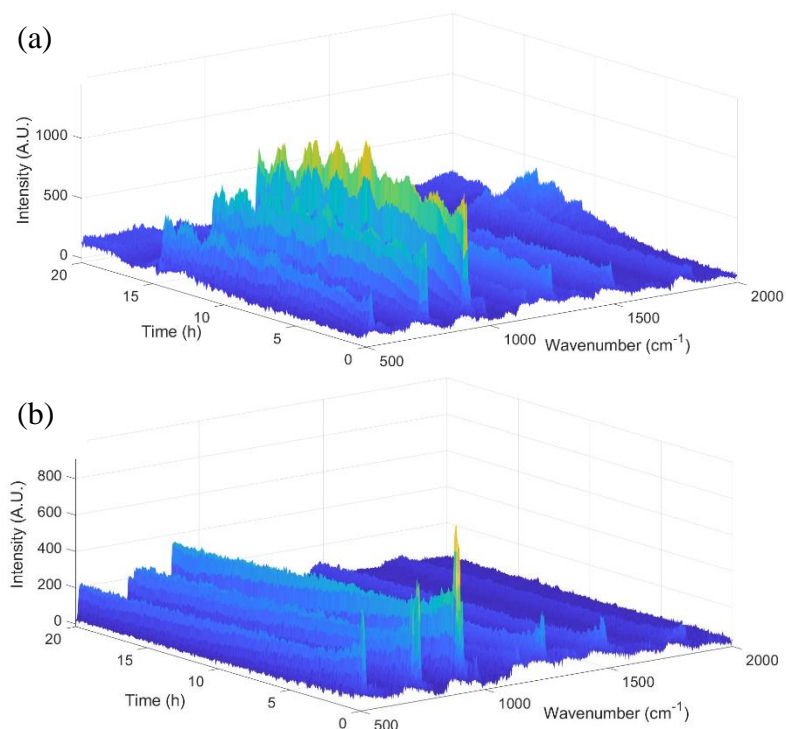


Figure 5.9. Operando Raman spectra recorded during deposition/stripping cycles in (a) 1M LiTFSI EC:DMC and (b) 1M LiTFSI EC:DMC + 50 mM NH_4PF_6 at current density of 0.5 mA cm^{-2} and a charge capacity of 0.5 mAh cm^{-2} , 4 acquisition, 15 s time per scan, every 5 minutes.

During cycling, Raman spectra were recorded every 5 minutes with a sample exposure time to the laser of 60 s (Figure 5.09). In the case of 1M LiTFSI EC:DMC, lithium dendrites enter the zone where the laser is focused, and the signal of the electrolyte are not yet visible. Representative bands of the electrolyte components were integrated, and corresponding values were plotted versus the voltage profile (Figure 5.10). For every band of interest, the variation of the integrated signals can provide evidence of the variation in the concentration of the electrolyte components.

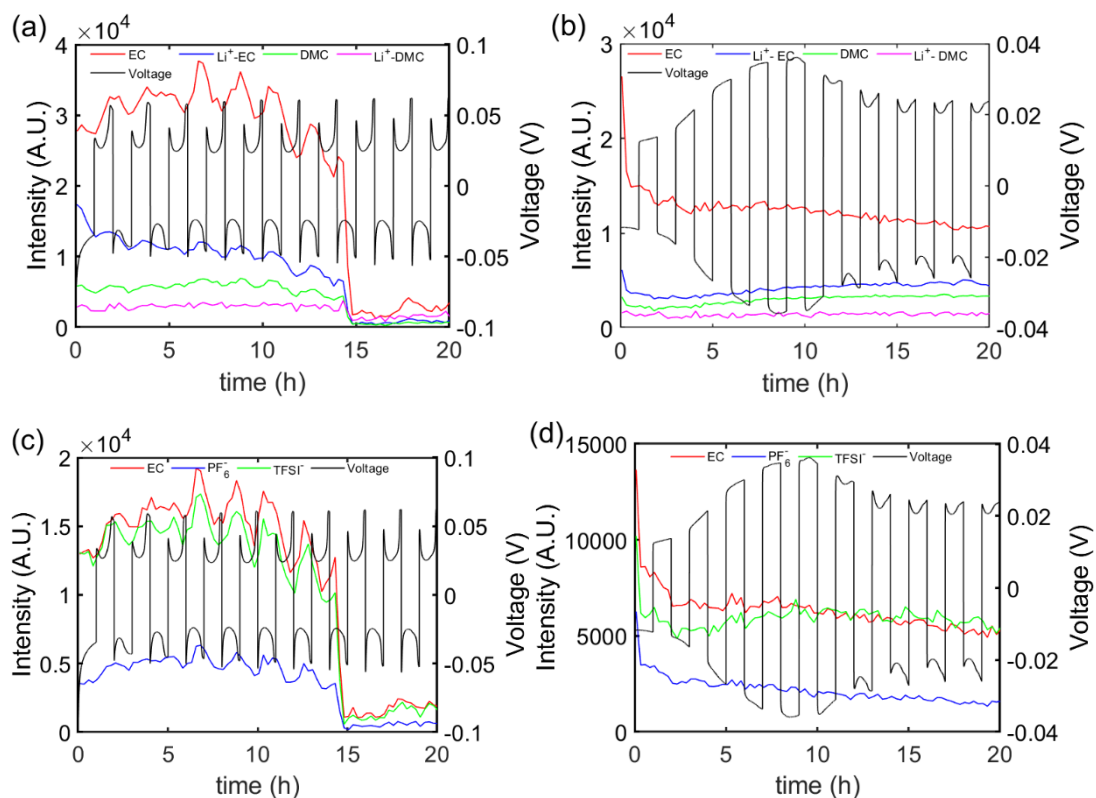


Figure 5.10. Operando Raman signals variation during lithium deposition-stripping in (a,c) 1M LiTFSI EC:DMC, (b,d) 1M LiTFSI EC:DMC + 50 mM NH_4PF_6 in the intervals (a,b) $880\text{-}945\text{ cm}^{-1}$ and (c,d) $705\text{-}725\text{ cm}^{-1}$. The Li//Li cell with glass fiber separator operates at 0.5 mA cm^{-2} .

As shown in Figure 5.10a and 5.10c, in the absence of NH_4PF_6 , the Raman signals fluctuate following the deposition/stripping cycles. The signals generally decrease during deposition and increase upon plating. Upon deposition, in a dendrite generating system, the lithium gets close to the laser spot, decreasing the electrolyte signal. After 14 hours, the freshly deposited lithium arrives in the field of view of the Raman laser; consequently, the electrolyte signals are not visible.

When NH_4PF_6 is present, the signal behaviour is characterized by a significant drop in the first reduction, even if the lithium is far from the region the laser hits. In particular, the EC and the LiTFSI:EC signals showed the most prominent decrease associated with their reaction at the electrode. This suggests that the presence of the additive can assist the reaction of the electrolyte component to form the interphase.

Evidence of the interlayer kinetic formation can be obtained by increasing the current density to 1 mA cm^{-2} and the capacity and 1 mAh cm^{-2} . In an electrochemically driven process, the kinetic of the formation of the interlayer is influenced by the increased current (electrolyte signals decrease). On the other hand, a pure chemical process is not dependent on the current density but depends only on the concentration of the reacting species. The operando Raman spectra are reported in Figure 5.11, and the integrals of the representative band of the electrolyte components are plotted versus the voltage profile (Figure 5.12). The in situ optical microscope shows a particular texture due to the wet glass fiber separator (Figure 5.13). After cycling, lithium growth is visible in the left part of the interphase, showing that dendrites formation is present by increasing the current density. However, the lithium did not reach the area where the laser was focused.

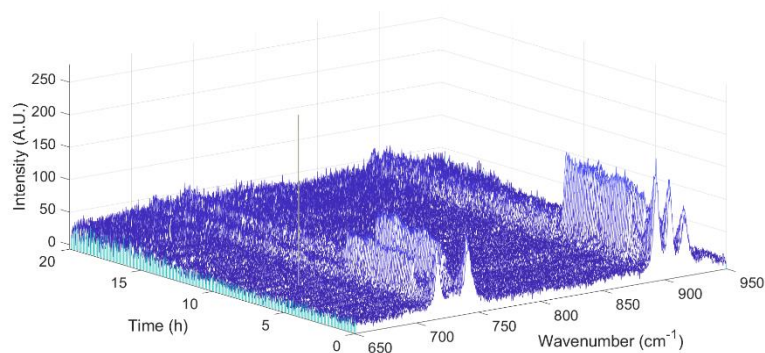


Figure 5.11. Operando Raman spectra recorded during deposition/stripping cycles in $1\text{M LiTFSI EC:DMC} + 50 \text{ mM NH}_4\text{PF}_6$ at current density of 1 mA cm^{-2} and a charge capacity of 1 mAh cm^{-2} , 4 acquisition, 15 s time per scan, every 5 minutes.

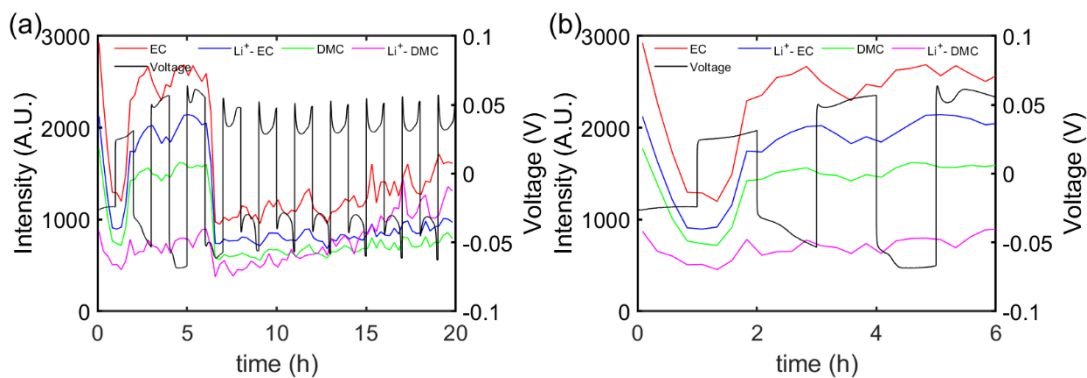


Figure 5.12. Operando Raman signals variation during lithium deposition-stripping in 1M LiTFSI EC:DMC + 50 mM NH_4PF_6 (a) in the interval $880\text{-}945\text{ cm}^{-1}$ and (b) signal variation in the first 3 cycles. The Li/Li cell with glass fibre separator operates at 1 mA cm^{-2} .

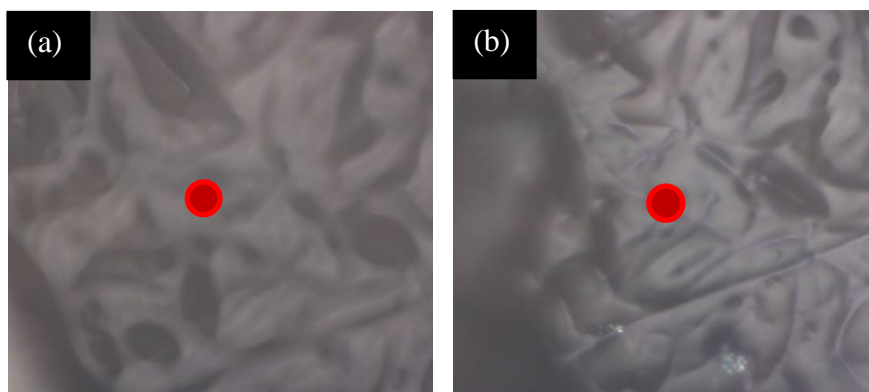


Figure 5.13. In situ optical microscopy images (50x) (a) before and (b) after cycling at 1 mA cm^{-2} in 1M LiTFSI EC:DMC + 50 mM NH_4PF_6 . The red spots indicate the position in which the laser has been focused.

The voltage profile (Figure 5.12) shows comparable behaviour to the cell cycled at 0.5 mA cm^{-2} . The overpotential increases in the first three cycles (up to 55 mV) and stabilizes around 0.45 mV. As expected, the overpotentials are generally higher, but the interlayer formation reaches an equilibrium earlier with respect to the five cycles needed at 0.5 mA cm^{-2} . In addition, it is well-visible that the integrated values of the cell operating at $1\text{ mA cm}^{-2} / 1\text{ mAh cm}^{-2}$ drop earlier with respect to those of the cell cycled at $0.5\text{ mA cm}^{-2} / 0.5\text{ mAh cm}^{-2}$ (Figure 5.10). These suggest that the role of the additive in the formation of the interlayer is electrochemically promoted. The electrolyte reaction mechanism at interphase is supposed to work as an

electrocatalysed chemical reaction. When the lithium metal meets the electrolyte, slight gas evolution from lithium samples occurs. After 24 hours, the lithium is covered by a dark grey layer (Figure 5.14).

Considering that the formation of gas could be a potential safety issue, it will be of interest to investigate the possibility of performing a pre-treatment of lithium anodes.

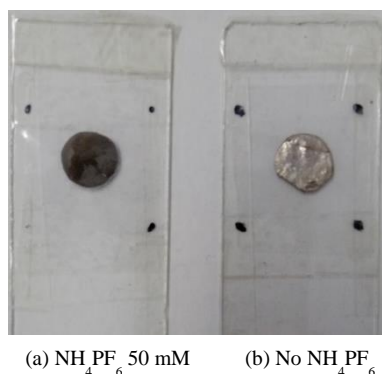
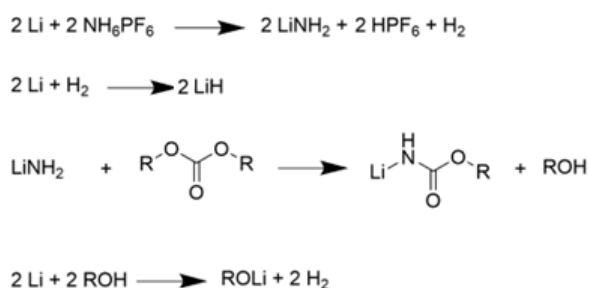


Figure 5.14. Lithium disk immersed in electrolytic solutions for 24h.

The hypothesized mechanism involves the direct reaction of lithium with ammonium by forming lithium amide. This strong basis can react with organic carbonate by nucleophilic substitution forming organic amide. Side products such as hydrogen and organic alcohol can enrich the SEI of LiH and lithium organic oxides. These reactions (examples in Scheme 5.1) should result in a nitrogen-enriched SEI. However, further investigation will be carried out by X-ray photoelectron spectroscopy on cycled lithium electrodes to define the composition of the reaction products of the electrolyte with the lithium electrode (SEI).



Scheme 5.1. Proposed reactions involving lithium metal due to the presence of ammonium hexafluorophosphate.

Increasing the concentration of the additive (100 mM) is possible to verify the influence of the NH_4PF_6 on the formation of the interlayer. As shown by in situ optical microscopy images (Figure 5.15), increasing the concentration leads to a dramatic formation of dendrites in 10 cycles. This is also confirmed by the evolution of the Raman spectra (Figure 5.16).

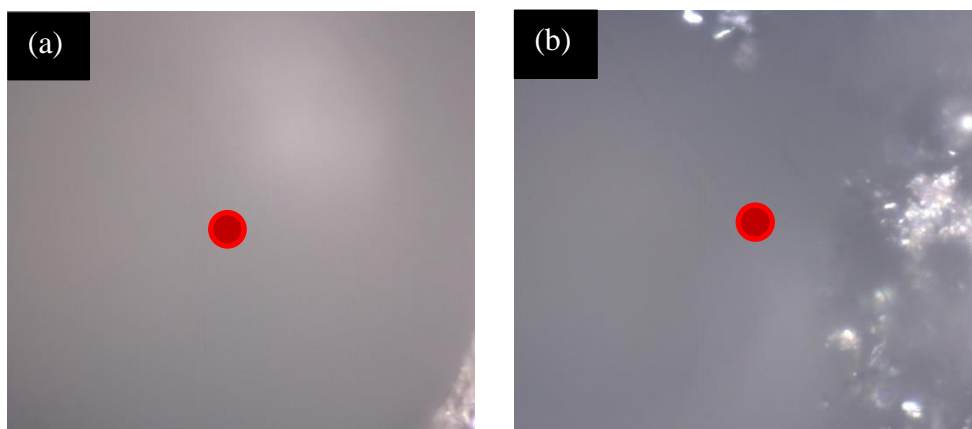


Figure 5.15. In situ optical microscopy images (50x) (a) before and (b) after cycling at 0.5 mA cm^{-2} in $1\text{M LiTFSI EC:DMC} + 100 \text{ mM NH}_4\text{PF}_6$. The red spots indicate the position in which the laser has been focused.

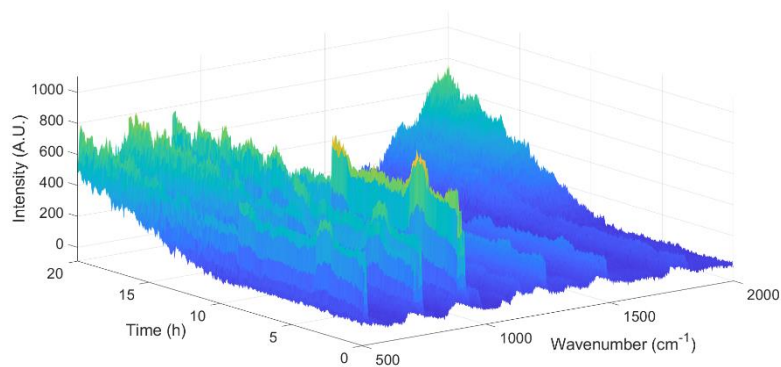


Figure 5.16. Operando Raman spectra recorded during deposition/stripping cycles in $1\text{M LiTFSI EC:DMC} + 100 \text{ mM NH}_4\text{PF}_6$ at current density of 0.5 mA cm^{-2} and a charge capacity of 0.5 mAh cm^{-2} , 4 acquisition, 15 s time per scan, every 5 minutes.

The voltage profile (Figure 5.17) at $0.5 \text{ mA cm}^{-2}/0.5 \text{ mAh cm}^{-2}$ shows an increasing overvoltage that reaches its maximum in five cycles (analogous to 1M LiTFSI

EC:DMC + 50 mM NH_4PF_6). The overvoltages are generally higher compared with experiments with 50 mM NH_4PF_6 .

This is in perfect agreement with the hypothesis of an electrocatalytic mechanism. If an electrochemical reaction is not diffusion limited, the kinetics depends on the current density, that in galvanostatic mode, is constant. The higher resistivity can be related to the more resistive interphase formed. If hydrogen evolution is too strong, it does not have sufficient time to react with lithium and may form a non-homogeneous SEI. Consequently, if the interphase does not stop forming, it can lead to a thick, resistive SEI. If the SEI mechanical properties are not good enough, preferential pathways favouring a lithium dendritic morphology can be formed. The electrolyte signals in the Raman spectra show a progressive decrease in the first deposition (excluded the hexafluorophosphate anion) that continues to decrease also in the following cycles.

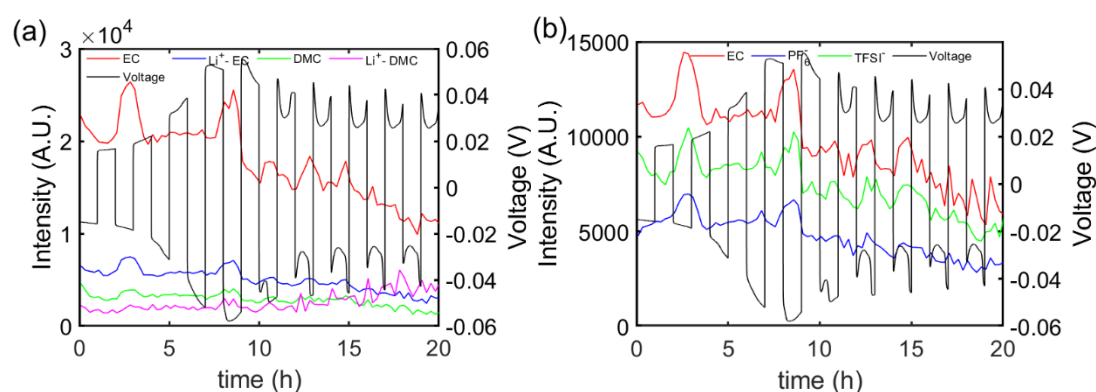


Figure 5.17. Operando Raman signals variation during lithium deposition-stripping in 1M LiTFSI EC:DMC + 100 mM NH_4PF_6 (a) in the interval $880\text{-}945\text{ cm}^{-1}$ and (b) signal variation in the first 3 cycles (b). The Li//Li cell with glass fibre separator operates at 1 mA cm^{-2}

It is possible to monitor the variations at the interphase by focusing the laser on the lithium interphase. In 1M LiTFSI EC:DMC, the massive dendritic growth does not allow to focus the laser at the interphase because, in the first deposition, the lithium completely occupies the measured area (Figure 5.18).

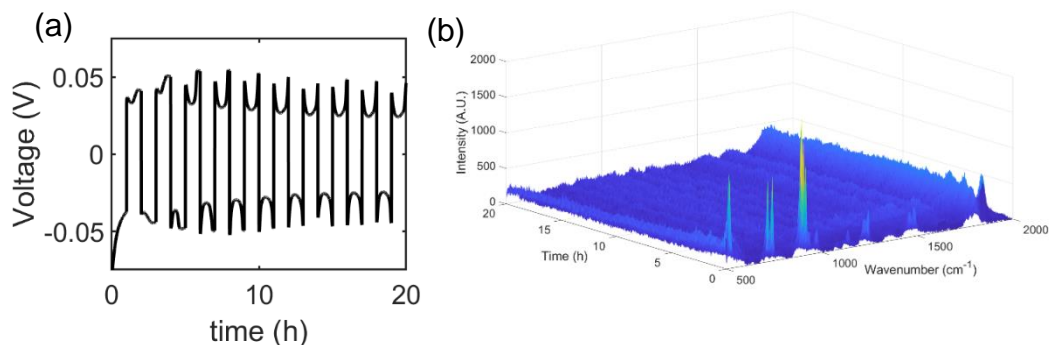
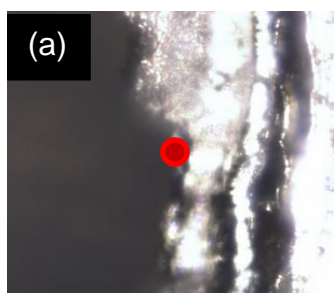


Figure 5.18. (a) Voltage profile of a Li//Li cell in 1M LiTFSI EC:DMC + 100 mM NH_4PF_6 , glass fibre separator at $0.5 \text{ mA cm}^{-2}/0.5 \text{ mAh cm}^{-2}$; (b) Operando Raman spectra recorded during deposition/stripping cycles, 4 acquisition, 15 s time per scan, every 5 minutes.

In 1M LiTFSI EC: DMC + 50 mM NH_4PF_6 , the small dendritic growth allows for the Raman signals' visualisation for the first ten cycles (Figure 5.19). After the 10th cycle, the lithium deposit occupies the measured area. The signals of DMC and coordinated LiTFSI: EC decrease progressively in the first three cycles, while the EC signal shows a continuous progressive decrease. In addition, small fluctuation coincides with the deposition/stripping process. Integrating the Raman spectra between $1825\text{-}1885 \text{ cm}^{-1}$ is possible to observe the products from laser-induced local degradation of species initially present on the lithium surface. Carbon-based components can degrade upon irradiation generating disordered lithium acetylide species of limited size on the lithium surface [190].



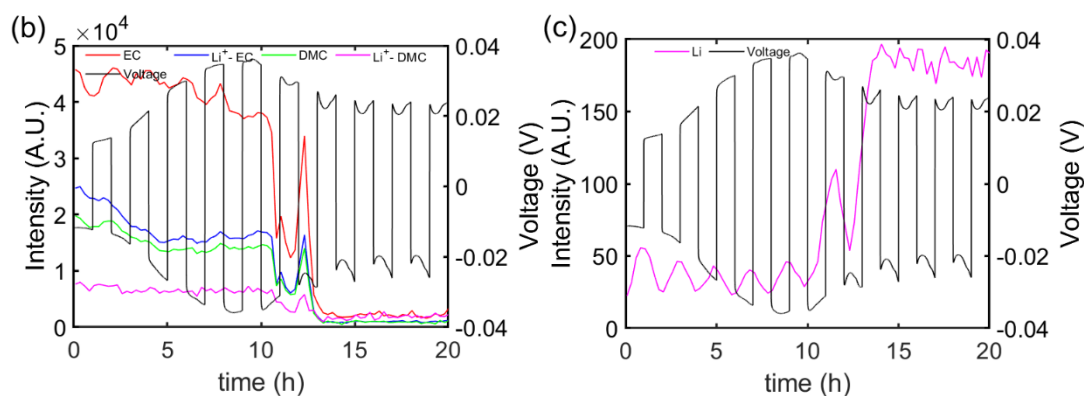


Figure 5.19. (a) Image of the lithium-electrolyte interphase. The red spot indicates the position in which the laser has been focused. Operando Raman signals variation during lithium deposition-stripping in 1M LiTFSI EC:DMC + 50 mM NH_4PF_6 in the interval (b) $880\text{-}945\text{ cm}^{-1}$ and (c) $1825\text{-}1895\text{ cm}^{-1}$. The Li/Li cell with glass fibre separator operates at $0.5\text{ mA cm}^{-2}/0.5\text{ mAh cm}^{-2}$.

Figure 5.19c reports the 1845 cm^{-1} integrated band is associated with the lithium-electrolyte interphase.

The ratio between the Raman signals at the end of each step of a single cycle indicates the movement of the lithium-electrolyte interphase during the deposition/stripping processes. Ratios comprised between 85% and 97% indicate small volumetric changes of electrodes, suggesting a high efficiency of the deposition/stripping process.

In conclusion, the action exerted by NH_4PF_6 regards the generation of a diverse interphase. Even if the direct reaction is spontaneous, operando Raman analysis suggests that the interlayer formation interlayer is electrocatalysed. The PEIS measurements indicate a less resistive behaviour of the cell with NH_4PF_6 and the appearance of a well-developed interphase from the earliest stage of the measurements without altering the charge transfer process. Deposition/stripping cycles show superior stability in the presence of the ammonium salt. This results in agreement with the in situ optical microscope images showing no dendrites formation in the micrometre scale at 0.5 mA cm^{-2} .

5.6. Application and specifications

As reported in this chapter, adopting a lithium metal anode guarantees the increase of the energy density of the corresponding batteries, depending on the cathode chemistry.

For academic honesty, despite the high specific capacity, the low-bulk density of metallic lithium (0.53 g cm^{-3}) negatively impacts its volumetric capacity that results lower than silicon anodes. It must be considered, however, that silicon-based anodes require additional void volume to adsorb the significant volume expansion upon lithiation [192].

As described for LIBs, the cell voltage is determined by the potential difference between the redox potential of the electrode materials. Figure 5.20 reports the potentials and volumetric capacities of different electrode materials. Different chemistries of the positive electrode materials result in potentials from the 2.8 V of sulphur cathode up to 5 V reached by LMNO. Also, the capacities range from 362 mAh cm^{-3} [193] to 2500 mAh cm^{-3} of Li_2O_2 [194.]

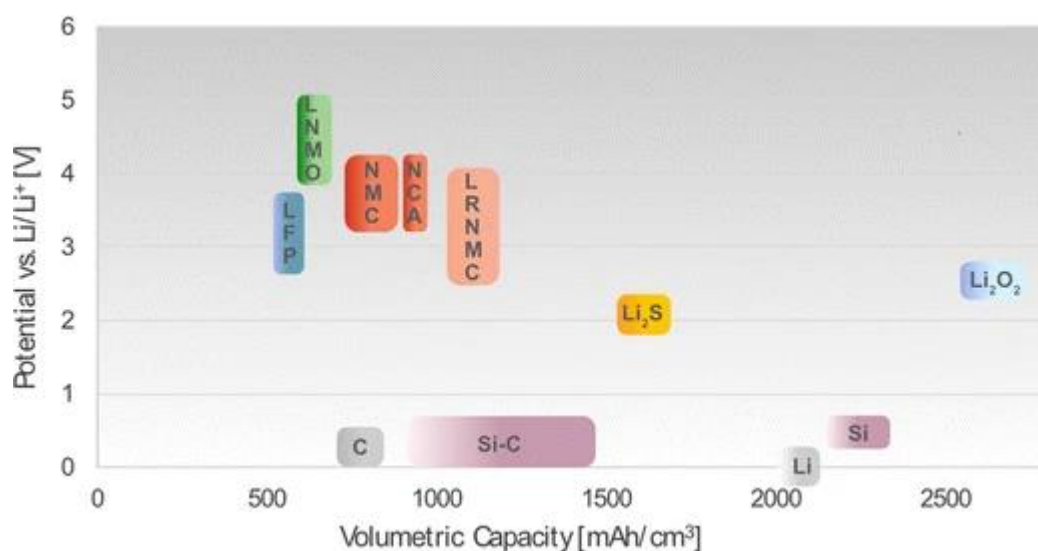


Figure 5.21. Plot of the redox potential of positive and negative active materials for rechargeable lithium batteries versus their volumetric capacities [mAh cm^{-3}] (LRNMC = Li-rich NMC, LNMO = $\text{LiNi}_{0.5}\text{Mn}_{1.5}\text{O}_4$, LFP = LiFePO_4). Reproduced from reference [195] with permission from Springer Nature.

In addition to the inorganic cathodes described in Section 4.1, lithium metal anode is highly studied in lithium-sulphur and lithium-oxygen systems.

In Li-S systems, metallic lithium is coupled with an elemental sulphur cathode, exhibiting a higher theoretical capacity (1675 mAh g^{-1}) compared with commonly studied inorganic materials. Indeed Li-S batteries with increased safety, higher energy density, and lower cost because of sulphur's high availability result in promising automotive application technology. However, its practical application is far due to its

complicated reaction routes, which are affected by several factors. The electrode composition requires additional conductive additives because of the electronically insulating nature of elemental sulphur and Li_2S . In addition, the soluble intermediates can shuttle to the lithium side, causing even worse problems. Polysulphides may be reduced on the lithium depositing Li_2S . This results in a loss of active material, an increased electrical resistance, and the corrosion of the lithium metal electrode.

Li-O_2 batteries possess the highest theoretical energy density of $\approx 3600 \text{ Wh kg}^{-1}$ based on the battery reaction, $2\text{Li} + \text{O}_2 \rightleftharpoons \text{Li}_2\text{O}_2$ ($E^\circ = 2.96 \text{ V}$), where oxygen comes from the atmosphere (air) or from a tank. However, in these systems, apart from Li dendrites discussed in Section 5.2, the corrosion of lithium metal and the decomposition of the electrolyte due to oxygen and moisture crossover cannot be underestimated.

In these two systems, strategies to prevent the polysulfide shuttling in Li-S cells and moisture permeation in Li-O_2 cells make use of physical/chemical barriers. Alternatively, it is possible to improve the Li/electrolyte interfacial stability.

Another important aspect of lithium metal batteries is related to fire risk by short-circuits provoked by dendrite growth throughout the separator. If not controlled, the local temperature increase can lead to thermal runaway, with the risk of explosion. [196]. Solid electrolytes are a potential solution to this aspect, presenting superior mechanical properties for suppressing the dendrites formation. In addition, they considerably reduced the fire risk of the cell, thanks to the absence (or decrease) of flammable organic liquid electrolytes. Polymer electrolytes, however, present low ionic conductivity between 10^{-8} and $10^{-5} \text{ S cm}^{-1}$ at room temperature and far below that of commonly-used liquid electrolytes ($10^{-3} \text{ S cm}^{-1}$). Alternatively, inorganic ceramic or glassy electrolyte shows higher ionic conductivity (up to $10^{-2} \text{ S cm}^{-1}$). However, they pose inherent challenges such as tricky processability, high costs, high grain boundary resistance, insufficient wettability, and, in some cases, side reactions with Li metal anode [197].

6. Redox Flow Batteries (RFB)

As mentioned in Chapter 3, electrification requires a solution that fits different needs. This Chapter focuses on technology for large-scale applications. In particular, Chapter 6 introduces the topic of Redox Flow Batteries (RFB) by reviewing the most used chemistries.

To date, LiBs are ubiquitous and, in 2019, stored 8.8 GWh of energy in stationary facilities. The use of LiBs can be limited by adopting a battery system that fits the requirements for stationary applications with lower costs and drawbacks (e.g., limited and geographically available).

In order to be used in large-scale systems, batteries must require long life in terms of cyclability and calendar life. Meanwhile, in terms of costs, targets have been set to $0.05 \text{ € kW}^{-1}\text{h}^{-1} \text{ cycle}^{-1}$) [198].

Among the various battery architectures, RFBs are an ideal choice for large stationary applications. In this system, the electrolytes contain the electroactive species that flow through an electrochemical cell. The electrolyte is stored externally in tanks and is pumped through the cell. This guarantees a modular, scalable, potentially low-cost system in which energy and power density are decoupled. Energy density depends on the electrolyte volume and concentration, while power density depends on the size and kinetics of the electrodes. A general scheme is shown in Figure 6.1.

RFBs are characterized by high round trip efficiency (RTE), depth of discharge (DoD), fast responsiveness and negligible environmental impact (e.g., aqueous RFBs). On the other hand, power and energy density are limited compared to other technologies, such as LiBs. They are easily scalable and fit with large-stationary applications.

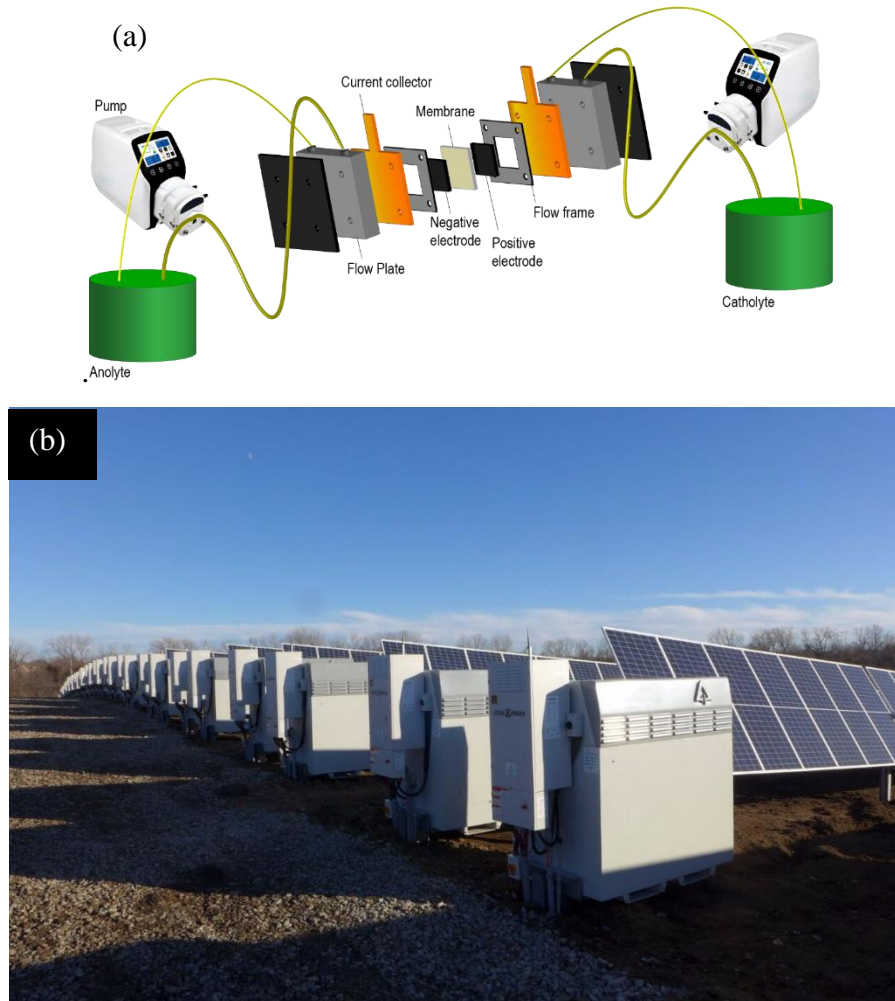


Figure 6.1. (a) Schematic representation of a redox flow cell architecture, (b) vanadium redox flow batteries connected to a solar array.

In standard RFBs, active species are dissolved in either oxidized or reduced-state electrolytes. Alternatively, the so-called hybrid- RFBs comprise one solid electroactive material that is deposited or stripped during the cycling (e.g., Cu or Fe-based RFBs). In those systems, the deposition-stripping process limits the decoupling of power and energy. In fact, in hybrid RFBs. The maximum amount of energy that can be stored can be limited by the maximum number of electroactive species that can be deposited.

6.1. Standard configuration

6.1.1. Vanadium-based systems

RFBs have been developed based on different chemistries in the last few decades. The most impactful system is the all-vanadium RFB (VRFB), mainly developed by Maria Skyllas-Kazacos, who first demonstrated vanadium dissolution in sulfuric acid in the 1980s [199]. A VRFB is a standard RFB, so the positive and negative electrolytes are stored in two separate external reservoirs, from which they are pumped into the electrochemical cells (Figure 6.2). This system takes advantage of the four-oxidation states of vanadium, so only vanadium ions are used in the electrochemical reactions.

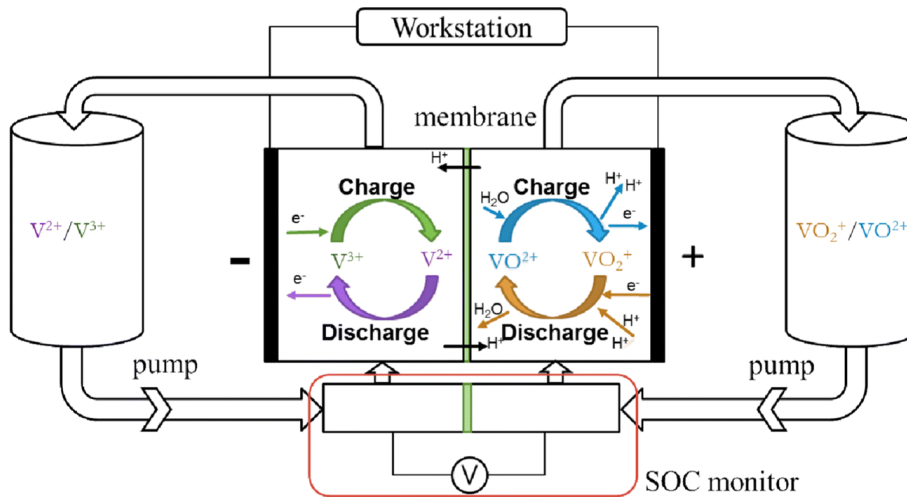
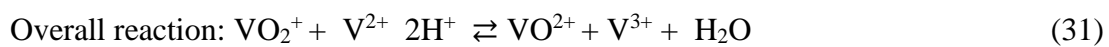


Figure 6.2. Schematic representation of an all-vanadium RFB. Reproduced from reference [200] with permission from Springer Nature

Hence, during charging, the oxidation of V^{4+} (VO_2^+) to V^{5+} (VO_2^{2+}) take place in the positive half-cell, while the reduction of V^{3+} to V^{2+} occurs in the negative compartment. The electrochemical half-reactions produced by these solutions in the cells are:



This system is known as generation 1 (G1), and it is characterized by an open circuit voltage of 1.6 V at 100% state of charge (SoC) [201]. However, important obstacles are the stability of the species V^{4+} and V^{5+} in some common electrolytes (e.g., HCl or NaOH) and the low solubility of compound V^{5+} . Indeed, as reported by Maria Skyllas-Kazacos and Robert Robins, the rate of dissolution of V_2O_5 is very slow at room temperature, taking hours to dissolve completely [202], for this reason at least 2 M H_2SO_4 electrolyte is required. The main critical points for the G1 VRFB are the relatively high toxicity, high cost of vanadium oxides, the required fine thermal regulation systems (between 10 °C and 40 °C) to avoid precipitation of vanadium species, and the deterioration of cell components (e.g., ion exchange membranes and the positive electrode) due to the high oxidation properties of V^{5+} [203].

On the other hand, the main advantage of a G1 is that vanadium ions are the only active species. The event of a cross-mixing consists only of the self-discharge and can be solved easily by recharging the electrolyte. In another system presented in this section with different metals, the mixed liquids would have to be replaced or removed and treated externally in case of cross-contamination.

In order to solve some of the criticism of G1 VRFB, some variations are applied to this system like the use of bromide to the positive half-cell.

This, known as the G2 vanadium redox flow battery [204], make use of vanadium bromide solution in both half cells avoiding cross-contamination. The electrochemical reactions are:



The main features of V/Br RFBs are the higher solubility of V/Br, which makes it possible to use concentrations up to 3–4 M (energy densities up to 50–70 Wh·L⁻¹), the possibility to decrease the operating temperature and, the absence of the problematic V^{5+} . The problem with this system is the evolution of halides gases. At this purpose, complexing agents have been studied and tested to decrease prevent the emissions of toxic bromine vapor, e.g., quaternary ammonium bromide [205]. This approach shows successful results at the expense of increasing membrane resistance and a high cost.

Alternatively, the positive half-cell redox couple can be replaced with a positive air electrode. This guarantees a higher energy density and, as in G2 VRFB, a minor amount of vanadium due to the different positive half-cells. However, the catalyst cost required for oxygen reduction mostly influences its penetration into the market. In addition, the critical challenges are long-term stability, efficiency, low power density and water management at the cathode [200].

6.1.2. Organic redox flow batteries

Since most of the problems of this technology arise from the availability and the cost of the redox active species and the replacement of the electrolyte containing them, one highly studied approach results in the employment of organic redox active species.

The advantage is the incredible possibility of tailoring what the organic synthesis offers. In addition, redox active organic molecules are based on earth-abundant elements (e.g., C, H, O, N, S, P and Fe). Hence, in principle, the molecular structure of the active species can be tuned to increase the solubility and cell voltage required for high energy density systems. This can be achieved by modification with electro-withdrawing (EWG) or electro-donating (EDG) substituents to the desired molecule. At this purpose, some molecules (e.g., viologen-based molecules) can lead to multiple electron transfer reactions.

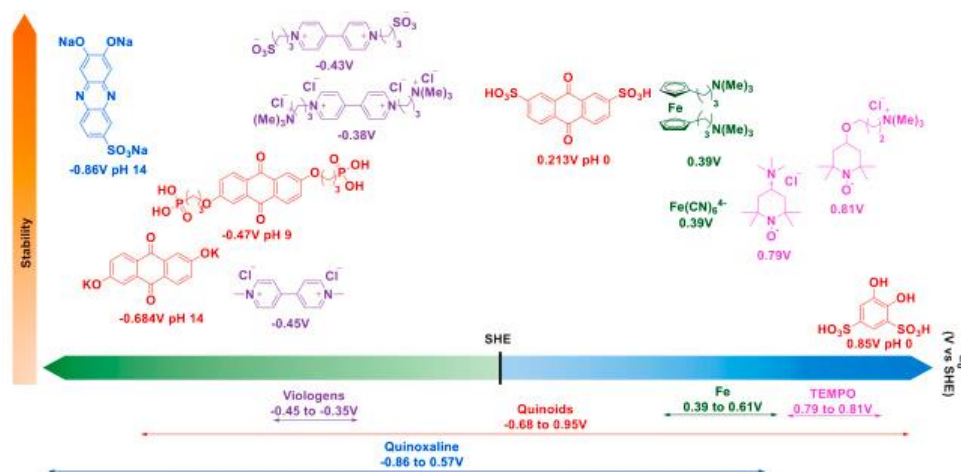


Figure 6.3. Overview of organic redox active compounds classified according to their stability and redox potential recalculated to a SHE reference. Adapted from [198].

However, organic molecules showed a limited durability and more frequent replacement of the electrolyte must be considered. Thus, this effect must be considered in the capital cost [206].

To date, there is a concentrated research effort to face off the mentioned problem and, usually, a compromise between stability and performance must be accepted.

6.2. Hybrid configurations

In addition to the RFBs mentioned above, several systems operate in a hybrid configuration. Hybrid flow batteries involve a metal as the negative electrode. Indeed, the negative half-cell process results in the deposition/stripping of metal on an inert collector during charge. If not optimized, this may limit the energy that can be stored to the amount of metal that can be hosted by the cell [207]. Hence, this hybrid RFBs need additional studies to optimize the reversibility of metal deposition in terms of the charging methods, the cell geometry, the electrolyte composition and hydrodynamics, the metal deposit morphology, adhesion and, density.

6.2.1. Zinc-based systems

In the Hybrid RFBs field, zinc's significant negative standard potential (-0.76 V vs SHE) has been considered in combination with different positive half-cell chemistries as zinc-air [208], zinc-lead dioxide [209], zinc-cerium [210] and zinc-bromine.[211] As an example, the first zinc-cerium RFBs was reported in 2000 by Plurion Inc. (UK) and patented in the 2004 [212].

This system take advantage from the large differences between the redox couple's standard electrode potentials in aqueous solution (c.a. 2.4 V) corresponding to a large maximum energy density. However, an appropriate selection of the materials to suppress hydrogen and oxygen evolution must be adopted.

Usually, at the negative electrode, the zinc is electrodeposited and stripped on deposition/stripping of zinc in carbon/polyvinyl-ester composite material [213]



In the positive half-cell, the Ce(III) is oxidized during charge and Ce(IV) is reduced back during discharge (35). Depending on the supporting electrolytes, the potential of the process lies between 1.28 and 1.72 V vs. Ag/AgCl [14].



Hence, the overall cell reaction of the zinc–cerium redox flow battery is (36)



One of the most proposed supporting electrolytes is the methanesulfonic acid, since its conductivity is comparable to that of HCl, and is less corrosive than sulphuric acid. In addition, the metals solubility limits result higher compared to other mineral acids [214].

Challenges in the zinc-cerium RFB include leakage of species across the ion-exchange membrane causing mixing of the respective active components of the electrolytes, achieve long cycle life and improving energy efficiencies. The formation of zinc dendrites during the charging cycle limits the cycle life to about 1500-2000 cycles.

The zinc-bromine RFBs becomes appealing due to its high energy density, relatively high cell voltage and use of abundant and low-cost materials (lower than in Zinc-Cerium RFBs) [210]. In a Zn-Br RFB, the electrochemical reactions are:



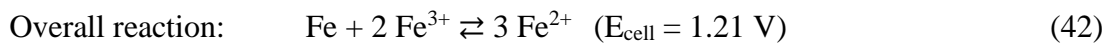
During charging process, the metallic zinc deposits onto the negative electrode (as in zinc-cerium RFB) and elemental bromine evolves at the positive electrode while, during discharge, zinc and bromide ions are formed at the respective electrodes. The main drawback of this system is represented by the low operating current density (20 mA cm⁻²), hence low power density, which is caused by the large internal resistance and the large polarization of the positive electrode [210].

The low power density leads to a larger stack size having larger materials consumption for its build, and higher cost. For this reason, much work has been conducted to

enhance the electrocatalytic activity of the positive electrode modifying, for example, the positive electrode with carbon nanotubes [215]. In addition, this system uses ZnBr_2 solution as electrolyte showing low electrolyte conductivity, which increases the internal resistance of the cell. This problem is not present in other RFBs showing high electrolyte conductivity through the use of strong acid. Moreover, the wettability and the kinetics towards Br_2/Br^- redox reaction is not trivial and does not allow the employment of simple conventional electrode materials (e.g., graphite felt (GF), carbon felt (CF)) [216].

6.2.2. All-iron RFBs

As with LFP in LiBs, iron is an attractive element for increasing safety, sustainability, and lowering the system cost. The first appearance of this all-iron RFB is 1981 by Hruska and Savinell [217] system takes advantage of the simultaneous presence of iron in the three oxidation states reducing the crossover effects. The electrochemical processes involve the iron deposition/stripping in the negative half-cell (40) while ferrous and ferric cation are electrochemically converted at the positive electrode (41).



Usually, the electrolyte is composed of iron chloride salt with highly concentrated NH_4Cl supporting electrolyte. This system reached, using a low-cost membrane, and 2 M FeCl_2 / 2.8 M NH_4Cl electrolyte at 60 °C, energy efficiencies of 50% at 60 mA cm^{-2} . One of the most important drawbacks regards the precipitation of Fe^{2+} ($\text{Fe}(\text{OH})_2$) due to the competitive hydrogen evolution reaction (HER). Indeed, HER is responsible for the consumption of protons and leads to a chemical imbalance. For this reason, daily pH maintenance in the anolyte is needed to keep an acid environment (between 2-3). Many efforts were carried out on this aspect leading to significant reductions in hydrogen generation. However, it was not possible to eliminate it [218, 219].

7. All-Copper RFBs

Chapter 6 introduced the different RFB technologies' chemistries and critical points. This Chapter presents RFBs based on copper as valuable and sustainable systems taking advantage of the well-established copper European supply chain. Experimentally, electrolytes (section 7.2. from ref. [IV, V]) electrodes (section 7.4.2.1. from ref. [VI]) and membranes (section 7.4.4. from ref. [VII]) are intensively examined to improve performance and cell stability. In addition, a new methodology to probe the active species crossover and predict the cell failures is in section 7.5 (ref. [VIII]).

All-copper battery made its first appearance in 1974 by Kratochvil and Betty in 1974 [220]. The reported system, with an OCV of 1.35V, was composed of CuClO_4 and acetonitrile as salt and solvent, respectively. In this system, acetonitrile acts as a ligand for Cu(I) and Cu(II) cations forming thermodynamically stable complexes. This study, combined with research on chlorocuprate ionic liquids [221], resulted in the static all-copper battery with an OCV of 0.85V.

In 2012, Sanz and co-workers started using copper chloro-complexes in the positive half-cell of conventional vanadium redox flow batteries (VRFBs) [222]. This demonstrated the excellent reversibility of the Cu(I)/Cu(II) redox reaction in aqueous chloride solutions [223]. However, as in many mixed metal batteries, the crossover of copper species in solution to the negative half-cell limit the cyclability.

The first all-copper flow battery was developed in 2013 with a choline chloride based deep eutectic solvent [224]. This system showed promising preliminary results with a relatively low OCV of 0.81V and Coulombic efficiency greater than 95%. The major drawback was the low current density (max 4 mA cm^{-2}), which was due to the typical low conductivity of non-aqueous electrolytes (20 to 30 mS cm^{-1} at the temperatures of interest). This is orders of magnitude lower than the conductivity of the aqueous solutions presented in the next chapter.

The research moved towards cost-effective materials and possibly of regenerating starting materials using waste-heat [225].

The first practical all-copper RFB was explored in 2014, using an aqueous electrolyte, stabilizing Cu(I) by chloro-complexation. The reported system [226] showed a good

current density and paved the way for utilisation of cost-effective components. The impressive reversibility and the good reaction kinetics in a wide temperature range made the interest in CuRFB growing.

Savinell group at Case Western Reserve University in Cleveland in 2015 proposed copper bromo-complexes based system, which has a higher OCV (0.85V) compared to systems based on chloro-complexes [227]. The other important variation proposed consisted of using copper slurries in the negative half-cell, which can configure the CuRFB system as a standard RFB [228].

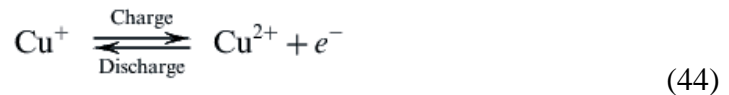
7.1. Principle of operation

The CuRFB take advantage of the three oxidation states of copper. As Cu(I) is not stable in aqueous media, the system is based on the chlorocomplexation of the copper cations. Indeed, the Cu(I) complexes (CuCl_2^- , CuCl_3^{2-}) are formed in concentrated chloride solutions and are stable to disproportionation. The resulting cell has a hybrid configuration with the chemical reactions shown in Equations (43) and (44).

At the negative electrode:



At the positive electrode:



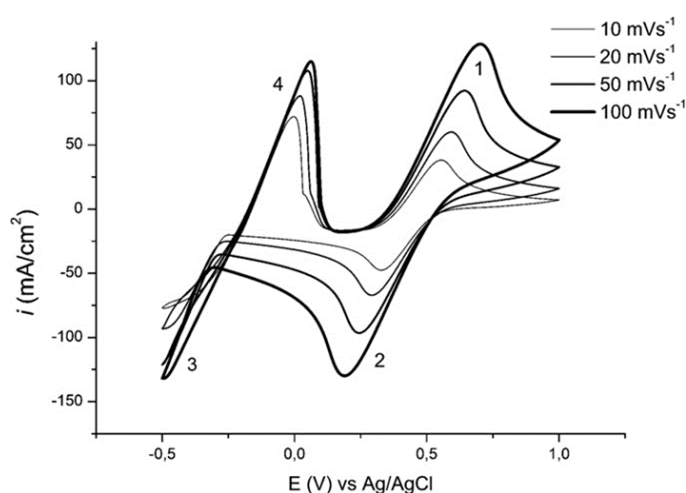


Figure 7.1. Cyclic voltammograms of 1 M CuCl₂/3.5 M CaCl₂ electrolyte; the selected Cu:Cl ratio was 1:9; the experiments were performed varying the scan rate, $\nu = 0.01, 0.02, 0.05$ and $0.1 \text{ V} \cdot \text{s}^{-1}$ at $40 \text{ }^\circ\text{C}$. Reproduced from reference [223] with permission from Elsevier.

In the cell, during charge, cuprous ions are oxidized to cupric ions at the positive electrode while are reduced to metallic copper in the negative-half cell. During discharge, the reverse reactions take place.

Furthermore, in this system, the problem of cross-contamination is minimized, considering that copper is the only active material, and the supporting electrolyte is shared between the two compartments. Hence, for long-term applications, the electrolytes can be regenerated easily. However, the problem of cross-contamination is minimized but not eliminated. Diffusion of Cu(II) from the positive into the negative half-cell results in self-discharge. Indeed, Cu(II) spontaneously comproportionate (45) with the copper deposit.



As a final benefit, the CuRFB profits from the use of low-cost and Earth-abundant raw materials already employed in other sectors. That means that CuRFB system can take advantage and take part in the Europe copper supply chain. As an example, acid mining drainage from mining activities can be a source of the copper [229], and the technologies to recycle copper with high rates and purity is already developed [229].

7.2. Formation of chlorocomplexes

The aqueous all-copper RFB is based on stabilising Cu(I) ions by complexation. However, the distribution of chloro-complexes species also determines the electrochemical reaction's thermodynamics and kinetics and plays a crucial role in developing a highly performing CuRFB system.

Cu(I) and Cu(II) showed several forms in a chloride-rich aqueous solution. For Cu(II), there are at least five species (Cu^{2+} , CuCl^+ , CuCl_2 , CuCl_3^- , and CuCl_4^{2-}). Meanwhile, there are at least six complexes for Cu(I) (Cu^+ , CuCl , CuCl_2^- , CuCl_3^{2-} , $\text{Cu}_2\text{Cl}_4^{2-}$, and $\text{Cu}_3\text{Cl}_6^{3-}$). The distribution of these complexes strongly depends on the concentration of copper and chloride with respect to the solvent [230-233].

Determining stability constants and competitive thermodynamic equilibria between the various complexes provided much efforts [234,235] but without considering the ionic strength and the dependency on the copper-to-solvent ratio. Thus, the results disagree with the different contributions due to changes in the molecular environment and the complexation at different Cl^- concentrations.

Currently, to optimize the physical-chemical properties of new electrolytes for CuRFB is mandatory to pursue a deeper study of the stability of the copper chloro-complexes in real solutions. The Bard group has carried out several studies in dilute solutions of copper [236, 237] with ultramicroelectrodes (UME) accounting for the ionic strength's influence with the highest concentration of 1.5 M. They proposed a model to determine the stability constant of the complex at various temperatures. This work indicates that the main Cu(II) complexes in high chloride concentration is CuCl_4^{2-} and the main Cu(I) complexes are CuCl_2^- and CuCl_3^{2-} . Also, increasing the temperature or Cl^- concentration can avoid insoluble Cu(I)Cl intermediates that deactivate the electrode surface.

The stabilization of the electroactive species becomes crucial to optimize the cell performance, such as the coulombic efficiency ($\text{CE}_\%$) and kinetics and thermodynamics of the electrode reaction reflected in the voltage efficiency (VE) and energy efficiency (EE). Moreover, detecting and avoiding any possible reason for failures in the long-term application becomes fundamental [238].

It is fundamental, indeed, to elucidate the speciation of copper (II) in diluted CuRFB electrolytes to achieve better performance in CuRFB. Spectroelectrochemical test in

diluted solution gives information on the electrochemical behaviour of electrolytes with a different chloro-complexes distribution. Monitoring the absorbance profile at two different wavelengths during the cyclic voltammetry shows the effect of copper chlorocomplexes stability on the spectrophotometric and voltametric hysteresis. Also, the information from NIR absorption spectra is used to lay the groundwork for studies in concentrated solution. Results of the following sections are reported in ref. [IV] and [V].

- Experimental Section

Chemicals

The electrolytes were prepared with hydrochloric acid (37%, Sigma-Aldrich, Merck KGaA, Darmstadt, Germany), calcium chlorides dehydrates (>99%, ACS reagent, Sigma Aldrich, Merck KGaA, Darmstadt, Germany) as supporting electrolytes and copper (II) chloride dehydrates (99.99 + %, Sigma Aldrich) and copper (I) chloride (>99.995% trace metal basis, Sigma Aldrich). After complete dissolution, the electrolytes were deaerated in Ar for ten minutes and sealed.

Spectro-electrochemical experiments

The spectro-electrochemical measurements were carried out with a PAR273A potentiostat/galvanostat and a Solartron SI 1255 frequency response analyser interfaced with the potentiostat. The absorption spectra were acquired with a Perkin Elmer UV/VIS/NIR Spectrophotometer Lambda19 (PerkinElmer, UK) in 0.25 mm quartz cuvette (ALS, Japan) with three electrode set-up. Pt mesh was used as working electrode (WE, A: 0.691 cm²), Pt wire as counter electrode (CE) and Ag/AgCl reference electrode (RE, ALS, Japan) as reference electrode. All the solutions were deaerated for 15 minutes in Ar and the cuvette was sealed for maintaining the Ar atmosphere during the experiments. To avoid problems of linearity in the Lambert-Beer law, the increasing of Cu(II) concentration was coupled with decreasing of optical path length. Different quartz spacers were used to the optical path length to 300µm, 200µm, 100µm and 50µm. The absorption spectrum of Cu(II) chloride-rich solution is characterized by a ligand-to-metal charge transfer transition (LMCT) in the ultraviolet (UV) region and a metal centred (MC) transition in the near-infrared (NIR) region of the absorption spectrum. The first, from 220 nm to 390 nm, has a vibrational

structure of the band influenced by the degree of complexation of the cation. The latter is d-d transition in which the different chlorocomplexes influences the crystal field splitting parameter Δ and shift the MC band [239]. Also, the MC transition is characteristic of the Cu(II) and is not allowed in Cu(I) due to electronic configuration [Ar] 3d¹⁰ 4s¹, which does not permit a d-d based transition.

Conventional cell experiments

The active area of the working electrode was determined in a conventional three electrode cell with a graphite rod (d: 6 mm, Gamry) as counter electrode and a saturated calomel electrode (SCE, AMEL, 303/SCG/6J) as reference electrode at 40 °C by using a Voltalab PGZ301 (Radiometer Copenhagen, Denmark) in 5 mM ferrocene methanol (FM, 97%, Sigma Aldrich) in phosphate buffer solution 1x (PBS, Oxoid itd, tablets). The cyclic voltammetry experiments were carried out with an identical set up with Pt disk WE (4 mm).

- Calculations

Copper-chloride molecular clusters, explicitly solvated with water molecules, were initially generated with the code Packmol [240], by considering cubic boxes of lateral length ranging from 10 Å to 20 Å. The copper-chloride molecular clusters considered were *i*) [CuCl]⁺, *ii*) [CuCl₂]⁰ and *iii*) [CuCl₃]⁻, as coordinated with water molecules giving the (stoichiometric) supramolecular clusters [CuCl(H₂O)₅]⁺, [CuCl₂(H₂O)₄]⁰, and [CuCl₃(H₂O)₃]⁻. To investigate the effects induced by a variable number of water molecules, each copper-chloride cluster *i*-*iii*) was solvated with a number of water molecules ranging from 1 up to 200.

The geometry optimization of each structure was initially performed at the semiempirical level, namely adopting the density functional tight-binding scheme GFN n -xTB (Geometry Frequency Non-covalent interactions-eXtended Tight Binding, specifically GFN2-xTB [241-243] (v. 6.4.1). For the stoichiometric supramolecular clusters [CuCl(H₂O)₅]⁺, [CuCl₂(H₂O)₄]⁰, and [CuCl₃(H₂O)₃]⁻ GFN2-xTB metadynamics were carried out with the algorithm CREST (v 2.11) for sampling the conformational space [244]. Most stable conformers were optimized at the GFN2-xTB level with very-tight geometry-convergence thresholds and further re-optimized at the DFT level.

For the DFT calculations (i.e., geometry optimizations) the range-separated ω B97X-D functional was considered. For hydrogen, oxygen and chloride atoms the Pople double-split basis set with polarization functions 6-31G* was used, while for copper the fully relativistic pseudopotential ECP10MDF [245] with the double-split basis set ECP10MDF_VDZ [246] was adopted.

Excited states (up to 300 states) were calculated both at the semiempirical time-dependent DFT level, namely the Tamm-Dancoff sTDA and the sTD-DFT approaches [247], and at the TD-DFT level. DFT-based semiempirical calculations were carried out by using the code xTB [241]. DFT and TDDFT calculations were carried out by using the code Gaussian16 [248].

Optimized geometries of the supramolecular clusters $[\text{CuCl}(\text{H}_2\text{O})_5]^+$, $[\text{CuCl}_2(\text{H}_2\text{O})_4]^0$, and $[\text{CuCl}_3(\text{H}_2\text{O})_3]^-$ (i.e., the clusters considered for interpreting the experimental data, *vide infra*) are reported in Supplementary Information. All other cluster geometries modelled in this work are available under request to the corresponding author.

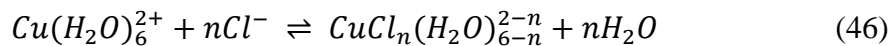
- Results and discussion

Cu(II) speciation dependence from HCl concentration

In RFBs, the electrolyte concentration is one of the most critical parameters that determine the energy of the whole system. The stabilization of Cu(I) by the chlorides complexing agents makes possible the employment of Cu(I) in CuRFB application. Hence, Cu(I) stabilization in an aqueous environment represents an essential milestone to achieve valuable performance in an electrochemical cell. For this purpose, the addition of hydrochloric acid increases the conductivity of the solutions, and the chloride ions stabilize the Cu(I)/Cu(II) redox couple.

The distribution of Cu(II) chloride complexes at different copper and chloride concentrations were obtained from deconvolution of the UV/Vis spectra. In this region, the ligand-to-metal charge transfer (LMCT) transition gives information about the coordination of the copper cation. This transition, from 220 nm to 390 nm, has a band structure influenced by the degree of complexation of the cation [239]. In the quantitative analysis of the LMCT band, 50 mM Cu(II) is the concentration limit (optical path of 50 μm) to have a linear relationship between the absorbance and the Cu(II) concentration. Instead, the band investigation is limited by commonly used detectors to a Cu(II) of 0.1 M for qualitative observations.

For the complexation equilibrium (46) and the equilibrium constant (47), the chloride concentration is more impacting than the copper concentration in the distribution of the complexes (48).



$$\beta_n = \frac{[\text{CuCl}_n(\text{H}_2\text{O})_{6-n}^{2-n}][\text{H}_2\text{O}]^n}{[\text{Cu}(\text{H}_2\text{O})_6^{2+}][\text{Cl}^-]^n} \quad (47)$$

$$[\text{CuCl}_n(\text{H}_2\text{O})_{6-n}^{2-n}] = \beta_n[\text{Cu}(\text{H}_2\text{O})_6^{2+}][\text{Cl}^-]^n \quad (48)$$

With a fixed 50 mM concentration of copper chloride, the HCl concentration was varied from 1 to 6 M. For each copper complex, the absorption spectrum (Figure 7.2) was deconvoluted using Gaussian functions with the parameters obtained by the spectrophotometric data reported by Brugger et al. [239]. In the absorption spectrum of Figure 7.2c, the contribution at c.a. 280 nm (cyan curve) is given by the overlapping of the absorption band of both $[\text{CuCl}_2]^0$ and $[\text{CuCl}_3]^-$ complexes. The high superimposition of the two contributions in the 260-310 nm spectral region makes difficult the deconvolution of this part of the spectrum. After having identified a spectral region in which only one complex absorbs, the absorbance can be used to estimate the percentual composition of the chlorocomplexes (Figure 7.3). For $[\text{CuCl}_2]^0$ and $[\text{CuCl}_3]^-$ complexes, the distributions were obtained from the band at 210-260 and 340-420 nm, respectively. In the 1 M HCl solution (Figure 7.2a), the mainly prevalent complex is the $[\text{Cu}(\text{H}_2\text{O})_6]^{2+}$, with a gradually smaller presence of $[\text{CuCl}]^+$ and $[\text{CuCl}_2]^0$. Increasing the HCl concentration to 3M (Figure 7.2b), there is a red shift of the LMCT band from 250 nm to 258 nm, indicating a higher concentration of the $[\text{CuCl}_2]^0$ (absorbing at 277 nm). At a concentration of HCl of 6 M, a small band at 384 nm indicates the presence of $[\text{CuCl}_3]^-$ which displays two bands at 273 nm and 384 nm. According to Equation (47), highly coordinated copper complexes become favoured by increasing chloride concentration. However, the percentage distribution indicates that CuCl_4^{2-} is not present even with a Cl^- concentration of 6 M.

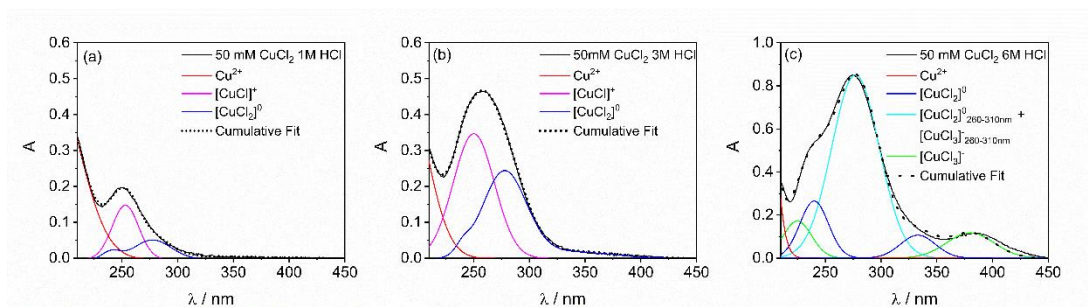


Figure 7.2. UV/Vis absorption spectra of 50 mM CuCl_2 electrolytes with different concentrations of HCl in $50\mu\text{m}$ quartz cuvette. (a) 1 M, (b) 3 M, (c) 6M.

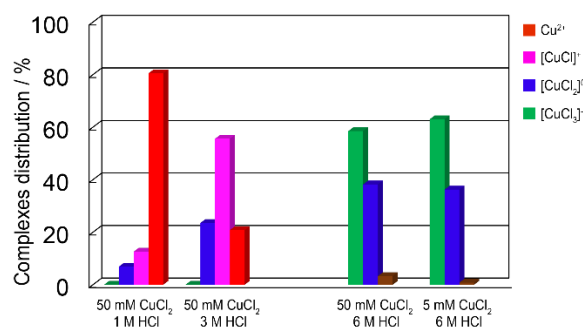


Figure 7.3. Cu(II) chlorocomplexes distribution at different concentrations of HCl and CuCl_2 obtained by deconvolution of the UV/Vis spectra.

Table 7.1 reports the electrochemical properties of electrolytes tested with different concentrations of copper and hydrochloric acid obtained from cyclic voltammetries (CVs, Figure 7.4) in a three-electrode conventional cell. The electrolytes have been evaluated in term of peak potentials of the anodic and cathodic processes (E_+ and E_-), separation between the peak potentials (ΔE), potential of the redox couple Cu(I)/Cu(II) calculated by the half-sum of the peak potentials, anodic and cathodic peak current densities (i_{pa} and i_{pc}) and their ratios. Varying the chloride concentration from 1 M to 6 M, the reversibility and the current increase as a consequence of the higher conductivity. Indeed, the i_{pa}/i_{pc} ratio gets close to 1, and the ΔE diminishes. On the other hand, the $(E_+ + E_-)/2$ of the process shifts towards positive potential. This effect does not depend on the enhanced conductivity but refers to the different equilibria involving the redox species.

CuCl ₂ HCl		E ₊	E ₋	ΔE	(E ₊ +E ₋)/2	i _{pa}	i _{pc}	i _{pa} /i _{pc}
mM	M	V vs. Ag/AgCl	V vs. Ag/AgCl	V	V vs. Ag/AgCl	mA cm ⁻²	mA cm ⁻²	
50	1	0.361	0.227	0.134	0.294	1.02	1.72	0.59
50	3	0.415	0.309	0.106	0.362	2.14	2.62	0.82
50	6	0.438	0.338	0.100	0.388	2.50	2.70	0.93

Table 7.1. Electrochemical properties on Pt at 0.01 V s⁻¹ and 40°C of copper electrolytes with different concentrations of HCl in three-electrode conventional cell, WE: Pt disk, CE: graphite rod, RE: Ag/AgCl. The relative errors of potential measurements are ca. 0.5% and those related to the current measurements are ca. 1%.

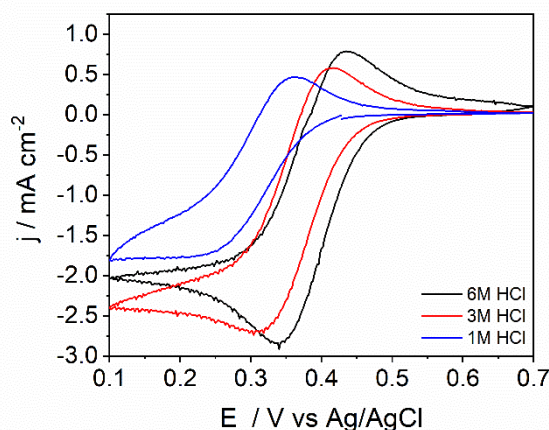


Figure 7.4. CVs at 0.01 V s⁻¹ of 50 mM CuCl₂ electrolytes with different concentrations of HCl in three-electrode conventional cell, WE: Pt disk, CE: graphite rod, RE: Ag/AgCl.

Moreover, decreasing the HCl from 6 M to 1 M makes both anodic and cathodic peaks less evident. If the concentration of Cl⁻ is not high enough, Cu(I) is not stabilized and can disproportionate or be oxidized forming Cu(II) at the electrode interphase. Hence, the cathodic current is given by the combination of the electrochemical reduction of Cu(II) to Cu(I) and the chemical-electrochemical process involving the reduction of newly formed Cu(II). Indeed, the Cu(I) concentration at the electrode decreases, and there is less cuprous cation for oxidation at the electrode.

Quantum chemical calculations: structures and electronic transitions of water solvated copper-chloride clusters.

Quantum chemical calculations were performed to interpret the variations observed in the experimental absorption spectra (see Figure 7.2) of copper-chloride complexes by increasing the HCl concentration. Figure 7.5a (top panel) shows the optimized lowest-energy supramolecular clusters (see section Calculations) for the water solvated species $[\text{CuCl}(\text{H}_2\text{O})_5]^+$, $[\text{CuCl}_2(\text{H}_2\text{O})_4]^0$, and $[\text{CuCl}_3(\text{H}_2\text{O})_3]^-$. Clusters with a variable number of water molecules (up to 200) were also taken into account and results are reported in Supplementary Information. We observed that by increasing the number of ligands the Cu-Cl distance lowers from 2.24 Å for $[\text{CuCl}]^+$ to 2.15-2.08 Å for $[\text{CuCl}_3]^-$ showing, for the latter, strong metal-ligand interactions. Similarly, the distance between the copper ion and the oxygen atom of the nearest-neighbour solvated water molecules shrinks from 2.27/2.11 Å to 1.88 Å, showing relevant local non-bonded interactions. Furthermore, from a preliminary analysis of the radial distribution function between the copper ion and the oxygen atoms $g_{\text{Cu-O}}(r)$, calculated on supramolecular clusters featuring 50 to 200 water molecules (as optimized at the GFN2-xTB level), we observed that by moving from $[\text{CuCl}]^+$ to $[\text{CuCl}_3]^-$ $g_{\text{Cu-O}}(r)$ decreases, as well as the total number of nearest-neighbour water molecules (i.e., first solvation shell) solvating the metal ion. Such result, though preliminary as being not based on extended and equilibrated molecular dynamics simulations (subject for next investigations), suggests that by increasing the number of chlorine ions, the amount of water molecules accessible to solvate the metal-ion centre decreases. Our structural data are in good agreement with previously reported computational studies [249-251]. The ground-to-excited state electronic transitions of each cluster were computed both at the sTDA/sTD-DFT and TD-DFT levels. Here we discuss only TD-DFT results.

Figure 4b (bottom left panel) shows the computed (vertical) excited state transitions for the three clusters $[\text{CuCl}(\text{H}_2\text{O})_5]^+$, $[\text{CuCl}_2(\text{H}_2\text{O})_4]^0$, and $[\text{CuCl}_3(\text{H}_2\text{O})_3]^-$ in two spectral regions: 100-600 nm and 600-1050 nm. By increasing the number of chlorine ions (see $[\text{CuCl}_2(\text{H}_2\text{O})_4]^0$ and $[\text{CuCl}_3(\text{H}_2\text{O})_3]^-$), intense transitions appear in the 200-300 nm spectral region (TDDFT energies are unscaled). Such excitations can be assigned to single-particle transitions from *multiple* occupied molecular orbitals to the lowest unoccupied molecular orbital (LUMO). For both $[\text{CuCl}_2(\text{H}_2\text{O})_4]^0$ and $[\text{CuCl}_3(\text{H}_2\text{O})_3]^-$ the occupied molecular orbitals involved in the transitions can be

described as linear combinations of ligand-metal atomic orbitals of p- and d-type, as delocalized over the cluster. Partial contributions are also borrowed from the molecular orbitals of the closest interacting water molecules. The LUMO is instead confined in the tetrahedral plane as defined by the copper-chlorine ions and it involves d-type atomic orbitals of the metal combined also with the unoccupied orbitals of the closest interacting water molecules. Such transitions are of type LMCT and they can be assigned to the observed broad absorption band at around 250 nm, Figure 7.2.

For both $[\text{CuCl}_2(\text{H}_2\text{O})_4]^0$ and $[\text{CuCl}_3(\text{H}_2\text{O})_3]^-$ weak bands are also present around 400 nm and 500 nm. Such transitions are weak LMCT excitations involving various occupied molecular orbitals and the LUMO. We assigned these bands to the absorption shoulder (at 400 nm) observed in the experimental spectra by increasing the HCl concentration (Figure 7.2).

The cluster $[\text{CuCl}(\text{H}_2\text{O})_5]^+$ shows intense high energy electronic transitions (below 200 nm, see Figure 4b bottom left panel), however it does not show any prominent dipole allowed electronic transitions neither in the 250-300 nm region nor at lower energy.

Notably, a distinguished transition is computed around 900 nm (Figure 4b bottom right panel) for the $[\text{CuCl}_3(\text{H}_2\text{O})_3]^-$ cluster. Such excitation is characterized by a very low oscillator strength ($f = 5 \times 10^{-3}$) as compared to those of the 200-300 nm region ($f = 2 \times 10^{-1}$), and it can be described as a pure HOMO-LUMO transition, showing a clear LMCT character. The cluster, $[\text{CuCl}(\text{H}_2\text{O})_5]^+$ does not show such excitation, whereas the $[\text{CuCl}_2(\text{H}_2\text{O})_4]^0$ shows it though featuring a very low oscillator strength ($f < 10^{-3}$). Consequently, based on the model-clusters here considered, we can assign the NIR transitions around 900 nm (Figure 7.7) to Cu(II) clusters coordinated with an increased number of chloride ions, in particular to $[\text{CuCl}_3]^-$ species.

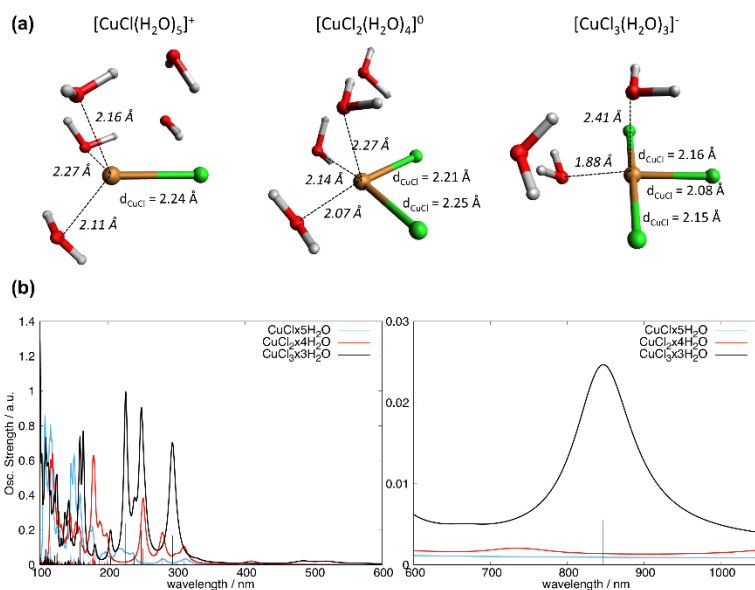


Figure 7.5. Top panel, (a): optimized $[\text{CuCl}(\text{H}_2\text{O})_5]^+$, $[\text{CuCl}_2(\text{H}_2\text{O})_4]^0$, and $[\text{CuCl}_3(\text{H}_2\text{O})_3]^-$ clusters, showing the relevant interatomic distances. Bottom panels, (b): Computed TD-DFT electronic transitions (sticks) and absorption spectra (solid lines, Lorentzian convolution) for $[\text{CuCl}(\text{H}_2\text{O})_5]^+$, $[\text{CuCl}_2(\text{H}_2\text{O})_4]^0$, and $[\text{CuCl}_3(\text{H}_2\text{O})_3]^-$ clusters (respectively, light-blue, red and black lines). Two spectral regions are reported: 100-600 nm and 600-1050 nm. TD-DFT energies are not scaled.

Cu(II) speciation dependence from Cu(II) concentration

As indicated in Equation (47), the copper speciation is more influenced by the chloride concentration instead of the copper concentration. In a 5 mM Cu(II) 6 M HCl solution, the deconvolution of the UV/Vis absorption spectrum (Figure 7.6a) shows a copper speciation comparable to that observed in a 50 mM CuCl_2 6 M HCl (speciation of copper in Figure 7.2).

Based on our deconvolution (Figure 7.2) and quantum-chemical (Figure 7.5) analyses, the absorption spectrum of Cu(II) chloride-rich solution can be described by an intense LMCT band in the UV region, and one in the NIR region. The latter corresponds to a broad band that is weakly influenced by the Cu(II) coordination. Furthermore, this transition is characteristic of the Cu(II) and is not visible in Cu(I) solution.

In order to monitor the Cu(II) concentration by the NIR transition, a wavelength λ_{abs} of 870 nm was selected as probing wavelength. Indeed, the NIR transition results useful for the Cu(II) monitoring because of the low molar extinction coefficient ($60\text{--}90 \text{ M}^{-1} \text{ cm}^{-1}$) that allow the absorbance measurements even in highly concentrated

solutions like those of practical interest in CuRFB. Voltabsorbometric experiments (Figures 7.6b and 7.6c) were carried out by recording CVs and absorption spectra simultaneously. The CV of the 5mM CuCl₂ solution reported in Figure 7.4b shows Nernstian reversibility, as evinced by the separation between the cathodic and the anodic peak potentials ($\Delta E < 2.22 RT/F$ that corresponds to 59 mV at 40°C) [14]. The current ratio $i_{pa}/i_{pc} = 0.96$ indicates a decent stability of the Cu(I) in the chloride environment.

The absorbance percentage in Figure 7.5b follow the variation of Cu(II) concentration. During the reduction step of the voltametric experiment, the concentration of Cu(II) decrease in favour of the Cu(I). Consequently, the absorbance percentage of the electrolyte decreases approaching zero. Then, re-oxidizing the Cu(I) to Cu(II), the absorbing species are regenerated, and the absorbance percentage returns at the initial value. The absorbance variation during CV is characterized by a hysteresis that can be related to the presence of metastable species.

In particular, the signal recorded during the first step is originated by the electrochemical reaction of cupric stable species producing metastable ones. Afterwards, the backward reaction involves the reactivity of a cuprous metastable species with facilitated oxidation. Thus, the absorbance profile of the backward scan of the cyclic voltammetry anticipates the forward reduction due to the metastability of the reduced species (Cu(I)). In Figure 7.6b is reported the absorbance percentage profile affected by hysteresis. The absorbance variation and hysteresis are related to all the copper chlorocomplexes present in the solution. The less stabilized complexes [CuCl₂]⁰, [CuCl]⁺ and Cu²⁺ contribute to an increased hysteresis in the absorbance profile (Figure 7.6c). Indeed, the signal increases in the forward scan of the voltammetry after the minimum (mostly Cu(I) in solution) and decrease in the backward scan after reaching the maximum (mostly Cu(II)).

The absorbance percentage at 385 nm, where only the most stabilized complexes absorb ([CuCl₃]⁻ and [CuCl₄]²⁻), displays a decreased hysteresis suggesting less interaction factors. Thus, a prevalence of high coordinated copper cation is recommended. The deconvolution of the LMCT band when the copper concentration is increased by ten times, from 5 to 50 mM, indicates an increased concentration of [CuCl_x]^{2-x} with $x < 3$. Analogously, the absorbance profile at 870 nm exhibits a stronger hysteresis imputable at the increased concentration of metastable species.

Figure 7.6c reports the CV of a 50 mM CuCl₂ solution in 6 M HCl and the absorbance values were recorded at 870 nm during the CV. The wavelength was selected close to the maximum of the absorption spectrum of the solution. Even if the CV is characterized by a i_{pa}/i_{pc} ratio closer to 1, the reported absorbance curve suffers an higher hysteresis. Hence, NIR spectroscopy results a suitable and sensible techniques to compare different complexes distributions. The hysteresis evidenced in the absorbance profile can be ascribed to the higher presence of less stabilized complexes (Cu²⁺/[CuCl]⁺/[CuCl₂]⁰) with respect to 5 mM CuCl₂ 6 M HCl solution.

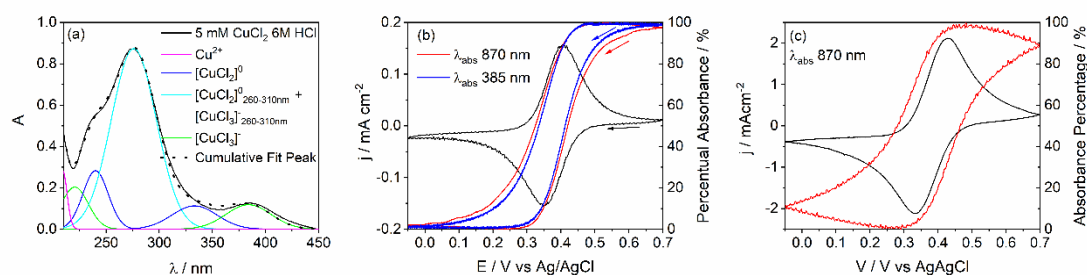


Figure 7.6. (a) UV/Vis spectra of 5 mM CuCl₂ 6 M HCl electrolyte in 50µm quartz cuvette, (b) CV at 2 mV s⁻¹ in 5 mM CuCl₂ 6 M HCl monitoring the absorbance at 385 nm and 870 nm. Optical path 1 cm, WE: Pt mesh, CE: Pt wire, RE: Ag/AgCl. (c) CV at 2 mV s⁻¹ in 50 mM CuCl₂ 6 M HCl monitoring the absorbance at 870 nm. Optical path 1 cm, WE: Pt mesh, CE: Pt wire, RE: Ag/AgCl.

To achieve the condition required for a highly performing redox flow battery, is mandatory to increase the copper concentration. It is important to consider that at high concentrations also other factors contributes to the electrochemical properties of the electrolyte.

Specifically, the salt solubility and diffusion coefficients are of paramount importance in these systems. The diffusion coefficients (D) of both Cu⁺ and Cu²⁺ range from 10⁻⁵ to 10⁻⁶ cm² s⁻¹, with D(Cu⁺) higher than D(Cu²⁺), the higher are the values the higher is the temperature [252]. However, the increase of the copper concentration, needed to RFB for delivering high energy, brings a tremendous increase of the ionic strength of the solution to maintain a suitable copper-to-halide ratio. In these conditions, the interactions between ions are stronger, and the decrease of water activity highly affects the physicochemical parameters like the viscosity and the density, as well as the conductivity and the diffusion coefficient [253,254].

The Cu(II) concentration was increased from 5 mM to 2 M in 6 M HCl solutions. In this range of concentrations, the absorbance has monitored in the NIR region taking advantage of the low molar extinction coefficient. The wide range of concentrations required different optical paths (OPs) for not having deviation from linearity of the absorbance with the increasing of Cu(II) concentration.

The 5 mM Cu(II) solution shows a maximum at 930 nm while the solutions with higher concentrations have the maximum at 920 nm. The small bathochromic shift suggests a decrease in the Cu(II) coordination as also confirmed by the chlorocomplexes distribution at different Cu(II) concentrations (Figure 7.3). Although there is a difference in magnitude, there is little variation in the distribution of complexes between the 5 mM and 50 mM. Similarly, the concentration increase by a further order of magnitude would not be expected to produce a much larger variation in the Cu(II) coordination. In fact, no differences are evidenced in the shape of the NIR absorption spectra (Figure 7.7a-d).

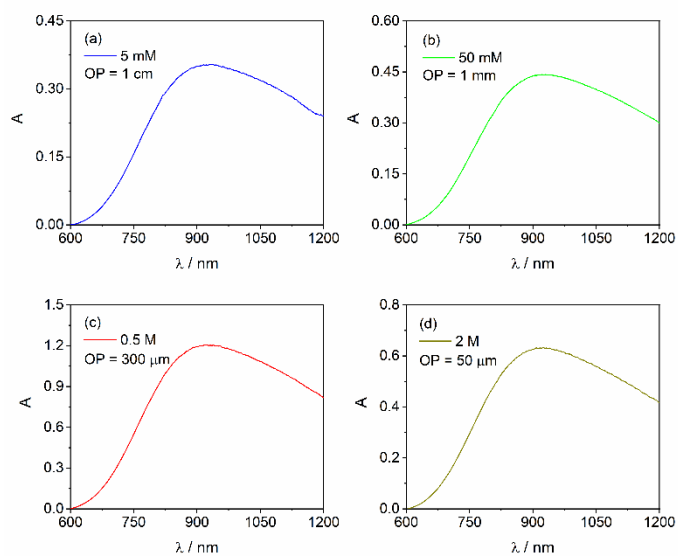


Figure 7.7. NIR spectra of (a) 5 mM CuCl₂ 6 M HCl electrolyte (OP 10 mm), (b) 50 mM CuCl₂ 6 M HCl electrolyte (OP 1 mm), (c) 0.5 M CuCl₂ 6 M HCl electrolyte (OP 300 μm), and (d) 2 M CuCl₂ 6 M HCl electrolyte (OP 50 μm) in quartz cuvette.

CuCl ₂	HCl	E ₊	E ₋	ΔE	(E ₊ +E ₋)/2	i _{pa}	i _{pc}	i _{pa} /i _{pc}	Ref
M	M	V vs. Ag/AgCl	V vs. Ag/AgCl	V	V vs. Ag/AgCl	mA cm ⁻²	mA cm ⁻²		
0.005	6	0.404	0.355	0.049	0.380	0.14	0.15	0.96	
0.05	6	0.427	0.334	0.093	0.380	2.12	2.05	1.03	
0.5	6	0.432	0.334	0.098	0.387	22.52	25.66	0.88	
2	6	0.465	0.343	0.120	0.403	151	-151	1.00	[27]

Table 2. Electrochemical properties on Pt at 0.01 V s⁻¹ and 40°C of copper electrolytes with different Cu(II) concentrations in the spectroelectrochemical cell, WE: Pt mesh, CE: Pt wire, RE: Ag/AgCl. Ref [253] is made in a three-electrode conventional cell. The relative errors of potential measurements are ca. 0.5% and those related to the current measurements are ca. 1%.

Table 7.2 summarizes the electrochemical information obtained by CVs in a spectroelectrochemical cell (showed in Figure 7.6a-b). The 2M CuCl₂ 6 M HCl electrolyte has been evaluated in three-electrode conventional cell in Ref [253]. Generally, both anodic and cathodic potentials increase, with a decrease in term of Nernstian reversibility, by increasing copper concentration. This could be related to the lower coordination of the copper as well as to other limitations due to the higher concentration (e.g., high ionic strength, high viscosity, lower diffusion coefficient etc.). As expected, the current densities increase with the raising of the concentration of the redox active species. In 0.5 M CuCl₂ 6 M HCl, the peak separation ΔE and the potentials are similar to the 50 mM solution suggesting a similar coordination of Cu(II).

- Conclusion

The optimization of new electrolytes plays a crucial role in developing a highly-performing CuRFB. In this system, the presence of chlorides as ligands is essential to stabilize the Cu(I)-to-Cu(II) process occurring in the positive compartment of the redox flow cell.

UV-Vis spectroscopy, supported by quantum-chemical modelling, allowed the investigation of the copper complexes distributions in diluted solutions from the analysis of the LMCT bands. Tight-binding-DFT and DFT calculations revealed the structure of water solvated copper-chloride clusters, showing that by increasing the

number of chlorine ions ($[\text{CuCl}(\text{H}_2\text{O})_5]^+$, $[\text{CuCl}_2(\text{H}_2\text{O})_4]^0$, and $[\text{CuCl}_3(\text{H}_2\text{O})_3]^-$), the amount of water molecules accessible to solvate the metal-ion centre decreases. Through TDDFT calculations the electronic transitions of the supramolecular clusters were characterized, identifying the LMCT excitations both in the UV-Vis and NIR regions. By increasing the number of chlorides, NIR LMCT transitions activate for Cu(II). The absorbance of Cu(II) at different wavelengths during CVs showed an hysteresis due to the different distribution of chlorocomplexes. The absorbance hysteresis in the NIR, at 870 nm where all the Cu(II) complexes absorb, is more marked than at 385 nm, i.e. in the absorbance region of the most stabilized complexes ($[\text{CuCl}_3]^-$ and $[\text{CuCl}_4]^{2-}$). Thus, highly coordinated copper cations are recommended to increase the reversibility of the Cu(I)/Cu(II) redox process. NIR bands allow the study of highly concentrated systems by tuning the optical path of the cell. Small shift in the NIR band and no shape variation suggest no significant differences in the Cu(II) speciation, among low and high concentrated solutions, also confirmed by comparing the electrochemical properties of 0.05 M and 0.5 M CuCl_2 solutions.

- CuRFB electrolyte

At this point, to achieve the condition required for the functioning of the redox flow battery is mandatory to increase the copper concentration. It is important to consider that other factors also contribute to the electrolyte's electrochemical properties at high concentrations. Specifically, their solubility and diffusion coefficients are of paramount in these systems. The diffusion coefficients of Cu^+ and Cu^{2+} range from 10^{-5} to $10^{-6} \text{ cm}^2 \text{ s}^{-1}$, with higher values for higher temperatures for Cu^+ than for Cu^{2+} [238]. However, the increase of the copper concentration needed to achieve high energy RFB brings a tremendous increase in the ionic strength of the solution to maintain a suitable copper-to-halide ratio. In these conditions, the interactions between ions are more intense, and the decrease of water activity strongly affects physicochemical parameters like viscosity and density, as well as conductivity and diffusion coefficient. Several studies have been carried out in concentrated solutions of copper halides in electrolyzer technology for hydrogen production to evaluate thermodynamic parameters [255,256, 257-259]. The diffusion coefficients of Cu(II) chlorocomplexes at 40°C in 2M CuCl_2 solutions were found to be in the range 10^{-5} to $10^{-7} \text{ cm}^2 \text{ s}^{-1}$ depending on the solution composition [223, 235, 260-261]. The lowest values were reached with the increase of

Cl⁻ concentration by changing the Cl⁻ source from HCl to CaCl₂ while maintaining the Cu:Cl ratio constant [260].

In order to achieve RFB technology with high performance and cycle life, the total concentration of copper and chloride in the electrolytes must be considered. Sanz et al. [262] demonstrated that a Cu:Cl ratio of 1:5 is mandatory in order to ensure salt solubility and cuprous cation stability by Cl-complexation. The choice of chloride sources as supporting electrolytes influences the physical properties of the copper-chloride electrolytes and the electrochemical properties of the Cu(II)/Cu(I) redox couple. Using HCl or CaCl₂ alone as supporting electrolyte limits the minimum temperature and the electrolyte concentration in which the solution does not show precipitates. On the contrary, solutions containing both HCl and CaCl₂ are stable without precipitates over a wide range of temperatures, from 5 to 70 °C, affording their practical application in the CuRFB [235, 260, 262].

In this section, I report and discuss the results of physicochemical and electrochemical characterization of 2M solutions of Cu(I) and Cu(II) with copper-to-chloride ratios of 1:5 and 1:7, where the concentration and the counter-ion of the chloride complexing agent are varied. The cell operating temperature is maintained between 40°C and 60°C to reproduce the real use conditions of RFB, where low temperatures are preferable to reduce system heating costs. The low temperature range requires that the state of charge (SoC) never exceeds 90% to avoid CuCl₂ precipitation. In addition, in concentrated CuCl solutions the pH must be controlled to allow the total solubilization of the salt. For this reason, the HCl concentration was maintained 6 M.

- Experimental section

For the solutions CuCl₂ (99.99 + %, Sigma Aldrich), CuCl (≥99.995% trace metal basis, Sigma Aldrich, HCl (37%, Sigma-Aldrich), CaCl₂ (≥99%, ACS reagent, Sigma Aldrich), NH₄Cl (99.5, Sigma Aldrich) and H₃PO₄ (≥85 wt. % solution in water, ACS reagent, Sigma Aldrich) were used. After complete dissolution in deionized water, the solutions were deaerated with Ar for ten minutes and sealed. The solution composition is given in the tables in the results and discussion section, and the solutions are indicated with a number. Conductivity tests were carried out with Sension + EC71 Hach Instruments, viscosity tests were performed with SVM 3000 Stabinger Anton Paar and density was measured by DMA 4500 Anton Paar at different temperatures.

Electrochemical tests were carried out under Ar atmosphere in a conventional V-cell, kept in a water bath at 40°C, with a Voltalab PGZ301 (Radiometer Copenhagen, Denmark). The cell contained 10 mL solution. A glassy carbon (GC, 3 mm diameter) was used as working electrode, a graphite rod (6 mm diameter, 15 cm length, Gamry) as counter electrode and a saturated calomel electrode (SCE, AMEL, 303/SCG/6J) as reference electrode. Cyclic voltammetry (CVs) studies were carried out at 40°C at different scan rates, from 0.1 to 0.005 V s⁻¹. CVs in solutions containing NH₄Cl were performed at 60°C. The voltammograms are not live-IR corrected. Scanning Electron Microscopy (SEM) images were collected with an FEI Quanta 650 Scanning Electron Microscope (Oregon, USA). Spectrophotometric tests were performed with a Perkin Elmer Lambda 19 in quartz cells with an optical path length of 50 μm in the ultraviolet-visible (UV-Vis) region and 500 μm in the near infrared (NIR) region.

- Results and discussions

Solutions with only CuCl or CuCl₂ as copper salt, and solutions with copper concentration shared between CuCl and CuCl₂ to simulate the 0%, 100% and 50% SoC, with Cu:Cl ratios 1:5 and 1:7, were selected and analyzed with a view to CuRFB technology. While physicochemical parameters have an impact on the energy consumption of CuRFB hydraulic system, electrochemical properties are fundamental to determine the reaction kinetics and overall battery performance.

Table 7.3 summarizes the composition of the solutions 1-6 (from here on indicated with a number) containing CaCl₂, the conductivity, the viscosity and the density at 40°C, and Figure 7.8 shows the above parameters at different temperatures.

N	CuCl ₂ M	CuCl M	CaCl ₂ M	HCl M	Cu: Cl	σ mS cm ⁻¹	η mPa s	ρ kg m ⁻³
1	/	2	1	6	1:5	634	1.41	1312
2	1	1	0.5	6	1:5	605	1.78	1291
3	2	/	/	6	1:5	645	1.38	1308
4	/	2	3	6	1:7	364	2.80	1442
5	1	1	2.5	6	1:7	359	2.93	1431
6	2	/	2	6	1:7	417	2.10	1404

Table 7.3. Physicochemical properties at 40°C of copper electrolytes with different concentration of copper and calcium chloride with Cu:Cl ratios of 1:5 and 1:7. The relative errors of conductivity, viscosity and density measurements are 0.5%, 0.35% and 0.1%, respectively.

Solutions with low Cl⁻ concentration (1-3, Cu:Cl ratio 1:5) show higher conductivity (Figure 7.8a) than the solutions with high Cl⁻ concentration (4-6, Cu:Cl ratio 1:7). The addition of increasing amount of CaCl₂ causes a significant increase in viscosity and density (Figures 7.8b-c). The solution 6 is the best performing with Cu:Cl 1:7 ratio, according to the lower concentration of CaCl₂ than solutions 4 and 5.

Figure 7.9 shows the CVs of the 1-6 solutions carried out at 40°C and 0.1 V s⁻¹. Solutions 1-3 (Figure 7.9a) show lower separation between the anodic and cathodic peaks (ΔE) and the highest reversibility with respect to the 4-6 solutions (Figure 7.9b). In particular, the reversibility is higher for solution 3, without CaCl₂, and for the mixed Cu⁺/Cu²⁺ solution 2. For Cu(I) and mixed Cu(I)/Cu(II) electrolytes, the addition of more calcium chloride increases the ionic strength and the conductivity of the solutions and does not lead to a positive shift of the potentials.

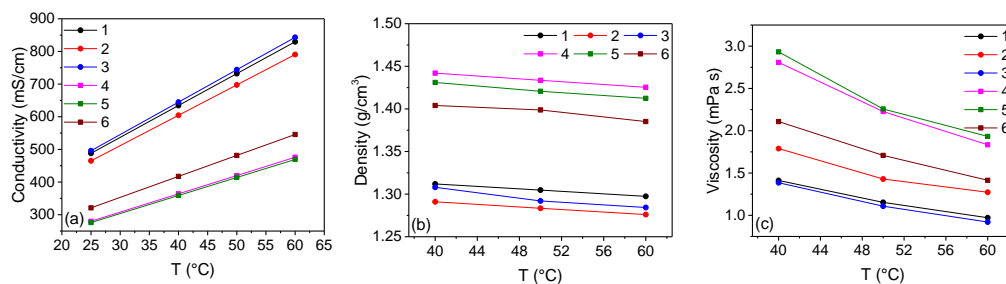


Figure 7.8. Conductivity (a), density (b), and viscosity (c) of copper electrolytes with Cu:Cl ratios of 1:5 (solutions 1-3) and 1:7 (solutions 4-6) at different temperatures. The solution total copper and HCl concentrations were 2 M and 6 M, respectively. Solution compositions are in Table 7.3.

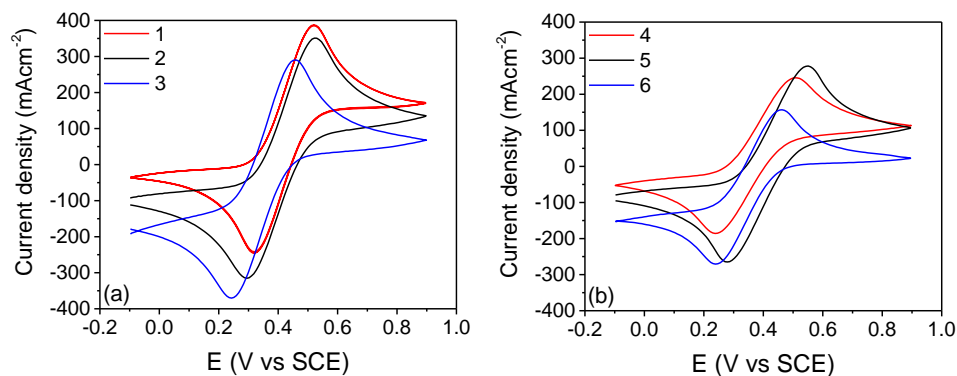


Figure 7.9. CVs of GC electrode in solutions with different concentrations of copper and calcium chloride with Cu:Cl ratio 1:5 (a) and 1:7 (b) at 0.1 V s^{-1} and 40°C .

Our systems do not display a Nernstian reversibility, given the high separation between the cathodic and the anodic peak potentials (ΔE), higher than 2.22 RT/F (59 mV at 40°C) [14]. However, we focus our attention on the i_{pa}/i_{pc} ratio that for a totally reversible system must be 1 independently of the scan rate [14]. This denotes if an active species can be subsequently reduced and oxidized.

Data from CVs are collected in Table 7.4 that reports the open circuit potential vs. SCE (OCP), the peak potentials vs. saturated calomel electrode (SCE) of the anodic and cathodic processes (E_+ and E_-), the separation between the peak potentials (ΔE), the potential of the redox couple $\text{Cu}^+/\text{Cu}^{2+}$ calculated by the half-sum of the peak potentials, the anodic and cathodic peak current densities (i_{pa} and i_{pc}) and their ratios.

N	OCP V vs. SCE	E ₊ V vs. SCE	E ₋ V vs. SCE	ΔE V	(E ₊ +E ₋)/2 V	i _{pa} mA cm ⁻²	i _{pc} mA cm ⁻²	i _{pa} /i _{pc}
1	0.309	0.483	0.347	0.136	0.415	149	-171	0.87
2	0.409	0.469	0.340	0.129	0.405	162	-163	0.99
3	0.622	0.419	0.299	0.120	0.359	151	-151	1
4	0.302	0.447	0.296	0.151	0.372	112	-107	1.05
5	0.417	0.481	0.340	0.141	0.411	117	-118	0.99
6	0.525	0.430	0.293	0.137	0.362	107	-113	0.95

Table 7.4. Electrochemical properties at 40°C of copper electrolytes with different concentrations of copper and calcium chloride for Cu:Cl ratios of 1:5 (solutions 1-3) and 1:7 (solutions 4-6). The relative errors of potential measurements are ca. 0.5% and those related to the current measurements are ca. 1%.

The combination of HCl with CaCl₂ with Cu:Cl ratio 1:5 seems the most promising in terms of conductivity, viscosity and density as positive copper-chloride electrolytes. However, considering that the formation constant for CuCl_x^{2-x} depends on [Cl⁻], the chloride concentration plays a crucial role in the copper speciation. Adding calcium chloride, the chloride concentration, i.e the availability of complexing agents for copper, should be increased. The (E₊+E₋)/2 does not change significantly when the chloride concentration increases. In high concentrated solution, calcium chloride is not completely dissociated [263] and theoretical work [264] shown that Ca²⁺ can coordinate chloride to form chlorocomplexes even if the [CaCl_x]^{2-x} (x = 4-6) clusters can become metastable when hydration is considered. The high ionic strength of the solution used imply a low water content for a complete solvation of calcium.

Hence, for increasing the chlorides availability in copper solutions and improve the solutions' chemical-physical properties, two main approaches are outlined. The former is the use of a different chloride source, CaCl₂ concentration representing the critical factor in terms of conductivity and viscosity as shown for solutions 4-6. The latter is the use of an additive able to interact with Ca²⁺ and, in turn, to weaken the interaction between Ca²⁺ and Cl⁻.

Solutions containing NH₄Cl as chloride source.

The chloride salts and additives selection for CuRFB technology is not very wide because of solubility and overall sustainability. CaCl₂ was the preferred source of chloride ions in previous works due to its high solubility, low cost, and availability, being also a bi-equivalent source of chloride. However, a high amount of calcium chloride leads to increased viscosity and density, which adversely impacts the electrolyte hydraulic circuit of the CuRFB, and to a decreased conductivity.

Among the different chloride salt, NH₄Cl shows high solubility in water and low cost. The solutions 7 and 8 were prepared by replacing calcium chloride with ammonium chloride, as shown in Table 7.5, and Figure 7.10 displays conductivity, density and viscosity at different temperature. The conductivity (Figure 10a) of the solutions 7 and 8 are significantly higher than that of the corresponding solution with CaCl₂ (solutions 1 and 2). The density (Figure 7.10b) and the viscosity (Figure 7.10c) values are comparable and even lower than those of the solutions 1 and 2 (Table 7.3).

N	T	CuCl ₂	CuCl	CaCl ₂	HCl	NH ₄ Cl	Cu: Cl	σ	η	ρ
	°C	M	M	M	M	M		mS cm ⁻¹	mPa s	kg m ⁻³
7a	40	/	2	/	6	2	1:5	812	1.08	1296
7b	60	/	2	/	6	2	1:5	1003	0.76	1283
8a	40	1	1	/	6	1	1:5	819	1.33	1250
8b	60	1	1	/	6	1	1:5	1012	0.83	1236

Table 7.5. Physicochemical properties at 40°C and 60°C of copper electrolytes with different concentration of copper and ammonium chloride with Cu:Cl ratio of 1:5. The relative errors of conductivity, viscosity and density measurements are 0.5%, 0.35% and 0.1%, respectively.

The CVs reported in Figure 7.11a and 7.11b for the solutions 7a and 8a at 40°C show a resistive shape due to crystal precipitation on the electrode surface during the reduction. CVs become more reversible by increasing the temperature up to 60°C. Indeed, the ΔE decreases both in the Cu(I) and in the Cu(I)/Cu(II) solutions. Additionally, by increasing the temperature, the potentials shift toward positive values, and i_{pa}/i_{pc} ratio becomes closer to 1 (especially for solution 7), as shown in the Table 7.6. From the electrochemical results, it is evident that, despite the good

physicochemical properties, the solutions with NH_4Cl are not preferable to those with CaCl_2 in the positive half-cell of the CuRFB. On the other hand, looking at the deposition-stripping processes occurring in the negative half-cell, the addition of ammonium chloride to the electrolytes greatly improves the coulombic efficiency ($\text{CE}_\%$). CVs in the potential range of copper deposition-stripping in the electrolyte with calcium chloride (Figure 7.11c) revealed a $\text{CE}_\%$ around 50% on GC electrode. After 10 consecutive cycles, the potential at which the copper deposition starts decreases from 0.325 V to 0.300 V vs SCE due to the incomplete stripping of copper deposit. Adding NH_4Cl to the electrolyte (Figure 7.11d), the $\text{CE}_\%$ increases to 85% and the overpotential of the copper deposition results were unvaried upon cycling. The addition of NH_4Cl to the negative half-cell electrolyte leads to increased reversibility of the negative process by restoring the electrode surface after the copper stripping. It is worth noting that ammonium chloride is used in metalworks for polishing metal surfaces by metal oxides [265].

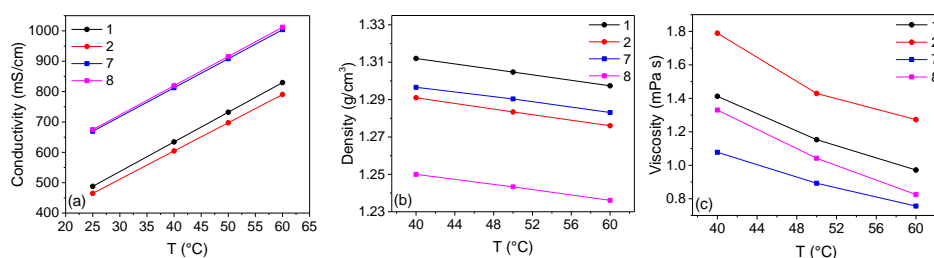


Figure 7.10. Conductivity (a), density (b), and viscosity (c) of copper electrolytes with Cu:Cl ratio of 1:5 (solutions 7 and 8, see Table 3) at different temperatures. The total copper and HCl concentrations were 2 M and 6 M, respectively.

Figures 7.11e and 7.11f show the SEM images of copper deposited on Sigracell FR10 graphite at 80 mA cm^{-2} for 1200 s at $60 \text{ }^\circ\text{C}$ in solution 1 and solution 7b. The images show that smaller grain copper deposits are achieved from the calcium chloride (solution 1) while a larger grain deposit is observed from the ammonium chloride (solution 7b) based electrolyte. The deposits from solution 1 also appear to have more isolated (some triangular type) crystalline features which could be detached from the surface during dissolution without contributing to the efficiency of the reaction. The more coherent deposit from solution 7b may explain why a significantly higher $\text{CE}_\%$ is attained in that electrolyte.

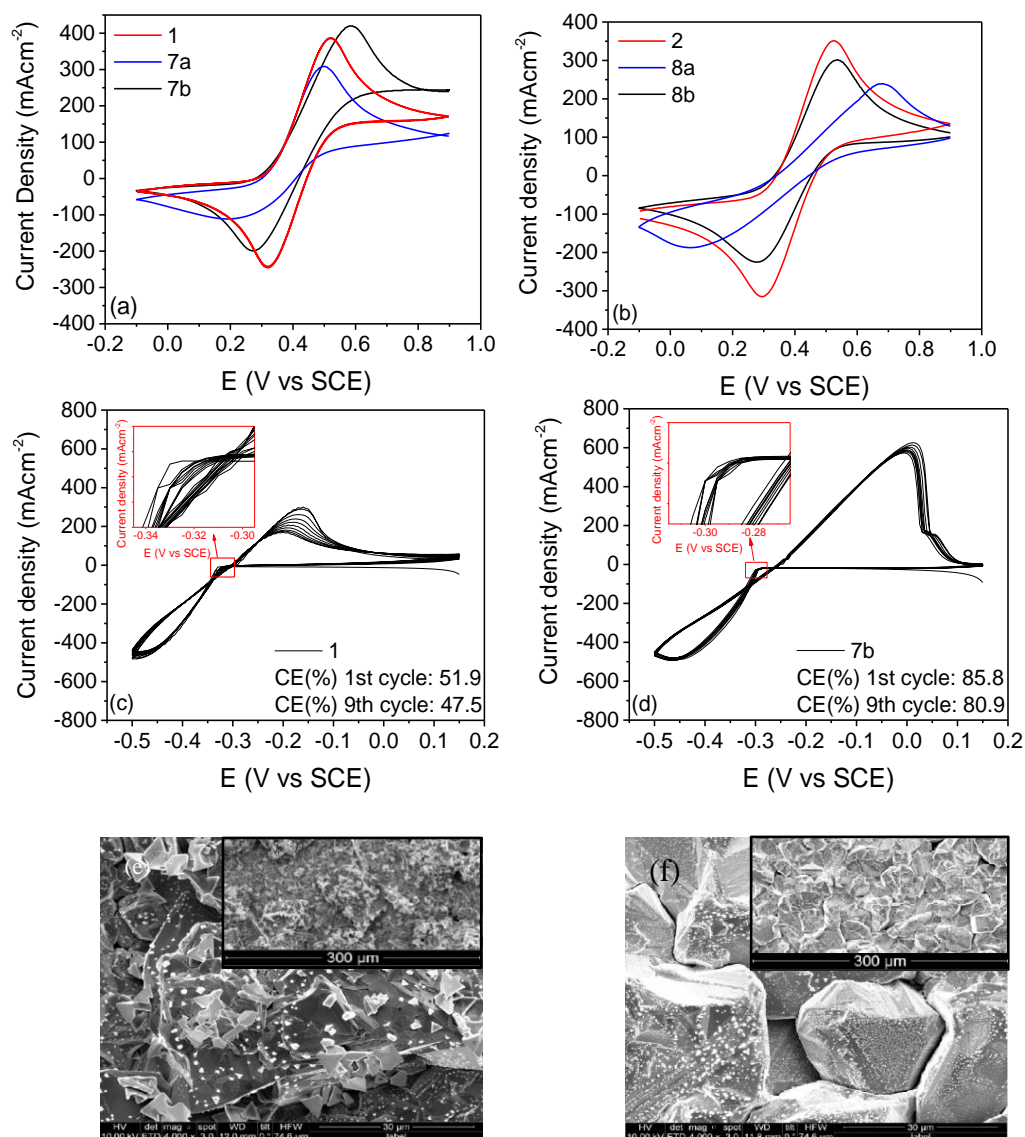


Figure 7.11. CVs of GC electrode at 0.1 V s^{-1} of (a) the solution 1, 7 and (b) 2, 8 in which 1,2, 7a and 8a were carried out at 40°C , while 7b and 8b were at 60°C ; Cu deposition stripping at 0.1 V s^{-1} and 60°C of (c) solution 1 and (d) solution 7b; SEM images (4000x) of copper deposited at 60°C in solution 1 (e) and in solution 7b (f). In the inset are the images at 400x magnification.

N	T	OCP	E ₊	E ₋	ΔE	(E ₊ +E ₋)/2	i _{pa}	i _{pc}	i _{pa} /i _{pc}
	°C	V vs SCE	V vs SCE	V vs SCE	V	V	mA/cm ⁻²	mAcm ⁻²	
7a	40	0.324	0.548	0.283	0.265	0.416	150	-126	1.19
7b	60	0.324	0.550	0.309	0.241	0.430	211	-216	0.98
8a	40	0.375	0.528	0.270	0.258	0.399	125	-143	0.87
8b	60	0.380	0.484	0.326	0.158	0.405	146	-170	0.86

Table 7.6. Electrochemical properties at 40°C and 60°C of copper electrolytes with different concentration of copper and NH₄Cl with a Cu:Cl ratio of 1:5. The relative errors of potential measurements are ca. 0.5% and those related to the current measurements are ca. 1%.

Table 7.6 shows the electrochemical parameters of the solutions 7 and 8 at 40°C and 60°C.

Diffusion coefficients were evaluated for selected solutions by chronoamperometric techniques at a potential of (i_{pa} + 0.1 V) vs SCE for Cu(I) oxidation or (i_{pc} - 0.1 V) vs SCE for Cu(II) reduction. The tests were carried out with a GC working electrode (3 mm diameter) in order to avoid contribution of edge effects originating from radial contributions [268].

Figure 7.12 shows the chronoamperometric curves of the solutions 1, 4 and 7a at 40°C and the fitting of the curves i vs. $t^{-1/2}$ according to the Cottrell equation in a time range from 0.5 s to 2 s. As shown in Figure 7.12b, solution 4 has the lowest diffusion coefficient, even lower than solution 1. The presence of two cations with interconnected equilibria of complexation with the same ligand can decrease the coordination. Less coordinated complexes can show higher diffusion coefficients due to a smaller radius. However, increasing the concentration of calcium chloride, i.e. increasing the Cu: Cl ratio from 1:5 to 1:7, the diffusion coefficients decrease. The increase of the ionic strength of the solutions decreases the mobility of the ions. As previously discussed, increasing the Cu: Cl ratio from 1:5 to 1: 7 is not beneficial for electrochemical performance. Substituting the CaCl₂ with NH₄Cl, the diffusion coefficient increases in consequence of the lower viscosity of solution 7a with respect to solution 1, given that NH₄⁺ is a water destructuring ion. This confirms the suitability of ammonium chloride as a chloride source for the negative half-cell.

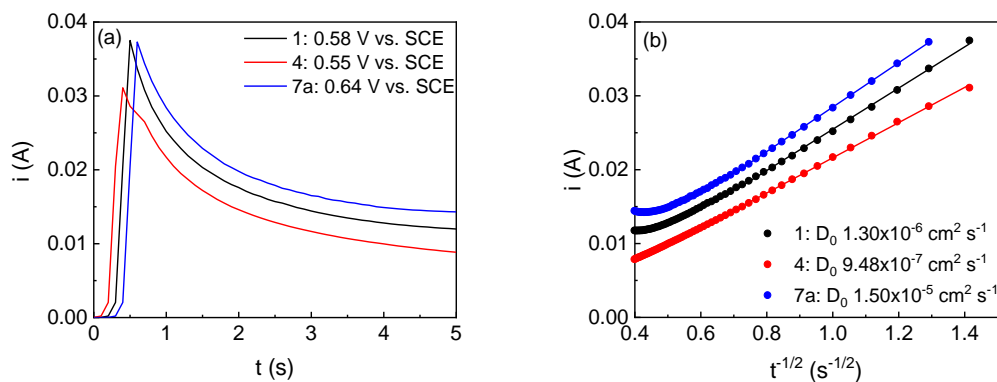


Figure 7.12. (a) Chronoamperometric curves at ($i_{pa} + 0.1$ V vs SCE) of solution 1, 4 and 7. (b) fitting of the curves i vs. $t^{-1/2}$ according to the Cottrell equation in a time range from 0.5 s to 2 s (b).

Solutions containing H_3PO_4 as additive

Additives including big anions can influence Cu^+ and Ca^{2+} chloro-complexes equilibria. As an example, Ca^{2+} and PO_4^{3-} interact and $CaCl_2$ and H_3PO_4 are used as precursors for the formation of calcium phosphates [267]. For this reason, orthophosphoric acid can be used to decrease the calcium chloride coordination. Ca^{2+} chloro-complexes are destabilized, and the “free” Cl^- could shift the equilibrium of copper complex formation toward more coordinated species. Additionally, the introduction of protons instead of other cations could be favourable for the conductivity and to avoid further foreign species in the electrolyte.

Two solutions containing H_3PO_4 have been prepared: solution 10, where H_3PO_4 was added to formulation 1 (0% SoC), and solution 11, in which both $CuCl$ and $CuCl_2$ were present and $CaCl_2$ has a concentration 1 M for a better comparison with solutions 1 and 10. Considering that, in the RFB system, the SoC is limited at the 90%, the mixed Cu^+/Cu^{2+} solutions prepared should mimic the 90% SoC. In order to investigate the effect of phosphate on calcium chloride dissociation, solution 9 with the same composition of solution 11 without H_3PO_4 was also prepared. Table 7.7 reports the physicochemical parameters of these solutions with and without H_3PO_4 additive.

N	CuCl ₂ M	CuCl M	CaCl ₂ M	HCl M	H ₃ PO ₄ M	Cu: Cl	σ mS cm ⁻¹	η mPa s	ρ kg m ⁻³
1	/	2	1	6	/	1:5	634	1.41	1312
9	1.8	0.2	1	6	/	1:5.9	569	1.73	1347
10	/	2	1	6	1	1:5	714	1.62	1300
11	1.8	0.2	1	6	1	1:5.9	508	1.66	1334

Table 7.7. Physico-chemical properties at 40°C of copper electrolytes with different concentration of copper and H₃PO₄ with Cu:Cl ratio of 1:5. The relative errors of conductivity, viscosity and density measurements are 0.5%, 0.35% and 0.1%, respectively.

Figure 7.13 summarizes the results of conductivity, density, and viscosity at different temperature of the solution reported in Table 7.7.

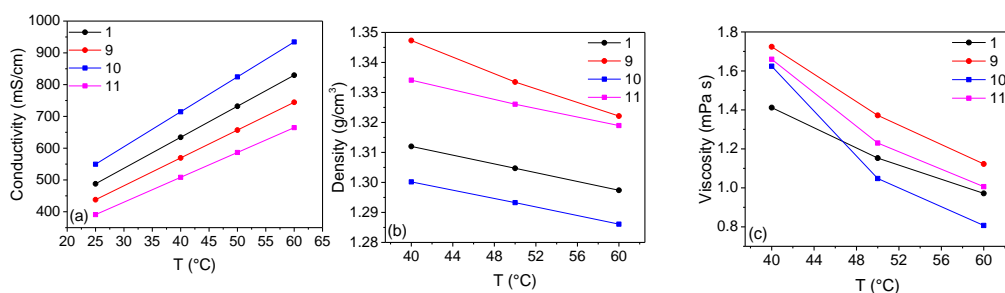


Figure 7.13. Conductivity (a), density (b), and viscosity (c) of copper electrolytes with Cu:Cl ratio of 1:5 (solutions 1 and 9 without H₃PO₄, and solution 10 and 11, with H₃PO₄) at different temperatures. The total copper and HCl concentrations were 2 M and 6 M, respectively.

Figure 7.13 shows that the addition of phosphoric acid to formulation 1 (solution 10) leads to a conductivity increase, due to the increase in H₃O⁺ concentration, despite a higher viscosity. The parameters of solutions show the opposite trend for solutions 9 and 11, with a decreased conductivity for solution 11 and a slight decrease of density and viscosity with respect to solution 9. The latter solutions have higher ionic strength (Cu: Cl ratio of 1:5.9) than the solutions 1 and 10, and the addition of phosphoric acid further increases it. In this case, presumably, the conduction mechanism of H₃O⁺ is hindered by the increase of Cl⁻ concentration, being Cl⁻ a water-structuring ion.

Table 7.8 reports the electrochemical properties of the solutions of Table 7.7 and Figure 7.14 displays the CVs at 40°C. For the solution of Cu(I) (Figure 7.14a), the addition of orthophosphoric acid increases and improve the reversibility of the CV (i_{pa}/i_{pc} ratio), with the potential of the redox couple shifted towards less positive values. In highly concentrated Cu(II) electrolytes, the reversibility results increased (Figure 7.14b) despite the lower conductivity of the solution 11 with respect to 9. The ΔE reduces from 268 mV to 167 mV and, the i_{pa}/i_{pc} ratio approaches 1.

In solution with a chloride concentration higher than 5M, Cu(I) is preferentially present as the most chloro-coordinated species $CuCl_3^{2-}$ [230]. The increased availability of chloride ligands is more effective for Cu(II)-rich electrolytes. In the same condition, Cu(II) chlorocomplexes favour the lower coordination number, and changes in chloride concentration, even at high ligand concentration, can affect the copper chlorocomplexes distribution [268]. Hence, Cu(I) is less affected by a higher amount of uncomplexed chloride anions than Cu(II). In oxidized solutions, the chloride released due to the presence of phosphoric acid can coordinate the Cu(II) cations leading to a more reversible and electrochemically stable redox couple.

N	OCP V vs SCE	E_+ V vs SCE	E_- V vs SCE	ΔE V	$(E_+ + E_-)/2$ V	i_{pa} mA cm ⁻²	i_{pc} mA cm ⁻²	i_{pa}/i_{pc}
1	0.309	0.483	0.347	0.136	0.415	149	-171	0.87
9	0.490	0.477	0.209	0.268	0.343	127	-120	1.06
10	0.297	0.473	0.309	0.164	0.391	142	-154	0.92
11	0.427	0.444	0.277	0.167	0.361	125	-120	1.04

Table 7.8. Electrochemical properties at 40°C of copper electrolytes with $CaCl_2$, with and without H_3PO_4 with a Cu:Cl ratio of 1:5. The relative errors of potential measurements are ca. 0.5% and those related to the current measurements are ca. 1%.

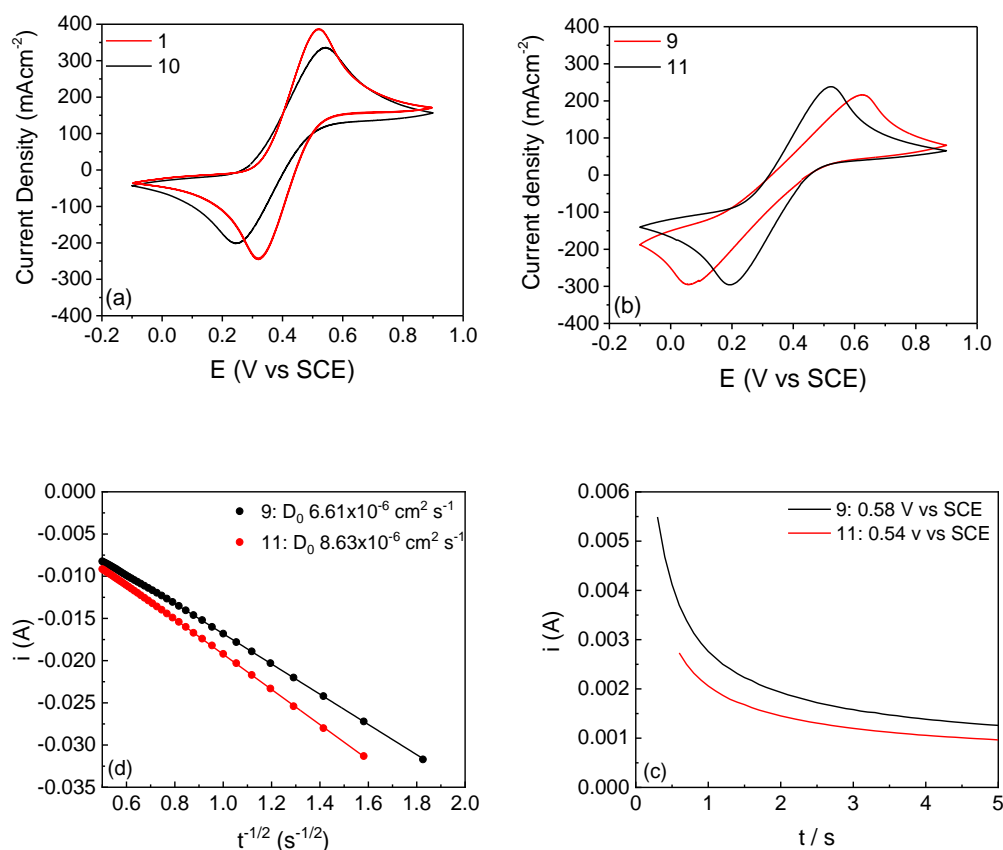


Figure 7.14. CVs of GC electrode at 0.1 V s^{-1} and 40°C in solutions with different concentrations of copper and calcium chloride with and without H_3PO_4 (a) at 0% SoC and (b) at 90% SoC. (c) Chronoamperometric curves of Cu(II) at ($i_{\text{pc}} - 0.1 \text{ V}$) vs SCE of 9 and 11 solutions (0% SoC), (d) fitting of the curves i vs. $t^{-1/2}$ according to the Cottrell equation in a time range from 0.5 s to 2 s.

In the solution 9 with 1.8 M Cu(II), the diffusion coefficient obtained from Cottrell equation (Figure 7.14c-d) increases with the addition of 1M H_3PO_4 even if the conductivity of the solution decreases from 569 mS cm^{-1} to 508 mS cm^{-1} as a consequence of the higher ionic strength. As observed in CV measurements, H_3PO_4 is more effective on the Cu(II) chemical environment with respect to the Cu(I). Hence, Cu(II) diffusion coefficient varies from $6.6 \cdot 10^{-6} \text{ cm}^2 \text{ s}^{-1}$ to $8.6 \cdot 10^{-6} \text{ cm}^2 \text{ s}^{-1}$.

Absorption spectroscopy of Cu(II) halide-complexes has been intensively discussed in Section 7.2

In concentrated solution, the LMCT is too intense, hence, changes in the coordination sphere can be established from the MC band. From the crystal field theory, ligands modify the ligand-field splitting parameter Δ that determines the energy of the MC

transition. The presence of chloride ligands in the copper coordination sphere reduces the Δ and red shift of the MC band with respect to aquo-complex [238].

Figure 7.15a reports the absorption spectrum in the Vis/NIR region of the high concentrated Cu(II)/Cu(I) solution with the unvaried concentration of CaCl₂, i.e. solution 9 and 11.

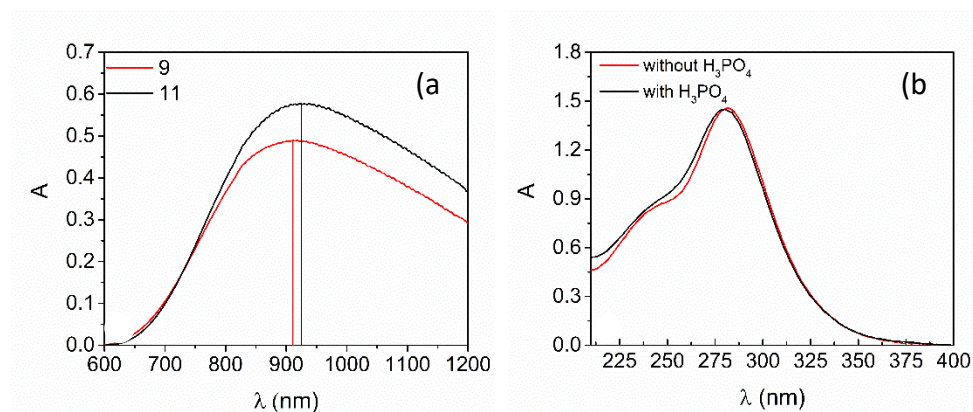


Figure 7.15. Absorption spectra: (a) MC band of concentrated 9 and 11 solutions with optical path of 50 μm and (b) LMCT band of 10 mM CuCl₂, 10 mM CaCl₂, 30 mM HCl with and without 10 mM H₃PO₄ (optical path 500 μm).

The addition of H₃PO₄ leads to a red shift of MC from 925 nm to 910 nm. According to deconvolution of the MC band [239], this shift can be interpreted as a decreasing of low chloride-coordinated complexes and increasing of the component for CuCl₃⁻. Differences in absorbance are justified by the different molar extinction coefficients of the complexes involved. On the other hand, phosphate anions do not enter the inner coordination sphere of the copper [269] as demonstrated by spectra in Figure 7.15b of a diluted solution (200 times) with the same composition of solutions 9 and 11. These spectra show the LMCT bands with the unvaried presence of the CuCl₃⁻.

In order to summarize the effect of calcium chloride as supporting electrolytes solution with a Cu:Cl ratio of 1:5 and 1:7 were tested. Solutions with 1:5 Cu:Cl ratio display the best performance. The substitution of calcium chloride with ammonium chloride increases the conductivity up to 1000 mS cm⁻¹ without improving the Cu(I)/Cu(II) couple redox processes. On the other hand, the addition of NH₄Cl to Cu(I) electrolyte leads to improved reversibility of the copper deposition-stripping processes with CE_% reaching 80%.

The interaction of phosphate with Ca²⁺ suggested that H₃PO₄ could be a viable additive to decrease the complexation of calcium with chloride and to improve Cu(II) chloro-

complexes stability. UV-VIS spectroscopy demonstrates that phosphate does not take part in the coordination sphere of Cu(II). The addition of H₃PO₄ in concentrated solution leads to a shift in the distribution of copper chlorocomplexes toward more coordinated species visible in the NIR absorption spectrum. Electrochemically, the addition of phosphoric acid is not effective on Cu(I)-rich electrolyte due to the lower amount of chloride required for coordination. The increased availability of chloride anions in solution stabilizes the Cu(II)-rich solution and leads to increased reversibility of the Cu(II)/Cu(I) redox process and higher Cu(II) diffusion coefficients.

7.4. Cell components

Optimizing the cell components is required to overcome the limitation of RBF. Most work usually involves the application of different electrode materials and the optimization of the membrane. As expected, the standard or hybrid configuration of the system plays a crucial role in selecting the electrode components. In a hybrid configuration, the negative electrode surface should be metallophilic enough. This guarantees homogenous nucleation of the metal, limiting the dendrites formation. On the other hand, the positive electrode must be adapted to the chemistry of the RFB, guaranteeing rapid kinetics and reversibility. Usually, for the electrodes are used carbonaceous materials such as low-cost carbon-polymer composites [270], graphite and carbon felts[130], cloth[271], and paper[272].

In flow batteries, the essential function of the membrane is to prevent the cross-over of redox couples involved in electrode reactions while allowing the transfer of charge carriers across the membrane at a high rate to complete the electric circuit.

In CuRFBs, Sanz et al. [273] achieved an energy density of 20 Wh dm⁻³, using a 2 M copper solution. However, coulombic and voltage efficiencies remained relatively low (coulombic efficiency: c.a. < 90%; voltage efficiency: c.a 60%). The main problems of the reported system regard the permeation of the Cu(II) through the separator and high electrode overpotentials of two-dimensional planar electrodes.

7.4.1. Negative electrode

In a hybrid configuration, the cell's total capacity risk is limited by the maximum amount of metal deposited and the metal adhesion on the electrode. In order to

overcome this limitation, 2D and 3D electrode structures were evaluated as negative electrodes. As previously reported [273], stainless steel and titanium showed higher coulombic efficiencies than carbonaceous substrates. However, the employment of hydrochloric acid as a supporting electrolyte causes the corrosion of these metals and dissolution. The electrolyte contamination can affect the copper deposition, forming alloys.

Copper substrates represent a promising alternative to reduce the overpotential of the deposition/stripping process thanks to their excellent electrical conductivity and high affinity to copper ions. For the negative half-cell, different copper morphologies are studied to evaluate the best condition of nucleation and stripping. A tri-dimensional structure is reported to encourage regulated plating like copper mesh.

For all electrode materials the polarizations of all electrode materials tend to increase at higher charge/discharge current densities. Among these materials, the three-dimensional materials tended to show a less potential drop, which can be attributed to their larger surface areas. Reported results have shown deposition peak current densities of three-dimensional electrodes about 16.7 and 7.8 times higher than those of planar carbon and copper electrodes. Activation overpotential can be evaluated from Tafel or Butler-Volmer equations depending on the overpotential magnitude. At 90 mA cm⁻², the resulting activation overpotential values are 254 mV for planar copper, 196 mV for copper mesh, 155 mV for copper foam, and 31 mV for copper fibres. The activation overpotential reduction is mainly attributed to the higher surface area, leading to a lower local current density at the electrode surfaces.

7.4.2. Positive electrode

As reported for negative electrodes, polarization losses (activation, ohmic and concentration) must be minimized. Several forms of carbonaceous materials have been studied over the last decades as graphite [274] or carbon felts [130], carbon fibers [275], carbon cloth [271], carbon paper, carbon nanotubes (CNTs) [272], thermal, hydroxylated and acid treated graphite and carbon-polymer composite materials, iridium-modified (Ir-modified) carbon felt [276] and graphene oxide (GNO) nanoplatelets [272].

Standard electrodes in RFBs are porous carbons. However, due to their low mechanical properties, they are used in the form of composites with polymer binders and conductive particles as negative electrodes for LIBs [277].

For example, in VRFBs, the carbon morphology in the electrode greatly influences the redox reactions especially in terms of the heterogeneous electrode rate constant (Table 7.9).

Material	Redox couple	k_0 cm s ⁻¹	D cm ² s ⁻¹
GC (glassy carbon)	V ³⁺ /V ²⁺	1.7 · 10 ⁻⁵	1.41 · 10 ⁻⁶
PG (pyrolytic graphite or PG in the c-plane)	V ³⁺ /V ²⁺	5.5 · 10 ⁻⁴	4.0 · 10 ⁻⁶
PFC (plastic formed carbon)	V ³⁺ /V ²⁺	5.3 · 10 ⁻⁴	2.4 · 10 ⁻⁶
CP (carbon paper)	V ³⁺ /V ²⁺	1.1 · 10 ⁻³	4.0 · 10 ⁻⁶
GC	VO ₂ ⁺ /VO ²⁺	7.5 · 10 ⁻⁴	1.4 · 10 ⁻⁶
PG (c-plane)	VO ₂ ⁺ /VO ²⁺	1.3 · 10 ⁻⁴	2.4 · 10 ⁻⁶
PFC	VO ₂ ⁺ /VO ²⁺	8.5 · 10 ⁻⁴	3.9 · 10 ⁻⁶
CP	VO ₂ ⁺ /VO ²⁺	1.0 · 10 ⁻³	2.4 · 10 ⁻⁶

Table 7.9. k_0 = heterogeneous electrode rate constant; D = diffusion coefficient of electro-active species (in this case vanadium).

Many flow batteries use carbon felt electrodes due to their low cost and adequate electrical conductivity. However, these electrodes show limited power density due to their low activity towards many redox couples.

7.4.2.1. Short thermal treatment of carbon felts for CuRFBs

As above mentioned, the electrodes should display low resistivity and high surface area, and provide a good electron transfer with the electroactive species. Taking a closer look at the system described in ref. [226], the CuRFB is a hybrid system in which the copper is plated and stripped from the negative electrode while the Cu(II)/Cu(I) redox couple reacts at the positive electrode. The present section is focused on the reaction occurring at a carbon felt positive electrode, which is usually used as positive electrode in RFBs.

Hoyt et al. proved the possible employment of carbon felt also for copper plating in a hybrid Cu-Fe cell reaching high plating density (up to 560 mAh cm⁻²) but with failure problem due to the deposit growth close to the membrane [278]. Several studies have been performed to modify the electrode material in order to improve the redox processes. While the problems related to mass transfer can be easily adjusted by applying suitable flow rates, the issues related to the kinetics of the reaction can be solved only by improving the charge transfer between the surface of the electrode and the active species in solution. In addition, also the ohmic losses due to the electrolyte properties and to the contact resistance, including the electric resistance of the electrode, strongly affect the cell performance. It is evident that a holistic approach to improve the electrolyte properties (concentration of the active species, density, and viscosity), as well as the bulk and interfacial electrode properties is necessary. For VRFBs, chemical and electrochemical treatments have been suggested for altering the morphology and the chemical composition of the electrode surface [279-282], resulting in improved electrode kinetics. Chemical modification with Bi nanosphere, thanks to strong interfacial Bi-C bonding, improve the mechanical properties of the electrodes under flow rates and catalyse the negative vanadium redox reactions with appreciable activity [279]. Also, chemical modification followed by a thermal enrichment of heteroatoms (e.g., oxygen and nitrogen) to obtain a multiscale-pore-network structured carbon felt was carried out by Wu et al. [280] showing improved properties with respect to pristine carbon felt. Zhou et al. [281] proposed a nano porous structuring of the felt achieving excellent long-term stability up to 2000 cycles. The electrochemical treatments of carbon felts in H₂SO₄ gave very good results in terms of cell performance, with an increase of coulombic, energy and voltage efficiency [282]. Thermal treatments have been demonstrated be effective in producing surface modification of carbon felt, resulting in improved electrochemical performance in ref [VI] While chemical and electrochemical methods have their advantages, they are limited in their practical application where low-cost materials and process are required, thus thermal treatment are more appropriate for upscale electrode production [130, 283-285]. The results of thermal treatment of carbon felt electrodes are reported in this section and discussed in relation to materials employment in CuRFB. Indeed, even if the positive effects of thermal treatments on vanadium reaction are well known [283], there is a lack of information in literature about the effects of the surface treatment of

carbon felt on a different chemistry, where copper chloro-complexes dominate the electrochemical processes.

- Materials and methods

The carbon felts (CFs) under study are based on polyacrylonitrile (Ceramaterials, 1/8") and rayon (Ceramaterials, 1/8"). CFs were used as received (CF_R, CF_P), where R and P stay for rayon and polyacrylonitrile, and thermally treated in air at 400°C for 6 h and 25 h (CF_R_6h, CF_P_6h and CF_P_25h) by using a ZE muffle furnace (Zetalab). Due to high mass loss values after initial treatment the CF_R was only treated for a maximum of 6 h.

The pristine and thermally treated CFs were investigated by scanning electron microscopy (SEM), Fourier-transform infrared spectroscopy experiments (FTIR), X-ray photoelectron spectroscopy (XPS), Raman spectroscopy, thermogravimetric analysis (TGA) and cyclic voltammetry (CV). The electrical resistivity of felts was evaluated in two-probe measurement at different compression. Samples with area of 1.5 cm² were compressed with different calibration weight. The resistance values were evaluated using Ohms law recording the voltage under a current applied of 10 mA. A scheme of the apparatus is reported in Figure 7.16 in the supplementary information. The current was applied with a AMEL 2053 potentiostat and the voltage was recorded with HP 3478A multimeter.

SEM images were collected by a Zeiss EVO 50 microscope and Raman spectroscopy by a microscope RENISHAW Mod INVIA with an Argon ion Laser ($\lambda = 514$ nm, 5 scan, 20s, resolution 1-2 cm⁻¹, 50x).

The electrical resistivity of carbon felts was measured with a two-probe technique. The sample (3.1 mm thickness) was placed between two PTFE spacers. The electrical contact was taken with Cu strips. Different compressions were achieved by placing calibrated weights on the samples. The spacers allow avoiding short circuits with the calibrated weights. After applying the load, a current of 10 mA was applied. The sample was left 5 minutes before taking the voltage value with a multimeter. The electrical resistivity of the materials was obtained according to Ohm's law and the geometry of the measurement system.

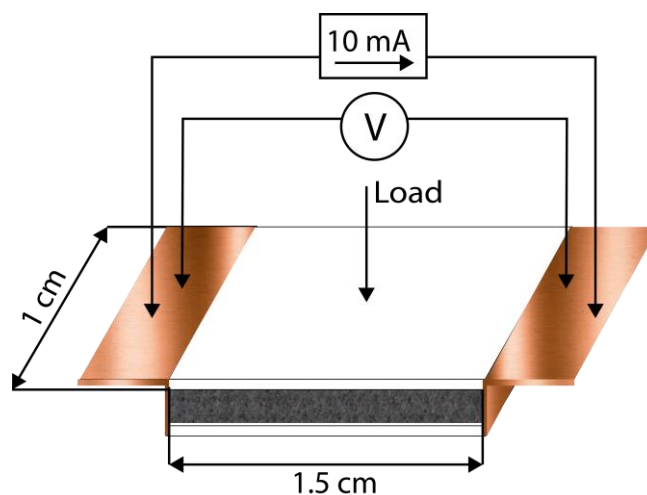


Figure 7.16. Experimental apparatus for resistivity measurements at different compression.

XPS studies were performed on CF_P samples using a Specs EnviroESCA instrument equipped with an AlK α excitation source ($h\nu = 1486.7$ eV). Survey spectra were collected at an operating pressure of *ca.* 10^{-6} mbar in the binding energy (BE) range between 0 and 1460 eV, acquiring data at 100 eV of pass energy, every 1.0 eV \cdot step $^{-1}$, and at 0.1 sec \cdot step $^{-1}$. High resolution scans were collected at 40 eV of pass energy, 0.1 eV \cdot step $^{-1}$, and at 0.5 s \cdot step $^{-1}$. XPS curves (BE uncertainty = ± 0.2 eV) were fitted by means of the Keystone software provided by Specs and applying a Shirley-type background function [286]. The shift in terms of binding energy was corrected assigning a value of 284.1 / 284.4 eV to the C1s peak attributed to carbon sp 2 -type [130, 131, 287]. Atomic percentages (at. %) quantification is obtained using the sensitivity factors of integrated peak areas supplied by Specs.

TGA was performed by a TA Instrument Q50 in different conditions: a ramp from 10 °C min $^{-1}$ up to 650 °C, or from 10 °C min $^{-1}$ up to 400 °C and thermal conditioning at 400 °C for 6 h. TGA were carried out with Ar both as the purge gas at 60 mL min $^{-1}$ and the sample gas (O $_2$ 0) at 40 mL min $^{-1}$; Ar at 60 mL min $^{-1}$ (purge) and O $_2$ (O $_2$ 40) at 40 mL min $^{-1}$ (sample); Ar at 80 mL min $^{-1}$ (purge) and O $_2$ as sample gas (O $_2$ 20) at 20 mL min $^{-1}$ (sample). Some CF_R samples were dried at 60 °C for 20 h before TGA analysis.

FTIR spectra were collected by using a Bruker Alpha by accumulating a minimum of 24 scans per sample with a resolution of 5 cm $^{-1}$. The CF material was ground with

KBr in the weight ratio of 1:200 and the mix of powders was pressed at 6 ton for 2.5 min.

CV experiments were carried out in a three-electrode conventional cell (Lithium Battery Cell Gamry) with a graphite rod (6 mm diameter, Gamry) as counter electrode and a saturated calomel electrode (SCE, AMEL, 303/SCG/6J) as reference electrode at 40°C by using a Voltalab PGZ301 (Radiometer Copenhagen, Denmark). The working electrode was a carbon felt (CF, 0.15 cm²) fixed in the electrode holder by the screw cap and a silicon gasket, an electric contact assured via a Ti current collector. The solution (25 mL) was degassed with Ar before starting the measurements. The CF, fixed in the silicon gasket, were kept in the diluted solutions over night before assembly in the holder, and for 30 minutes in concentrated solution. A glassy carbon electrode (GC, 0.11 cm²) was used as working electrode for comparison.

The electrochemical tests were carried out in the following solutions: (a) 5 mM ferrocene methanol (FcMe⁺) in phosphate buffer solution (PBS) to evaluate the effective active area of CFs, (b) a diluted 5 mM CuCl₂ in 1 M HCl solution to evaluate the electrochemical response of CFs and (c) a concentrated 2 M CuCl₂ in 6 M HCl to simulate the RFB conditions. The conductivity of the solutions was measured by a four-point conductivity cell (Radiometer analytical CDC86IT, Copenhagen, Denmark) by impedance spectroscopy (EIS) using a BioLogic VSP multichannel potentiostat/galvanostat/FRA. The EIS was performed with a 100 kHz-10 kHz frequency range and 5mV AC perturbation, acquiring 10 points.

The in-house made redox flow cell (RFC) consisted of the CF_P_6h positive electrode and a graphite bipolar plate (Sigracell) as substrate for deposition of copper separated by a commercial separator (Daramic-CL) and the electrolyte solution (2 M CuCl – 1 M CaCl₂ – 6 M HCl) corresponding to 0% SoC. The RFC and the cell scheme are shown in Figure 7.17.

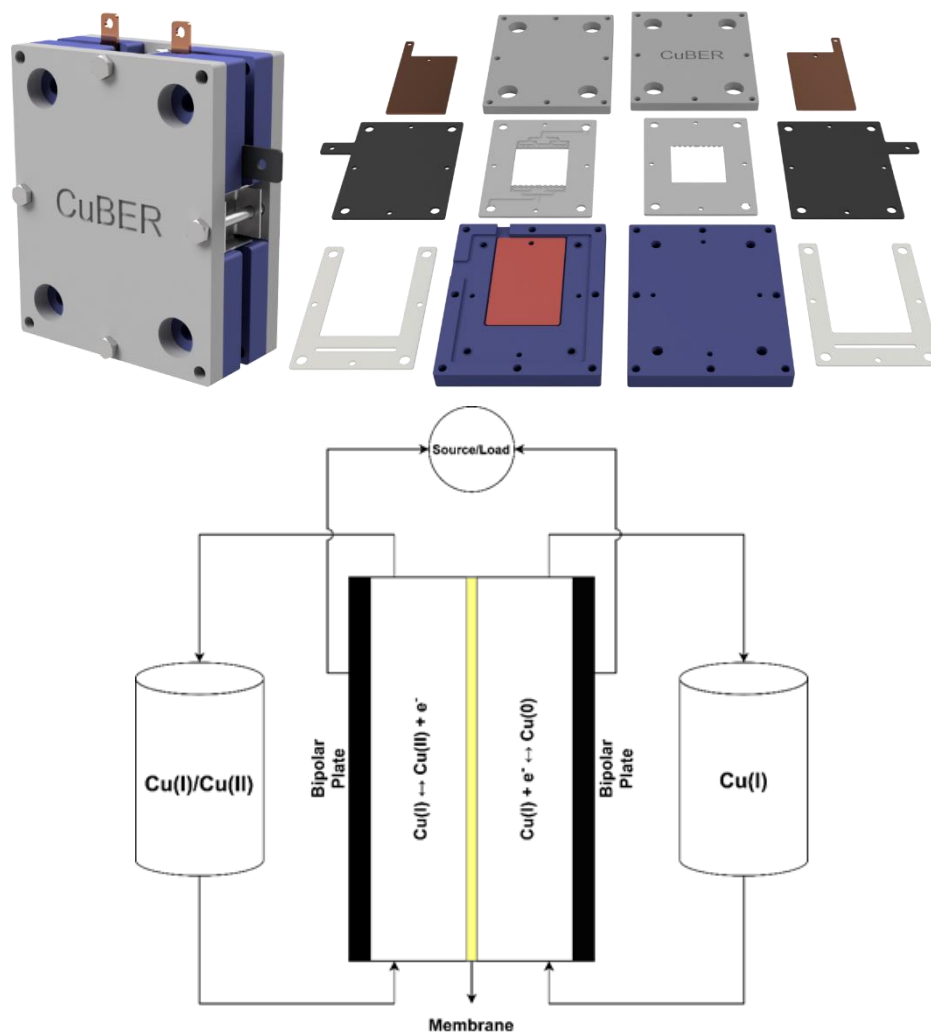


Figure 7.17. Redox flow cell.

Galvanostatic charge/discharge tests were performed with a flow rate of 60 mL min^{-1} (referred to pure water), by using a peristaltic pump (model 323, Watson Marlow) with Marprene tubes at 60 rpm. The tanks with 50 mL electrolyte each were maintained in a thermostatic bath (Julabo Labortechnik GmbH) at $60 \text{ }^\circ\text{C}$ and the cell temperature was kept constant with two electric heating pads applied to the aluminium end plates. The galvanostatic test consisted of 5 cycles at different current density (20 mA cm^{-2} , 30 mA cm^{-2} , 40 mA cm^{-2} and 50 mA cm^{-2}), performed in continuous mode and maintaining the same solution till the end, setting cut off voltages of 0 V and 0.9 V. The CF_P_6h electrode and the Daramic-CL separators were kept in 6 M HCl before assembly in RFC. The electrolytes were circulated for 30 minutes for pre-conditioning the system before testing was commenced.

The values of coulombic efficiency are calculated by the ratio between the supplied charge (Q_{dis}) and the stored charge (Q_{ch}) as shown in (13).

The values of voltage efficiency are calculated by the ratio between the average voltage during discharge mode (V_{dis}) and average voltage during charge mode (V_{ch}) as shown in (14).

The chemicals PBS (Oxoid ltd, tablets), ferrocene methanol (FM, 97%, Sigma Aldrich), CuCl_2 (99.99 + %, Sigma Aldrich), CuCl ($\geq 99.995\%$ trace metal basis, Sigma Aldrich), HCl (37%, Sigma-Aldrich), CaCl_2 ($\geq 99\%$, ACS reagent, Sigma Aldrich) were used as received. MilliQ water (18 $\text{M}\Omega$ cm) was used for the solutions that were deaerated with Ar for ten minutes.

- Results and discussion

To evaluate the appropriate temperature for the treatment of the CFs, TGA analyses have been carried out to study the thermal stability of the carbon felt materials. Figure 7.18a shows the thermal degradation of the two pristine CFs in the presence of O_2 (O_240). The response of the two samples to the oxidative atmosphere differs, and it can be ascribed to different precursor materials and manufacturing techniques employed for either felt [285]. For its polysaccharide precursors, rayon has a higher capacity to adsorb water content in air atmosphere compared to polyacrylonitrile and this behaviour is highlighted by the higher mass loss at low temperature (< 100 °C) of CF_R, which is ascribed to water evaporation. In rayon-based felt, a continuous mass loss is observed with the increasing of the temperature due to superficial degradation of the material. The complete degradation of the felts structure occurs when the temperature exceeds 420 °C, where the fibre chains are entirely decomposed. On the other hand, the initial degradation of CF_P sample starts when exceeding 500°C with a loss of about 20 % of weight at 650 °C. The CF_R sample analysed in Ar atmosphere (blue line) was not dried before TGA. During the TGA the CF_R sample displayed 12% initial mass loss, caused by evaporation of water content, with thermal degradation started when temperatures above 470 °C was achieved. Figure 7.18b displays the behaviour of CF_R samples in conditions that mimic the thermal treatment in air. The O_2 flow over sample was decreased to 20 mL min^{-1} (O_220), and the isothermal test at 400 °C was performed after a short ramp that simulates the increasing temperature of the muffle furnace up to reaching 400 °C. During this temperature

ramping a continuous mass loss is evident: 14 % weight is lost during the heating ramp in the first 40 min, and 68 % in the 6 h at 400 °C. The mass losses during TGA are higher than those found after thermal treatment in the muffle furnace (> 50%). The behaviour can be attributed to the continuous flow of O₂ on the sample during TGA, removing degraded fibres and exposing new fibres to the oxidation process. This flow and removal of degraded fibres does not occur in the static conditions inside the muffle furnace. The high weight loss of CF_R indicates the lower thermal stability of the material with respect to CF_P. Hence, the CF_R exposure at high temperature was limited to 6 h, to prevent excessive degradation of the CF_R carbon felt.

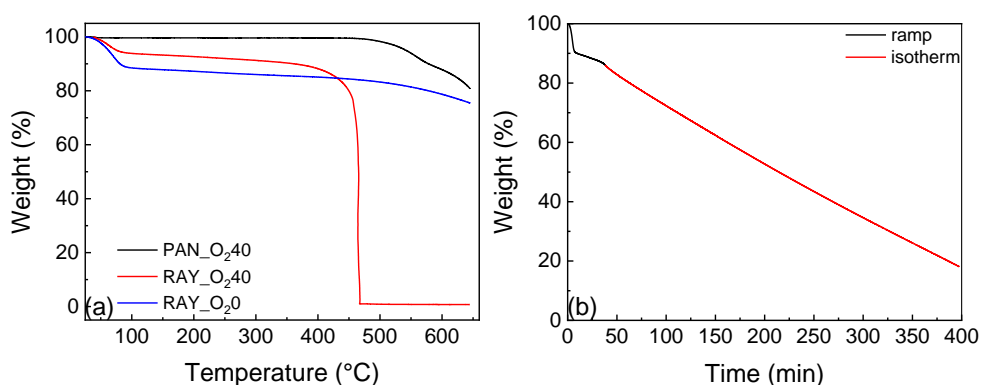


Figure 7.18. Thermogravimetric analysis ($10\text{ }^{\circ}\text{C min}^{-1}$) of pristine CF materials (a) CF_R (red) and CF_P (black) in presence of O₂ (O₂40) and CF_R (blue) in Argon (O₂0) (b) CF_R in presence of O₂ (O₂20) in isothermal condition at 400 °C (red) after a short ramp (ca. 40 min, $10\text{ }^{\circ}\text{C min}^{-1}$) up to 400 °C (black).

Electrode morphology

The morphologies of the different CFs are shown in Figure 7.19. All samples show randomly distributed fibres, with the morphology depending on the starting material and manufacturing route employed [278]. The CF_R consists of bundles of smooth fibres in contrast to polyacrylonitrile-based felt consisting of single fibres with surface veining. The diameter of CF_R bundles and CF_P fibres were similar (ca. 20 μm) while the diameter of the individual fibres of the CF_R felt are nearly a few μm across. The two different precursors showed dissimilar responses to the thermal treatment at 400 °C, as expected through TGA analysis. The CF_R samples degradation largely depends on the duration of thermal treatment as the degradation process is initiated near 400°C. In Figure 7.19b, yellow arrows highlight the presence of cavities on the

surface of CF_R fibres giving an irregular shape to the edges. On the contrary, CF_P fibers in Figures 7.19d and 7.19e do not show other modifications of the morphology other than the observed increase of roughness.

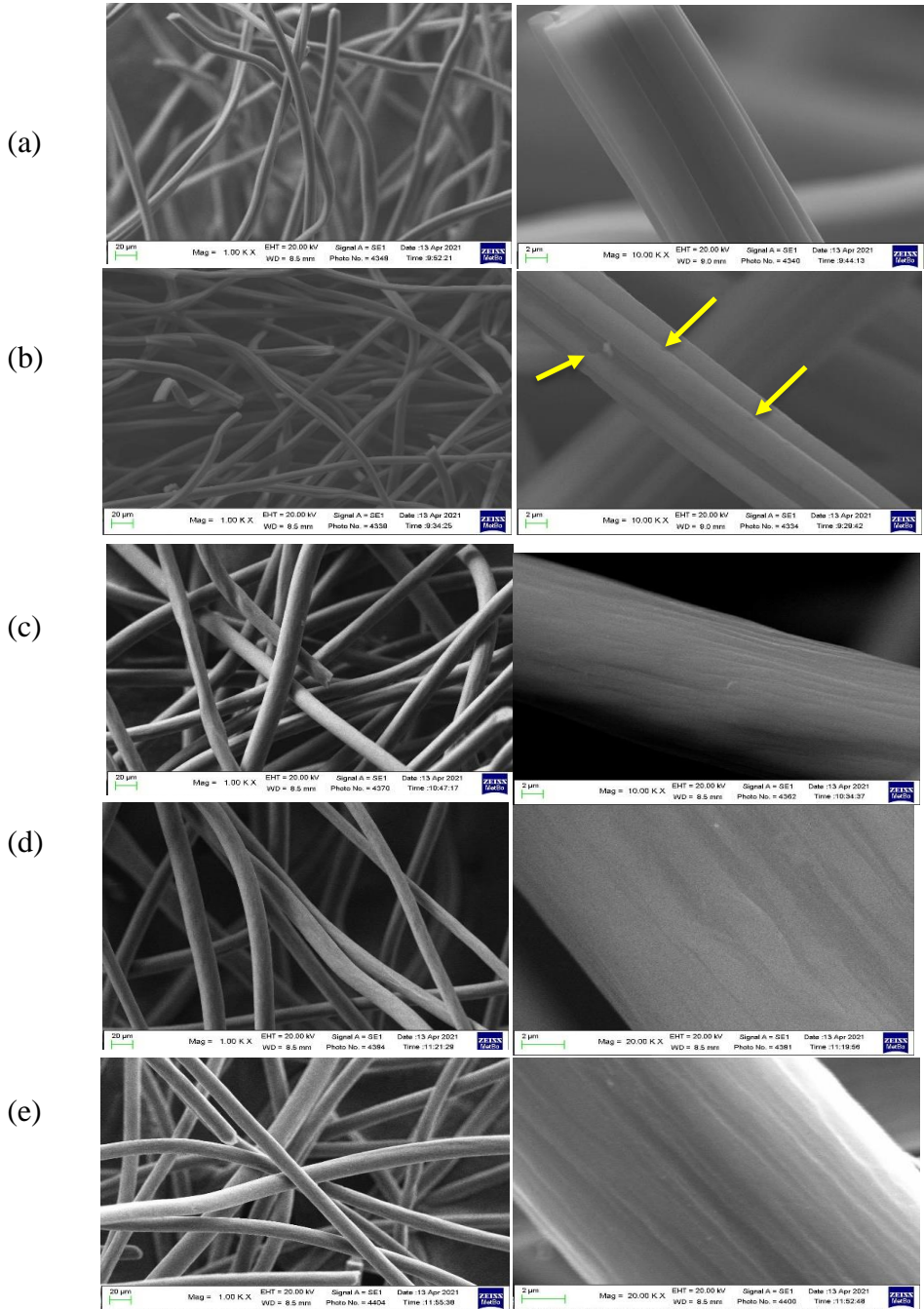


Figure 7.19. SEM images of thermal treated samples: (a) CF_R; (b) CF_R_6h; (c) CF_P; (d) CF_P_6h and (e) CF_P_25h

Chemical analysis

The spectra of rayon-based carbon felt before and after the thermal treatment are reported in Figure 7.20a. The spectra exhibit a broad band at 3434 cm^{-1} due to the O-H vibration, bands at 2919 and 2848 cm^{-1} of C-H stretching. At 1736 and 1638 cm^{-1} are present the C=O and C=C stretching followed by the -CH bending at 1370 cm^{-1} . At wavenumber between 1000 cm^{-1} and 1300 cm^{-1} are present the vibration of C-O and C-C.

After the thermal treatment, the material presents a decrease of intensity of C=C vibrations and an increase of the C=O vibration intensity. Thus, the thermal treatment in air results in an oxygen-enrichment of the material. In Figure 7.20b are reported the FTIR spectra of the PAN-based carbon felts. With the thermal treatment, the C=C band decrease while the CH₂ bending, C-C stretching, and C-H stretching increase. Also, the C-O and C=O increase with respect to the C=C band with the thermal treatment. For PAN-based CF, XPS analyses are also reported in Figure 7.22.

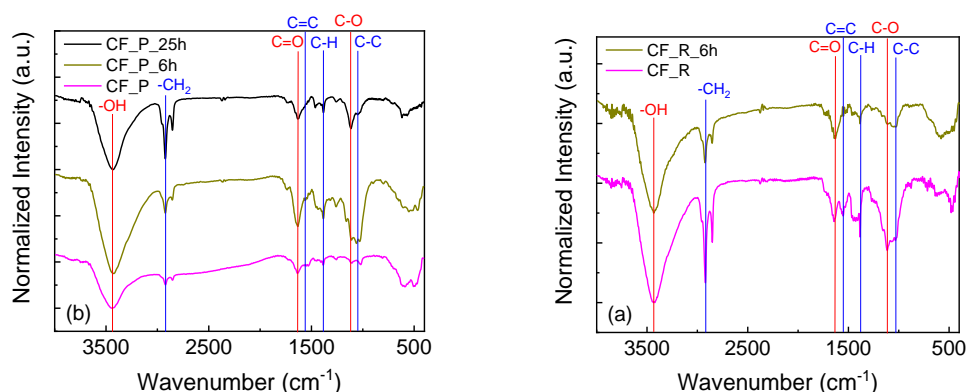


Figure 7.20. FTIR spectra of (a) CF_R and CF_R_6h, and (b) CF_P and CF_P_6h and CF_P_25h.

In Figure 7.21 the full survey XPS spectra of CF_P, CF_P_6h, and CF_P_25h show the characteristic peaks of C1s and O1s at 284 eV and 532 eV , respectively. The integrals of these signals indicating the atomic content (Table 7.10) is influenced by the thermal treatment duration. In CF_P, the C1s band are the main contribution in the survey XPS spectra. Increasing the treatment duration, the signal relative at the O1s increases indicating a higher presence of oxygen groups in the material. In Table 7.10 the atomic content obtained by integration of the bands are reported.

In Figure 7.21 the full survey XPS spectra of CF_P, CF_P_6h, and CF_P_25h show the characteristic peaks of C1s and O1s at 284 eV and 532 eV, respectively. Increasing the treatment duration, the signal relative at the O1s increases indicating the higher presence of oxygen groups in the material.

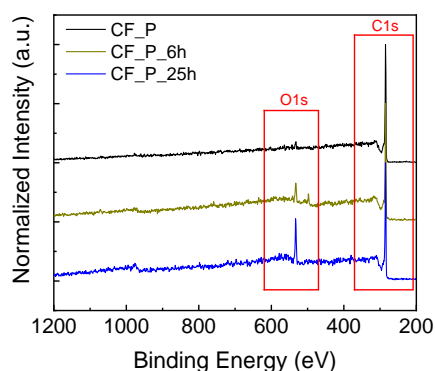


Figure 7.21. XPS survey spectra of polyacrylonitrile-based carbon felts.

Sample	C1s	O1s
CF_P	95.6%	3.8%
CF_P_6h	90.7%	9.0%
CF_P_25h	81.1%	18.8%

Table 7.10. Atomic content of polyacrylonitrile-based carbon felts from integrals of C1s and O1s signals.

The XPS high resolution of C1s exhibit contributions of C=C carbon at 284.1 eV, C-H at 284.9 eV, C-O-R at 286.0 eV, and C=O at 288.2 eV [130, 131]. The effect of the thermal treatment (Figure 7.22b and c) reflects on the higher amount of C-H and C-O groups with respect to the C=C presented in CF_P (Figure 7.22a). The high-resolution spectrum of the O 1s region shows two peaks for all the samples with binding energy at 533.5 eV and 531.0 eV, corresponding to the C-O and C=O functional groups, respectively. However, the two different contributions change significantly with the thermal treatment. In contrast to the CF_P (Figure 7.22d), the CF_P_6h significantly increases oxygen functional groups with the C=O that increases more respect to the C-O (Figure 7.22e). Proceeding in the thermal treatment (CF_P_25h in Figure 7.22f), the

oxygen content continues to grow with the increment of C-O functionalities at the expense of carbonyl functional groups.

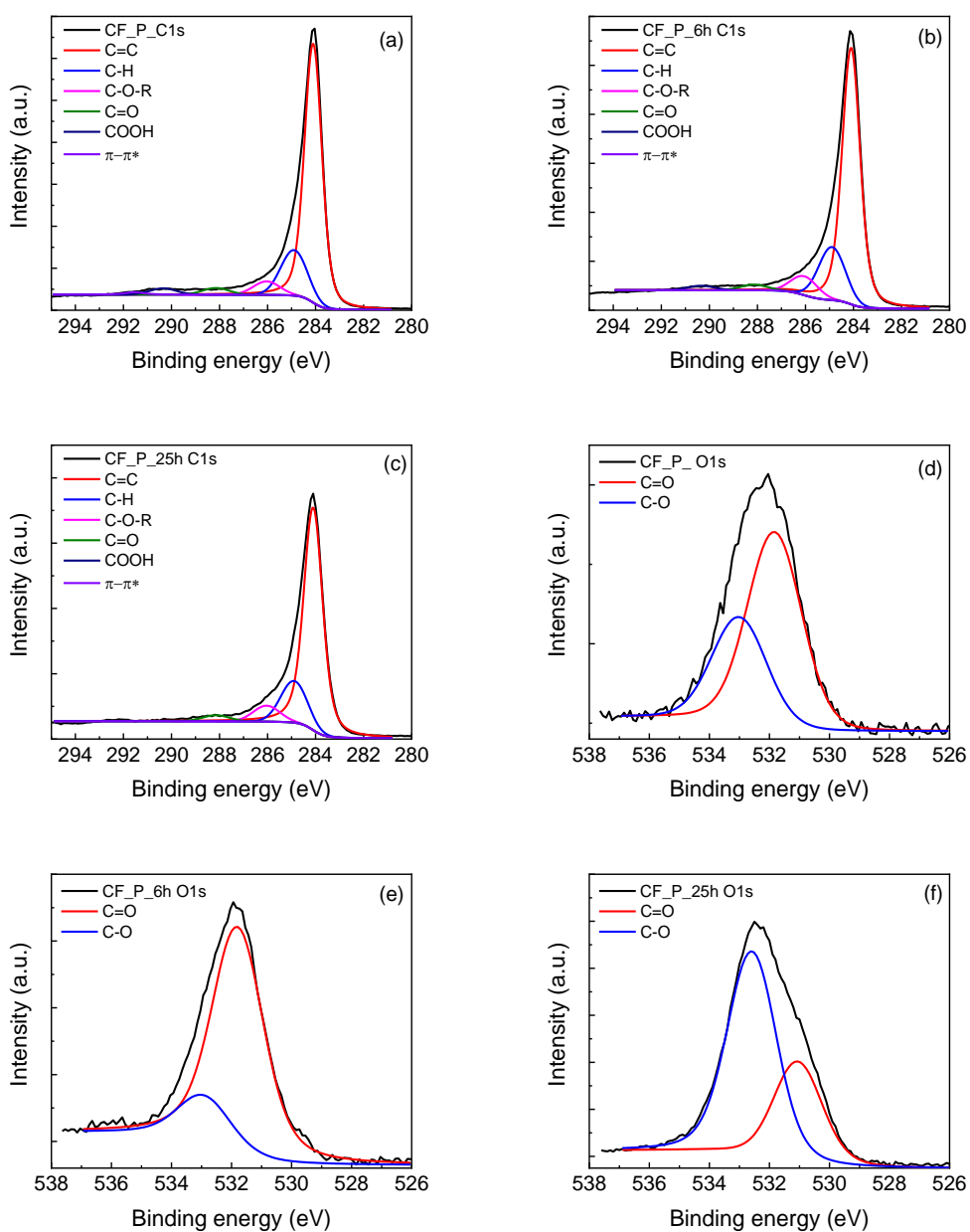


Figure 7.22. High-resolution XPS spectra of C1s region (a-c) and O1s region (d-f) fitting of the polyacrylonitrile-based carbon felts: CF_P (a,d), CF_P_6h (b, e) and CF_P_25h (c, f).

The carbonaceous structure of pristine and thermally treated CFs was investigated using Raman analysis. The different hybridization of carbon atoms and the distribution of disorder are considered to define the carbon materials' structure. An ordered structure, like graphene, is highlighted by the presence of the G band that is related to

the vibration of sp^2 carbon atoms. On the other hand, defects or heteroatoms characterize the D band [288, 289].

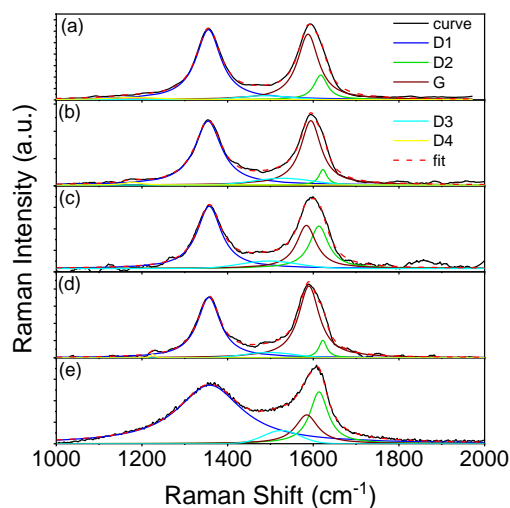


Figure 7.23. Raman spectra of carbon materials. a) CF_P; b) CF_P_6h; c) CF_P_25h; d) CF_R; e) CF_R_6h.

Sample	Area	Centre (cm ⁻¹)	FWHM (cm ⁻¹)	I_{D1}/I_G	I_{D1}/I_{G+D1}
CF_P	$64.8 \cdot 10^3$ (D1)	1355 (D1)	70 (D1)	1.25	0.55
	$51.5 \cdot 10^3$ (G)	1587 (G)	60 (G)		
CF_P_6h	$26.4 \cdot 10^3$ (D1)	1354 (D1)	76 (D1)	1.28	0.56
	$20.5 \cdot 10^3$ (G)	1594 (G)	58 (G)		
CF_P_25h	$8.9 \cdot 10^3$ (D1)	1357 (D1)	66 (D1)	1.75	0.63
	$5.1 \cdot 10^3$ (G)	1584 (G)	55 (G)		
CF_R	$17.1 \cdot 10^3$ (D1)	1356 (D1)	59 (D1)	0.92	0.47
	$18.5 \cdot 10^3$ (G)	1590 (G)	65 (G)		
CF_R_6h	$342.3 \cdot 10^3$ (D1)	1358 (D1)	183 (D1)	5.32	0.84
	$64.2 \cdot 10^3$ (G)	1584 (G)	64 (G)		

Table 7.11. Calculated parameters of deconvoluted function of Raman spectra of the different samples.

The deconvolution of the acquired spectra has been done in the range of wavenumber between 1000 and 2000 cm^{-1} and involves 4 Lorentzian and 1 Gaussian functions, as shows in Figure 7.23. The I_{D1}/I_G and I_{D1}/I_{G+D1} (D-to-G ratios) values were calculated

using the integrated intensity, the results of which are reported in Table 7.11. In the case of polyacrylonitrile-based samples, the D-to-G ratios for pristine and 6h-thermal treated electrodes are moderately similar, and only slight variations occur after 25h-treatment of treatment. In PAN-based felts, the full width at half maximum (FWHM) of D-band is higher than that of G-band, and this does not vary with thermal treatment. It suggests that there are no significant changes in the structural organization of the felt. In the case of the rayon-based felt, the pristine and 6h-treated samples show a higher difference of the D-to-G ratios. In the pristine sample, the contribution of the D band is lower than that of the G band, suggesting a high content of ordered atoms. Indeed, the FWHM-G is higher than of FWHM-D. On the other hand, with the treatment, the FWHM-D increases by three times, indicating a more extensive oxidation of the surface.

Resistivity measurements

The electrical resistivity of the carbon felts was evaluated under varying load and compression values. As previously reported [290, 291], the resistivity of these materials decreases linearly with compression for the first 20% to reach an asymptotic value. At low compression, contact points are scarce and the characteristic value of the material can be taken by increasing the compression to over 20%.

Figure 7.24 shows that CF_R has the maximum resistivity ($1.60 \Omega \text{ cm}$) among the samples tested, reaching the highest compression of 40% with a load of 315 g cm^{-2} . Additionally, after thermal treatment, sample CF_R became brittle and difficult to handle and was thus not tested. Alternatively, the PAN-based felts show the lowest resistivity, $0.17\text{-}0.14 \Omega \text{ cm}$ in the asymptotic part of the curve. The CF_P_6h and pristine CF_P felts show similar compression, exhibiting ca. a 20% of thickness variation with a load of 315 g cm^{-2} . On the contrary, CF_P_25h shows 40% compression with the same load. The highest stiffness of the CF_P_6h ensures a better performance in the RFB cell in which the materials are under pressure generated from the hydraulic system.

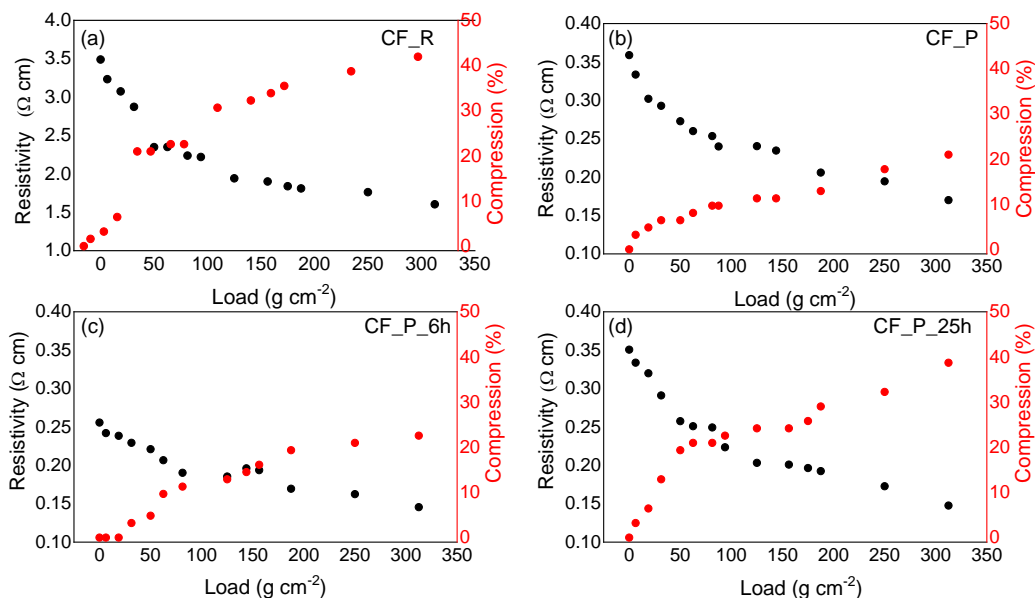


Figure 7.24. Electrical resistivity and compression vs applied load for CF_R (a), CF_P (b), CF_P_6h (c), CF_P_25h (d).

Electrochemical characterization

Electrochemical tests were performed using a three-electrode cell. The samples were immersed in the testing solution before assembly in an electrode holder as described. Pristine CF_R samples showed higher wettability compared to the PAN-felts, with the higher hydrophilicity of the rayon carbon felt leading to the presence of polar groups in the carbon structure [278]. However, thermal treatment causes the rayon-based felt to become brittle, leading to fibres becoming lost/broken during handling and immersion in the solution. This is also the reason why attempts to perform the CV tests as described below for the rayon-based felts failed. In contrast, the thermal treatment on CF_P samples improved the electrode wettability by increasing the content of oxidized groups on the surface without affecting the mechanical integrity of the material.

The polyacrylonitrile-based felts were fixed into a circular gasket and tested in 5 mM FcMe^+ - PBS to evaluate their effective area (EA_{CF}) compared to that of a GC electrode. The redox couple $\text{FcMe}^+/\text{FcMe}$ was selected because of its redox potential (0.4 V vs SHE [292]) is in the same range of the potential of the $\text{Cu(I)}/\text{Cu(II)}$ couple. The CVs at 10 mV s^{-1} in Figure 7.24a and at 100 mV s^{-1} in Figure 7.24b reveal the different areas of the CFs and of the GC electrode. EA_{CF} was calculated by the ratio of

the anodic peak current density of the CFs and of the GC. All the felts, once well wet, reach a similar current showing unvaried reactivity after the thermal treatment. The carbon felt areas are at least 30 times higher than that of GC, with the resulting areas being summarized in Table 7.12. The peak separation (ΔE) for felt electrodes is smaller than 0.057 V indicating a good reversibility of the process on carbon felt surface. Accordingly, the i_{pc}/i_{pa} ratio is close to 1. For all the samples the $(E_{++}+E_{-})/2$ is around 0.185 V vs SCE.

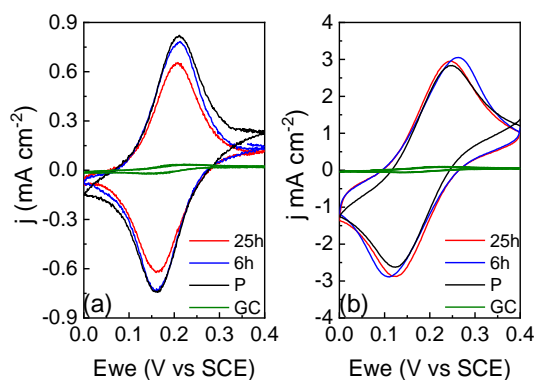


Figure 7.25. CVs at 40 °C on GC, pristine, and treated polyacrylonitrile-based carbon felts in 5 mM ferrocene-methanol in PBS solution at (a) 10 mV s⁻¹ and (b) 100 mV s⁻¹.

Sample	i_{pa} mA cm ⁻²	A/A _{GC}	i_{pc}/i_{pa}	ΔE V	$(E_{++}+E_{-})/2$ V vs SCE
GC	0.020	1	0.95	0.080	0.184
CF_P	0.538	27	1.2	0.048	0.186
CF_P_6h	0.698	35	0.93	0.055	0.185
CF_P_25h	0.556	29	0.97	0.042	0.184

Table 7.12. Summary values of different carbon felts in 5mM FcMe⁺ - PBS at 10 mV s⁻¹.

Tests in diluted solution of CuCl₂ were carried out using the same assembly and procedure previously described to evaluate the effect of a different chemistry (Cu(II)/Cu(I) vs. FcMe⁺/FcMe). The CVs of the polyacrylonitrile-based felts in 5 mM CuCl₂ – 1 M HCl and in 2 M CuCl₂ – 6 M HCl are shown in Figure 7.26. The pristine CF_P shows a well-defined oxidation peak and a flattened reduction peak at low scan rate (Figure 7.26a). The flattened peak can be attributed to the slower kinetics of the electron transfer process due to the higher resistivity of pristine CF_P compared with

the thermal treated CF_P_6h and CF_P_25h. The increasing in scan rate exacerbates this feature (Figure 7.26b). The reduction process needs higher overpotential to occur and the shape of the current profile, almost constant at potential lower than 0.2 V, indicates a kinetically limited behaviour. After the thermal treatment, the CVs becomes more reversible, even with only 6h treatment.

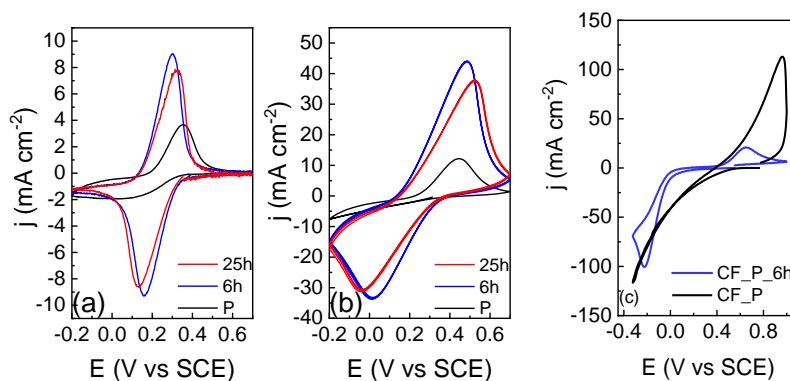


Figure 7.26. CVs at 40 °C of pristine, and treated polyacrylonitrile-based carbon felts in 5 mM CuCl₂ - 1 M HCl solution at (a) 10 mV s⁻¹ and (b) 100 mV s⁻¹, and (c) in 2 M CuCl₂ – 6 M HCl solution at 10 mV s⁻¹.

In Table 7.13 the electrochemical parameters obtained from the CVs at 10 mV s⁻¹ are reported. In all the tested samples, the high ΔE values suggest the quasi-reversibility of the electrochemical processes, and the lowest peak separation is achieved by the CF_P_6h (0.140 V). The i_{pa}/i_{pc} ratio is 2.12 for the pristine felt, which decrease significantly with the thermal treatment and reaches values near 1.

Sample	i_{pa}/i_{pc}	ΔE V	$(E_{+}+E_{-})/2$ V vs SCE	OCV V
CF_P	2.12	0.252	0.226	0.386
CF_P_6h	1.11	0.140	0.230	0.391
CF_P_25h	1.03	0.190	0.228	0.355

Table 7.13. Electrochemical parameters from CVs at 10 mV s⁻¹ of different carbon felts in 5 mM CuCl₂ 1 M HCl solution at 40 °C.

The better performance of CF_P_6h demonstrates that the optimal surface modification is reached after 6 h of thermal treatment to produce a wettable electrode

able to exchange electrons with the copper chloro-complexes present in the electrolyte; whereas CFs for vanadium RFB have been demonstrated to require 25-30 h of thermal activation [293].

Figure 7.26c displays the CVs of the polyacrylonitrile-based carbon felts in the concentrated solution 2M CuCl₂ with 6M HCl. While the concentrated electrolyte displays higher conductivity than the diluted one (634 vs. 325 mS cm⁻¹ at 40°C), the higher ionic strength and viscosity affects ion diffusion. In addition, the types of chloro-complex present in the solution and their stability, which affect the potentials of the redox processes, also depends on the ratio Cu:Cl:H₂O [236, 237]. The shift of both anodic and cathodic processes to higher and lower potential, respectively, indicates kinetic limitations of the electron transfer. CF_P displays the anodic process peak near 0.9 V, while the cathodic one is close to the copper plating process and cannot be observed. CF_P_6h shows the processes peaks within the potential stability window, although with a ΔE of ca. 0.87 V, and $(E_{++}+E_{-})/2$ of 0.215 V. In the concentrated electrolyte, the higher viscosity and density of the solution made the voltammetric investigation possible also on CF_R_6h, even if only few cycles could be performed, which are reported in Figure 7.27. Repeated CVs were also carried out (and reported in Figure 7.28), evidencing that no poisoning effects are observed due to the presence of chloride ions.

In concentrated solution, the higher density and viscosity permit to obtain some voltammetric cycles also with CF_R and CF_R_6h before the electrode loses the electrical contact with the current collector, as it happens with more diluted and, hence, less viscous solutions. The CVs on rayon-based carbon felts in concentrated solution are reported in Figure 7.27. The CF_R displays a resistive behaviour similar to CF_P, and CF_R_6h shows peak separation similar to CF_P_6h. The lower currents of CF_R_6h are probably due to the lowest effective area, given the highest mass lost with 6h-thermal activation. The electrochemical tests confirm that polyacrylonitrile-based carbon felts give better results than rayon-based felts.

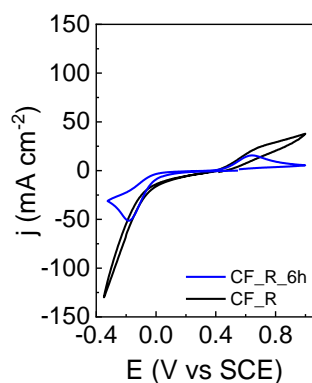


Figure 7.27. CVs at 10 mV s^{-1} and 40°C of pristine, and thermally treated rayon-based carbon felts in $2 \text{ M CuCl}_2 - 6 \text{ M HCl}$ solution.

Figure 7.28 reports stability test by repeated CVs (50 cycles) of CF_P (a), CF_P_6h (b) and CF_P_25h (c) to evidence if poisoning phenomena occur over cycling in presence of chloride ions. The CVs were carried out at 100 mV s^{-1} at 40°C in 5 mM CuCl_2 1 M HCl solution.

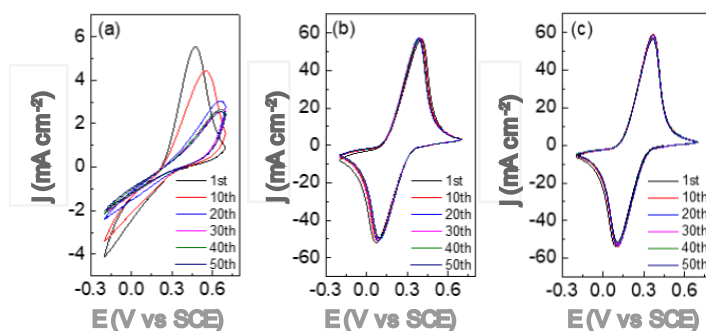
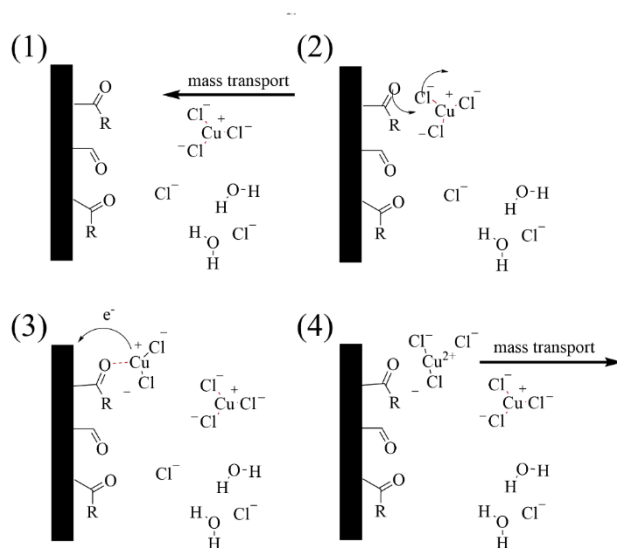


Figure 7.28. CVs in $5 \text{ mM CuCl}_2 - 1 \text{ M HCl}$ at 100 mV s^{-1} and 40°C of CF_P (a), CF_P_6h (b), and CF_P_25h (c).

Summarizing the information from physicochemical and electrochemical characterizations, some aspects of the electrochemical process occurring at the positive electrode of a CuRFB can be compared with the process occurring in VRFB. In VRFB, the oxygen-containing groups act as electrocatalytic active sites. In fact, in the positive half-cell, the charge and discharge processes at the positive electrode involve the transfer of an oxygen atom, which can be the rate determining step in the overall reaction. So, the availability of oxygen groups on the electrode surface affects the rate of the reaction. The electron transfer from the VO^{2+} to the electrode occurs along with

the -C-O-V- bond and transfer of one oxygen atom on the C-O functional group to the VO^{2+} , forming a surface VO_2^+ . Hence, a long thermal treatment is necessary for VRFB in order to enrich the carbon surface of -C-O functionalities. In an all-copper redox flow system, the interaction of copper with the electrolyte and the electrode surface is regulated by intermolecular interactions. The presence of C=O groups on the electrode surface can assist the electrochemical reaction coordinating copper cations without covalently bonding the electroactive species to the electrode surface. Moreover, C-O-R ends group results sterically hindered (R=aliphatic groups) or protonated (R=H) and less electron donating in acid environment than C=O functionalities. As proposed in Scheme 7.1, after the mass transport from the bulk to the electrode interphase of the electroactive species (1), the Cu chlorocomplexes approach to the electrode surface can be assisted by the Cu-O non-covalent interaction (2). The electron transfer occurs (3) and the Cu(II) formed species move away from the electrode-electrolyte interphase. Furthermore, the presence of more carbonyl groups than CO guarantees a better conductivity of CF_P_6h compared to CF_P_25h due to the possible electronic conjugation of double bonds to the extended aromatic coordination of the carbonaceous matrix.



Scheme 7.1. Proposed mechanism for Cu(I)-Cu(II) redox reaction with C=O functional groups on the electrode surface as high affinity coordinating site. (1) mass transport of the Cu(I) chlorocomplexes at the electrode interphase; (2) complexation of copper with C=O of the electrode surface; (3) electron transfer; (4) mass transport of the Cu(II) toward bulk electrolyte.

Galvanostatic charge/discharge cycles in redox flow cell.

A redox flow cell (RFC) with the CF_P_6h as positive electrode, graphite bipolar plate for the negative process, 2 M CuCl – 1 M CaCl₂ – 6 M HCl solutions as the electrolyte and a Daramic-CL porous separator were assembled and tested. Charge-discharge cycles (30 min charge followed by 30 min discharge) between 20 and 50 mA cm⁻² were carried out to evaluate the electrode behaviour in the RFC (Figure 7.29). Starting from 0 % SoC the cell can reach only a 10 % of charge in 30 min. The voltage profiles at the different current densities are very similar, with the current values mainly affecting the charging process rather than the discharge. Initial OCV values were taken 0.515 V, i.e. the voltage after the first 5 cycles at 20 mA cm⁻², and as final value the OCV measured after the 5 cycles at 50 mA cm⁻² (0.568 V), as can be seen in Table 7.14. During discharge, the processes of Cu dissolution and Cu(II) reduction shows a low overpotential even at high currents, changing the average discharge voltage from ca. 0.43 V at 20 mA cm⁻² to 0.38 V at 50 mA cm⁻².

The optimization of the plating process at the negative electrode is one of the most critical issues in a hybrid RFB system as it could reduce the electrode overpotential, and further improvement in membrane performance and in the flow management can increase the coulombic efficiency by preventing electrolyte crossover phenomena. Table 7.14 reports the values of coulombic efficiency (CE%) and voltage efficiency (VE) for the average of 5 cycles at each current density. Without any optimizations, the RFC shows a CE% of 87 % and a VE of 60 % at 30 mA cm⁻², thus demonstrating the effectiveness of the short thermal treatment of PAN carbon felts.

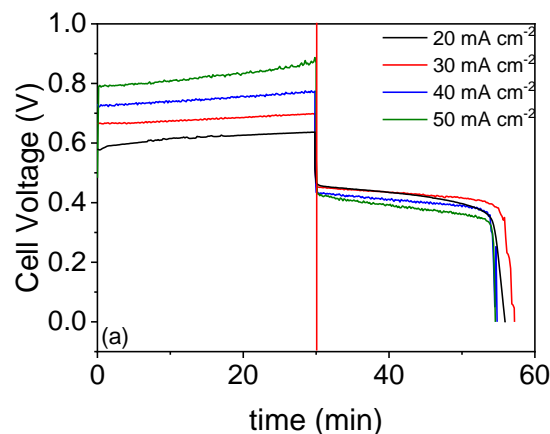


Figure 7.29. Voltage profile of the 5th cycle at each current density of the RFC with 30 min charge and 30 min discharge cycles at 60 °C.

Current density	OCV	CE%	VE
mA cm ⁻²	V	%	%
20	-	79	68
30	0.515	87	60
40	0.526	85	53
50	0.549	83	56

Table 7.14. Open current voltage of the 1st cycle, average values of coulombic efficiency and voltage efficiency of 5 galvanostatic cycles at different current densities with CF_P_6h positive electrode.

In conclusion, the activation of carbon felts to be used as positive electrodes in all-copper RFBs is one of the key issues for achieving good battery performance. In this work, two carbon felts using the polyacrylonitrile and rayon precursors, have been investigated together with thermal activation of these felts. As expected, they needed thermal activation to improve their wettability for the use in aqueous media. However, thermal treatment affects the structural integrity of the two materials, with the rayon-based treated carbon felt becoming very brittle and difficult to handle. On the other hand, polyacrylonitrile-based carbon felt demonstrated an excellent stability and the best electrochemical performance after 6 hours of thermal treatment at 400 °C. Differently from CFs for VRFB electrodes, which require longer activation periods due to the reaction at the positive electrode involving covalent bonds with CO surface groups, the CF used in copper RFBs need a shorter activation time because the oxygen groups only assist the reaction by intermolecular interactions. The feasibility of the short heat treatment for polyacrylonitrile-based CF electrodes has been demonstrated also in an RFC configuration. Although the RFC assembly and components were not optimised, an efficiency of 92 % (last cycle at 30 mA cm⁻²) and the ability to sustain currents up to 50 mA cm⁻² have been proved.

Finally, some considerations on cost and sustainability. The total cost of a cell comprises the cost of materials and material processing and is considered both in terms of cost and energy consumption. A thermal treatment of 6h was proved to be sufficient to improve the electrochemical performance of the electrode, which is an important result towards the scale up of the all-copper RFB, since shortening the thermal

treatment of the electrodes positively affects the total cost of cells and stacks, as well as the carbon footprint associated to the manufacturing processes. If the energy used for these processes is not sourced from renewable sources, the shortening of thermal treatments means lower energy consumed and lower carbon dioxide emission, which are key issues for the value chain of CuRFBs.

7.4.3. Membranes

A great effort in RFBs research is deputed to select suitable membranes. Considering that most of the RFBs work in acidic media (e.g., HCl and H₂SO₄), an ideal membrane should offer enough chemical stability under acidic conditions and resistance to oxidizing and reducing potentials (lower than for LiBs). In addition, low electrical resistance is required to achieve high current densities. Then, to prevent the crossover of the species, selecting a membrane with low permeability of the active redox species (copper cations in CuRFBs) is essential, which also blocks the preferential transfer of water resulting in flooding of one half-cell while diluting the other. Hence, the membrane should allow the transfer of charge-carrying ions, completing the electrical circuit [294, 295].

The most straightforward systems consist of porous membranes composed of a polymeric matrix with defined pores (Figure 7.30a), which has the advantage of being based on stable, low-cost polymers (e.g., polyethylene PE, polypropylene (PP)). However, porous membranes represent only a physical barrier for the crossover of the species, remaining unsolved the problem of ion selectivity.

For this reason, the membrane represents one of the main obstacles in commercializing many RFBs. A solution to increase the selectivity of the crossing species is found by incorporating charged functional groups in the polymeric chain. The resulting membranes are called Ion Exchange Membranes (IEM). The cross-linking is crucial to prevent polymer dissolution in water [296]. The charged groups act as exchange sites, forming electrostatic interaction with ions of opposite charge, which replaces the mobile counter-ions. In this sense, the ions exchange, so the species crossover through the membrane is reversible with the displacement of ionic species along the polymeric matrix. The ionic conduction of the species is depending on the strength of the ionic interactions [297].

IEMs can allow the cation or the anion exchange depending on the ionic functionalities attached to the membrane's matrix. Cation exchange membranes (CEM) contain anionic moiety in the polymeric chain as $-\text{SO}_3^-$, $-\text{COO}^-$, $-\text{PO}_3^{2-}$, $-\text{PO}_3\text{H}^-$, $-\text{C}_6\text{H}_4\text{O}^-$. These groups on the polymeric backbone allow cation transport, blocking the anions (Figure 7.30b). Meanwhile, in Anion Exchange Membranes (AEM), the polymer is functionalized with positively charged groups as $-\text{NH}_3^+$, $-\text{NRH}_2^+$, $-\text{NR}_2\text{H}^+$, $-\text{NR}_3^+$, $-\text{PR}_3^+$, $-\text{SR}_2^+$, allowing anions transport (Figure 7.30c).

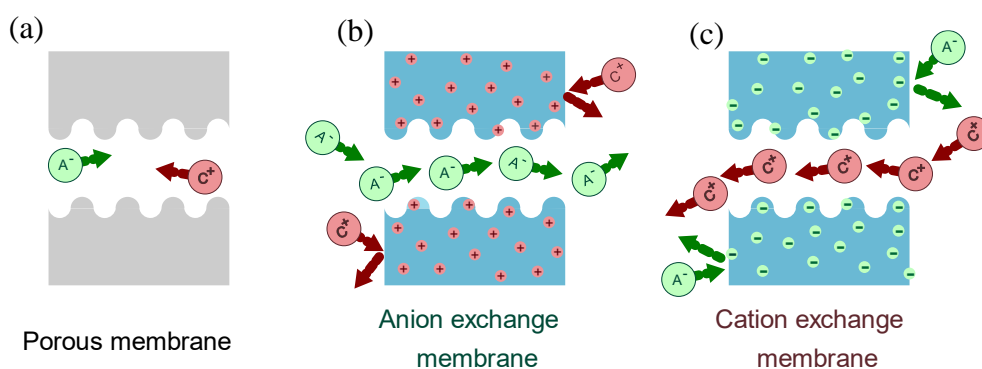


Figure 7.30. Schematic representation of a porous membrane (a), an anion exchange membrane (b), and a cation exchange membrane (c).

In addition, membranes can be further classified based on many factors like the material's nature, pore size, morphology, and composition. Most conventional hydrocarbon-based ion exchange membranes are sensible to oxidizing agents. For this reason, perfluorinated membranes are used for their excellent chemical stability, high conductivity, and mechanical strength. Typically, perfluorinated ion exchange membranes are copolymers derived from tetrafluoroethylene (TFE) and perfluoro vinyl ether terminated by a sulfonyl fluoride group [298].

7.4.4. Scanning electrochemical microscopy method for Cu^{2+} permeability investigation on membranes for Redox Flow Battery

In Redox Flow Batteries, the essential function of an IEM is to isolate the ions of redox couples involved in electrode reactions, allowing the high-rate transport of charge carriers across the membrane. Hence, the membrane's selectivity determines the crossover and then, the coulombic efficiency of the system. Every RFB chemistries

take advantage of diverse redox couple and charge carriers, requiring specific limitation and selectivity in the membrane ion transport (Table 7.15).

In some cases, as a polysulfide bromine system, a CEM ensures the separation between polysulfides and the counter ions. Meanwhile, another system requires AEM to block cationic active species' crossover. However, the transport of H^+ is desirable.

For example, in polysulfide bromine batteries with a cation exchange membrane (CEM), the sole selectivity required is the separation between counter- and coions. However, more often, selectivity between the metal cations and H^+ ions is desirable. The particular “ H^+ leakage” through anion exchange membranes (AEMs) bearing fixed positive charges are utilized in all vanadium [299] and chromium bromine batteries and leads to very high coulombic efficiency.

System	Negative half-cell	Positive half-cell	Charge carrier
All Vanadium	VO_2^+/VO^{2+}	V^{2+}/V^{3+}	H^+
V-bromine	Cl^-, Br^-	V^{2+}/V^{3+}	H^+
Polysulfides-bromine	Br_3^-/Br^-	S_4^{2-}/S_2^{2-}	Na^+
All Iron	Fe/Fe^{2+}	Fe^{2+}/Fe^{3+}	Cl^- and H^+
All Copper	Cu/Cu^+	Cu^+/Cu^{2+}	Cl^- and H^+

Table 7.15. Negative and positive redox couples in different RFB chemistries.

In all-copper RFBs, when charging the battery, the electrochemical conversion of cuprous cation to cupric cation occurs (Cu^+/Cu^{2+}), while in the negative half-cell the metallic copper deposition/stripping takes place (Cu^+/Cu^0). During the battery charging, the Cu^{2+} permeation in the negative half-cell leads to the dissolution of the copper deposit. Hence, the comproportionating reaction results in the battery's self-discharge and unbalance of the electrolyte [262]. In this section, resulting from ref. [VII], scanning electrochemical microscopy (SECM) is evaluated as a method for the permeability investigation of RFB electroactive species (here Cu^{2+}) on membranes (results from ref. [VII]).

Several commercial and modified membranes were tested in a customized PTFE electrochemical cell with three electrode set-up by cyclic voltammetry and approach curves (AC).

The CVs were performed with the ultramicroelectrode working (UME) positioned away from the membrane in the solution bulk, they provide copper process information and are used to determine suitable conditions for the ACs. During the approach curve, the UME SECM probe was stepped from the solution bulk toward the membrane. If the species is present, the recorded current can be correlated with the concentration of copper (II) in space, by biasing the UME in order to reducing copper (II). ACs can be used to visualize the Cu(II) diffusion profile evolution over time. In combination with modelling, these measurements return quantitative and qualitative information on membrane permeability to electroactive species of interest.

- Experimental section

The electrolytes used in the SECM measurements were obtained from calcium chlorides dehydrates (>99%, ACS reagent, Sigma Aldrich, Merck KGaA, Darmstadt, Germany) and copper (II) chloride dehydrates (99.99 + %, Sigma Aldrich).

Commercial and modified membranes were tested and reported in Table 7.16. Commercial membranes were kept in water. Modified membranes consist of commercial membranes coated with sulfonated poly(ether-ether-ketone) (SPEEK). Poly(ether-ether-ketone) sulphonation was carried out in sulfuric acid at 80°C for four hours under vigorous stirring. Then, the dry SPEEK polymer was dissolved in NMP and cast on the substrate. Different composite membranes were obtained with the described method, which is indicated with “SP” after the substrate name (DAR-SP). Dar-SP50, Dar-SP75, and Dar-SP100 were obtained using different amounts (12.5, 12.5 and 7.5 wt%, respectively) and loadings (50, 75, and 100%, respectively) of SPEEK during the coating with the addition of thermal treatment at 80°C [300]. In particular, various amounts (wt.%) of a cross-linker were added to the reported amount of SPEEK solutions, stirred for 30 min, and cast onto a glass plate after vacuum outgassing for 30 min. The samples were dried and then thermally treated under vacuum at 150 °C for a few more days.

Label	Membrane	Type	Thickness	Supplier
Dar	Daramic	Porous	0.9 mm	Daramic®
NAF115	Nafion 115	CEM	127 μm	Nafion™
FAP330	Fuma Tech FAP-330	AEM	33 μm	Fuma Tech
FS950	Fuma Tech FS-950	CEM	50 \pm 5 μm	Fuma Tech
Dar-SP	Daramic+SPEEK	Porous+CEM	922 \pm 2 μm	-
Dar-SP50	Daramic+SPEEK	Porous+CEM	922 \pm 2 μm	-
Dar-SP75	Daramic+SPEEK	Porous+CEM	922 \pm 2 μm	-
Dar-SP100	Daramic+SPEEK	Porous+CEM	922 \pm 2 μm	-

Table 7.16. List of RFB membranes tested.

The measurements were carried out in the air with a 910B SECM (CH Instruments) coupled with a bipotentiostat (range, ± 10 V). SECM motors and piezoelectric components controlled the UME movements. The potentiostat was used to bias the UME and/or at the substrate versus the reference electrode and to measure all the currents. The SECM probe (CH Instruments) was a Pt ultramicroelectrode (UME) with a diameter of 10 μm and RG of 10 (overall radius of the electrode/Pt radius), sealed in a glass capillary under vacuum. The tip was cleaned before use with diamond paper, put under a sonicator bath for few seconds, and carefully dried.

An SECM cell was specifically designed (Figure 7.31) to separate the two different solutions of the half-cells with a membrane. The solutions are not in contact, and any passage from one compartment to the other can only occur through the membrane. The upper SECM semi-cell accommodate the counter (Pt wire) and the reference electrodes (Ag/AgCl). A Pt ultramicroelectrode (UME) probe serves as the working electrode. The bottom part of the cell was filled with 50 mM CuCl_2 solution as a copper source, while the upper part of the cell was filled with 50 mM CaCl_2 . The equal concentration contributes to the decrease of the osmotic contribution to mass transport. The UME was used in the upper cell and approached the membrane from above at 25 $\mu\text{m s}^{-1}$. The permeation of the species causing unwanted self-discharge phenomena can be followed as a function of the faradic current due to the permeated species recorded at the UME probe. The copper permeation was investigated by keeping the SECM probe at four micrometers from the membrane surface, showing the concentration in the bulk

solution. These measurements also allow time-resolved studies and kinetics studies elucidating the membrane performance over time and in working conditions.

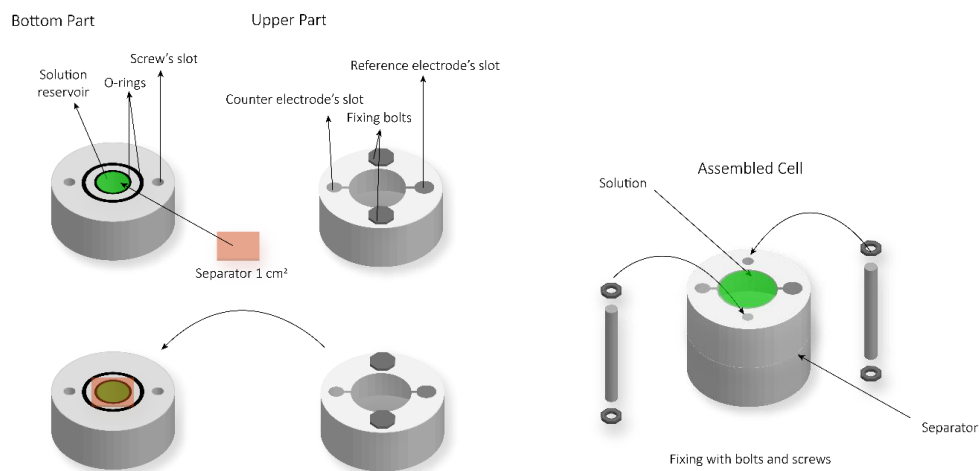


Figure 7.31. Scheme of the SECM cell made in Aalto University.

Static contact angle measurements were performed on the selected membranes using a KSV CAM101 instrument under ambient conditions by recording the side profiles of electrolyte drops for image analysis. The shape of the drop was recorded in a time range of 10 s by collecting an image every 0.2 ms. At least five drops for each sample were tested.

- Results and Discussion

Various membranes were tested by cyclic voltammetry with the ultramicroelectrode working (UME) positioned 4 mm away from the membrane in the solution bulk. These CVs (Figure 7.32a) provide copper process information and are used to determine suitable conditions for the ACs. During the approach curve, the SECM probe (UME) was stepped from the solution bulk toward the membrane. By biasing the UME toward reducing copper (II), if the species is present, the recorded current can be correlated with the concentration of Cu(II) in space. ACs at increasing times can be used to visualize the Cu(II) diffusion profile evolution in time. In combination with modelling, these measurements return quantitative and qualitative information on membrane permeability to electroactive species of interest.

For example, in a porous membrane, Cu(II) starts immediately to pass through the membrane (Figure 7.32b), and during the AC we see the diffusion front advancing.

Depending on the Cu(II) concentration in bulk, typical copper processes can also be observed in the voltammogram. As the copper continues to cross the membrane driven by diffusion (Figure 7.32c), the diffusion front advances and becomes less pronounced. Then, copper also starts to arrive in the bulk, and the current detected by the AC grows far from the membrane (Figure 7.32d). After 24 hours, the presence of copper in bulk is massive and clearly visible (Figure 7.32e). The current feedback on the membrane indicates whether the copper is still diffusing from the membrane (positive) or the solutions reached a steady state (neutral or negative).

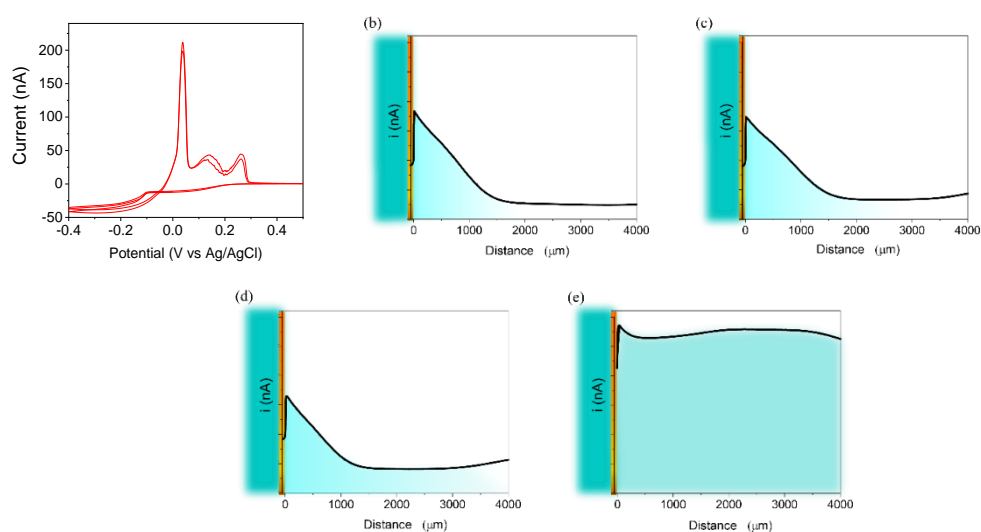


Figure 7.32. (a) Typical CV at 0.05 V s^{-1} on Pt UME showing the copper processes. (b-e) evolution of the approach curve showing the copper diffusion, (b-e) evolution of the approach curves over time.

Figure 7.33a-d reports the voltammograms and the copper concentration obtained from the approach curves of different commercial membranes. After 2 hours from CVs at 0.05 V s^{-1} , the copper deposition stripping process clearly shows the presence of Cu(II) in the solution bulk (Figure 7.33a). In the approach curve (Figure 7.33b), the current response below 1 nA demonstrates a low Cu(II) presence. When the UME approach the membrane, the current signal increases demonstrating an increasing copper concentration. The lowest current is detected with FAP330 showing a minor permeability to Cu(II) cations. This agrees with the AEM nature of the membrane. FS950 and NAF115 show comparable currents as the similar molecular structure of the cation exchange polymer. The difference between the two membranes is in terms of thickness, NAF115 is the thicker membrane, which results in longer times to

observe the same diffusion (lag time). After 24 hours, a not-selective membrane as DAR shows higher currents, while AEM FAP330 shows high copper blocking capabilities. Even after 24 hours, the UME feedback on the membrane is positive, testifying that Cu(II) diffusion is still occurring.

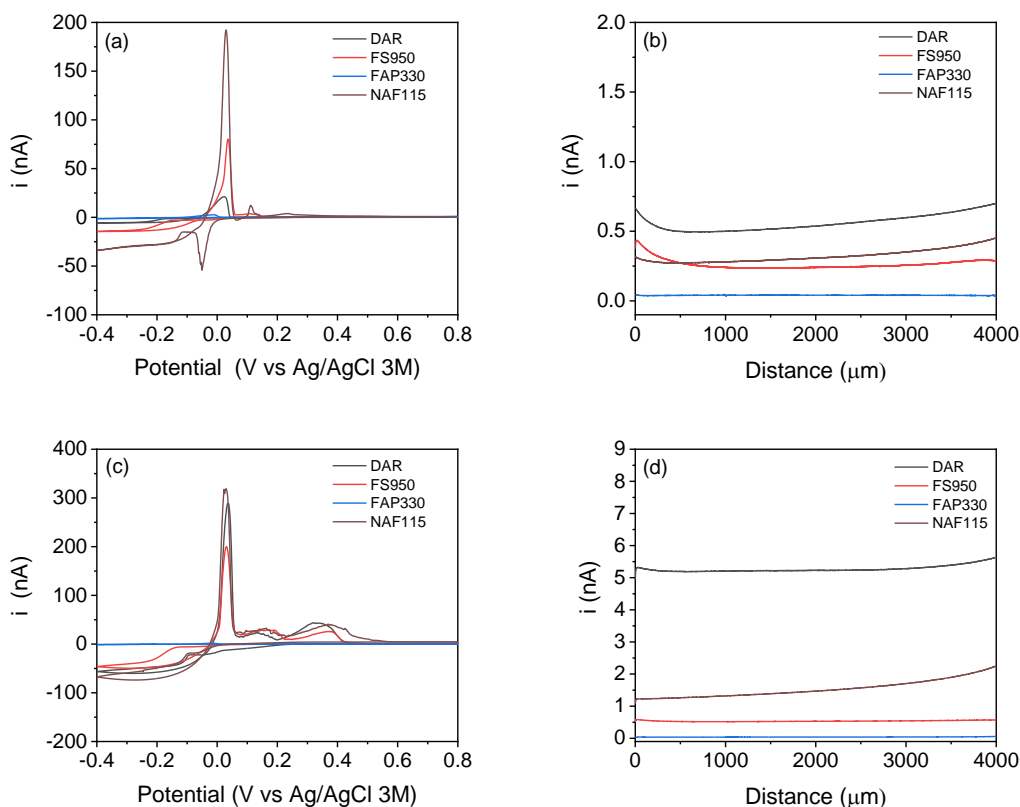


Figure 7.33. SECM experiments on different commercial membranes, (a) CV after 2 hours in the solution bulk (v : 0.05 V s^{-1}), (b) approach curves starting from 4 mm away from the membrane stepped at $25 \mu\text{m s}^{-1}$), (c) CV after 24 hours in the solution bulk (v : 0.05 V s^{-1}), (d) approach curves starting from 4 mm away from the membrane stepped at $25 \mu\text{m s}^{-1}$). WE: Pt UME positioned 4 mm away from the membrane, CE: Pt wire, RE: Ag/AgCl 3M, upper solution: 0.05 M CuCl_2 , bottom solution 0.05 M CaCl_2 .

The results obtained with commercial membranes show the reliability of the methodology presented. Thus, the Cu(II) permeability results in the order porous>CEM>AEM, as expected. In addition, the thickness of two CEM membranes seems relevant, retarding the Cu(II) crossover.

The described methodology can be used to test the effectiveness of membranes. In this case, differences in Cu(II) concentration can be used as an easy tool to guide

membrane optimization. In the present work, DAR porous polypropylene membrane has been modified with SPEEK polymer, exhibiting CEM selectivity (Figure 7.34a-d).

After 2 hours, DAR bare membrane shows the highest current in CV and approach curve (Figure 7.34a,b). The SPEEK modification results in lower Cu(II) crossover as visible after 2 hours. In such a small time-scale, DAR-SP and DAR-SP75 showed the lowest current corresponding to low Cu(II) crossover. As the Nafion membrane is the most employed CEM in RFBs, it is used as the benchmark for the reported system. DAR-SP100 results in a less selective membrane; this can be due to less amount of SPEEK dissolved in the casting solution. On the other hand, DAR-SP50 shows a lower current with respect to NAF115. As expected, after 2 hours, the feedback is still positive demonstrating that the Cu (II) cations are still passing through the membranes. After 24 hours (Figure 7.34c,d), all the modified membranes shows advances for DAR bare membrane except for the DAR-SP75. It must be considered with increasing time, the Cu(II) cations pass through the membrane driven by diffusion. Also, in this case, the current increases approaching the membrane, indicating that no-steady state is reached. Among the tested membranes, DAR-SP100 and DAR-SP75 showed completely different results in a longer time scale. DAR-SP75 passed from being the best performing membrane to be the more permeable, while DAR-SP100 allowed less copper to pass through the membrane. This can be attributed to the different wettability of the membranes.

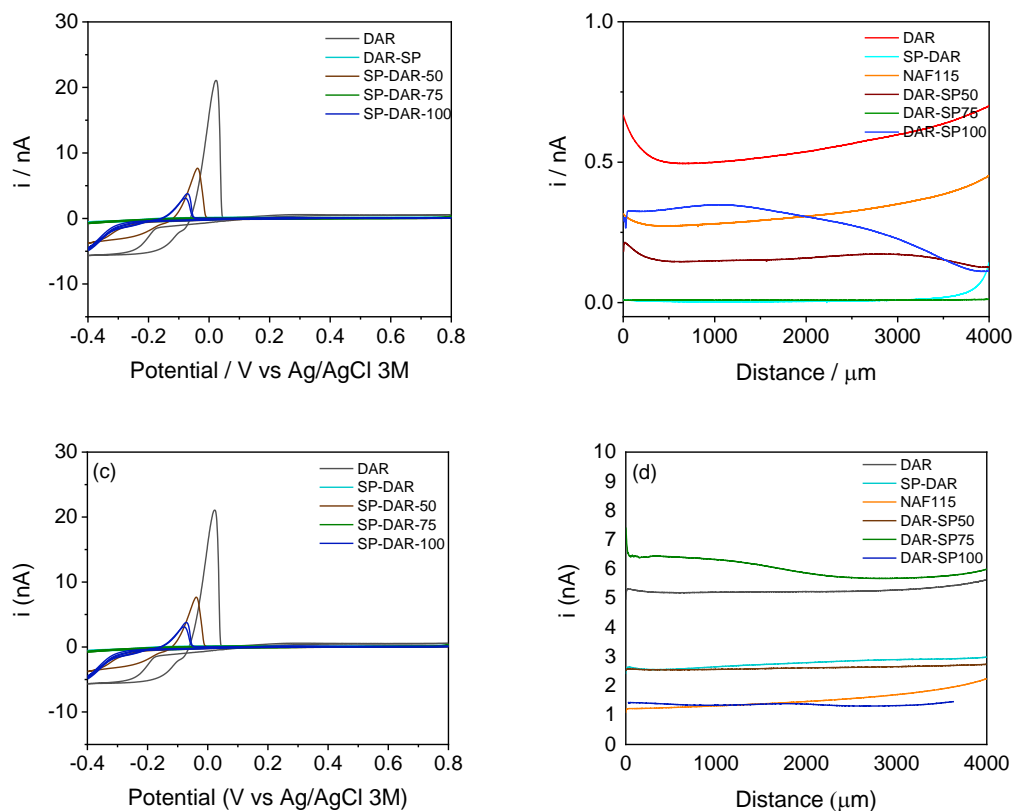


Figure 7.34. SECM experiments on different modified membranes: (a) CV after 2 hours in the solution bulk (v : 0.05 V s^{-1}), (b) approach curves starting from 4 mm away from the membrane stepped at $25 \mu\text{m s}^{-1}$), (c) CV after 24 hours in the solution bulk (v : 0.05 V s^{-1}), (d) approach curves starting from 4 mm away from the membrane stepped at $25 \mu\text{m s}^{-1}$). WE: Pt UME positioned 4 mm away from the membrane, CE: Pt wire, RE: Ag/AgCl 3M, upper solution: 0.05 M CuCl_2 , bottom solution 0.05 M CaCl_2 .

To have a more impactful visualization of the copper concentration, the current recorded in the approach curve can be correlated to the active species concentration by Equation (50)

$$i = 4 \cdot n \cdot F \cdot r \cdot D_{\text{Cu(II)}} \cdot C_{\text{Cu(II)}}^0 \quad (50)$$

where n is the number of electrons, F is the Faraday constant, r is the UME's radius, $D_{\text{Cu(II)}}$ is the diffusion coefficient ($1.2 \cdot 10^{-5} \text{ cm}^2 \text{ s}^{-1}$ [301]), and $C_{\text{Cu(II)}}^0$ is copper concentration. The copper concentration was verified spectroscopically to assess the diffusion coefficient used. Results are summarized in Table 7.17.

Membranes	2 h	24h
FS 950	0.19	0.25
FAP330	0.02	0.02
NAF115	0.13	0.51
DAR	0.28	2.21
DAR-SP	<0.01	1.12
DAR-SP50	0.06	2.70
DAR-SP75	<0.01	0.61
DAR-SP100	0.15	1.08

Table 7.17. Copper concentrations [mM] in the upper part of the SECM cell during the experiments after 2 and 24 hours obtained from the approach curves (500 μm from the membrane).

As be noted that the initial copper (II) solution is 50 mM. Hence, the maximum concentration that can be reached is 25 mM. In two hours, the copper concentration coming from the crossover ranges in the sub-micromolar amounts. It increases up to 2-3 mM just in the case of unselective DAR and DAR-SP50 membranes. As expected, CEMs and AEMs are less permeable (20 μM in 24 hours for FAP330). However, SPEEK-modified membranes represent a promising compromise between cost and performance comparable to Nafion membranes.

Membrane wettability is one essential aspect of a well-performing membrane in an electrochemical cell. Ideally, in RFBs, the membrane should be wettable and ionic conductive for the charge carriers. Thus, the best membrane, being selective, should be highly compatible with aqueous systems. Wettability was evaluated by contact angle measurement, where the angle between a water droplet and the membrane surface is monitored by a camera (Figure 7.35a-h). Contact angle measurement is a qualitative way to evaluate whether the surface has hydrophobic or hydrophilic behaviour, which is based on the effect of the different intermolecular interactions between the surface and a drop of water when the drop meets the surface, resulting in different surface tensions. For a surface exhibiting a hydrophobic character, the contact angles of an aqueous droplet are expected to be closer or even higher than 90°. Contrarily, a surface with hydrophilic properties shows contact angles smaller than

65° [298]. DAR membrane shows the most hydrophilic surface with angles c.a. 52°, and commercial CEM and AEM membranes show a more hydrophobic surface around 80°C. From this point of view, membrane modification with SPEEK increases the hydrophobicity of the scaffold (DAR) with a result still lower than other IEMs.

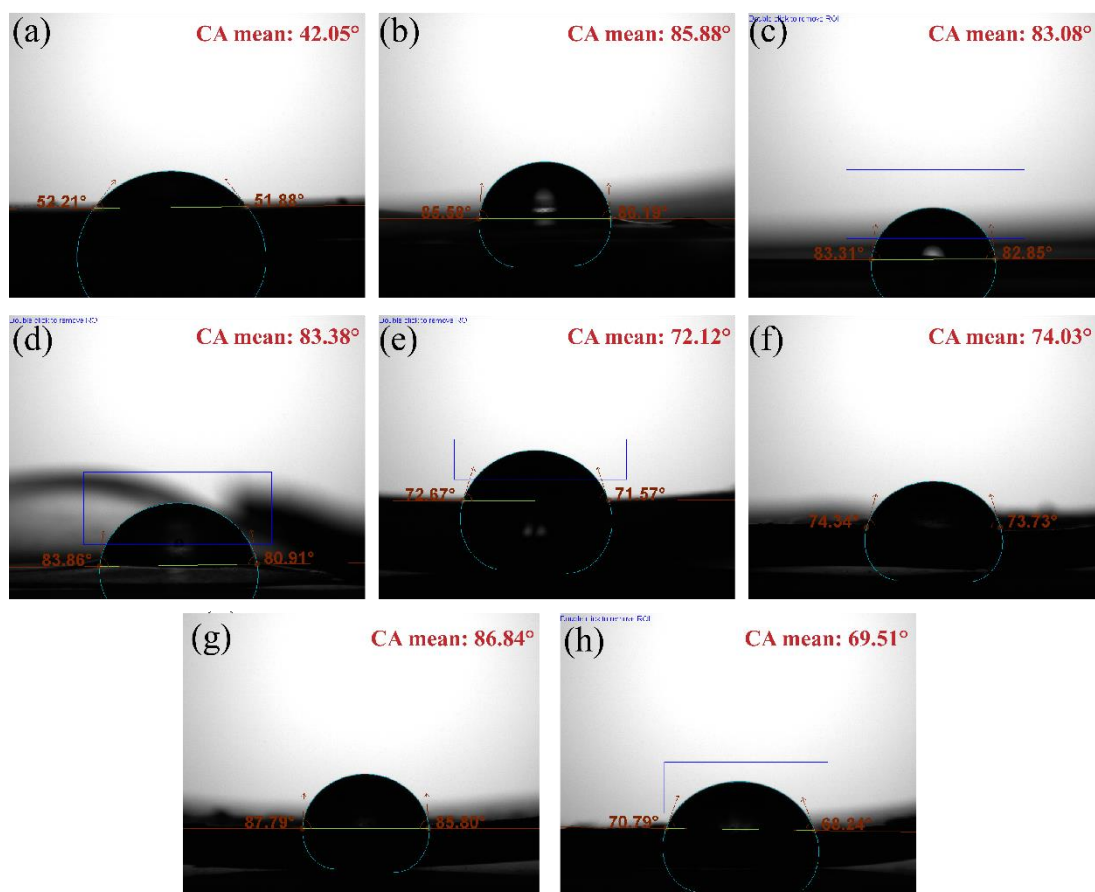


Figure 7.35. Contact angle picture after 10 s from the water drops meeting with the surface of DAR (a), FS950 (b), FAP330 (c), NAF115 (d), DAR-SP (e), DAR-SP50 (f), DAR-SP75 (g), DAR-SP100 (h).

Further details can be found by looking at the behaviour of the contact angle during the time. On a wettable surface, the water drops are absorbed progressively and, correspondingly, the angle decreases. Contrarily, by increasing the hydrophobicity, surfaces tend to absorb slower the water drop. Figure 7.36a,b shows the variation in the contact angle in 10 seconds. Porous membrane (DAR) shows the highest hydrophilicity and wettable surface. Indeed, the starting angle of 57° progressively decreases, approaching 52°, demonstrating the high wettability of the surface. CEM membrane as NAF115 and FS950 have a more hydrophobic surface with an angle that

increases due to a slight membrane deformation if wetted. It must be considered that all the membranes selected form angles with water lower than 90° , indicating a hydrophilic surface.

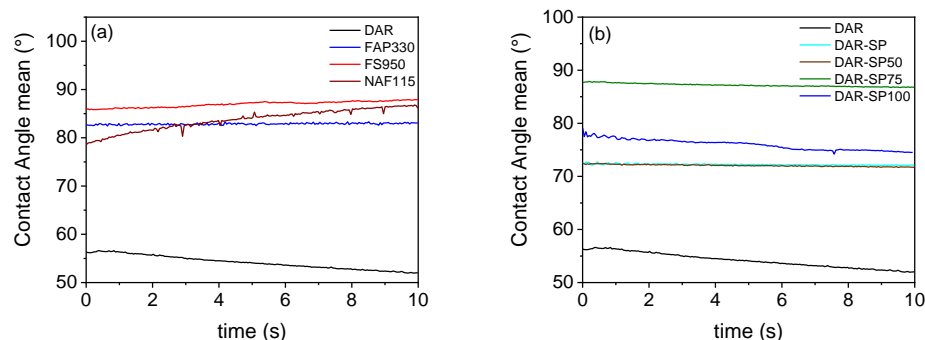


Figure 7.36. Contact-angle variation vs time.

As shown by Figure 7.36b, the coating of DAR with SPEEK increases its hydrophobicity, but DAR-SP100 shows a well-wettable surface, as can be seen by the continuous angle decreasing. Hence, in the SECM cell, it is wetted faster than other membranes, showing higher permeability to Cu(II) on short time-scales (Figure 7.32b) but higher selectivity at long time-scales. On the other hand, DAR-SP75 has a slower water absorption. Indeed, at short time-scales the membrane is not well-wetted, and eventually possible, permeation of copper cations is hindered. At longer time-scales, the membrane is soaked, and copper cations can pass through it. Consequently, the DAR-SP100 which results competitive with the other CEMs, prevents the permeation of Cu(II) ions even when the amount of SPEEK is lower.

In conclusion, in all-copper redox flow batteries (RFB), the membrane must solve the problem of Cu(II) crossover. It has been demonstrated that SECM can be used as a powerful tool to evaluate the permeability of membranes to Cu(II). The methodology presented results consistent for a model system with commercial membranes with different selectivities. As expected, an AEM resulted in the membrane with the lowest permeability to Cu(II). In addition, SECM can be used to study the permeability in modified systems. This approach can assist in optimizing the system and guiding it to the most suitable solution. Thickness and wettability of the system play essential roles in evaluating the membranes, contributing to understanding the permeation in different time scales. The described results will be completed by a theoretical model able to fit

the AC at different times, providing quantitative information about permeability. This methodology can be integrated and adapted for studying the membrane permeability at every redox active species employed in Redox Flow Battery.

7.5. SoC sensors

One of the most significant drawbacks of RFBs is the crossover of the active species, leading to electrolyte unbalancing or self-discharge. For this purpose, it is fundamental to monitor the state of charge (SoC) during the RFB operation to recognize the need for rebalancing or restoring the electrolyte and prevent system failure [303]. Different SoC monitoring methods have been investigated, such as real-time conductivity measurements of the electrolytes [304, 305], the open-circuit voltage (OCV) [306], and the potentiometric titration [307].

For example, conductivity measurements allow the SoC monitoring just under constant temperature and concentration in which conductivities of anolyte and catholyte vary linearly as a function of SoC. Usually, the RFB system's temperature varies to minimize costs. Hence, the need to collect various calibration data in different temperature ranges. Titration methods collide with the necessity of placing the electrodes in each half-cell reservoir, avoiding any interfering factor that drifts the electrode potential [304]. Last, OCV calculation needs deep modelling of the battery based on a deep knowledge of the battery chemistries [308].

UV/Vis/NIR spectroscopy is a suitable technique for real-time SoC monitoring. The independence from temperature and electrochemistry of the sample paves the way for developing sensors that could be integrated into the electrolyte reservoir, which are able to detect the oxidation state of the species in solution [309].

For this reason, the UV/Vis/NIR spectroscopy method was investigated for vanadium RFB (VRFB) [309] and Organic RFB [310]. All copper RFB has the advantage of efficiently monitoring the absorption spectrum in the positive half-cell. In the latter, the electrochemical conversion of Cu(I) to Cu(II) occurs and spectral properties change during operation.

These studies help increasing the control of the processes occurring in the CuRFB by understanding copper spectral characteristics. As described in Section 7.2, the Cu(II) absorption spectrum is characterized by two prominent bands of different electronic natures as shown in Figure 7.37.

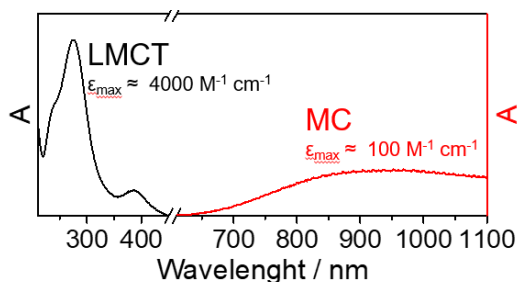


Figure 7.37. Typical absorption spectrum of a Cu(II) electrolyte in 6 M HCl.

A ligand-to-metal charge transfer transition in the UV part of the spectrum is present, which strongly depends on the copper solvation shell (information about the Cu(II) choro-complexes speciation). Meanwhile, a broad metal-centered transition (MC) present in the NIR region can be simplified to an electronic transition involving the orbital of the Cu(II). In this transition, the chloride coordination can be ignored, and the magnitude of the absorption mostly depends on the Cu (II) concentration.

The Lambert-Beer Equation (51) describes the light absorbance recorded in these measurements.

$$A = \epsilon b [c] \quad (51)$$

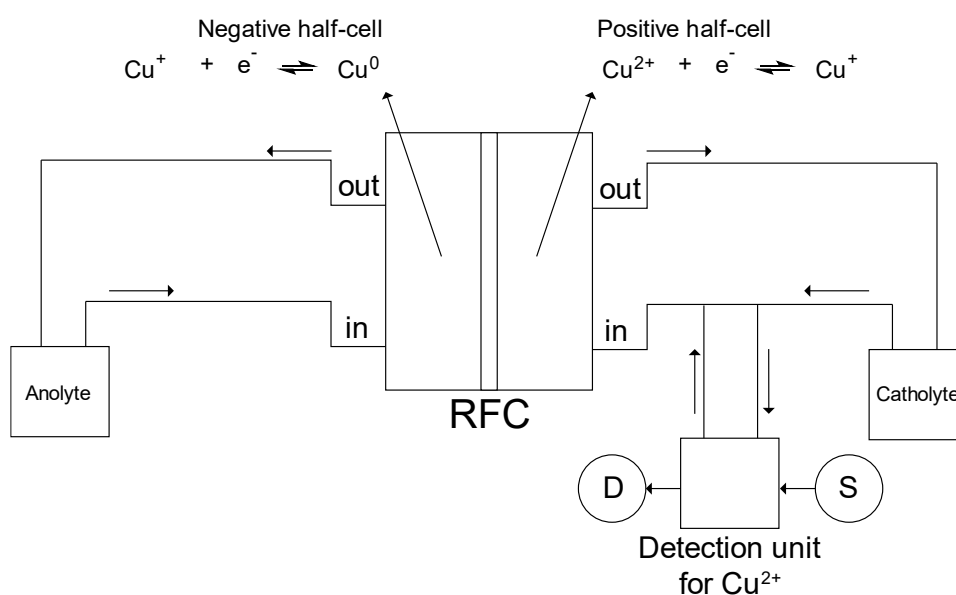
where b is the optical path, ϵ is the molar extinction coefficient, and $[c]$ is the molar concentration of the active species. Generally, MC transitions are usually much less intense than LMCT transitions due to ≈ 15 times lower ϵ . MC bands allow studying highly concentrated systems by tuning b thickness. In addition, the MC transition is not present in the Cu(I) absorption spectrum, which simplifies the data elaboration (no deconvolution required). However, an optimal SoC monitoring system could perform SoC measurements on the anolyte/catholyte independently, so that the onset and extent of problems may be quantified and accounted for. In this Section, regarding the activity of ref. [VIII], two different spectrophotometric approaches will be described to develop a SoC monitoring system both for negative and positive half-cells.

Systems description

For SoC determination, the reversible electrochemical conversion of Cu(I) to Cu(II) occurs at the positive electrode. Limiting to this half-cell, the SoC can be written as a function of the Cu(II) concentration (52).

$$SoC(\%) = \frac{[Cu(II)_x]}{[Cu(II)_{max}]} \times 100 \quad (52)$$

where the $[Cu(II)_{max}]$ is the maximum molar concentration of Cu(II) (2M), and $[Cu(II)_x]$ is the Cu(II) molar concentration in the positive half-cell after an x amount of charge. Hence, non-destructive Cu(II) determination can be used to calculate the SoC of an operating battery. The electrolyte flowing from the positive reservoir can be tested in flow with a detection unit constituted by a light source (S), the sample and a single wavelength detector (D) as showed in Scheme 7.2.



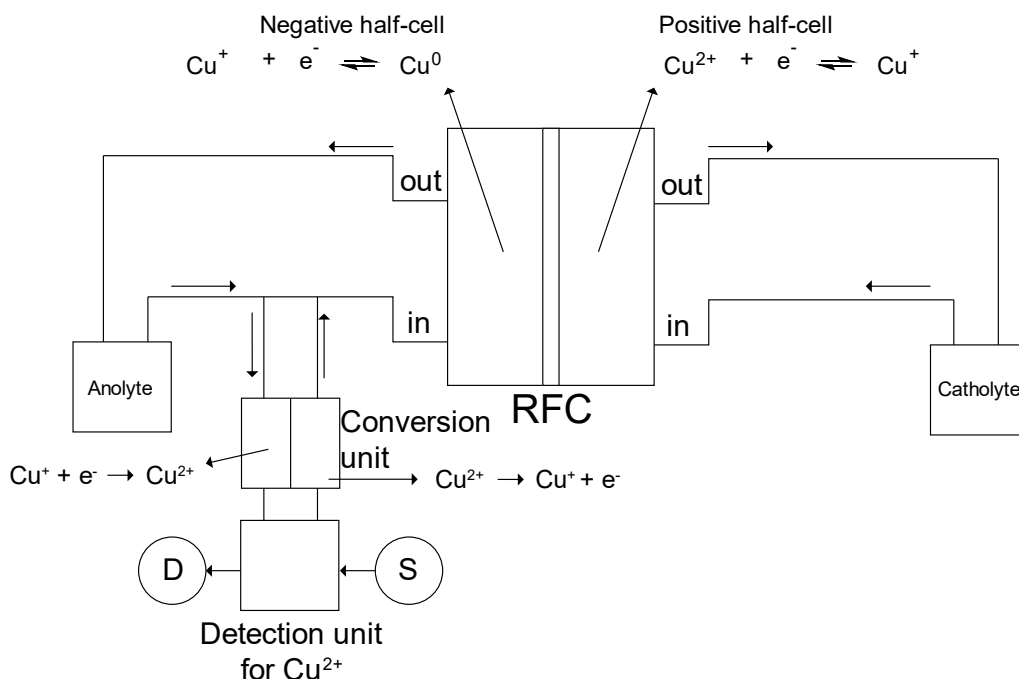
Scheme 7.2. Positive half-cell detection scheme.

In this section, the detection system is a UV/Vis/NIR spectrophotometer. Nevertheless, after properly determining of the testing, conditions could be replaced by a small led/diode laser and a single-wavelength detector (e.g., colorimeter).

In the negative half-cell, the electrochemical process consists of the copper deposition/stripping from Cu(I). In this half-cell, copper (II) must not be present, otherwise Cu(II) comproportionate with Cu(0), leading to the battery self-discharge. For this purpose, the observation of Cu(I) is difficult due to the high intrinsic absorptivity of the absorption band in the UV region of the spectrum. As discussed in the Section 7.2, Cu(I) does not show the MC transition. In order to determine the Cu(I) concentration, the Cu(I) can be converted reversibly in Cu(II) before the detection unit, as reported in Scheme 7.3. The detection unit can be used with the same set-up as for

the positive half-cell electrolyte. After flowing through the detection unit, the Cu(II) must be converted back to Cu(I) before returning to the cell's flow system.

The copper conversion system can be designed as a small Redox flow cell that converts Cu(I) into Cu(II) in one half-cell and reconverts Cu(II) to Cu(I) in the other half-cell. This cell can work with low flow capacity and voltage to limit energy consumption.



Scheme 7.3. Negative half-cell detection scheme.

- Experimental section

Electrolytes tested were prepared with CuCl_2 (99.99 + %, Sigma Aldrich), CuCl ($\geq 99.995\%$ trace metal basis, Sigma Aldrich), HCl (37%, Sigma-Aldrich), CaCl_2 ($\geq 99\%$, ACS reagent, Sigma Aldrich) were used as received.

Preliminary spectro-electrochemical measurements were carried out using a Biologic SP300 potentiostat/galvanostat/FRA. The absorption spectra were acquired with a Perkin Elmer UV/VIS/NIR Spectrophotometer Lambda19 (PerkinElmer, UK) in 0.25 mm quartz cuvette (ALS, Japan) with three electrode set-ups. Pt mesh was used as working electrode (WE, A: 0.691 cm^2), Pt wire as CE and Ag/AgCl reference electrode (RE, ALS, Japan) as reference electrode. All the solutions were deaerated for 15 minutes in Ar and the cuvette was sealed for maintaining the Ar atmosphere during the experiments.

A home-made cell (Figure 7.38) is used both as redox flow cell and a conversion unit. The cell is composed by reticulated vitreous carbon (RVC 100 ppi) electrodes with titanium grids current collectors and silicon gaskets. Fumatech FAP330 AEM separates the two compartments. The electrochemical testing was performed with a flow rate of 10 mL min^{-1} (referred to pure water), by using a peristaltic pump (model 323, Watson Marlow) with Marprene tubes. The reservoirs with 50 mL electrolyte each were kept in a thermostatic bath (Julabo Labortechnik GmbH) at $60 \text{ }^\circ\text{C}$. For operando experiments, a flow cuvette (optical path $50 \text{ }\mu\text{m}$) was connected to the hydraulic circuit and positioned in the spectrophotometer. The absorbance was monitored at a λ_{obs} of 920 nm , recording the value every 0.1 s .



Figure 7.38. Components of the home-made redox flow cell.

- Results and discussions

The development of a suitable sensor for SoC determination in the positive electrolyte is also propaedeutic for the negative system described. For this purpose, spectroscopic condition for estimating the Cu(II) concentration is required. Firstly, spectroelectrochemical measurements were performed in a spectroelectrochemical cell with operando monitoring of Cu(II) MC transition ($\lambda_{\text{obs}} = 920 \text{ nm}$).

Spectroelectrochemical experiments were carried out in a three-electrode configuration by chronoamperometry, simulating the charge-discharge cycle of the positive compartment of the CuRFB. Galvanostatic experiments consist of two cycles with different current densities (Figure 7.40a and 7.40b). The Cu(II) concentration (Figure 7.40c) was estimated as shown in Equation (52) and (53):

$$[\text{Cu}^{II}]_{\text{pot}} = \frac{Q(\text{C})}{\frac{F}{V}} \quad (52)$$

$$[\text{Cu}^{II}]_{\text{opt}} = \frac{A}{\varepsilon b} \quad (53)$$

The absorbance profile in Figure 7.40c (related to the concentration of Cu(II)) reliably traces the potential curve. Figure 7.40b, reports the copper concentration obtained from the charge and absorbance. The two signals show comparable Cu(II) concentrations.

Two main aspects must be considered: (1) even if the optical path of the spectroelectrochemical cell is 0.5 mm, 0.5 M of Cu(II) is considered the maximum concentration detectable with this set-up to remain in the limit of linearity of the Lambert-Beer Equation. (2) in the spectroelectrochemical cell, counter and working electrode are not separated by a membrane. Thus, the Cu(II) just formed can freely diffuse far from the optical path, leading to a negative deviation in concentration detected.

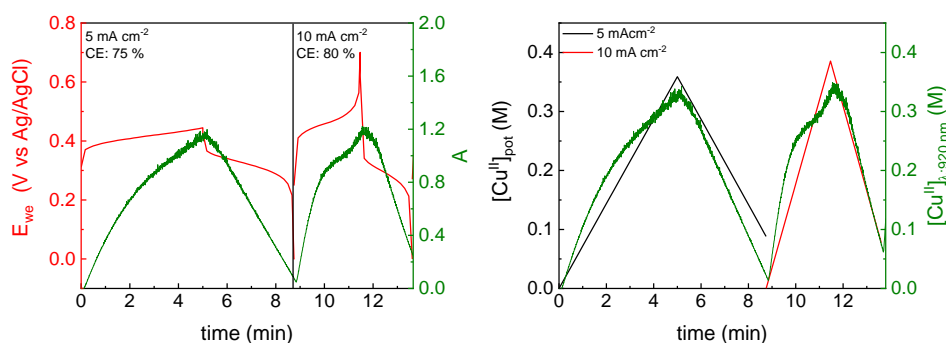


Figure 7.40. Experiment in the spectro-electrochemical cell (b : $500 \mu\text{m}$) set-up (a) composed by Pt grid working electrode, Cu grid counter electrode, saturated Ag/AgCl RE in a $30\mu\text{L}$ 0.5 M CuCl_2 6 M HCl electrolyte. In operando monitored absorbance of the Cu(II) absorption band ($\lambda_{\text{obs}} = 920 \text{ nm}$) during galvanostatic cycling. (c) estimated Cu(II) concentration during the experiment.

The SoC monitoring system of the positive half-cell was tested in a flow cell. To minimize the system's complexity, a symmetric RFC was assembled using RVC electrodes, FAP330 anion exchange membrane, and 50 mL of 1 M CuCl , 0.5 M CaCl_2 , 6 M HCl electrolyte flowed at 20 mL/min . The absorbance at 920 nm was monitored during Cu(I) oxidation to Cu(II) in galvanostatic mode (10 mA cm^{-2}). Spectroscopic operando monitoring allows calculating the system's real-time SoC (Figure 7.41) by Equation (52). The absorbance variation results are characterized by two different slopes that can be connected to two different regimes. (Q_{max}). Figure 7.41c reports the charge obtained from the real-time absorbance monitoring (Q_{eff}) versus the integral of the current over time. The slope of the represented curve is related to the process efficiency η . In the first two hours, the spectroscopic efficiency of the electrochemical process monitored results at 95% . After that, it decreases to 71% . The lower efficiency can be attributed to the crossover of the species through the membrane and not to an

electrochemical process. Indeed, if copper cations cross the membrane, the catholyte results depleted in terms of Cu(II) concentration. This results in a lower absorbance and, so, in a lower Q_{eff} , decreasing the efficiency.

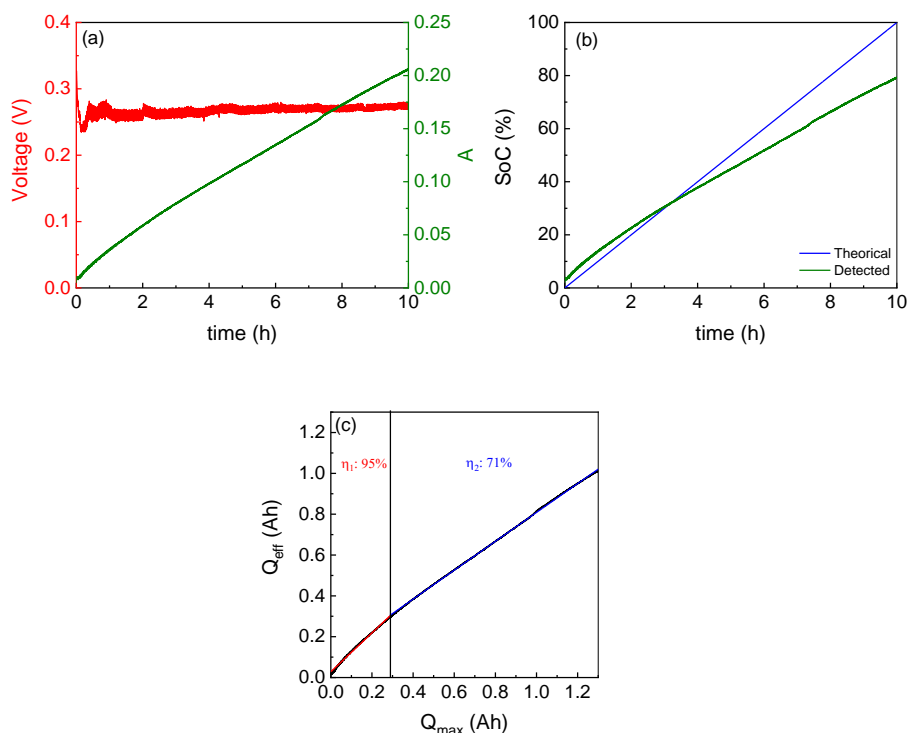


Figure 7.41. (a) Real-time absorbance monitoring (λ_{obs} 920 nm) of the oxidation of Cu(I) to Cu(II) at 10 mA cm^{-2} , (b) SoC derived from the absorbance variation, (c) charge derived by the absorbance vs integral of the current over time. Symmetric RFC with RVC electrode, RVC electrodes, FAP330 membrane, and 50 mL of 1M CuCl, 0.5 M CaCl₂, 6M HCl electrolyte (20 mL/min).

The presence of parasite process as the copper crossover is one of the main problems that must be solved in RFB systems. The work presented in this section consists of the preliminary results of an ongoing study. The copper crossover hypothesis will be further validated by studying the effect of the membrane on the Q_{eff} vs Q_{max} curve. The following steps will include developing the system presented for the negative half-cell and combining the two for a complete SoC monitoring system.

7.6 Applications and specifications

As described in Chapter 6, RFBs are candidates for large-energy storage systems. For this purpose, many RFB systems share some peculiarities that can be compared with well-known LiBs. The many advantages and disadvantages over present lithium-ion storage systems make clear the concept of energy storage system diversification. RFBs can allow: >90% depth of discharge capability daily.

- High-capacity retention enabling 5000+ cycles.
- Low fire risk as aqueous electrolyte.
- No need for cooling systems (heating system can be required).
- Use of low cost and earth-abundant materials.
- Potentially easy of end-of-life recycling due to the modular architecture.

On the other hand, these systems show:

- Lower energy and power densities.
- Lower round trip efficiency than Li-ion.

Theoretically, an RFB can be totally discharged without damaging the electrodes and the electrolytes, ensuring low-capacity losses. However, specific specifications depending on the chemistry of the system. Table 7.18 summarizes the specification of many RFBs systems (including CuRFBs).

	Volumetric Energy density Wh L ⁻¹	Power density mW cm ⁻²	Electrolyte cost \$/kWh	System cost \$/kWh	Refs
Vanadium- based RFBs	25–70	100-370	80	200–750.	[310]
Zinc-based RFBs	40	100	5-40	200	[311-314]
Organic	5-25	1-10	50	-	[315]
All-Iron	11.5	50	6	110	[316]
All-copper	20	37	50	80-160	[260]
LiBs	250	10-30	-	350-550	[32, 36]

Table 7.18. Practical achieved volumetric energy and power densities and costs for different battery technologies.

It must be considered that many technologies are still on a lab scale, and practical energy densities closer to the theoretical one are needed. However, none of the RFBs in Table 7.18 shows energy density comparable with that of LiBs. Nevertheless, because of their moderate cost, modularity, and flexible operation, RFBs are promising for stationary applications [317].

8. Conclusions

The investigation of fundamental processes and the study of new materials and methodologies are essential for the development of new technologies. In this thesis, the attention has been mainly focused on lithium-based technologies and redox flow batteries (RFB), which are electrochemical systems covering most of the energy and power requirements needed for the electrification of our society.

Among electrochemical energy storage, lithium-ion batteries are one of the most used. For this system, the attention was focused on materials and fundamental aspects of negative electrodes. The reversible insertion of ions in the lattice of the electrodes often implies volume changes. During operation, the very negative potentials cause electrolyte reactions forming the solid electrolyte interphase (SEI). These reactions are often accompanied by gas evolution. New methodologies to investigate the dilatation phenomena are required to predict the lifetime and long-term stability of the cell. For this purpose, the thickness variation of the graphite-model electrode in carbonate-based electrolytes was tested by in-situ electrochemical dilatometry (developed in collaboration with Marposs S.p.a.), revealing simultaneous processes (insertion/deinsertion, solvent evaporation, SEI formation, gas evolution, and exfoliation). A distinctive feature of the instrument allows the variation of the external force applied to the cell. Insertion/deinsertion process at different forces helps to distinguish the volume expansion from gas evolution.

From the materials side, a valuable approach to overcome the energy and sustainability limits of LiBs consists of obtaining graphite by sustainable synthetic strategies. For example, carbon dioxide transformation technology is a valuable approach to use CO₂ captured in industrial processes and, by indirect way, to contribute to the decrease of CO₂. Alternatively, other materials have been studied to substitute graphite. Manganese oxides have attracted significant attention as negative electrode materials thanks to the multiple valences, the earth-abundancy, and one of the lowest potentials for the conversion reaction compared to other metal oxides. In Chapter 4, a new carbon-Mn oxides composite was obtained by molten salt CO₂ capture and electrochemical transformation (MSCC-ET) method. In the synthesized composite, manganese oxides are present as nanocrystals embedded in the carbonaceous matrix, as coherently demonstrated by chemical-physical characterization studies. The

obtained material had been tested as a negative electrode for LiBs with an environmentally sustainable aqueous process. The electrochemical conversion of manganese is demonstrated as the principal faradic process contributing to the electrode capacity. However, varying the specific current, the electrode capacity approaches the theoretical graphite capacity asymptotically. At the same time, charge-discharge cycles at 0.1 A g^{-1} show the feasibility of the manganese oxide phase cycling with high specific capacity (c.a. 400 mAh g^{-1}). The electrochemical properties of the presented material ought to be optimized, mainly in terms of adhesion to the current collector and granulometry of the active material.

One strategy to overcome the energy density limits of LiBs is employing lithium metal anodes. On the one hand, lithium metal is the lightest metal in the periodic table, guaranteeing an enormous specific capacity (3860 mAh g^{-1}) and the most negative redox potential (-3.04 V vs. SHE). On the other hand, the uncontrolled dendritic deposition of lithium leads to safety concerns. In addition, similarly to graphite electrodes, the low negative potentials lead to the electrolyte decomposition forming a SEI. An unstable SEI lowers the $\text{CE}_{\%}$ and consumes electrolyte. In this framework, ammonium hexafluorophosphate has been used as an additive in a carbonate-based electrolyte to improve SEI characteristic. The electrochemical behaviour of Li symmetric cells in the selected electrolytes has been explored through galvanostatic deposition/stripping cycles and electrochemical impedance spectroscopy to evaluate the effect of additives on the electrochemical performance. A protic additive modifies the composition of the SEI, leading to stable cycling. Operando confocal Raman spectroscopy has been used to study lithium metal-electrolyte interphase in the presence of the additive in combination with in situ optical microscopy. During deposition/stripping at 0.5 mA cm^{-2} , real-time monitoring of the electrolyte signals evidenced that presence of the additive can assist the reaction of the electrolyte component to form the interphase. Increasing the current density to 1 mA cm^{-2} and the capacity and 1 mAh cm^{-2} , earlier stabilization of the interphase formation suggested that the role of the additive in the formation of the interlayer is electrochemically promoted. The activities described in Chapter 5 were carried out at the Division of Material Physics of the Chalmers Institute of Technology. Future efforts will be focused on the investigation of the interlayer composition.

As stressed many times in this thesis, global electrification requires a solution that fits different needs. For large stationary applications, RFBs are an ideal choice. Between the different chemistries that can be exploited, all-copper aqueous RFB (CuRFB), make use of low-cost, earth-abundant raw materials with a well-defined European supply chain. The CuRFB takes advantage on the three oxidation states of copper. As Cu(I) is not stable in aqueous media, the system is based on the chlorocomplexation of the copper cations. Indeed, it is fundamental to elucidate the speciation of copper (II) in diluted electrolytes to achieve better performance in CuRFB. Spectro-electrochemical test in diluted solution gives information on the electrochemical behaviour of electrolytes with a different chloro-complexes distribution. Monitoring the absorbance profile at two different wavelengths during the cyclic voltammetry shows the effect of copper chlorocomplexes stability on the spectrophotometric and voltametric hysteresis. In concentrated solutions, electrolyte composition was optimized by varying copper to chloride ratios, the concentration and the counter-ion of the chloride complexing agent. In particular, the effect of calcium chloride as supporting electrolyte was tested varying the Cu:Cl ratio, with 1:5 displaying the best performance. Using ammonium chloride, the conductivity increases up to 1000 mS cm^{-1} and improving the reversibility of the copper deposition-stripping processes, with a coulombic efficiency up to 80%. Also, orthophosphoric acid has been studied as additive to sequester calcium ions from the chloro-complexation equilibria. The increased availability of chloride anions leads to increased reversibility of the Cu(II)/Cu(I) redox process and higher Cu(II) diffusion coefficients.

On the electrode side, there is lack of information in literature about the electrode materials and their modifications. Carbon felts (CF) are interesting materials with low cost and adequate electrical conductivity. To improve the kinetics of the reaction, a thermal treatment of 6 hours at $400 \text{ }^\circ\text{C}$ was proved to be sufficient to improve the electrochemical performance of the electrode. This is an important result for the decreasing of the carbon footprint associated to the manufacturing processes. CuRFB needs the oxygen groups only assist the reaction by intermolecular interactions. The feasibility of the short heat treatment for polyacrylonitrile-based CF electrodes has been demonstrated in conventional electrochemical cell as also in an redox flow cell (RFC) configuration. Although the RFC assembly and components were not

optimized, an efficiency of 92% (30 mA cm^{-2}) and the ability to sustain currents up to 50 mA cm^{-2} were reached.

One of the main challenges in RFB research is the selectivity of the separator membranes. The essential function of a membrane is to isolate the ions of redox couples involved in electrode reactions, allowing the transport of charge carriers. Hence, the membrane's selectivity determines the crossover and then, the coulombic efficiency of the system. A new method for permeability studies was designed using scanning electrochemical microscopy (SECM). The Cu(II) permeability of several commercial were tested by cyclic voltammetry (CV) and approach curves (AC) with the SECM. The CVs were performed in the solution bulk, providing copper process information. During the AC, the SECM probe (UME) was stepped from the solution bulk toward the membrane. By biasing the probe in order to reducing copper (II), the recorded current can be correlated with the concentration of copper (II) in space. With commercial membranes, the Cu(II) permeability follows the trend: porous membranes > cation exchange membranes > anion exchange membranes, as expected. Hence, SECM was used to study the effect of porous membrane modification with a cation exchange polymer (SPEEK). In this field, the SECM method can assist in optimizing the modification. Wettability (evaluated by contact-angle measurements) of the system plays essential roles in evaluating the membranes, contributing to understanding the permeation in different time scales. Simulation model will be developed to fit the AC at different times, providing quantitative information about permeability. This methodology can be integrated and adapted for studying the membrane permeability at every redox active species employed in RFB field.

The effect of the copper crossover is electrolyte unbalancing or self-discharge. For this purpose, the state of charge (SoC) monitoring during the RFB operation is fundamental. Two different spectrophotometric approaches were designed for SoC monitoring systems, both for negative and positive half-cells. In the positive half-cell, direct observation of the Cu(II) is possible by NIR spectroscopy at 920 nm. In the negative half-cell, Cu(II) is not present, and Cu(I) does not have the same electronic transition. In order to determine the Cu(I) concentration, the Cu(I) can be converted reversibly in Cu(II) before the detection unit, where copper is detected as Cu(II). After flowing through the detection unit, the Cu(II) must be converted back to Cu(I) (Red

unit) before returning to the cell's flow system. For this purpose, preliminary results show the feasibility of this concept.

9. Appendix

9.1. List of publications

Articles published:

- G. Lacarbonara, M. Rahmanipour, J. Belcari, L. Lodi, A. Zucchelli, C. Arbizzani, “Dilatometric analysis: a powerful tool for testing and improving cell performance”, *Electrochemical Acta* 375 (2021) 137938. <https://doi.org/10.1016/j.electacta.2021.137938>.
- G. Lacarbonara, C. Arbizzani, S. Chini, S. Ratso, I. Kruusenberg, “Graphitic carbon from CO₂ for sustainable Li ion battery anodes”, *Mater. Adv.*, 3 (2022) 7087-7097, <https://doi.org/10.1039/D2MA00583B>.
- G. Lacarbonara, L. Faggiano, S. Porcu, P. C. Ricci, S. Rapino, D. P. Casey, J. F. Rohan, C. Arbizzani, “Copper chloro-complexes concentrated solutions: an electrochemical study”, *Batteries*, 7 (2021) 83, <https://doi.org/10.3390/batteries7040083>.
- L. Faggiano, G. Lacarbonara, W. D. Badenhorst, L. Murtomäki, L. Sanz, C. Arbizzani, “Short thermal treatments of carbon felts for copper-based redox flow batteries”, *Journal of Power Sources*, 520 (2022) 230846. <https://doi.org/10.1016/j.jpowsour.2021.230846>.
- L. Bargnesi, A. Rozzarin; G. Lacarbonara; S. Tombolesi; C. Arbizzani, Sustainable modification of chitosan binder for capacitive electrodes operating in aqueous electrolytes, *ChemElectroChem*, (2023) e202201080, <https://doi.org/10.1002/celec.202201080>.

Book chapter:

- L. Sanz, W. D. Badenhorst, G. Lacarbonara, L. Faggiano, D. Lloyd, P. Kauranen, C. Arbizzani, L. Murtomäki, All-copper Flow Batteries, in: C. Roth, J. Noack, M. Skyllas-Kazacos, Part 5: Chemistries other than Vanadium, *Flow Batteries From Fundamentals to Applications*, Vol. 2, Ch. 38 (2023) 855-873, DOI:10.1002/9783527832767.

Papers submitted:

- D. Di Cillo, L. Bargnesi, G. Lacarbonara, C. Arbizzani, “Ammonium and Tetraalkylammonium Salts as Additives for Li metal electrodes”, Accepted from Batteries.
- G. Lacarbonara, D. Fazzi, N. Albanelli, C. Arbizzani, “A spectroelectrochemical study of copper chloro-complexes for high performance copper redox flow batteries”, *Electrochemical Acta*, under review.

Paper in preparation:

- G. Lacarbonara, L. Bargnesi, D. Di Cillo, M. Saad, J. Ritzell, A. Matic, C. Arbizzani, Stabilizing lithium metal interphase by ammonium hexafluorophosphate electrolyte additive for stable cycling, Manuscript in preparation.
- S. Rapino, G. Lacarbonara, S. De Zio, R. Petruzzelli, M. Malferrari, W. D. Badenhurst, L. Murtomäki, Scanning electrochemical Microscopy method for Cu^{2+} permeability investigation on membranes for Redox Flow Battery, Manuscript in preparation.
- R. Petruzzelli, G. Lacarbonara, C. Arbizzani, State of Charge monitoring in Redox Flow Batteries, Manuscript in preparation.
- G. Lacarbonara, R. Petruzzelli, E. Paolasini, S. Grilli, W. D. Badenhurst, L. Murtomäki, C. Arbizzani, Determination of kinetic parameters for the optimization of a Cu-based redox flow battery, Manuscript in preparation.

9.2. Participation at conferences

- 31/08-04/09/2020** **Poster presentations in 71st International Society of Electrochemistry annual meeting “Belgrade Online”**
G. Lacarbonara, M. Rahmanipour, J. Belcari, L. Lodi, A. Zucchelli, C. Arbizzani, “Investigation of structural changes in different metal ion battery electrodes by in-situ dilatometry”.
M. Rahmanipour, G. Lacarbonara, C. Arbizzani, “Lithium Interphase Enhancement for Lithium-Sulphur Batteries”
- 24-26/02/2021** **Oral presentation in 1st IWES 2021 workshop**, G. Lacarbonara, J. Belcari, L. Lodi, C. Arbizzani, “Gas Evolution in Li-ion batteries revealed by Electrochemical In-Situ Dilatometry”.
- 9/03/2021** **Invited seminar at Marposs S.p.a.**, G. Lacarbonara, “Experimental validation of the In-situ Electrochemical Dilatometer performed in the Laboratory of Electrochemistry of Materials for Energetics”.
- 11/03/2021** **Oral presentation in Flow Camp Next Generation Flow Battery conference and networking event**, G. Lacarbonara, L. Faggiano, S. Rapino, C. Arbizzani, L. Sanz, C. Ricci, L. Murtomäki, W. Badenhorst, J. Rohan, M. Boaventura, J. Cruz, T. Müller, T. Gerber, R. La Gioia, I. Guedea, A. Alvarez, C. Barbu, “Aqueous copper-based flow batteries for renewables integration and sustainable energy storage”.
- 14-23/09/2021** **Oral presentation in SCI2021**, G. Lacarbonara, N. Albanelli, L. Faggiano, C. Arbizzani, “A spectroelectrochemical study of copper chloro-complexes for high performance copper redox flow batteries”.
- 31/08-04/09/2021** **Oral and Poster presentation in 72nd International Society of Electrochemistry annual meeting**
Oral: L. Faggiano, G. Lacarbonara, W. D. Badenhorst, L. Murtomäki, L. Sanz and C. Arbizzani, “Electrochemical characterization of carbonaceous electrodes for Copper based redox flow battery” .
Poster: G. Lacarbonara, L. Faggiano, C. Arbizzani, “Copper Chloro-Complexes Stability and Dynamics for High Performance Aqueous Redox Flow Batteries”.

- 12-16/09/2022** **Oral presentation in 73rd International Society of Electrochemistry annual meeting, G. Lacarbonara, N. Albanelli, D. Fazzi, C. Arbizzani, “Spectroelectrochemical Characterization and Modeling of Copper Chloro-Complexes Solutions for Redox Flow Batteries”.**
- 11-15/09/2022** **Oral presentation at Giornate dell’Elettrochimica Italiana (GEI) 2022, G. Lacarbonara, R. Petruzzelli, S. De Zio, W. D. Badenhorst, M. Malferrari, L. Murtomäki, C. Arbizzani, S. Rapino, “Scanning ElectroChemical Microscopy method for Cu²⁺ permeability investigation on membranes for Redox Flow Battery”.**
- 22-25/01/2023** **Poster contribution to "30 years of INSTM: past, present and future of the Consortium", L. Bargnesi, A. Rozzarin, G. Lacarbonara, S. Tombolesi, C. Arbizzani, “Sustainable modification of chitosan binder for electrodes operating in aqueous electrolyte”.**
- 25-27/01/2023** **Oral presentation at Second Italian Workshop on Energy Storage – IWES2023, G. Lacarbonara, L. Bargnesi, D. Di Cillo, C. Arbizzani, “Tetraalkylammonium salts for a stable lithium metal-electrolyte interphase” awarded as best oral presentation.**

Acknowledgments

Completing this thesis was only possible with the support of many different people and organizations.

First and foremost, I want to thank my supervisor Prof. Catia Arbizzani, who gave me the opportunity for continuous support during my first steps in the electrochemistry field. Thanks for being a brilliant supervisor who has given me many chances to grow. I want to thank all my colleagues in these years. We have spent many pleasant moments in the lab, and each of you has helped me complete this thesis.

A special thank goes to Prof. Aleksandar Matic, who welcomed me in Sweden, making me feel at home. The Material Physics division at Chalmers is a constructive and unique environment in which I have worked with you having a lot of fun. Thanks to Dr Matthew Sadd and Josef Ritzel, I will never forget your help and the constructive discussions with you.

In this regard, I would like to thank the Marco Polo programme for the funds that helped me during my time abroad in Sweden.

A special thanks to Dr Juri Belcari and Marposs S.p.A. that kindly provided the equipment for dilatometry tests to the Laboratory of Electrochemistry of Materials for Energetics, Department of Chemistry “Giacomo Ciamician”. I would like to thank Prof. Ivar Kruusenberg and Dr Sander Ratso of the National Institute of Physics and Biophysics of Tallin for the possibility of working with you on an enthusiastic sustainable theme.

I would like to thank MiSE-ENEA, Electrical System Research, PTR 2019-2021, for funding part of my research.

I would like to thank the European Union - Horizon 2020 research and innovation programme for allowing us to investigate all-copper RFBs in the framework of the CUBER - Copper-Based Flow Battery for Energy storage project Renewables Integration H2020 - LC - BAT_2019 under grant agreement No. 875605. All the Project Partners are also acknowledged for the fruitful discussion.

Finally, thank the Department of Excellence program financed by the Minister of Education, University and Research (MIUR, L. 232 del 01/12/2016) for the doctoral scholarship.

References

- I. G. Lacarbonara, M. Rahmanipour, J. Belcari, L. Lodi, A. Zucchelli, C. Arbizzani, “Dilatometric analysis: a powerful tool for testing and improving cell performance”, *Electrochemical Acta* 375 (2021) 137938. <https://doi.org/10.1016/j.electacta.2021.137938>
- II. G. Lacarbonara, C. Arbizzani, S. Chini, S. Ratso, I. Kruusenberg, “Graphitic carbon from CO₂ for sustainable Li ion battery anodes”, *Mater. Adv.*, 3 (2022) 7087-7097, <https://doi.org/10.1039/D2MA00583B>
- III. G. Lacarbonara, L. Bargnesi, D. Di Cillo, M. Saad, J. Ritzell, A. Matic, C. Arbizzani, Stabilizing lithium metal interphase by ammonium hexafluorophosphate electrolyte additive for stable cycling, Manuscript in preparation.
- IV. G. Lacarbonara, D. Fazzi, N. Albanelli, C. Arbizzani, “A spectroelectrochemical study of copper chloro-complexes for high performance copper redox flow batteries”, Manuscript submitted to *Electrochemical Acta*.
- V. G. Lacarbonara, L. Faggiano, S. Porcu, P. C. Ricci, S. Rapino, D. P. Casey, J. F. Rohan, C. Arbizzani, “Copper chloro-complexes concentrated solutions: an electrochemical study”, *Batteries*, 7 (2021) 83, <https://doi.org/10.3390/batteries7040083>
- VI. L. Faggiano, G. Lacarbonara, W. D. Badenhurst, L. Murtomäki, L. Sanz, C. Arbizzani, “Short thermal treatments of carbon felts for copper-based redox flow batteries”, *Journal of Power Sources*, 520 (2022) 230846. <https://doi.org/10.1016/j.jpowsour.2021.230846>
- VII. S. Rapino, G. Lacarbonara, S. De Zio, R. Petruzzelli, M. Malferrari, W. D. Badenhurst, L. Murtomäki, Scanning electrochemical Microscopy method for Cu²⁺ permeability investigation on membranes for Redox Flow Battery, Manuscript in preparation.
- VIII. R. Petruzzelli, G. Lacarbonara, C. Arbizzani, State of Charge monitoring in all-copper Redox Flow Batteries, Manuscript in preparation.

- [1] S. Pain, Power through the ages *Nature* 551 (2017) S134-S137 doi: <https://doi.org/10.1038/d41586-017-07506-z>
- [2] https://ec.europa.eu/eurostat/statistics-explained/index.php?title=Energy_statistics_-_an_overview
- [3] Goodenough, J. B.; Park, K.-S. The Li-Ion Rechargeable Battery: A Perspective. *J. Am. Chem. Soc.* 135 (2013) 1167–1176
- [4] G. Notton, L. Stoyanov, M. Ezzat, V. Lararov, S. Diaf, C. Cristofari, Integration Limit of Renewable Energy Systems in Small Electrical Grid, *Energy Procedia* 6 (2011) 651-665 <https://doi.org/10.1016/j.egypro.2011.05.075>
- [5] Butler P., Miller J.L, Taylor P.A. Energy storage opportunities analysis. Phase II Final report. A study for the DOE Energy storage systems program. Sandia Report SAND2002-1314. (2002)
- [6] Gogus Y, Mechanical energy storage. *Encyclopedia of Life Support Systems (EOLSS), Energy storage systems, vol. 1, <http://www.eolss.net/sample-chapters/c08/E3-14-03.pdf>*
- [7] M. Krüger, J. Haunstetter, P. Knödler, S. Zunft, Slag as an Inventory Material for Heat Storage in a Concentrated Solar Tower Power Plant: Design Studies and Systematic Comparative Assessment, *Appl. Sci.* 9(9) (2019) 1833, <https://doi.org/10.3390/app9091833>.
- [8] V. A. Lebedev, A. E. Amer, Limitations of using phase change materials for thermal energy storage, *IOP Conf. Ser.: Earth Environ. Sci.* 378 (2019) 012044, <https://doi.org/10.1088/1755-1315/378/1/012044>.
- [9] H. Chen, T.N. Cong, W. Yang, C. Tan, Y. Li, Y. Ding Progress in electrical energy storage system: a critical review *Prog Nat Sci*, 19 (2009) 291-312
- [10] Stecca, M.; Ramirez Elizondo, L.; Batista Soeiro, T.; Bauer, P.; Palensky, P. A Comprehensive Review of the Integration of Battery Energy Storage Systems into Distribution Networks. *IEEEOpen J. Ind. Electron. Soc.* 1 (2020) 1

- [11] G. Giheung-Gu, Y.Si, G.-Do, Cathode Materials, the source of a Strong and Long-lasting Battery 17084 (2016) 150-20.
- [12] J. Jang, J. Oh, H. Jeong, W. Kang, C. Jo, A Review of Functional Separators for Lithium Metal, *Materials (MDPI)* 13(20) (2020) 4625.
- [13] S. Zhang, A review on the separators of liquid electrolyte Li-ion batteries, *Journal of Power Sources*, 164 (2007) 351–364, <https://doi.org/10.1016/j.jpowsour.2006.10.065>
- [14] A.J. Bard, L. Faulkner, *Electrochemical Methods: Fundamentals and Applications*, Wiley, 2000.
- [15] C. Brett, A. M. Brett, *Electrochemistry: Principles, Methods, and Applications*, Oxford Science Publications, 1993, DOI:10.1016/0013-4686(94)80035-9Corpus ID: 92734651
- [16] Southampton Electrochemistry Group (2002) *Instrumental Methods in Electrochemistry*, Ellis Horwood Limited
- [17] B. Dunn, H. Kamath, J.M. Tarascon, Electrical energy storage for the grid: A battery of choices, *Science* (80-.). 334 (2011) 928–935. <https://doi.org/10.1126/science.1212741>.
- [18] Reiner Korthauer, *Lithium-Ion Batteries: Basics and Applications*, Springer-Verlag GmbH Germany, part of Springer Nature 2018, <https://doi.org/10.1007/978-3-662-53071-9>
- [21] M. B. Tahir, M. Abrar, A. Tehseen, T. I. Awan, A. Bashir, G. Nabi, Chapter 11 - Nanotechnology: the road ahead, *Chemistry of Nanomaterials Fundamentals and Applications* (2020) 289-308 <https://doi.org/10.1016/B978-0-12-818908-5.00011-1>
- [22] T.P. Sumangala, M.S. Sreekanth, A. Rahaman, Applications of Supercapacitors. In: Kar, K.K. (eds) *Handbook of Nanocomposite Supercapacitor Materials III*. Springer Series in Materials Science, vol 313. Springer, Cham. (2021) https://doi.org/10.1007/978-3-030-68364-1_11

- [23] B. Riegel, Requirements for stationary application batteries. In: Korthauer, R. (eds) *Lithium-Ion Batteries: Basics and Applications*. Springer, Berlin, Heidelberg (2018) https://doi.org/10.1007/978-3-662-53071-9_32
- [25] Y. Shi, C. Eze, B. Xiong, W. He, H. Zhang, T.M. Lim, A. Ukil, J. Zhao, Recent development of membrane for vanadium redox flow battery applications: A review, *Applied Energy*, 238, (2019) 202-224, <https://doi.org/10.1016/j.apenergy.2018.12.087>.
- [26] J. B. Phipps, T. G. Hayes, P. M. Skarstad, D. F. Untereker, In-situ formation of a solid/liquid composite electrolyte in Li/I₂ batteries, *Solid State Ionics* 18-19 (1986) 1073-1077, [https://doi.org/10.1016/0167-2738\(86\)90311-5](https://doi.org/10.1016/0167-2738(86)90311-5).
- [27] B. Ramasubramanian, M. V. Reddy, K. Zaghbi, M. Armand, S. Ramakrishna, Growth Mechanism of Micro/Nano Metal Dendrites and Cumulative Strategies for Countering Its Impacts in Metal Ion Batteries: A Review, *Nanomaterials* 11(10) (2021) 2476 DOI:10.3390/nano11102476.
- [28] Whittingham M. S. Whittingham, Chemistry of intercalation compounds: Metal guests in chalcogenide hosts, *Progress in Solid State Chemistry* 12(1) (1978) 41-99, [https://doi.org/10.1016/0079-6786\(78\)90003-1](https://doi.org/10.1016/0079-6786(78)90003-1).
- [29] J.O.Besenhard, The electrochemical preparation and properties of ionic alkali metal-and NR₄-graphite intercalation compounds in organic electrolytes, *Carbon*, 14(2) (1976) 111 – 115 1976, [https://doi.org/10.1016/0008-6223\(76\)90119-6](https://doi.org/10.1016/0008-6223(76)90119-6)
- [30] https://www.shimadzu-webapp.eu/magazine/issue-2016-2_en/anti-aging-for-batteries/
- [31] B. Scrosati, History of lithium batteries, *J Solid State Electrochem*, 15 (2011) 1623-1630 DOI 10.1007/s10008-011-1386-8.
- [32] M. Hu, X. Pang, and Z. Zhou, Recent progress in high-voltage lithium ion batteries, *J. Power Sources*,. 237 (2013) 229–242

- [33] C. Julien and A. Mauger, A. Vijn, K. Zaghbi, Lithium Batteries, Springer International Publishing Switzerland 2016, <https://doi.org/10.1007/978-3-319-19108-9>.
- [34] J. F., M. Hasan, S. Patil, D. P., and T. Clancy, Energy Storage: Battery Materials and Architectures at the Nanoscale, ICT - Energy - Concepts Toward Zero - Power Inf. Commun. Technol., 2014.
- [35] J. B. Goodenough and K. Mizushima, Electrochemical cell with new fast ion conductors, 1981
- [36] F. Schipper and D. Aurbach, A brief review: Past, present and future of lithium ion batteries, Russ. J. Electrochem., 52(12) (2016) 1095– 1121. DOI: 10.1134/S1023193516120120
- [37] T. Kim, W. Song, D.-Y. Son, L. K. Ono Y. Qi, Lithium-ion batteries: outlook on present, future, and hybridized technologies, J. Mater. Chem. A, 7 (2019) 2942-2964, <https://doi.org/10.1039/C8TA10513H>.
- [38] D. E. Demirocak, S. S. Srinivasan, and E. K. Stefanakos, A review on nanocomposite materials for rechargeable Li-ion batteries, Appl. Sci., 165 (7) (2017), 1-26.
- [39] L. Baggetto, N. J. Dudney, G. M. Veith, Surface chemistry of metal oxide coated lithium manganese nickel oxide thin film cathodes studied by XPS, Electrochimica Acta, 90(15) (2013) 135-147, <https://doi.org/10.1016/j.electacta.2012.11.120>.
- [41] Steen, M., Lebedeva, N., Di Persio, F. and Boon-Brett, L., EU Competitiveness in Advanced Li-ion Batteries for E-Mobility and Stationary Storage Applications – Opportunities and Actions, EUR 28837 EN, Publications Office of the European Union, Luxembourg, 2017, ISBN 978-92-79-74292-7, doi:10.2760/75757, JRC108043.
- [42]

- [43] J. Li, Z.-F. Ma, Past and Present of LiFePO₄: From Fundamental Research to Industrial Applications, *Chem* 5(1) (2019) 3-6, <https://doi.org/10.1016/j.chempr.2018.12.012>.
- [44] N. Nitta, F. Wu, J. T. Lee, and G. Yushin, Li-ion battery materials: Present and future, *Materials Today*, 18(5), Elsevier Ltd., (2015) 252–264.
- [45] Lin, D.; Liu, Y.; Pei, A.; Cui, Y. Nanoscale Perspective: Materials Designs and Understandings in Lithium Metal Anodes. *Nano Res.* 10 (12) (2017) 4003-4026. <https://doi.org/10.1007/s12274-017-1596-1>.
- [46] Kalhoff, J.; Eshetu, G. G.; Bresser, D.; Passerini, S. Safer Electrolytes for Lithium-Ion Batteries: State of the Art and Perspectives. *ChemSusChem*, 8 (13) (2015) 2154-2175. <https://doi.org/10.1002/cssc.201500284>.
- [47] Balducci, A. Ionic Liquids in Lithium-Ion Batteries. In *Ionic Liquids II*; Kirchner, B., Perlt, E., Eds.; Topics in Current Chemistry Collections; Springer International Publishing: Cham, 2017, 1-27. https://doi.org/10.1007/978-3-319-89794-3_1.
- [48] G. Giheung-Gu, Y.Si, G.-Do, Cathode Materials, the source of a Strong and Long-lasting Battery, 17084 (2016) 150-20
- [49] J. Jang, J. Oh, H. Jeong, W. Kang, C. Jo, A Review of Functional Separators for Lithium Metal, *Materials* 13(20) (2020) 4625.
- [50] S. Zhang, A review on the separators of liquid electrolyte Li-ion batteries, *Journal of Power Sources* 164 (2007) 351-364.
- [51] P.-D. Jürgen, O. Besenhard, P. Heinz, H. P. Fritz, The Electrochemistry of Black Carbons, *Angew. Chem. Int. Ed. Engl.*, 95 (1983) 950
- [52] M. Winter, J. O. Besenhard, M. E. Spahr, P. Novák, Insertion Electrode Materials for Rechargeable Lithium Batteries, *Adv. Mater.* 10(10) (1998) 725-763, [https://doi.org/10.1002/\(SICI\)1521-4095\(199807\)10:10<725::AID-ADMA725>3.0.CO;2-Z](https://doi.org/10.1002/(SICI)1521-4095(199807)10:10<725::AID-ADMA725>3.0.CO;2-Z).

- [53] B. Horstmann, F. Single, A. Latz, Review on multi-scale models of solid-electrolyte interphase formation, *Current Opinion in Electrochemistry*, 13 (2019) 61-69, <https://doi.org/10.1016/j.coelec.2018.10.013>
- [54] K. Xu, Nonaqueous liquid electrolytes for lithium-based rechargeable batteries, *Chem. Rev.* 104(10) (2004) 4303-4417.
- [55] N.S. Hudak, Nanostructured electrode materials for lithium-ion batteries in *Lithium-ion batteries: Advances and Applications*, G. Pistoia Ed., Elsevier B. V., Amsterdam, The Netherlands, 2014, 57-82. <http://dx.doi.org/10.1016/B978-0-444-59513-3.00004-2>.
- [56] I. Lahiri, W. Choi, Carbon nanostructures in lithium ion batteries: past, present, and future, *Carbon Nanostructures in Lithium Ion Batteries: Past, Present, and Future*, *Crit. Rev. Solid State Mater. Sci.* 38 (2013) 128-166. <https://doi.org/10.1080/10408436.2012.729765>.
- [57] S. Goriparti, E. Miele, F. De Angelis, E. Di Fabrizio, R. Proietti Zaccaria, C. Capiglia, Review on recent progress of nanostructured anode materials for Li-ion batteries, *J. Power Sources*, 257 (2014) 421-443. <https://doi.org/10.1016/j.jpowsour.2013.11.103>.
- [58] X. Zhang, D. Wang, X. Qiu, Yingjie Ma, D. Kong, K. Müllen, X. Li, L. Zhi, Stable high-capacity and high-rate silicon-based lithium battery anodes upon two-dimensional covalent encapsulation, *Nature Communications* 11 (2020) 3826.
- [59] J. Christensen, V. Srinivasan, J. Newman, Optimization of Lithium Titanate Electrodes for High-Power Cells, *J. Electrochem. Soc.* 153 (2006) A560
- [60] Y. Zhao, X. Li, B. Yan, D. Xiong, D. Li, S. Lawes, X. Sun, Recent Developments and Understanding of Novel Mixed Transition-Metal Oxides as Anodes in Lithium Ion Batteries, *Advanced Energy Materials*, 6(8)8 (2016) 1502175 <https://doi.org/10.1002/aenm.201502175>
- [61] A. Rajkamal, R. Thapa, Carbon Allotropes as Anode Material for Lithium-Ion Batteries, *Adv.Mater. Technol.*, 4 (2019) 1900307, <https://doi.org/10.1002/admt.201900307>.

- [62] A. Casimir, H. Zhang, O. Ogoke, J. C. Amine, J. Lu, and G. Wu, Siliconbased anodes for lithium-ion batteries: Effectiveness of materials synthesis and electrode preparation, *Nano Energy*, 27 (2016) 359-376.
- [63] A. Yamada, Iron-based materials strategies, *MRS Bull.* 39 (2014) 423-428. <https://doi.org/10.1557/mrs.2014.89>.
- [64] M. Winter, G.H. Wrodnigg, J.O. Besenhard, W. Biberacher, P. Novák, Dilatometric Investigations of Graphite Electrodes in Nonaqueous Lithium Battery Electrolytes, *J. Electrochem. Soc.* 147 (2000) 2427. <https://doi.org/10.1149/1.1393548>.
- [65] V.L. Chevrier, G. Ceder, Challenges for Na-ion Negative Electrodes, *J. Electrochem. Soc.* 158 (2011) A1011. <https://doi.org/10.1149/1.3607983>.
- [66] B. Rieger, S. Schlueter, S. V. Erhard, J. Schmalz, G. Reinhart, A. Jossen, Multi-scale investigation of thickness changes in a commercial pouch type lithium-ion battery, *J. Energy Storage.* 6 (2016) 213–221. <https://doi.org/10.1016/j.est.2016.01.006>.
- [67] J.-S. Bridel, T. Azaïs, M. Morcrette, J.-M. Tarascon, D. Larcher, In Situ Observation and Long-Term Reactivity of Si/C/CMC Composites Electrodes for Li-Ion Batteries, *J. Electrochem. Soc.* 158 (2011) A750. <https://doi.org/10.1149/1.3581024>.
- [68] M. Li, Z. Wang, J. Fu, K. Ma, E. Detsi, In situ electrochemical dilatometry study of capacity fading in nanoporous Ge-based Na-ion battery anodes, *Scr. Mater.* 164 (2019) 52–56. <https://doi.org/10.1016/j.scriptamat.2019.01.030>.
- [69] G. Jeong, S.M. Lee, N.S. Choi, Y.U. Kim, C.K. Lee, Stabilizing dimensional changes in Si-based composite electrodes by controlling the electrode porosity: An in situ electrochemical dilatometric study, *Electrochim. Acta.* 56 (2011) 5095–5101. <https://doi.org/10.1016/j.electacta.2011.03.071>.

- [70] D. Sauerteig, S. Ivanov, H. Reinshagen, A. Bund, Reversible and irreversible dilation of lithium-ion battery electrodes investigated by in-situ dilatometry, *J. Power Sources*. 342 (2017) 939–946. <https://doi.org/10.1016/j.jpowsour.2016.12.121>.
- [71] R. Kumar, J.H. Woo, X. Xiao, B.W. Sheldon, Internal Microstructural Changes and Stress Evolution in Silicon Nanoparticle Based Composite Electrodes, *J. Electrochem. Soc.* 164 (2017) A3750–A3765. <https://doi.org/10.1149/2.0951714jes>.
- [72] M. Li, Z. Wang, E. Detsi, In Situ Electrochemical Dilatometry Study of (De)lithiation and Polysulfide Dissolution-Induced Dimensional Changes in Lithium-Sulfur Cathodes during Charging and Discharging, *J. Electrochem. Soc.* 167 (2020) 050505. <https://doi.org/10.1149/1945-7111/ab63c1>.
- [73] P.K. Nayak, L. Yang, K. Pollok, F. Langenhorst, D. Aurbach, P. Adelhelm, Investigation of $\text{Li}_{1.17}\text{Ni}_{0.20}\text{Mn}_{0.53}\text{Co}_{0.10}\text{O}_2$ as an Interesting Li- and Mn-Rich Layered Oxide Cathode Material through Electrochemistry, Microscopy, and In Situ Electrochemical Dilatometry, *ChemElectroChem*. 6 (2019) 2812–2819. <https://doi.org/10.1002/celec.201900453>.
- [74] T. Kim, S. Park, S.M. Oh, Solid-State NMR and Electrochemical Dilatometry Study on Li^{+} Uptake/Extraction Mechanism in SiO Electrode, *J. Electrochem. Soc.* 154 (2007) A1112. <https://doi.org/10.1149/1.2790282>.
- [75] M. Hahn, H. Buqa, P.W. Ruch, D. Goers, M.E. Spahr, J. Ufheil, P. Novák, R. Kötz, A dilatometric study of lithium intercalation into powder-type graphite electrodes, *Electrochem. Solid-State Lett.* 11 (2008) 150–154. <https://doi.org/10.1149/1.2940573>.
- [76] A. Tranchot, H. Idrissi, P.X. Thivel, L. Roué, Impact of the Slurry pH on the Expansion/Contraction Behavior of Silicon/Carbon/Carboxymethylcellulose Electrodes for Li-Ion Batteries, *J. Electrochem. Soc.* 163 (2016) A1020–A1026. <https://doi.org/10.1149/2.1071606jes>.
- [77] V.R. Rikka, S.R. Sahu, A. Chatterjee, P. V. Satyam, R. Prakash, M.S.R. Rao, R. Gopalan, G. Sundararajan, In Situ/ex Situ Investigations on the Formation of the Mosaic Solid Electrolyte Interface Layer on Graphite Anode for Lithium-Ion Batteries,

J. Phys. Chem. C. 122 (2018) 28717–28726.
<https://doi.org/10.1021/acs.jpcc.8b09210>.

[78] J.P. Pender, G. Jha, D.H. Youn, J.M. Ziegler, I. Andoni, E.J. Choi, A. Heller, B.S. Dunn, P.S. Weiss, R.M. Penner, C.B. Mullins, Electrode Degradation in Lithium-Ion Batteries, ACS Nano. 14 (2020) 1243–1295.
<https://doi.org/10.1021/acsnano.9b04365>.

[79] C. L. Berhaut, D. Lemordant, P. Porion, L. Timperman, G. Schmidt, M. Anouti, Ionic association analysis of LiTfDI, LiFSI and LiPF₆ in EC/DMC for better Li-ion battery performances, RSC Adv., 9 (2019) 4599-4608, DOI: 10.1039/C8RA08430K.

[79] G.-C. Chung, H.-J. Kim, S.-I. Yu, S.-H. Jun, J. Choi, M.-H. Kim, Origin of Graphite Exfoliation An Investigation of the Important Role of Solvent Cointercalation, J. Electrochem. Soc. 147 (2000) 4391.
<https://doi.org/10.1149/1.1394076>.

[80] H.Y. Song, S.K. Jeong, Investigating continuous co-intercalation of solvated lithium ions and graphite exfoliation in propylene carbonate-based electrolyte solutions, J. Power Sources. 373 (2018) 110-118.
<https://doi.org/10.1016/j.jpowsour.2017.11.015>.

[82] M. Onuki, Y. Sakata, M. Yanagidate, Y. Otake, S. Kinoshita, M. Ue, M. Deguchi, Identification of the Source of Evolved Gas in Li-Ion Batteries by Using ¹³C-Labeled Solvents, ECS Trans. 11 (2019) 43-47. <https://doi.org/10.1149/1.2897970>.

[83] T. Liu, L. Lin, X. Bi, L. Tian, K. Yang, J. Liu, M. Li, Z. Chen, J. Lu, K. Amine, K. Xu, F. Pan, In situ quantification of interphasial chemistry in Li-ion battery, Nat. Nanotechnol. 14 (2019) 50-56. <https://doi.org/10.1038/s41565-018-0284-y>.

[84] L. Wang, A. Menakath, F. Han, Y. Wang, P.Y. Zavalij, K.J. Gaskell, O. Borodin, D. Iuga, S.P. Brown, C. Wang, K. Xu, B.W. Eichhorn, Identifying the components of the solid–electrolyte interphase in Li-ion batteries, Nat. Chem. 11 (2019) 789-796.
<https://doi.org/10.1038/s41557-019-0304-z>.

- [85] B. Strehle, S. Solchenbach, M. Metzger, K.U. Schwenke, H.A. Gasteiger, The Effect of CO₂ on Alkyl Carbonate Trans-Esterification during Formation of Graphite Electrodes in Li-Ion Batteries, *J. Electrochem. Soc.* 164 (2017) A2513-A2526. <https://doi.org/10.1149/2.1001712jes>.
- [86] J.S. Shin, C.H. Han, U.H. Jung, S.I. Lee, H.J. Kim, K. Kim, Effect of Li₂CO₃ additive on gas generation in lithium-ion batteries, *J. Power Sources.* 109 (2002) 47-52. [https://doi.org/10.1016/S0378-7753\(02\)00039-3](https://doi.org/10.1016/S0378-7753(02)00039-3).
- [87] R. Bernhard, M. Metzger, H.A. Gasteiger, Gas Evolution at Graphite Anodes Depending on Electrolyte Water Content and SEI Quality Studied by On-Line Electrochemical Mass Spectrometry, *J. Electrochem. Soc.* 162 (2015) A1984-A1989. <https://doi.org/10.1149/2.0191510jes>.
- [88] B. Michalak, H. Sommer, D. Mannes, A. Kaestner, T. Brezesinski, J. Janek, Gas Evolution in Operating Lithium-Ion Batteries Studied in Situ by Neutron Imaging, *Sci. Rep.* 5 (2015) 1-9. <https://doi.org/10.1038/srep15627>.
- [89] M.R. Wagner, P.R. Raimann, A. Trifonova, K.C. Möller, J.O. Besenhard, M. Winter, Dilatometric and mass spectrometric investigations on lithium ion battery anode materials, in: *Anal. Bioanal. Chem.*, Springer, 2004, 272-276. <https://doi.org/10.1007/s00216-004-2570-9>.
- [90] M. Hahn, A. Würsig, R. Gallay, P. Novák, R. Kötz, Gas evolution in activated carbon/propylene carbonate based double-layer capacitors, *Electrochem. Commun.* 7 (2005) 925-930. <https://doi.org/10.1016/j.elecom.2005.06.015>.
- [91] C. Srilakshmi, E. Widjaja, M. Garland, B.G. Anderson, Deconvolution of pure component FT-Raman spectra from thermal emission of barium sulfate and graphite samples using the BTEM algorithm, *J. Raman Spectrosc.* 38 (2007) 349-355. <https://doi.org/10.1002/jrs.1652>.
- [92] P.K. Chu, L. Li, Characterization of amorphous and nanocrystalline carbon films, *Mater. Chem. Phys.* 96 (2006) 253-277. <https://doi.org/10.1016/j.matchemphys.2005.07.048>.

- [93] P. Poizot, S. Laruelle, S. Grugeon, L. Dupont, J. Tarascon, Nano-Sized Transition-Metal Oxides as Negative-Electrode Materials for Lithium-Ion Batteries, *Nature*, 407 (2000) 496. DOI: 10.1038/35035045.
- [94] R. Sun, Z. Qin, Z. Li, H. Fan, S. Lu, Binary zinc–cobalt metal–organic framework derived mesoporous ZnCo₂O₄@NC polyhedron as a high-performance lithium-ion battery anode, *Dalton Trans.*, 49 (2020) 14237-14242. <https://doi.org/10.1039/d0dt03132a>.
- [95] Y.-C. Tsai, C.-T. Kuo, S.-F. Liu, Y.-T. Lee, T.-R. Yew, Effect of Different Electrolytes on MnO₂ Anodes in Lithium-Ion Batteries, *J. Phys. Chem. C*, 125 (2021) 1221-1233. <https://doi.org/10.1021/acs.jpcc.0c09022>.
- [96] Y. Deng, L. Wan, Y. Xie, X. Qin, G. Chenb, Recent advances in Mn-based oxides as anode materials for lithium ion batteries, *RSC Adv.*, 4 (2014) 23914-23935, DOI: 10.1039/C4RA02686A.
- [97] T. Kokubu, Y. Oaki, E. Hosono, H. S. Zhou and H. Imai, Biomimetic Solid-Solution Precursors of Metal Carbonate for Nanostructured Metal Oxides: MnO/Co and MnO-CoO Nanostructures and Their Electrochemical Properties, *Adv. Funct. Mater.*, 21 (2011) 3673, <https://doi.org/10.1002/adfm.201101138>.
- [98] G. L. Xu, Y. F. Xu, H. Sun, F. Fu, X. M. Zheng, L. Huang, J. T. Li, S. H. Yang and S. G. Sun, Facile synthesis of porous MnO/C nanotubes as a high capacity anode material for lithium ion batteries, *Chem. Commun.*, 48 (2012) 8502, DOI <https://doi.org/10.1039/C2CC34218A>.
- [99] X. D. Liu, C. Z. Chen, Y. Y. Zhao, B. Jia, A Review on the Synthesis of Manganese Oxide Nanomaterials and Their Applications on Lithium-Ion Batteries, *J. Nanomater.*, 2013, 736375, <https://doi.org/10.1155/2013/736375>
- [100] X. W. Li, D. Li, L. Qiao, X. H. Wang, X. L. Sun, P. Wang, D. Y. He, Interconnected porous MnO nanoflakes for high-performance lithium ion battery anodes, *J. Mater. Chem.*, 2012, 22, 9189

- [101] K. F. Zhong, X. Xia, B. Zhang, H. Li, Z. X. Wang, L. Q. Chen, MnO powder as anode active materials for lithium ion batteries, *J. Power Sources*, 195 (2010) 3300, <https://doi.org/10.1016/j.jpowsour.2009.11.133>
- [102] W. Weng, L. Tang, W. Xiao, Capture and electro-splitting of CO₂ in molten salts, *J. Energy Chem.* 28 (2019) 128-143. <https://doi.org/10.1016/j.jechem.2018.06.012>.
- [103] A.-L. Remmel, S. Ratso, G. Divitini, M. Danilson, V. Mikli, M. Uibu, J. Aruväli, I. Kruusenberg, Iron catalyzed growth of crystalline multi-walled carbon nanotubes from ambient carbon dioxide mediated by molten carbonates, *ACS Sustain. Chem. Eng.*, 10(1) (2021) 134-145. <https://doi.org/10.1021/ACSSUSCHEMENG.1C05250>.
- [104] J. Asenbauer, T. Eisenmann, M. Kuenzel, A. Kazzazi, Z. Chen, D. Bresser, The success story of graphite as a lithium-ion anode material – fundamentals, remaining challenges, and recent developments including silicon (oxide) composites, *Sustainable Energy Fuels*, 4 (2020) 5387-5416. <https://doi.org/10.1039/D0SE00175A>.
- [105] Z. Ogumi and H. Wang, Carbon anode materials in Lithium-Ion Batteries - Science and Technologies, M. Yoshio, R. J. Brodd and A. Kozawa Eds., Springer-Verlag, New York, U.S.A., 1st edn, 2009, 49-73. <https://doi.org/10.1007/978-0-387-34445-4>
- [106] Environmental and socio-economic challenges in battery supply chains: graphite and lithium, 2020.
- [107] <https://westwaterresources.net/minerals-portfolio/graphite-market/>
- [108] J. Lau, G. Dey, S. Licht, Thermodynamic assessment of CO₂ to carbon nanofiber transformation for carbon sequestration in a combined cycle gas or a coal power plant, *Energy Convers. Manag.* 122 (2016) 400-410.
- [109] W. Weng, L. Tang, W. Xiao, Capture and electro-splitting of CO₂ in molten salts, *J. Energy Chem.* 28 (2019) 128-143, <https://doi.org/10.1016/j.jechem.2018.06.012>.

- [110] R. Jiang, M. Gao, X. Mao, D. Wang, Advancements and potentials of molten salt CO₂ capture and electrochemical transformation (MSCC-ET) process, *Curr. Opin. Electrochem.* 17 (2019) 38-46.
- [111] J. Ge, J. Wang, J. Cheng, S. Jiao, Electrochemical Conversion of CO₂ in Molten CaCl₂-LiCl-CaO Utilizing a Low-Cost (1-x)CaTiO₃-xNi Inert Anode, *J. Electrochem. Soc.* 163 (2016) E230–E234, DOI: 10.1149/2.1361608jes.
- [112] A. Douglas, R. Carter, N. Muralidharan, L. Oakes, C.L. Pint, Iron catalyzed growth of crystalline multi-walled carbon nanotubes from ambient carbon dioxide mediated by molten carbonates, *Carbon N. Y.* 116 (2017) 572–578, <https://doi.org/10.1016/j.carbon.2017.02.032>.
- [113] U.S. Energy Information Administration, Short-Term Energy Outlook March 2021, https://www.eia.gov/outlooks/steo/pdf/steo_full.pdf
- [114] P. Claes, D. Moyaux, D. Peeters, Solubility and solvation of carbon dioxide in the molten Li₂CO₃/Na₂CO₃/K₂CO₃ (43.5:31.5:25.0 mol-%) eutectic mixture at 973 K. - I. Experimental part, *Eur. J. Inorg. Chem.* (1999) 583–588. [https://doi.org/10.1002/\(sici\)1099-0682\(199904\)1999:4<583::aid-ejic583>3.0.co;2-y](https://doi.org/10.1002/(sici)1099-0682(199904)1999:4<583::aid-ejic583>3.0.co;2-y).
- [115] G.J. Janz, C.B. Allen, N.P. Bansal, R.M. Murphy, R.P.T. Tomkins, Physical Properties Data Compilations Relevant To Energy Storage - 2. Molten Salts: Data on Single and Multi-Component Salt Systems., *Natl. Bur. Stand. Natl. Stand. Ref. Data Ser.* (1979).
- [116] E. Olsen, V. Tomkute, Carbon capture in molten salts, *Energy Sci. Eng.* 1 (2013) 144-150. <https://doi.org/10.1002/ese3.24>.
- [117] W. Weng, L. Tang, W. Xiao, Capture and electro-splitting of CO₂ in molten salts, *J. Energy Chem.* 28 (2019) 128-143. <https://www.sciencedirect.com/science/article/pii/S2095495618304364#bib0001>

- [118] M.D. Ingram, B. Baron, G.J. Janz, The electrolytic deposition of carbon from fused carbonates, *Electrochim. Acta.* 11 (1966) 1629-1639. [https://doi.org/10.1016/0013-4686\(66\)80076-2](https://doi.org/10.1016/0013-4686(66)80076-2).
- [119] V. Kaplan, E. Wachtel, K. Gartsman, Y. Feldman, I. Lubomirsky, Conversion of CO₂ to CO by Electrolysis of Molten Lithium Carbonate, *J. Electrochem. Soc.* 157 (2010) B552. <https://doi.org/10.1149/1.3308596>.
- [120] J. Ren, J. Lau, M. Lefler, S. Licht, The Minimum Electrolytic Energy Needed to Convert Carbon Dioxide to Carbon by Electrolysis in Carbonate Melts, *J. Phys. Chem. C.* 119 (2015) 23342-23349. <https://doi.org/q>.
- [121] H. Lai, J. Li, Z. Chen, Z. Huang, Carbon Nanohorns as a HighPerformance Carrier for MnO₂ Anode in Lithium-Ion Batteries, *ACS Appl. Mater. Interfaces*, 4 (2012) 2325-2328. <https://doi.org/10.1021/am300378w>.
- [122] D.-S. Liu, D.-H. Liu, B.-H. Hou, Y.-Y. Wang, J.-Z. Guo, Q.-L. Ning, X.-L. Wu, 1D porous MnO@N-doped carbon nanotubes with improved Li storage properties as advanced anode material for lithium-ion batteries, *Electrochim. Acta*, 264 (2018) 292-300. <https://doi.org/10.1016/j.electacta.2018.01.129>.
- [123] H. Zhu, Z. Li, F. Xu, Z. Qin, R. Sun, C. Wang, S. Lu, Y. Zhang, H. Fan, Ni₃Se₄@CoSe₂ hetero-nanocrystals encapsulated into CNT-porous carbon interpenetrating frameworks for high-performance sodium ion battery, *J. Colloid Interface Sci.*, 611 (2022) 718–725. <https://doi.org/10.1016/j.jcis.2021.11.175>.
- [124] X.-X. Luo, W.-H. Li, H.-J. Liang, H.-X. Zhang, K.-D. Du, X.-T. Wang, X.-F. Liu, J.-P. Zhang, X.-L. Wu, Covalent Organic Framework with Highly Accessible Carbonyls and π -Cation Effect for Advanced Potassium-Ion Batteries, *Angew. Chem. Int. Ed.*, 61 (2022) e202117661. <https://doi.org/10.1002/anie.202117661>.
- [125] X. Wang, F. Sharif, X. Liu, G. Licht, M. Lefler, S. Licht, Magnetic Carbon Nanotubes: Carbide Nucleated Electrochemical Growth of Ferromagnetic CNTs from CO₂, *J. CO₂ Util.* 40 (2020) 101218. <https://doi.org/10.1016/J.JCOU.2020.101218>.

- [126] S. Arcaro, F.A. Berutti, A.K. Alves, C.P. Bergmann, MWCNTs produced by electrolysis of molten carbonate: Characteristics of the cathodic products grown on galvanized steel and nickel chrome electrodes, *Appl. Surf. Sci.* 466 (2019) 367-374. <https://doi.org/10.1016/J.APSUSC.2018.10.055>.
- [127] M. Demir, Z. Kahveci, B. Aksoy, N.K.R. Palapati, A. Subramanian, H.T. Cullinan, H.M. El-Kaderi, C.T. Harris, R.B. Gupta, Graphitic Biocarbon from Metal-Catalyzed Hydrothermal Carbonization of Lignin, *Ind. Eng. Chem. Res.*, 54 (2015) 10731-10739. <https://doi.org/10.1021/ACS.IECR.5B02614>.
- [128] C. Julien, M. Massot, R. Baddour-Hadjean, S. Franger, S. Bach, J.P. Pereira-Ramos, Raman spectra of birnessite manganese dioxides, *Solid State Ionics*, 159 (2003) 345-356. [https://doi.org/10.1016/S0167-2738\(03\)00035-3](https://doi.org/10.1016/S0167-2738(03)00035-3).
- [129] M. Rana, V. Sai Avvaru, N. Boaretto, V. A. de la Peña O'Shea, R. Marcilla, V. Etacheri, et al., High rate hybrid MnO₂@CNT fabric anodes for Li ion batteries: properties and a lithium storage mechanism study by in situ synchrotron X-ray scattering, *J. Mater. Chem. A*, 7 (2019) 26596-26606. <https://doi.org/10.1039/c9ta08800h>.
- [130] L. Eifert, R. Banerjee, Z. Jusys, R. Zeis, Characterization of Carbon Felt Electrodes for Vanadium Redox Flow Batteries: Impact of Treatment Methods, *J. Electrochem. Soc.*, 165 (2018) A2577-A2586. <https://doi.org/10.1149/2.0531811jes>.
- [131] V. Di Noto, E. Negro, S. Polizzi, P. Riello, P. Atanassov, Preparation, characterization and single-cell performance of a new class of Pd-carbon nitride electrocatalysts for oxygen reduction reaction in PEMFCs, *Applied Catalysis B: Environmental*, 111-112 (2012) 185-199. <https://doi.org/10.1016/j.apcatb.2011.09.034>.
- [132] H.W. Nesbitt, M. Scaini, H. Hochst, G.M. Bancroft, A.G. Schaufuss, R. Szargan, Synchrotron XPS evidence for Fe²⁺-S and Fe³⁺-S surface species on pyrite fracture-surfaces, and their 3D electronic states, *American Mineralogist*, 85 (2000) 850-857. <https://doi.org/10.2138/am-2000-5-628>.

- [133] M. Oku, K. Kichinosuke, S. Ikeda, X-ray Photoelectron Spectroscopy of Manganese-Oxygen System, *J. Electron. Spectros. Relat. Phenomena*, 7 (1975) 465-473. [https://doi.org/10.1016/0368-2048\(75\)85010-9](https://doi.org/10.1016/0368-2048(75)85010-9).
- [134] V. Di Castro, G. Polzonetti, XPS study of MnO oxidation, *J. Electron. Spectros. Relat. Phenomena*, 48 (1989)117-123. [https://doi.org/10.1016/0368-2048\(89\)80009-X](https://doi.org/10.1016/0368-2048(89)80009-X).
- [135] G. Elmacı, A. S. Ertürk, M. Sevim, Ö. Metin, MnO₂ nanowires anchored on mesoporous graphitic carbon nitride (MnO₂@mpg-C₃N₄) as a highly efficient electrocatalyst for the oxygen evolution reaction, *Int. J. Hydrog. Energy*, 44 (2019) 17995-18006. <https://doi.org/10.1016/j.ijhydene.2019.05.089>.
- [136] Ý. A. Mørch, I. Sandvig, Ø. Olsen, I. Donati, M. Thuen, G. Skjåk-Bræk, O. Haraldseth, C. Brekken, *Contrast Media and Molecular Imaging*, 7(2) (2012) 265-275. <https://doi.org/10.1002/cmimi.493>
- [137] C. Shen, G. Hu, L.-Z. Cheong, S. Huang, J.-G. Zhang, D. Wang, Direct Observation of the Growth of Lithium Dendrites on Graphite Anodes by Operando EC-AFM, *Small Methods*, 2 (2018) 1700298. <https://doi.org/10.1002/smt.201700298>.
- [138] G. Lacarbonara, M. Rahmanipour, J. Belcari, L. Lodi, A. Zucchelli, C. Arbizzani, Electro dilatometric analysis under applied force: A powerful tool for electrode investigation, *Electrochimica Acta*, 375 (2021) 137938. <https://doi.org/10.1016/j.electacta.2021.137938>.
- [139] A. Rimmel, S. Ratso, G. Divitini, M. Danilson, V. Mikli, M. Uibu, et al., Nickel and Nitrogen-Doped Bifunctional ORR and HER Electrocatalysts Derived from CO₂, *ACS Sustainable Chem Eng.* 10(1) (2022) 134145 <https://doi.org/10.1021/acssuschemeng.1c05250>.
- [140] X. Fang, X. Lu, X. Guo, Y. Mao, Y.-S. Hu, J. Wang, et al, Electrode reactions of manganese oxides for secondary lithium batteries, *Electrochemistry Communications*, 12 (2010) 1520-1523. doi:10.1016/j.elecom.2010.08.023.

- [141] I. Kovalenko, B. Zdyrko, A. Magasinski, B. Hertzberg, Z. Milicev, R. Burtovyy, A major constituent of brown algae for use in high-capacity Li-ion batteries, *Science*, 334 (2011) 6052 75-79 DOI: 10.1126/science.1209150.
- [142] W.-Y. Chou, Y.-C. Jin, J.-G. Duh, C.-Z. Lu, and S.-C. Liao, A facile approach to derive binder protective film on high voltage spinel cathode materials against high temperature degradation, *Appl. Surf. Sci.*, 355 (2015) 1272-1278. <https://doi.org/10.1016/j.apsusc.2015.08.046>.
- [143] F. Bigoni, F. De Giorgio, F. Soavi, C. Arbizzani, Sodium Alginate: A Water-Processable Binder in High-Voltage Cathode Formulations, *J. Electrochem. Soc.*, 164 (2017) A6171-A6177. <https://doi.org/10.1149/2.0281701jes>.
- [144] M. Aneke and M. Wang, “Energy storage technologies and real life applications â A state of the art review,” *Appl. Energy*, vol. 179, 2016
- [145] B. Diouf and R. Pode, “Potential of lithium-ion batteries in renewable energy,” *Renew. Energy*, vol. 76, 2015.
- [146] E. Chemali, M. Preindl, P. Malysz, and A. Emadi, “Electrochemical and Electrostatic Energy Storage and Management Systems for Electric Drive Vehicles: State-of-the-Art Review and Future Trends,” *IEEE J. Emerg. Sel. Top. Power Electron.*, 4(3) (2016).
- [147] 28 X. Luo, J. Wang, M. Dooner, and J. Clarke, “Overview of current development in electrical energy storage technologies and the application potential in power system operation,” *Appl. Energy*, vol. 137, 2015.
- [148] A.-I. Stan, M. Swierczynski, D.-I. Stroe, R. Teodorescu, S. Andreassen, Søren, Lithium-ion battery chemistries from renewable energy storage to automotive and back-up power applications — An overview, 2014 International Conference on Optimization of Electrical and Electronic Equipment, (OPTIM 2014). 713-720. 10.1109/OPTIM.2014.6850936.

- [149] D. L. J. Zheng , Q. Li, X. Xie, S. Ferrara, Z. Nie, L. B. Mehdi, N. D. Browning, J.-G. Zhang, G. L. Graff, J. Liu, J. Xiao, High Energy Density Lithium–Sulfur Batteries: Challenges of Thick Sulfur Cathodes, *Adv. Energy Mater.* 5 (2015) 1402290
- [150] E. Peled, S. Menkin, Review—SEI: Past, Present and Future, *J. Electrochem. Soc.* 164 (2017) A1703.
- [151] A. Wang, S. Kadam, H. Li, S. Shi, Y. Qi, Review on modeling of the anode solid electrolyte interphase (SEI) for lithium-ion batteries, *npj Computational Materials* 4 (2018) 15, <https://doi.org/10.1038/s41524-018-0064-0>.
- [152] Z. Hong, V. Viswanathan, Phase-Field Simulations of Lithium Dendrite Growth with Open-Source Software, *ACS Energy Lett.*, 3(7) (2018) 1737–174, <https://doi.org/10.1021/acseenergylett.8b01009>.
- [153] G. J. May, A. Davidson, B. Monahov, Lead Batteries for Utility Energy Storage: A Review. *Journal of Energy Storage*, 15 (2018) 145-157. <https://doi.org/10.1016/j.est.2017.11.008>.
- [154] E. Peled, The Electrochemical Behavior of Alkali and Alkaline Earth Metals in Nonaqueous Battery Systems—The Solid Electrolyte Interphase Model. *J. Electrochem. Soc.* 126 (12) (1979) 2047-2051. <https://doi.org/10.1149/1.2128859>
- [155] A. Jana, S. I. Woo, K. S. N. Vikrant, R. E. García, Electrochemomechanics of Lithium Dendrite Growth. *Energy Environ. Sci.*, 12 (12) (2019) 3595-3607. <https://doi.org/10.1039/C9EE01864F>
- [156] J. Niu, S. Kang, CHAPTER 1, New High-energy Anode Materials, *Future Lithium-ion Batteries*, The Royal Society of Chemistry", Editor: Ali Eftekhari (2019) 1-25, [10.1039/9781788016124-00001](https://doi.org/10.1039/9781788016124-00001).
- [157] S. Kharabadze, A. Thorn, E. A. Koulakova, A. N. Kolmogorov, Prediction of stable Li-Sn compounds: boosting ab initio searches with neural network potentials, *npj Computational Materials* 8 (2022) 103, <https://doi.org/10.1038/s41524-022-00825-4>.

- [158] Y. Liu, Q. Liu, L. Xin, Y. Liu, F. Yang, E. A. Stach, J. Xie, Making Li-metal electrodes rechargeable by controlling the dendrite growth direction, *Nature Energy* 2 (2017) 17083, <https://doi.org/10.1038/nenergy.2017.83>.
- [159] W. Ren, Y. Zheng, Z. Cui, Y. Tao, B. Li, W. Wang, Recent Progress of Functional Separators in Dendrite Inhibition for Lithium Metal Batteries, *Energy Storage Materials* 35 (2021) 157-168. <https://doi.org/10.1016/j.ensm.2020.11.019>.
- [160] N. Xu, J. Shi, G. Liu, X. Yang, J. Zheng, Z. Zhang, Y. Yang, Research progress of fluorine-containing electrolyte additives for lithium ion batteries, *J. Power Sources Adv.*, 7 (2021) 100043, [10.1016/j.powera.2020.100043](https://doi.org/10.1016/j.powera.2020.100043)
- [161] Z. Xie, Z. Wu, X. An, X. Yue, A. Yoshida, X. Du, X. Hao, A. Abudula, G. Guan, 2-Fluoropyridine: a novel electrolyte additive for lithium metal batteries with high areal capacity as well as high cycling stability, *Chem. Eng. J.*, 393 (2020) 124789, [10.1016/j.cej.2020.124789](https://doi.org/10.1016/j.cej.2020.124789)
- [162] Z. Xie, X. An, Z. Wu, X. Yue, J. Wang, X. Hao, A. Abudula, G. Guan, Fluoropyridine family: bifunction as electrolyte solvent and additive to achieve dendrites-free lithium metal batteries, *J. Mater. Sci. Technol.*, 74 (2021) 119-127, [10.1016/j.jmst.2020.10.017](https://doi.org/10.1016/j.jmst.2020.10.017)
- [163] X. Li, J. Liu, J. He, H. Wang, S. Qi, D. Wu, J. Huang, F. Li, W. Hu, J. Ma, Hexafluoroisopropyl trifluoromethanesulfonate-driven easily Li⁺ desolvated electrolyte to afford Li||NCM811 cells with efficient anode/cathode electrolyte interphases, *Adv. Funct. Mater.*, 31 (2021) 1-9, [10.1002/adfm.202104395](https://doi.org/10.1002/adfm.202104395)
- [164] J. Huang, J. Liu, J. He, M. Wu, S. Qi, H. Wang, F. Li, J. Ma, Optimizing electrode/electrolyte interphases and li-ion flux/solvation for lithium-metal batteries with qua-functional heptafluorobutyric anhydride, *Angew. Chem. Int. Ed.*, 60 (2021) 20717-20722, [10.1002/anie.202107957](https://doi.org/10.1002/anie.202107957)
- [165] F. Li, J. He, J. Liu, M. Wu, Y. Hou, H. Wang, S. Qi, Q. Liu, J. Hu, J. Ma, Gradient Solid Electrolyte Interphase and lithium-ion solvation regulated by bisfluoroacetamide for stable lithium metal batteries, *Angew. Chem. Int. Ed.*, 60 (2021) 6600-6608, [10.1002/anie.202013993](https://doi.org/10.1002/anie.202013993)

- [166] S. Chen, B. Ding, Q. Lin, Y. Shi, B. Hu, Z. Li, H. Dou, X. Zhang, Construction of stable Solid Electrolyte Interphase on lithium anode for long-cycling solid-state lithium–sulfur batteries, *J. Electroanal. Chem.*, 880 (2021), 114874, 10.1016/j.jelechem.2020.114874
- [167] X. Zhang, Q. Wu, X. Guan, F. Cao, C. Li, J. Xu, Lithium dendrite-free and fast-charging for high voltage nickel-rich lithium metal batteries enabled by bifunctional sulfone-containing electrolyte additives, *J. Power Sources*, 452 (2020) 227833, 10.1016/j.jpowsour.2020.227833
- [168] C. Forestier, P. Jankowski, A. Wizner, C. Davoisne, G. Gachot, L. Sannier, S. Grugeon, P. Johansson, M. Armand, S. Laruelle, Comparative investigation of Solid Electrolyte Interphases created by the electrolyte additives vinyl ethylene carbonate and dicyano ketene vinyl ethylene acetal, *J. Power Sources*, 345 (2017) 212-220, 10.1016/j.jpowsour.2017.01.131
- [169] J. Kasnatscheew, M. Börner, B. Streipert, P. Meister, R. Wagner, I. Cekic Laskovic, M. Winter, Lithium ion battery cells under abusive discharge conditions: electrode potential development and interactions between positive and negative electrode, *J. Power Sources*, 362 (2017) 278-282, 10.1016/j.jpowsour.2017.07.044
- [170] L. Frenck, G.K. Sethi, J.A. Maslyn, N.P. Balsara, Factors that control the formation of dendrites and other morphologies on lithium metal anodes, *Front. Energy Res*, 7 (2019), 10.3389/fenrg.2019.00115 [171] 23
- [172] F. Qiu, S. Ren, X. Zhang, P. He, H. Zhou, A high efficiency electrolyte enables robust inorganic–organic solid electrolyte interfaces for fast Li metal anode, *Sci. Bull.* (2021), 1-7, 10.1016/j.scib.2021.01.007
- [173] U. S. Meda, L. Lal, M. Sushantha, P. Garg, Solid Electrolyte Interphase (SEI), a boon or a bane for lithium batteries: A review on the recent advances, *Journal of Energy Storage* 47 (2022), 103564 <https://doi.org/10.1016/j.est.2021.103564>
- [174] Y. Li, Y. Sun, A. Pei, K. Chen, A. Vailionis, Y. Li, G. Zheng, J. Sun, Y. Cui, Robust Pinhole-Free Li₃N Solid Electrolyte Grown from Molten Lithium. *ACS Cent. Sci.*, 4 (1) (2018) 97-104. <https://doi.org/10.1021/acscentsci.7b00480>.

- [175] M. Wu, Z. Wen, Y. Liu, X. Wang, L. Huang, Electrochemical Behaviors of a Li₃N Modified Li Metal Electrode in Secondary Lithium Batteries. *J. Power Sources* 196(19) (2011) 8091-8097. <https://doi.org/10.1016/j.jpowsour.2011.05.035>.
- [176] G. Ma, Z. Wen, M. Wu, C. Shen, Q. Wang, J. Jin, X. A. Wu, Lithium Anode Protection Guided Highly-Stable Lithium-Sulfur Battery. *Chem. Commun.* 50(91) (2014) 14209-14212. <https://doi.org/10.1039/c4cc05535g>.
- [177] T. Foroozan, S. Sharifi-Asl, R. Shahbazian-Yassar, Mechanistic understanding of Li dendrites growth by in- situ/operando imaging techniques, *J. Power Sources* 461 (2020) 228135, <https://doi.org/10.1016/j.jpowsour.2020.228135>
- [178] M. Golozar, P. Hovington, A. Paoella, S. Bessette, M. Lagacé, P. Bouchard, H. Demers, R. Gauvin, K. Zaghbi, In Situ Scanning Electron Microscopy Detection of Carbide Nature of Dendrites in Li–Polymer Batteries, *Nano Lett.* 18 (2018) 7583-7589, <https://doi.org/10.1021/acs.nanolett.8b03148>.
- [179] W. Zhu, A. Paoella, C.-S. Kim, D. Liu, Z. Feng, C. Gagnon, J. Trottier, A. Vijn, A. Guerfi, A. Mauger, C. M. Julien, M. Armand, K. Zaghbi, Investigation of the reaction mechanism of lithium sulfur batteries in different electrolyte systems by in situ Raman spectroscopy and in situ X-ray diffraction, *Sustain. Energy Fuels* 2017, 1, 737-747, DOI <https://doi.org/10.1039/C6SE00104A>.
- [180] B. Dunn, H. Kamath, J.M. Tarascon, Electrical energy storage for the grid: a battery of choices, *Science* 334 (2011) 928-935.
- [181] W. Xu, et al. Lithium metal anodes for rechargeable batteries. *Energy Environ. Sci.* 7 (2014) 513–537.
- [182] M. Dollé, L. Sannier, B. Beaudoin, M. Trentin, J. M. Tarascon, Live scanning electron microscope observations of dendritic growth in lithium/polymer cells. *Electrochem. Solid State Lett.* 5 (2002) A286-A289.
- [183] R. L. Sacci, J. M. Black, N. Balke, N. J. Dudney, K. L. More, R. R. Unocic, Nanoscale Imaging of Fundamental Li Battery Chemistry: SolidElectrolyte Interphase

Formation and Preferential Growth of Lithium Metal Nanoclusters, *Nano Lett.* 15(2015) 2011-2018, DOI: 10.1021/nl5048626

[184] F. Sagane, R. Shimokawa, H. Sano, H. Sakaebe, Y. Iriyama, In-situ scanning electron microscopy observations of Li plating and stripping reactions at the lithium phosphorus oxynitride glass electrolyte/Cu interface. *J. Power Sources* 225, 245–250 (2013).

[185] S. Lv, T. Verhallen, A. Vasileiadis, F. Ooms, Y. Xu, Z. Li, Z. Li, M. Wagemaker, Operando monitoring the lithium spatial distribution of lithium metal anodes, *Nature Communications* 9 (2018) 2152, <https://doi.org/10.1038/s41467-018-04394-3>.

[186] L. Magnier, L. Lecarme, F. Alloin, A. King, R. Bouchet, A. Tengattini, D. Devaux, E. Maire, Tomography Imaging of Lithium Electrodeposits Using Neutron, Synchrotron X-ray, and Laboratory X-ray sources: A Comparison, *Front. Energy Res.* (2021) 9657712. 10.3389/fenrg.2021.657712.

[187] Y. R. Dougassa, J. Jacquemin, L. El Ouatani, C. Tessier, M. Anouti, Viscosity and Carbon Dioxide Solubility for LiPF₆, LiTFSI, and LiFAP in Alkyl Carbonates: Lithium Salt Nature and Concentration Effect, *J. Phys. Chem. B* 118(14) (2014) 3973-3980, [dx.doi.org/10.1021/jp500063c](https://doi.org/10.1021/jp500063c)

[188] M. R. Busche, T. Drossel, T. Leichtweiss, D. A. Weber, M. Falk, M. Schneider, M.-L. Reich, H. Sommer, P. Adelhelm, J. Janek, Dynamic Formation of a Solid-Liquid Electrolyte Interphase and Its Consequences for Hybrid-Battery Concepts. *Nature Chem.* 8(5) (2016) 426–434. <https://doi.org/10.1038/nchem.2470>

[189] Z. Hu, S. Zhang, S. Dong, Q. Li, G. Cui, L. Chen, Self-Stabilized Solid Electrolyte Interface on a Host-Free Li-Metal Anode toward High Areal Capacity and Rate Utilization. *Chem. Mater.* 30 (12) (2018) 4039-4047. <https://doi.org/10.1021/acs.chemmater.8b00722>

[190] C. Naudin, J. L. Bruneel, M. Chami, B. Desbat, J. Grondin, J. C. Lassègues, L. Servant, Characterization of the lithium surface by infrared and Raman spectroscopies, *Journal of Power Sources* 124(2) (2003) 518-522 [https://doi.org/10.1016/S0378-7753\(03\)00798-5](https://doi.org/10.1016/S0378-7753(03)00798-5)

- [191] L. Haneke, J. E. Frerichs, A. Heckmann, M. M. Lerner, T. Akbay, T. Ishihara, M. R. Hansen, M. Winter, T. Placke, Editors' Choice—Mechanistic Elucidation of Anion Intercalation into Graphite from Binary-Mixed Highly Concentrated Electrolytes via Complementary ¹⁹F MAS NMR and XRD Studies, *J. Electrochem. Soc.* 167 (2020) 140526, DOI:10.1149/1945-7111/abc437.
- [192] T. Placke, R. Kloepsch, S. Dühnen, M. Winter, Lithium ion, lithium metal, and alternative rechargeable battery technologies: the odyssey for high energy density, *Journal of Solid State Electrochemistry* 21 (2017) 1939-1964 (2017).
- [193] X. Wei, M. Zhang, B. Miao, R. Liu, Volumetric capacity enhancement in LiFePO₄ cathodes by hot isostatic pressing, *Scripta Materialia*, 194 (2021) 113638, <https://doi.org/10.1016/j.scriptamat.2020.113638>.
- [194] W.-J. Kwak, R. D. Sharon, C. Xia, H. Kim, L. R. Johnson, P. G. Bruce, L. F. Nazar, Y.-K. Sun, A. A. Frimer, M. Noked, S. A. Freunberger, D. Aurbach, Lithium–Oxygen Batteries and Related Systems: Potential, Status, and Future, *Chem. Rev.* 120(14) (2020) 6626-6683, <https://doi.org/10.1021/acs.chemrev.9b00609>
- [195] T. Placke, R. Kloepsch, S. Dühnen, M. Winter, Lithium ion, lithium metal, and alternative rechargeable battery technologies: the odyssey for high energy density, *Journal of Solid State Electrochemistry* 21 (2017) 1939-1964 (2017) https://doi.org/10.1007/s10008-017-3610-7_permesso
- [196] X.-B. Cheng, R. Zhang, C. -Z. Zhao, Q. Zhang, Toward Safe Lithium Metal Anode in Rechargeable Batteries: A Review, *Chem. Rev.* 2017, 117, 15, 10403–10473, <https://doi.org/10.1021/acs.chemrev.7b00115>.
- [197] J. R. Nair, L. Imholt, G. Brunklaus, M. Winter, Lithium Metal Polymer Electrolyte Batteries: Opportunities and Challenges, *Electrochem. Soc. Interface* 28 (2019) 55, <https://doi.org/10.1149/2.F05192if>.
- [198] E. Sánchez-Díez, E. Ventosa, M. Guarnieri, A. Trovò, C. Flox, R. Marcilla, F. Soavi, P. Mazur, E. Aranzabe, R. Ferret, Redox flow batteries: Status and perspective towards sustainable stationary energy storage, *Journal of Power Sources* 481(2021) 228804, <https://doi.org/10.1016/j.jpowsour.2020.228804>.

- [199] P. Alotto, M. Guarnieri, F. Moro, Redox-Flow Batteries for the storage of renewable energy: a review, *Ren. Sust. Energ. Rev.*, 29 (2014), 325-335, 10.1016/j.rser.2013.08.001.
- [200] S. Yin, L. Zhou, X. Du, Y. Yang, Influence of temperature on performance of all vanadium redox flow battery: analysis of ionic mass transfer, *Ionics* 25 (2019) 593-606, <https://doi.org/10.1007/s11581-018-2626-z>. permesso
- [201] A. Chatzivasileiadi, E. Ampatzi, I. Knight, Characteristics of electrical energy storage technologies and their applications in buildings, *Renewable and Sustainable Energy Reviews*, 25(2013) 814-830, <https://doi.org/10.1016/j.rser.2013.05.023>
- [202] G. Tomazic, M. Skyllas-Kazacos, Redox Flow Batteries, T. Moseley, J. Garche (Eds.), *Electrochemical Energy Storage for Renewable Sources and Grid balancing* (first ed.), Elsevier (Newnes) (2015).
- [203] C. Menictas, M. Skyllas-Kazacos, Final Report, SERDF grant, New South Wales Office of Energy, Australia (1997)
- [204] Y. Li, T. Van Nguyen, Core-shell rhodium sulfide catalyst for hydrogen evolution reaction/hydrogen oxidation reaction in hydrogen-bromine reversible fuel cell, *J. Power Sources*, 382 (2018) 152-159, 10.1016/j.jpowsour.2018.02.005
- [205] D. Kim, Y. Kim, Y. Lee, J. Jeon, 1, 2-Dimethylimidazole based bromine complexing agents for vanadium bromine redox flow batteries, *Int. J. Hydrogen Energy*, 44 (2019) 12024-12032, 10.1016/j.ijhydene.2019.03.050
- [206] F. R. Brushett, M. J. Aziz, K. E. Rodby, On Lifetime and Cost of Redox-Active Organics for Aqueous Flow Batteries, *ACS Energy Lett.* 5 (2020) 879-884, <https://doi.org/10.1021/acseenergylett.0c00140>.
- [207] K. L. Hawthorne, J. S. Wainright, R. F. Savinell, Maximizing plating density and efficiency for a negative deposition reaction in a flow battery, *Journal of Power Sources* 269 (2014) 216-224 <https://doi.org/10.1016/j.jpowsour.2014.06.125>
- [208] S. Müller, F. Holzer, O. Haas, Optimized zinc electrode for the rechargeable zinc-air battery, *J. Appl. Electrochem.* 1998, 28, 895–898.

- [209] P. K. Leung, Q. Xu, T. S. Zhao, High-potential zinc–lead dioxide rechargeable cells, *Electrochimica Acta* 79 (2012) 117-125, <https://doi.org/10.1002/cplu.20140210>.
- [210] F C. Walsh, C. Ponce de León, L. Berlouis, G. Nikiforidis, L. F. Arenas-Martínez, D. Hodgson, D. Hall, The Development of Zn–Ce Hybrid Redox Flow Batteries for Energy Storage and Their Continuing Challenges, *ChemPlusChem* 80(2) (2015) 288-311, <https://doi.org/10.1002/cplu.201402103>.
- [211] Q. Lai, H. Zhang, X. Li, L. Zhang, Y. Cheng, A novel single flow zinc–bromine battery with improved energy density, *Journal of Power Sources*, 235 (2013) 1-4, <https://doi.org/10.1016/j.jpowsour.2013.01.193>
- [212] L. Clarke, B.J. Dougherty, S. Harrison, P.J. Millington, S. Mohanta, US 2004/0202925 A1, Cerium Batteries, (2004)
- [213] Characterization of a zinc–cerium flow battery, *Journal of Power Sources* 196(11) (2011) 5174-5185, <https://doi.org/10.1016/j.jpowsour.2011.01.095>.
- [214] R. P. Kreh, R. M. Spotnitz, J. T. Lundquist, Mediated Electrochemical Synthesis of Aromatic Aldehydes, Ketones, and Quinones Using Ceric Methanesulfonate, *J. Org. Chem.*, 54 (1989) 1526-1531.
- [215] W. Geng, L. Zhang, Y.-N. Zhang, W.-M. Lau, L.-M. Liu, First-Principles Study of Lead Iodide Perovskite Tetragonal and Orthorhombic Phases for Photovoltaics, *J. Phys. Chem. C*, 118 (2014), 14795-14804, <https://doi.org/10.1021/jp504951h>.
- [216] L. Zhang, Z.-G. Shao, X. Wang, H. Yu, S. Liu, B. Yi, The characterization of graphite felt electrode with surface modification for H₂/Br₂ fuel cell, *J. Power Sources*, 242 (2013) 15-22, <https://doi.org/10.1016/j.jpowsour.2013.05.049>
- [217] L. W. Hruska, R. F. Savinell, Investigation of Factors Affecting Performance of the Iron-Redox Battery, *J. Electrochem. Soc.*, 128 (1981) 18-25, [10.1149/1.2127366](https://doi.org/10.1149/1.2127366)
- [218] A. Dinesh, S. Olivera, K. Venkatesh, M. S. Santosh, M. G. P. Inamuddin, A. M. Asiri, H. B. Muralidhara, Iron-based flow batteries to store renewable energies, *Environ. Chem. Lett.*, 16 (2018) 683-694, [10.1007/s10311-018-0709-8](https://doi.org/10.1007/s10311-018-0709-8)

- [219] S. Selverston, E. Nagelli, J. S. Wainright, R. F. Savinell, All-Iron Hybrid Flow Batteries with In-Tank Rebalancing, *J. Electrochem. Soc.* 166 (2019) A1725.
- [220] B. Kratochvil, K. R. Betty, A Secondary Battery Based on the Copper (II)-(I) and (I)- (0) Couples in Acetonitrile. *J. Electrochem. Soc.* 121 (7) (1974) 851–854.
- [221] W. W. Porterfield, J. T. Yoke, Room Temperature Fused Salts: Liquid Chlorocuprates(I). In: *Inorganic Compounds with Unusual Properties, Advances in Chemistry* (ed. King, R. B.), (1976) 104-111. Washington, DC: ACS Publications. [https://doi.org/ 10.1021/ba-1976-0150.fw001](https://doi.org/10.1021/ba-1976-0150.fw001).
- [222] D. Lloyd, T. Vainikka, S. Schmachtel, L. Murtomäki, K. Kontturi Simultaneous characterisation of electrode kinetics and electrolyte properties in ionic liquids using a rotating disc electrode *Electrochimica Acta*, 69 (2012) 139-145 <https://doi.org/10.1016/j.electacta.2012.02.104>
- [223] L. Sanz, J. Palma, E. García-Quismondo, M. Anderson, The effect of chloride ion complexation on reversibility and redox potential of the Cu(II)/Cu(I) couple for use in redox flow batteries, *Journal of Power Sources*, 224(15) (2013) 278-284 <https://doi.org/10.1016/j.jpowsour.2012.10.005>
- [224] D. Lloyd, T. Vainikka, K. Kontturi, The development of an all-copper hybrid redox flow battery using deep eutectic solvents, *Electrochim. Acta* 100 (2013) 18-23. <https://doi.org/10.1016/j.electacta.2013.03.130>.
- [225] P. Peljo, D. Lloyd, N. Doan, M. Majaneva, K. Kontturi, Towards a thermally regenerative all-copper redox flow battery. *Phys. Chem. Chem. Phys.* 16 (2014) 2831-2835, <https://doi.org/10.1039/C3CP54585G>.
- [226] E. A. Stricker, K. W. Krueger, R. F. Savinell, J. S. Wainright, Investigating a Bromide Supported Electrolyte for an All-Copper Flow Battery. *J. Electrochem. Soc.* 165 (9) (2018) A1797-A1804. <https://doi.org/10.1149/2.1031809jes>.
- [227] E. Agar, A. Nagelli, N. S. Sinclair, N. C. Hoyt, E. A. Stricker, R. F. Savinell, J. S. Wainright, Cost-Effective All-Copper Flow Battery Using Flowable Slurry

Electrode for Large-Scale Energy Storage. ECS Meeting Abst MA2015-02 (2015) 119. <https://ecs.confex.com/ecs/228/webprogram/Paper57696.html>.

[228] Chapter 5. Other important inorganic chemistries In Redox Flow Batteries, Roth, Noack, Skyllas-Kazacos (Eds.), Wiley-VCH GmbH in press (December 2022)

[229] S. Ahrland, J. Rawsthorne, The Stability of Metal Halide Complexes in Aqueous Solution, *J. Acta Chem. Scand.* 24 (1970) 157-172.

[230] J. J. Fritz, Chloride complexes of copper(I) chloride in aqueous solution, *J. Phys. Chem.* 84 (1980) 2241 - 2246, <https://doi.org/10.1021/j100455a006>.

[231] J. J. Fritz, Solubility of cuprous chloride in various soluble aqueous chlorides, *J. Chem. Eng. Data* 1982, 27, 188 – 193, <https://doi.org/10.1021/je00028a027>.

[232] W. Liu, D. C. McPhail, Thermodynamic properties of copper chloride complexes and copper transport in magmatic-hydrothermal solutions, *C. Chem. Geol.* 2005, 221, 21–39, [10.1016/j.chemgeo.2005.04.009](https://doi.org/10.1016/j.chemgeo.2005.04.009).

[233] R. W. Ramette, G. Fan, Copper(II) chloride complex equilibrium constants, *G. Inorg. Chem.* 22 (1983) 3323-3326, <https://doi.org/10.1021/ic00164a029>.

[234] R. W. Ramette, Copper(II) complexes with chloride ion, *Inorg. Chem.* 25 (1986) 2481-2482, <https://doi.org/10.1021/ic00234a044>.

[235] H. Zhao, J. Chang, A. Boika, A. J. Bard, Electrochemistry of High Concentration Copper Chloride Complexes. *Anal. Chem.* 85 (2013) 7696–7703. <https://doi.org/10.1021/ac4016769>.

[236] Y. Meng, A. J. Bard, Measurement of Temperature-Dependent Stability Constants of Cu(I) and Cu(II) Chloride Complexes by Voltammetry at a Pt Ultramicroelectrode. *Anal. Chem.* 87 (2015) 3498–3504. <https://doi.org/10.1021/acs.analchem.5b00052>.

[237] A. H. Whitehead, T. J. Rabbow, M. Trampert, P. Pokorny, Critical safety features of the vanadium redox flow battery, *Journal of Power Sources*, 351 (2017) 1-7, DOI:10.1016/j.jpowsour.2017.03.075.

[238] Miessler, G.; Tarr, D. Inorganic Chemistry. In Pearson Educational International, 3rd ed.; Prentice Hall, 2011; pp. 367–369. Available online: <https://hostnezt.com/cssfiles/chemistry/Inorganic%20Chemistry%20By%20GARY%20L.%20MIESSLER.pdf> (accessed on 30 November 2021).

[239] J. Brugger, D. C. McPhail, J. Black, L. Spiccia, Complexation of metal ions in brines: Application of electronic spectroscopy in the study of the Cu(II)-LiCl-H₂O system between 25 and 90 C. *Geoch. Cosmoch. Acta* 65 (2001) 2691-2708, [https://doi.org/10.1016/S0016-7037\(01\)00614-7](https://doi.org/10.1016/S0016-7037(01)00614-7).

[240] L. Martinez, R. Andrade, E. G. Birgin, J. M. Martinez, PACKMOL: A package for building initial configurations for molecular dynamics simulations, *Journal of Computational Chemistry*, 30 (2009) 2157-2164, DOI:10.1002/jcc.21224

[241] C. Bannwarth, E. Caldeweyher, S. Ehlert, A. Hansen, P. Pracht, J. Seibert, S. Spicher, S. Grimme, Extended tight-binding quantum chemistry methods, *WIREs Comput. Mol. Sci.*, 11 (2021) e1493, <https://doi.org/10.1002/wcms.1493>.

[242] S. Grimme, C. Bannwarth, P. Shushkov, A Robust and Accurate Tight-Binding Quantum Chemical Method for Structures, Vibrational Frequencies, and Noncovalent Interactions of Large Molecular Systems Parametrized for All spd-Block Elements (Z = 1–86), *J. Chem. Theory Comput.*, 13 (2017) 1989-2009, <https://doi.org/10.1021/acs.jctc.7b00118>.

[243] C. Bannwarth, S. Ehlert, S. Grimme, GFN2-xTB—An Accurate and Broadly Parametrized Self-Consistent Tight-Binding Quantum Chemical Method with Multipole Electrostatics and Density-Dependent Dispersion Contributions *J. Chem. Theory Comput.*, 15 (2019) 1652-1671, <https://doi.org/10.1021/acs.jctc.8b01176>.

- [244] P. Pracht, F. Bohle, S. Grimme, Automated exploration of the low-energy chemical space with fast quantum chemical methods, *Phys. Chem. Chem. Phys.*, 22 (2020) 7169-7192, <https://doi.org/10.1039/C9CP06869D>.
- [245] D. Figgen, G. Rauhut, M. Dolg, H. Stoll, Energy-consistent pseudopotentials for group 11 and 12 atoms: adjustment to multi-configuration Dirac–Hartree–Fock data, *Chem. Phys.* 311 (2005) 227, <https://doi.org/10.1016/j.chemphys.2004.10.005>.
- [246] K.A. Peterson, C. Puzzarini, Systematically convergent basis sets for transition metals. II. Pseudopotential-based correlation consistent basis sets for the group 11 (Cu, Ag, Au) and 12 (Zn, Cd, Hg) elements, *Theor. Chem. Acc.* 114 (2005) 283, <https://doi.org/10.1007/s00214-005-0681-9>
- [247] S. Grimme, A simplified Tamm-Dancoff density functional approach for the electronic excitation spectra of very large molecules, *J. Chem. Phys.*, 138 (2013) 244104, <https://doi.org/10.1063/1.4811331>.
- [248] M. J. Frisch, et al., *Gaussian 16, Revision C.01* (2016), Gaussian, Inc., Wallingford
- [249] F.-F. Xia, H.-B. Yi, D. Zeng, Hydrates of Copper Dichloride in Aqueous Solution: A Density Functional Theory and Polarized Continuum Model Investigation, *J. Phys. Chem. A*, 113 (2009) 14029-14038, <https://doi.org/10.1021/jp909092p>.
- [250] Hai-Bo Yi, F.-F. Xia, Q. Zhou, D. Zeng, $[\text{CuCl}_3]^-$ and $[\text{CuCl}_4]^{2-}$ Hydrates in Concentrated Aqueous Solution: A Density Functional Theory and ab Initio Study, *J. Phys. Chem. A*, 115 (2011) 4416-4426, <https://doi.org/10.1021/jp109723v>.
- [251] F.-F. Xia, H.-B. Yi, D. Zeng, Hydrates of Cu^{2+} and CuCl^+ in Dilute Aqueous Solution: A Density Functional Theory and Polarized Continuum Model Investigation, *J. Phys. Chem. A*, 114 (2010) 8406-8416, <https://doi.org/10.1021/jp1000804>.

- [252] A. C. F. Ribeiro, M. A. Estes, V. M. M. Lobo, A. J. M. Valente, S. M. N. Simoes, A. J. F. N. Sobral, H. D. Burrows, Diffusion Coefficients of Copper Chloride in Aqueous Solutions at 298.15 K and 310.15 K, *J. Chem. Eng. Data* 50 (2005) 1986-1990, <https://doi.org/10.1021/je050220y>
- [253] G. Lacarbonara, L. Faggiano, S. Porcu, P. C. Ricci, S. Rapino, D. P. Casey, J. F. Rohan, C. Arbizzani, Copper chloro-complexes concentrated solutions: an electrochemical study, *Batteries*, 7 (2021) 83, <https://doi.org/10.3390/batteries7040083>
- [254] L. Faggiano, G. Lacarbonara, W. D. Badenhorst, L. Murtomäki, L. Sanz, C. Arbizzani, Short thermal treatments of carbon felts for copper-based redox flow batteries, *Journal of Power Sources*, 520 (2022) 230846. <https://doi.org/10.1016/j.jpowsour.2021.230846>

- [255] L. Trevani, J. Ehlerova, J. Sedlbauer, P. R. Tremaine, Complexation in the Cu(II)–LiCl–H₂O system at temperatures to 423 K by UV-Visible spectroscopy. *Int. J. Hydrogen Energy* 35 (2010) 4893-4900.
- [256] R. Soltani, I. Dincer, M. A. Rosen, Electrochemical analysis of a HCl(aq)/CuCl(aq) electrolyzer: Equilibrium thermodynamics. *Int. J. Hydrogen Energy*, 41(19) (2016) 7835-7847. doi: 10.1016/j.ijhydene.2016.01.026.
- [257] R. Soltani, I. Dincer, M. A. Rosen, M. A.; Kinetic and electrochemical analyses of a CuCl/HCl electrolyzer. *Int. J. Energy Res.* 43(13) (2019) 6890-6906. doi: 10.1002/er.4703.
- [258] M. Hall, N. N. Akinfiev, E. G. LaRow, R. S. Schatz, S. N. Lvov, Thermodynamics and Efficiency of a CuCl(aq)/HCl(aq) Electrolyzer. *Electrochim. Acta* 143 (2014) 70-82. doi: 10.1016/j.electacta.2014.08.018.
- [259] N. Balashov, R. S. Schatz, E. Chalkova, N. N. Akinfiev, M. V. Fedkin, S. N. Lvov, CuCl Electrolysis for Hydrogen Production in the Cu–Cl Thermochemical Cycle. *J. Electrochem. Soc.*, 158(3) (2011) B266-B275. doi: 10.1149/1.3521253.
- [260] L. Sanz, D. Lloyd, E. Magdalena, J. Palma, M. Anderson, K. Kontturi, Study and characterization of positive electrolytes for application in the aqueous all-copper redox flow battery. *J. Power Sources*, 278 (2015) 175-182.
- [261] Z.-C. Wu, Y. Awakura, S. Ando, H. Majima, Determination of the Diffusion Coefficients of CuCl₂, FeCl₃, CuSO₄, and Fe₂(SO₄)₃ in Aqueous Solutions. *Mater. Trans., JIM* 31(1990) 1065-1071.
- [262] P. Leung, J. Palma, E. Garcia-Quismondo, L. Sanz, M. R. Mohamed, M. E. Anderson, Evaluation of electrode materials for all-copper hybrid flow batteries. *J. Power Sources*, 310 (2016) 1-11.
- [263] Q. Dai, J. J. Xu, H. J. Li, H. B. Yi, Ion association characteristics in MgCl₂ and CaCl₂ aqueous solutions: a density functional theory and molecular dynamics

investigation. *Molecular Physics* 113(22) (2015) 3545-3558
<http://dx.doi.org/10.1080/00268976.2015.1039618>

[264] M. Wang, C. Wang, H. Cai, Y. Li, Q. Zhang, H. Yi, Molecular dynamics simulation study on distinctive hydration characteristics of highly coordinated calcium chloride complexes. *J. Molecular Liquids*, 274 (2019) 261-269.

[265] S. A. Kusmanov, S. A. Silkin, P. N. Belkin, Effect of Plasma-Electrolytic Polishing on the Corrosion Resistance of Structural Steels after Their Anodic Saturation with Nitrogen, Boron, and Carbon. *Russian Journal of Electrochemistry*, 56 (2020) 356-364.

[266] K. Ngamchuea, S. Eloul, K. Tschulik, R. G. Compton, Planar diffusion to macro disc electrodes—what electrode size is required for the Cottrell and Randles-Sevcik equations to apply quantitatively? *J. Solid State Electrochem.*, 18 (2014) 3251-3257.

[267] M. V. Nikolenko, K. V. Vasylenko, V. D. Myrhorodska, A. Kostyniuk, B. Likozar, Synthesis of Calcium Orthophosphates by Chemical Precipitation in Aqueous Solutions: The Effect of the Acidity, Ca/P Molar Ratio, and Temperature on the Phase Composition and Solubility of Precipitates, *Processes*, 8 (2020) 1009.

[268] L. M. S. G. A Applegarth. C. R. Corbeil, D. J. W. Mercer, C. C. Pye, P. R. Tremaine, Raman and ab Initio Investigation of Aqueous Cu(I) Chloride Complexes from 25 to 80 °C. *J. Phys. Chem. B*, 118 (2014) 204-214.

[269] S. E. Manahan, R. T. Iwamoto, Chloro Complexes of Copper(II) and Copper(I) in Acetonitrile. *Inorg. Chem.*, 4(10) (1965) 1409-1413.

[270] M. Kazacos, M. Skyllas-Kazacos, Performance Characteristics of Carbon Plastic Electrodes in the All-Vanadium Redox Cell, *J. Electrochem. Soc.* 136 (1989) 2759.

[271] H. Kaneko, K. Nozaki, Y. Wada, T. Aoki, A. Negishi, M. Kamimoto, Vanadium redox reactions and carbon electrodes for vanadium redox flow battery, *Electrochimica Acta* 36(7) (1991) 1191-1196, [https://doi.org/10.1016/0013-4686\(91\)85108-J](https://doi.org/10.1016/0013-4686(91)85108-J)

- [272] M. H. Chakrabarti, N. P. Brandon, S. A. Hajimolana, F. Tariq, V. Yufit, M. A. Hashim, M. A. Hussain, C. T. J. Low, P. V. Aravind, Application of carbon materials in redox flow batteries, *Journal of Power Sources* 253 (2014) 150-166, <https://doi.org/10.1016/j.jpowsour.2013.12.038>
- [273] L. Sanz, D. Lloyd, E. Magdalena, J. Palma, K. Kontturi, Description and performance of a novel aqueous all-copper redox flow battery *Journal of Power Sources* 268 (2014) 121-128, <https://doi.org/10.1016/j.jpowsour.2014.06.008>
- [274] D. S. Aaron, Q. Liu, Z. Tang, G. M. Grim, A. B. Papandrew, A. Turhan, T. A. Zawodzinski, M. M. Mench, Dramatic performance gains in vanadium redox flow batteries through modified cell architecture, *Journal of Power Sources* 206 (2012) 450-453, <https://doi.org/10.1016/j.jpowsour.2011.12.026>
- [275] L. Yue, W. Li, F. Sun, L. Zhao, L. Xing, Highly hydroxylated carbon fibres as electrode materials of all-vanadium redox flow battery, *Carbon* 48(11) 2010 3079-3090, <https://doi.org/10.1016/j.carbon.2010.04.044>.
- [276] C. H. Chang, T. S. Yuen, Y. Nagao, H. Yugami, Electrocatalytic activity of iridium oxide nanoparticles coated on carbon for oxygen reduction as cathode catalyst in polymer electrolyte fuel cell, *Journal of Power Sources* 195(18) (2010) 5938-5941, <https://doi.org/10.1016/j.jpowsour.2010.01.049>
- [277] S. Zhong, M. Kazacos, R. P. Burford, M. Skyllas-Kazacos, Fabrication and activation studies of conducting plastic composite electrodes for redox cells, *Journal of Power Sources*, 36(1) (1991) 29-43, [https://doi.org/10.1016/0378-7753\(91\)80042-V](https://doi.org/10.1016/0378-7753(91)80042-V)
- [278] N. C. Hoyt, K. L. Hawthorne, R. F. Savinell, J. S. Wainright, Plating Utilization of Carbon Felt in a Hybrid Flow Battery. *J. Electrochem. Soc.* 163 (1) (2016) A5041-A5048. <https://doi.org/10.1149/2.0061601jes>.
- [279] X. Zhou, X. Zhang, L. Mo, X. Zhou, Q. Wu, Densely Populated Bismuth Nanosphere Semi-Embedded Carbon Felt for Ultrahigh-Rate and Stable Vanadium Redox Flow Batteries. *Small*, 16 (2020) 1907333. <https://doi.org/10.1002/sml.201907333>.

- [280] Q. Wu, X. Zhang, Y. Lv, L. Lin, Y. Liu, X. Zhou, Bio-inspired multiscale-pore-network structured carbon felt with enhanced mass transfer and activity for vanadium redox flow batteries. *J. Mater. Chem. A* 6 (2018) 20347-20355. <https://doi.org/10.1039/C8TA06445H>.
- [281] X. Zhou, X. Zhang, Y. Lv, L. Lin, Q. Wu, Nano-catalytic layer engraved carbon felt via copper oxide etching for vanadium redox flow batteries. *Carbon*, 153 (2019) 674-681. <https://doi.org/10.1016/j.carbon.2019.07.072>.
- [282] W. Zhang, J. Xi, Z. Li, H. Zhou, L. Liu, Z. Wu, X. Qiu, Electrochemical activation of graphite felt electrode for $\text{VO}^{2+}/\text{VO}_2^+$ redox couple application, *Electrochim. Acta* 89 (2013) 429–435. <https://doi.org/10.1016/j.electacta.2012.11.072>
- [283] B. Sun, M. Syllas-Kazacos, Modification of graphite electrode materials for vanadium redox flow battery application-1. Thermal treatment. *Electrochim. Acta* 37 (1992) 1253-1260. [https://doi.org/10.1016/0013-4686\(92\)85064-R](https://doi.org/10.1016/0013-4686(92)85064-R).
- [284] S. Zhong, C. Padeste, M. Kazacos, M. Skyllas-Kazacos, Comparison of the physical, chemical and electrochemical properties of rayon- and polyacrylonitrile-based graphite felt electrodes. *J. Power Sources* 45 (1993) 29-41. [https://doi.org/10.1016/0378-7753\(93\)80006-B](https://doi.org/10.1016/0378-7753(93)80006-B).
- [285] L. F. Castañeda, F. C. Walsh, J. L. Nava, C. Ponce de Leon, Graphite felt as a versatile electrode material: Properties, reaction environment, performance and applications. *Electrochim. Acta* 258 (2017) 1115-1139. <https://doi.org/10.1016/j.electacta.2017.11.165>.
- [286] D.A. Shirley, High-resolution X-ray photoemission spectrum of the valence bands of gold, *Phys. Rev. B*, 5 (1972) 4709-4714. <https://journals.aps.org/prb/pdf/10.1103/PhysRevB.5.4709>.
- [287] G. Daniel, Y. Zhang, S. Lanzalaco, F. Brombin, T. Kosmala, G. Granozzi, A. Wang, E. Brillas, I. Sirés, C. Durante, Chitosan-Derived Nitrogen-Doped Carbon Electrocatalyst for a Sustainable Upgrade of Oxygen Reduction to Hydrogen Peroxide

in UV-Assisted Electro-Fenton Water Treatment, *ACS Sustainable Chemistry & Engineering*, 8 (2020) 14425-14440. <https://doi.org/10.1021/acssuschemeng.0c04294>.

[288] M. Angelo do Amaral Junior, J. T. Matsushima, M. C. Rezende, E. S. Gonçalves, J. Saldanha Marcuzzo, M. R. Baldan. Production and Characterization of Activated Carbon Fiber from Textile PAN Fiber, *Journal of Aerospace Technology and Management* 9(4) (2017) 423. <http://dx.doi.org/10.5028/jatm.v9i4.831>.

[289] A. Sadezky, H. Muckenhuber, H. Grothe, R. Niessner, U. Pöschl, Raman microspectroscopy of soot and related carbonaceous materials: Spectral analysis and structural information. *Carbon* 43 (2005) 1731-1742. <https://doi.org/10.1016/j.carbon.2005.02.018>.

[290] R. Banerjee, N. Bevilacqua, A. Mohseninia, B. Wiedemann, F. Wilhelm, J. Scholta, R. Zeis, Carbon felt electrodes for redox flow battery: Impact of compression on transport properties. *Journal of Energy Storage* 26 (2019) 100997. <https://doi.org/10.1016/j.est.2019.100997>.

[291] J. Gonzàlez-Garcìa, P. Bonete, E. Expòsito, V. Montiel, A. Aldaza, R. Torregrosa-Macià, Characterization of a carbon felt electrode: structural and physical properties. *J. Mater. Chem.* 9 (1999) 419-426. <https://doi.org/10.1039/A805823G>.

[292] A. E. Rue1, M. M. Collinson, Size and Shape Control of Gold Nanodeposits in an Array of Silica Nanowells on a Gold Electrode. *International Journal of Electrochemistry* 2012 971736. <https://doi.org/10.1155/2012/971736>.

[293] M. Lundström, J. Aromaa, O. Forsén, Redox potential characteristics of cupric chloride solutions. *Hydrometallurgy* 95 (2009) 285-289. <https://doi.org/10.1016/j.hydromet.2008.06.009>.

[294] B. Schwenzer, J. Zhang, S. Kim, L. Li, J. Liu, Z. Yang, Membrane development for vanadium redox flow batteries. *Chem. Sus. Chem*, 4 (2011) 1388-1406, <https://doi.org/10.1002/cssc.201100068>

[295] T. Mohammadi, M. Skyllas-Kazacos, Characterisation of novel composite membrane for redox flow battery applications. *J. Membr. Sci.* 98 (1995) 77-87.

- [296] T. Xu, Ion exchange membranes: State of their development and perspective. *J. Membr. Sci.* 263 (2005) 1-29
- [297] T. Kyu, Structure and properties of perfluorinated ion-exchange membranes. *ACS Symposium Series 269, Materials Science of Synthetic Membranes 18* (1985) 365-405 , DOI: 10.1021/bk-1985-0269.ch018
- [298] H. Prifti, A. Parasuraman, S. Winardi, T. M.Lim, M. Skyllas-Kazacos, Membranes for Redox Flow Battery Applications, *Membranes 2(2) (2012) 275-306*, <https://doi.org/10.3390/membranes2020275>
- [299] T. Mohammadi, M. Skyllas-Kazacos, Modification of anion-exchange membranes for vanadium redox flow battery applications, *Journal of Power Sources 63(2) (1996) 179-186*, [https://doi.org/10.1016/S0378-7753\(96\)02463-9](https://doi.org/10.1016/S0378-7753(96)02463-9)
- [300] S. D. Mikhailenko, K. Wang, S. Kaliaguine, P. Xing, G. P. Robertson, M. D. Guiver, Proton conducting membranes based on cross-linked sulfonated poly(ether ether ketone), *Journal of Membrane Science, 233(1-2) (2004) 93-99*, <https://doi.org/10.1016/j.memsci.2004.01.004>.
- [301] L. Feng, X. Sun, S. Yao, C. Liu, W. Xing, J. Zhang, 3 - Electrocatalysts and Catalyst Layers for Oxygen Reduction Reaction, *Rotating Electrode Methods and Oxygen Reduction Electrocatalysts (2014) 67-132*, <https://doi.org/10.1016/B978-0-444-63278-4.00003-3>.
- [302] C. Stolze, M. D. Hager, U. S. Schubert, State-of-charge monitoring for redox flow batteries: A symmetric open-circuit cell approach, *Journal of Power Sources 423 (2019) 60-67*, <https://doi.org/10.1016/j.jpowsour.2019.03.002>.
- [303] M. Skyllas-Kazacos, M. Kazacos, State of charge monitoring methods for vanadium redox flow battery control, *Journal of Power Sources 196, 20 (2011) 8822-8827*, <https://doi.org/10.1016/j.jpowsour.2011.06.080>.
- [304] K. Ngamsai, A. Arpornwichanop, Measuring the state of charge of the electrolyte solution in a vanadium redox flow battery using a four-pole cell device,

Journal of Power Sources 298 (2015) 150-157,
<https://doi.org/10.1016/j.jpowsour.2015.08.026>.

[305] K. W. Knehr, E. C. Kumbur, Open circuit voltage of vanadium redox flow batteries: Discrepancy between models and experiments, *Electrochemistry Communications* 13, 4 (2011) 342-345, <https://doi.org/10.1016/j.elecom.2011.01.020>.

[306] M. R. Mohamed, H. Ahmad, M. N. Abu Seman, Estimating the State-of-Charge of all-Vanadium Redox Flow Battery using a Divided, Open-circuit Potentiometric Cell, *Electronics* 19 (2013) 3, <https://doi.org/10.5755/j01.eee.19.3.1623>.

[307] Z. Wei, S. Meng, K. J. Tseng, T. M. Lim, B. H. Soong, M. Skyllas-Kazacos, An adaptive model for vanadium redox flow battery and its application for online peak power estimation, *Journal of Power Sources* 344 (2017) 195-207, <https://doi.org/10.1016/j.jpowsour.2017.01.102>.

[308] S. Kyung-Hee, J. Chang-Soo, S. Jae-Young, P. Se-Kook, K. Dong-Ha, Y. Sun-Hwa, Real-time monitoring of the state of charge (SOC) in vanadium redox-flow batteries using UV–Vis spectroscopy in operando mode, *Journal of Energy Storage* 27 (2020) 101066, <https://doi.org/10.1016/j.est.2019.101066>.

[309] G. Kwon, S. Lee, J. Hwang, H.-S. Shim, B. Lee, M. H. Lee, Y. Ko, S.-K. Jung, K. Ku, J. Hong, K. Kang, Multi-redox Molecule for High-Energy Redox Flow Batteries, *Joule* 2(9) (2018) 1771-1782, <https://doi.org/10.1016/j.joule.2018.05.014>.

[310] S. Roe, C. Menictas, M. Skyllas-Kazacos, A High Energy Density Vanadium Redox Flow Battery with 3 M Vanadium Electrolyte, *J. Electrochem. Soc.* 163 (2016) A5023-A5028, [10.1149/2.0041601jes](https://doi.org/10.1149/2.0041601jes).

[311] L. Zhang, Q. Lai, J. Zhang, H. Zhang, A High-Energy-Density Redox Flow Battery based on Zinc/Polyhalide Chemistry, *ChemSusChem* Volume 5(5) (2012) 867-869, <https://doi.org/10.1002/cssc.201100530>.

[312] H. S. Lim, A. M. Lackner, R. C. Knechtli, Zinc-Bromine Secondary Battery, *J. Electrochem. Soc.*, 124 (1977) 1154, <https://doi.org/10.1149/1.2133517>

- [313] A. Khor A, P. Leung, M. R. Mohamed, C. Flox, Q. Xu, L. An, R. G. A. Wills, J. R. Morante, A. A. Shah, Review of zinc-based hybrid flow batteries: from fundamentals to applications. *Mater Today Energy* 8 (2018) 80–108. <https://doi.org/10.1016/j.mtener.2017.12.012>.
- [314] K. Amini, M. D. Pritzker, Improvement of zinc-cerium redox flow batteries using mixed methanesulfonate-chloride negative electrolyte, *Applied Energy* 255 (2019) 113894 <https://doi.org/10.1016/j.apenergy.2019.113894>
- [315] X. Li, Modeling and simulation study of a metal free organic–inorganic aqueous flow battery with flow through electrode, *Electrochimica Acta* 170 (2015) 98-109, <https://doi.org/10.1016/j.electacta.2015.04.075>.
- [316] M. C. Tucker, A. Phillips, A. Z. Weber, All-Iron Redox Flow Battery Tailored for Off-Grid Portable Applications, *ChemSusChem*, 8 (2015) 3996-4004, [10.1002/cssc.201500845](https://doi.org/10.1002/cssc.201500845).
- [317] Z. Xu, Q. Fan, Y. Li, J. Wang, P. D. Lund, Review of zinc dendrite formation in zinc bromine redox flow battery, *Renewable and Sustainable Energy Reviews*, 127 (2020) 109838 <https://doi.org/10.1016/j.rser.2020.109838>